Osswald, Rudolph

Polymer Rheology

Tim Osswald
Natalie Rudolph

Polymer Rheology

Fundamentals and Applications

HANSER

Hanser Publishers, Munich
Hanser Publications, Cincinnati

The Authors:

Tim Osswald,
Natalie Rudolph,

Polymer Engineering Center
Department of Mechanical Engineering
University of Wisconsin-Madison
Madison, WI 53706 USA

Distributed in North and South America by:
Hanser Publications
6915 Valley Avenue, Cincinnati, Ohio 45244-3029, USA
Fax: (513) 527-8801
Phone: (513) 527-8977
www.hanserpublications.com

Distributed in all other countries by
Carl Hanser Verlag
Postfach 86 04 20, 81631 München, Germany
Fax: +49 (89) 98 48 09
www.hanser-fachbuch.de

Authors' Disclaimer:
The data and information presented in this book have been collected by the authors and publisher from many sources that are believed to be reliable. However, the authors and publisher make no warranty, expressed or implied, to this book's accuracy or completeness. No responsibility or liability is assumed by the authors and publisher for any loss or damage suffered through reliance on any information presented in this book.
The authors do not purport to give any toxicity or safety information.

The final determination of the suitability of any information for the use contemplated for a given application remains the sole responsibility of the user.

Cataloging-in-Publication Data is on file with the Library of Congress

Bibliografische Information Der Deutschen Bibliothek
Die Deutsche Bibliothek verzeichnet diese Publikation in der Deutschen Nationalbibliografie;
detaillierte bibliografische Daten sind im Internet über <http://dnb.d-nb.de> abrufbar.

ISBN 978-1-56990-517-3
E-Book ISBN 978-1-56990-523-4

Editor: Christine Strohm
Production Management: Jörg Strohbach
Coverconcept: Marc Müller-Bremer, www.rebranding.de, München
Coverdesign: Stephan Rönigk
Layout: Manuela Treindl, Fürth
Printed and bound by Kösel, Krugzell
Printed in Germany

Dedication

We dedicate this book to our friend, colleague, and mentor Professor Dr.-Ing. Dr. h.c. Gottfried W. Ehrenstein. His lifelong commitment to learning, teaching, and research has inspired more than a generation of students and engineers, and has resulted in a continuous flow of ideas and innovation in plastics technology.

Preface

Designed to provide a polymer rheology background to both engineering students and practicing engineers, this book is written at an intermediate level with the technical information and practical examples required to enable the reader to understand the complex rheological behavior of polymers and its far-reaching consequences. It also provides the necessary decision-making tools for the appropriate choice of rheological testing methods, and the means to troubleshoot rheology related problems encountered in polymer processing. The organization of Polymer Rheology – Fundamentals and Applications and the practical examples throughout the book make it an ideal textbook and reference book, and the information provided is particularly valuable to processors and raw materials suppliers.

The authors would like to acknowledge the invaluable help of many during the preparation of this manuscript: our colleagues at the Polymer Engineering Center at the University of Wisconsin-Madison and at the Institute for Polymer Technology at the Friedrich-Alexander-University in Erlangen, Germany. In particular we would like to thank Dr. Andrew Schmalzer for serving as a sounding board and for his input, John Puentes for helping with the example problems in Chapter 4, Chuanchom Aumnate for the measurements used in the examples in Chapters 2 and 5, and Camilo Perez for reviewing Chapter 3. We are grateful to Tobias Mattner for his outstanding job in not only drawing the figures, but also making excellent suggestions on how to more clearly present the information. Thanks are due to Dr. Christine Strohm for her valuable expertise in editing this book. Dr. Nadine Warkotsch, Dr. Mark Smith and Jörg Strohbach of Carl Hanser Verlag in Munich are thanked for their support throughout this project. Above all, the authors would like to thank their families for their continued support of their work and their input throughout the writing of this book.

Summer 2014

Tim Osswald and *Natalie Rudolph*
Madison, Wisconsin, USA

Contents

Dedication V

Preface VII

1 Introduction to Rheology 1
- 1.1 The Field of Rheology 5
- 1.2 Viscous Liquids or the Newtonian Fluid 7
- 1.3 Linear Elasticity or the Hookean Spring 10
- 1.4 Viscoelasticity and the Maxwell Model 13
- 1.5 Time Scale and the Deborah Number 16
- 1.6 Deformation, Rate of Deformation, and the Deviatoric Stress Tensors . . . 18
- 1.7 Guide to the Book 20
- Problems 21
- References 21

2 Structure and Properties of Deforming Polymers 25
- 2.1 Molecular Structure of Polymers 25
- 2.2 Stress Relaxation Behavior 32
- 2.3 Shear Thinning Behavior 37
- 2.4 Normal Stresses in Shear Flow 40
- 2.5 Stress Overshoot during Start-up Flow 44
- 2.6 Melt Strength or Melt Fracture 45
- 2.7 Dynamic Response 47
- Problems 56
- References 57

3 Generalized Newtonian Fluid (GNF) Models 59
- 3.1 Temperature Dependence of Viscosity 61
- 3.2 Viscous Flow Models 65
  - 3.2.1 The Power Law Model 66
  - 3.2.2 The Bird-Carreau-Yasuda Model 68

3.2.3 The Cross-WLF Model 70
3.2.4 The Bingham Model 71
3.2.5 The Herschel-Bulkley Model 72
3.2.6 Accounting for Pressure Dependence in Viscous Flow Models . 73
3.2.6.1 Power Law 73
3.2.6.2 Carreau-WLF 73
3.2.6.3 Cross-WLF 74
3.2.6.4 Universal Temperature and Pressure Invariant Viscosity Function 75
3.3 Elongational Viscosity 80
3.4 Suspension Rheology 82
3.5 Chemo-Rheology 87
Problems 95
References 97

4 Transport Phenomena 101
4.1 Dimensionless Groups 102
4.2 Balance Equations 106
4.2.1 The Mass Balance or Continuity Equation 106
4.2.2 The Material or Substantial Derivative 107
4.2.3 The Momentum Balance or Equation of Motion 109
4.2.4 The Energy Balance or Equation of Energy 114
4.3 Model Simplification 117
4.3.1 Reduction in Dimensionality 119
4.3.2 Lubrication Approximation 123
4.4 Viscometric Flows 125
4.4.1 Pressure Driven Flow of a Newtonian Fluid through a Slit . . . 125
4.4.2 Flow of a Power Law Fluid in a Straight Circular Tube (Hagen-Poiseuille Equation) 126
4.4.3 Volumetric Flow Rate of a Power Law Fluid in Axial Annular Flow 129
4.4.4 Circular Annular Couette Flow of a Power Law Fluid 131
4.4.5 Squeezing Flow of a Newtonian Fluid between Two Parallel Circular Discs 134
4.4.6 Flow of a Power Law Fluid between Two Parallel Circular Discs 137
Problems 140
References 141

5 Viscoelasticity . . . 143

5.1 Linear Viscoelasticity . . . 144
  5.1.1 Relaxation Modulus . . . 144
  5.1.2 The Boltzmann Superposition Principle . . . 145
  5.1.3 The Maxwell Model – Relaxation . . . 147
  5.1.4 Kelvin Model . . . 148
  5.1.5 Jeffrey’s Model . . . 150
  5.1.6 Standard Linear Solid Model . . . 152
  5.1.7 The Generalized Maxwell Model . . . 154
  5.1.8 Dynamic Tests . . . 160
5.2 Non-Linear Viscoelasticity . . . 164
  5.2.1 Objectivity . . . 164
  5.2.2 Differential Viscoelastic Models . . . 166
  5.2.3 Integral Viscoelastic Models . . . 179
  References . . . 184

6 Rheometry . . . 187

6.1 The Sliding Plate Rheometer . . . 189
6.2 The Cone-Plate Rheometer . . . 191
6.3 The Parallel-Plate Rheometer . . . 194
6.4 The Capillary Rheometer . . . 196
  6.4.1 Computing Viscosity Using the Bagley and Weissenberg-Rabinowitsch Equations . . . 198
  6.4.2 Viscosity Approximation Using the Representative Viscosity Method . . . 201
6.5 The Melt Flow Indexer . . . 202
6.6 Extensional Rheometry . . . 203
6.7 High Pressure Rheometers . . . 209
6.8 Integrated Mold Sensors for Quality Control . . . 214
  Problems . . . 217
  References . . . 218

Subject Index . . . 221

1

Introduction to Rheology

On December 9th of 1929, a little over a month after the Wall Street crash, and seven years after he published his book *Fluidity and Plasticity* [1], Eugene Bingham (Fig. 1.1), a chemistry professor at Lafayette College in Easton, Pennsylvania, and a group of chemists, engineers, and physicists met for the first time in Washington D.C.; they called themselves the *Society of Rheology*. Hence, for the first time the word rheology, coined by Markus Reiner and Eugene Bingham in 1920, was officially used[1].

Figure 1.1
Professor Eugene Bingham, in 1945 shortly before his death (Courtesy of Special Collections & College Archives, Skillman Library, Lafayette College)

---

[1] The roots of the word rheology are the Greek “reo” (flow) and “logos” (study).

However, the history of the field of rheology goes back centuries prior to Bingham and Reiner. A historical review is not complete until the more important events and discoveries through time, and the people who made those events and discoveries possible, have been identified. In Table 1.1 we list these events, discoveries, and important publications. If we inadvertently left out some, we apologize.

Table 1.1 Historical overview of the field of rheology

When	Who	What	Ref
1663	B. Pascal	Published works on inviscid fluids	[2]
1678	R. Hooke	Published work on elastic springs	[3]
1687	I. S. Newton	Published work on viscous fluids	[4]
1705	Bernoulli brothers	Publish the Bernoulli equation	[5]
1807	T. Young	Proposes the elastic (Young's) modulus	[6]
1820	C. Navier	Describes behavior of Newtonian fluids which eventually becomes the Navier-Stokes equation	[7]
1822	A. Cauchy	Describes stress and strain and formulates the Cauchy deformation tensor	[7]
1829	S. Poisson	Describes Poisson's ratio, ν	[8]
1839	G. Hagen	Builds the first capillary viscometer	[9]
1840	J. L. M. Poiseuille	Studies the rheology of blood and builds a capillary viscometer	[10]
1845	G. G. Stokes	Formulates a three dimensional Newtonian fluid model	[11]
1849	G. G. Stokes	Studies the parabolic velocity distribution in a capillary	[5]
1851	G. G. Stokes	Sphere fall experiments	[12]
1859	A. V. Lourenço	Observes viscosity increase with an increase in molecular weight	[13]
1861	A. Lipowitz	Builds a penetrometer to measure the hardness of a gel with a sinking weight	[14]
1861	T. Graham	Coins the word "Colloid"	[15]
1867	J. C. Maxwell	Formulates the viscoelastic Maxwell model	[16]
1873	J. D. Van der Waals	Publishes work on intramolecular forces	[17]
1874	L. Boltzmann	Publishes the superposition principle	[18]
1876	L. Boltzmann	Publishes work on the memory function	[19]
1881	M. Margules	Derives equations that describe the viscosity in the shear flow between two concentric cylinders	[20]
1886	M. M. Couette	Derives equations that describe the viscosity in the shear flow between two concentric cylinders	[21]
1888	M. M. Couette	Builds the first concentric cylinder system to measure viscosity; the drag flow viscometer or the Couette device	[22]
1890	W. Thomson-Kelvin	Describes a "solid viscosity", meaning a viscoelastic solid, known today as the Kelvin model	[5]
1890	W. Voigt	Publishes experiments on viscoelastic solids	[23]
1891	W. Ostwald	Builds a capillary viscometer, Ostwald viscosimeter	[14]

Table 1.1 (*continued*) Historical overview of the field of rheology

When	Who	What	Ref
1894	J. Finger	Formulates the Finger-Strain Tensor for shear and elongational deformation test specimens	[24]
1905	F. T. Trouton	Derives the equation $\mu_E = 3\mu_S$, which describes the relation between elongational and shear viscosities, known today as the Trouton viscosity	[25]
1906	A. Einstein	Derives the equation $\mu = \mu_0 (1 + 2.5\phi)$, which defines the viscosity of a suspension as a function of the volume fraction of solid particles	[26]
1916	E. Bingham	Describes fluids with a yield stress; the Bingham fluid	[27]
1920	H. Staudinger	Describes polymers as rigid rods that he calls macromolecules	[28]
1922	E. Bingham	Publishes his book “Fluidity and Plasticity”	[29]
1923	A. de Waele	Derives a power relation between viscosity and rate of deformation; the power-law model.	[30]
1925	W. Ostwald	Two years after de Waele, derives the power relation between viscosity and rate of deformation; the power-law model or the Ostwald-de Waele model	[31]
1927	S. B. Ellis	Publishes work on flow behavior	[5]
1928	E. Hatschek	Publishes his book “The Viscosity of Liquids”	[32]
1929	E. Bingham	Founds the Society of Rheology	[33]
1929	R. Eisenschitz, B. Rabinowitsch and K. Weissenberg	Propose the rheological energy triangle	[34]
1929	B. Rabinowitsch	Derives a correction factor for the shear rate of non-Newtonian fluids in capillary viscometers	[35]
1929	H. Jeffreys	Publishes his book “The Earth”, in which he describes “elastoviscous” (viscoelastic fluids) materials	[36]
1930	C. W. Brabender	Builds a dough kneader; Farinograph or Extensograph	[14]
1931	A. Nadai	Publishes his book “Plasticity”	[37]
1934	M. Mooney	Proposes a “shearing disc viscometer” or parallel disc viscometer	[38]
1934	M. Mooney and R. H. Ewart	For the first time use a cone-and-plate rheometer	[39]
1935	H. Freundlich	Coins the word “Thixotropy” to describe changes in fluid behavior caused by movement	[40]
1935	J. M. Burgers	Develops a viscoelastic model by combining the Maxwell and the Kelvin-Voigt models	[41]
1936	E. Guth and R. Simha	Modify Einstein’s 1906 equation to $\mu = \mu_0 (1 + 2.5\phi + 14.1\phi^2)$ for the viscosity of a suspension	[42]
1938	G. W. S. Blair	Publishes his book “An Introduction to Industrial Rheology”, for the first time using the word “rheology” in the title of a book	[43]
1940	M. Mooney	Publishes work on rubber elasticity	[44]
1945	M. Reiner	Proposes that the theories of fluid viscosity also apply to polymer melts	[45]

Table 1.1 (*continued*) Historical overview of the field of rheology

When	Who	What	Ref
1945	Brookfield Company	First Brookfield rotational viscometer is marketed in Stoughton, Massachusetts	[46]
1946	M. S. Green and A. V. Tobolsky	Propose the Transient Network Model for uncross-linked polymers	[47]
1946	R. J. Russell	Measures normal stresses using parallel disc and cone-and-plate rheometers	[48]
1947	K. Weissenberg	Discovers the rod climbing effect, today known as the Weissenberg Effect	[49]
1948	R. S. Rivlin	Applies theories of fluid viscosity to polymer melts	[50]
1948	G. W. S. Blair	First International Congress on Rheology	[51]
1953	P. E. J. Rouse	Proposes a bead-spring model for cross-linked polymers; known as the Rouse model	[52]
1955	M. L. Williams, R. F. Landel and J. D. Ferry	Propose the time-temperature superposition principle	[53]
1955	Haake Company	Rotational viscometer is marketed in Berlin and Karlsruhe, Germany	[46]
1956	B. H. Zimm	Includes hydrodynamic interactions in the Rouse model for dilute polymeric suspensions: Rouse-Zimm model.	[54]
1956	A. Lodge	Expands the Transient Network Model by Green and Tobolsky	[55]
1956	F. R. Eyrich	Publishes his book "Rheology – Theory and Applications"	[56]
1957	E. B. Bagley	Derives the entrance pressure corrections for capillary viscometers, known today as Bagley end correction factor	[57]
1958	W. P. Cox and E. H. Merz	Propose a relation between frequency in the oscillatory test and rate of deformation in the rotational viscometer (Cox-Mertz relation)	[58]
1960	R. B. Bird, W. E. Stewart and E. Lightfoot	Publish their book "Transport Phenomena", nicknamed "BSL"	[59]
1960	A. S. Lodge	Publishes his book "Elastic Liquids"	[60]
1960	M. Reiner	Publishes his book" Deformation, Strain and Flow"	[61]
1962	A. Kaye	Develops the integral viscoelastic model that later became known as the K-BKZ model	[62]
1963	B. Bernstein, E. Kearsley and L. Zapas	Develop the integral viscoelastic model that Kaye published 2 years earlier. The model became known as the K-BKZ model	[63]
1965	M. M. Cross	Proposes the Cross model for shear-thinning fluids with a small shear rate Newtonian plateau	[64]
1966	H. Giesekus	Develops the differential viscoelastic model that became known as the Giesekus model	[65]
1967	S. F. Edwards	Proposes Entanglement Theory for polymers	[66]
1968	P. J. Carreau	Proposes a viscosity model with a small and large shear rate Newtonian plateau; Bird-Carreau Model	[67]

Table 1.1 (*continued*) Historical overview of the field of rheology

When	Who	What	Ref
1969	J. Meissner	Designs the uniaxial elongational rheometer	[68]
1971	P. G. DeGennes	Proposes the Reptation Model for polymer molecules	[69]
1977	R. B. Bird, R. C. Armstrong and O. Hassager	Publish their book “Dynamics of Polymeric Liquids”	[70]
1977	R. B. Bird, O. Hassager, R. C. Armstrong and C. F. Curtis	Publish their book “Kinetic Theory”	[71]
1982	J. M. Dealy	Publishes his book “Rheometers for Molten Plastics”	[72]
1985	R. B. Bird and H. Giesekus	Develop model for non-linear deformation behavior	[46]
1986	M. Doi and S. F. Edwards	Further develop the Reptation model	[73]
1990	J. M. Dealy and K. F. Wissbrun	Publish their book “Melt Rheology and Its Role in Plastics Processing”	[74]
1994	C. W. Macosko	Publishes his book “Rheology: Principles, Measurements and Applications”	[75]
1997	P. J. Carreau, D. C. R. DeKee and R. P. Chhabra	Publish their book “Rheology of Polymeric Systems – Principles and Applications”	[76]

1.1 The Field of Rheology

While the motto of the Society of Rheology has always been the quote by Simplicius and Heraclitus “Πάντα ῥεῖ” (Panta rei) [77–81] or “everything flows,” the field of rheology covers the behavior of perfectly viscous liquid (Newtonian fluid) materials and perfectly elastic solid (Hookean solid) materials, as depicted in the diagram in Fig. 1.2. From the outside, rheology is framed by the rigid solid, or Euclidean solid, and the ideal inviscid fluid, or Pascalian fluid. The Euclidean solid and Pascalian fluid are both mathematical idealizations. In the case of the Euclidean solid we assume that the body does not deform, and when it moves, it does so by pure translation and rotation. On the other hand, the assumption for the Pascalian fluid is that the stresses acting on the fluid are only a result of pressure, or hydrostatic stresses, and not the result of deformation during flow. From a material behavior point of view, a Euclidean solid has an infinite modulus, while a Pascalian fluid exhibits zero viscosity, two unrealistic extremes.

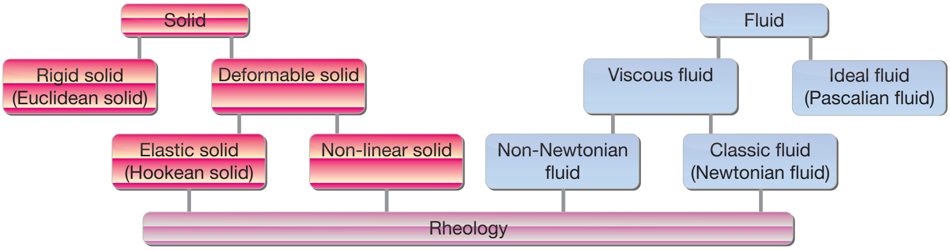

Figure 1.2 The field of rheology in perspective

While the field of rheology encompasses materials with a finite modulus and a measurable viscosity, most materials are neither perfectly viscous liquids nor perfectly elastic solids, but viscoelastic materials that can be described from a fluids or a solids point of view by a rheologist or a solid mechanician, respectively. Either way, when deforming complex materials such as polymers, there will always be a viscous and an elastic force component. To simplify our lives and make calculations and predictions possible, particularly when the flow geometry is complex, such as plastic flow during injection molding, we often drop the elastic response of plastics during flow.

In 1929, Eisenschitz, Rabinowitsch, and Weissenberg [7] proposed a triangular coordinate system (Fig. 1.3) to clarify the boundaries of the field of rheology. It represents the work or energy in all rheological phenomena in the form of kinetic energy, elastic or stored energy, and dissipated or lost energy. It is a simple and descriptive way to illustrate the interconnection between these energies or work. In most cases, the state of a body or system is represented by a point in the interior of the triangle, where the distance a is the fraction of the total energy represented by kinetic energy, b is the fraction representing elastic or stored energy, and c is the fraction representing dissipated or lost energy, such that

$$a + b + c = 1 \tag{1.1}$$

Eisenschitz, Rabinowitsch and Weissenberg called the line *AB* “Elasticity,” which represents a Hookean solid or perfectly elastic solid. Vertex *A* represents a pure Euclidean solid (or Pascalian liquid when on line *AC*) where all the external work is converted to kinetic energy, as would be the case for an infinitely stiff body. Furthermore, they called line *AC* “Viscosity,” which represents a Newtonian fluid or perfectly viscous liquid where all external work is dissipated or lost. On that line, vertex *A* represents an infinite Reynolds number in fluid mechanics. Line *BC*, which they called “Relaxation,” represents creeping viscoelastic flows, and is the domain where we typically see the field of rheology of highly viscous materials such as polymers. Vertex *C* represents a creeping flow or Stokes flow where the Reynolds number is very low. In such flows inertial effects are negligible when compared to the forces caused by viscous friction.

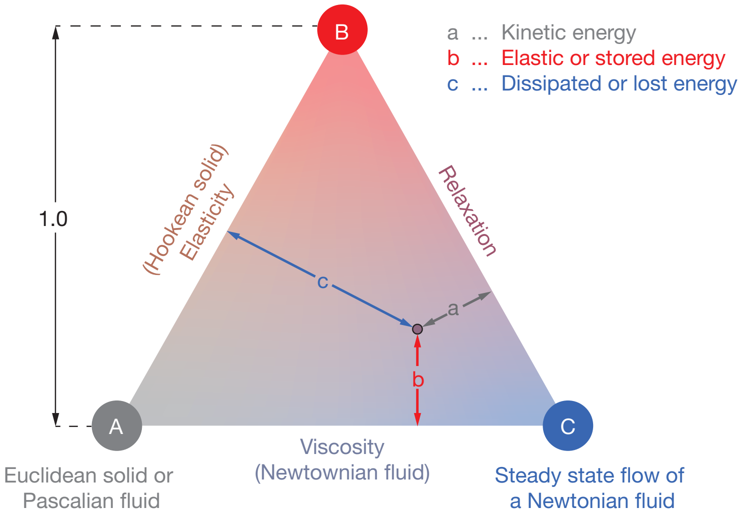

Figure 1.3 Rheological energy in triangular coordinates

1.2 Viscous Liquids or the Newtonian Fluid

Sir Isaac Newton (Fig. 1.4) was the first person to formulate a hypothesis that described the resistance to motion experienced by deforming fluids. In 1686 he published this work in Philosophiæ Naturalis Principia Mathematica [4] in a chapter titled "On the Circular Motion of Liquids". His hypothesis clearly states what we know today as a characterictic of a Newtonian fluid[2]:

That the resistance which arises from the lack of slipperiness of the parts of the fluid, other things being equal, is proportional to the velocity with which the parts of the liquid are separated from one another.

The phenomenon, described by Newton as "*defectu lubricitatis*," or "lack of slipperiness" between two fluid particles, was attributed to "*attritus*," meaning internal friction, or viscous friction. Since that time, the term "internal friction" and "viscous friction" have been used interchangeably. Although Newton's original work contains a mistake, corrected by Sir George Stokes [3] 150 years later, his main conclusion is still correct; it basically states that the force F required to maintain the motion between two fluid planes located at two arbitrary positions, say C and D in Newton's diagram (Fig. 1.5), is proportional to the difference between the velocity, u, of the

---

[2] The authors are using Emil Hatschek's translation from the Latin [2].

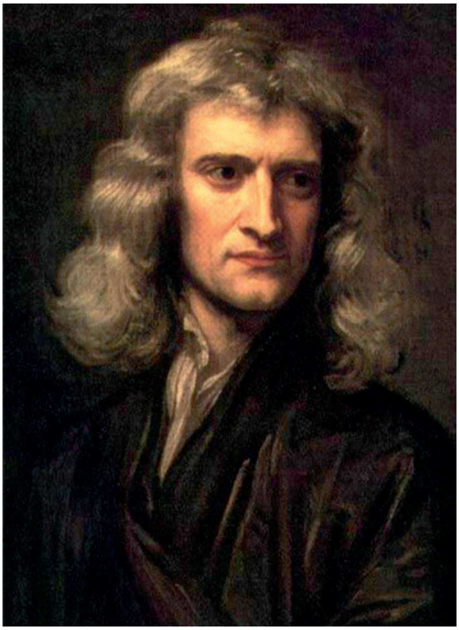

Figure 1.4
Sir Isaac Newton (1643–1727), painted in 1689 by Sir Godfrey Kneller

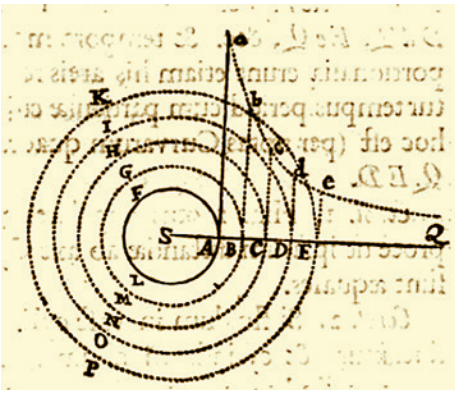

Figure 1.5
Diagram from Newton's 1686 publication [2]

two planes, and inversely proportional to the distance, r, between those two surfaces, the viscosity, η, and the area of the surfaces that separates them, A,[3]

$$F = A\eta \frac{u_{\mathrm{d}} - u_{\mathrm{c}}}{r_{\mathrm{D}} - r_{\mathrm{C}}} \tag{1.2}$$

---

[3] Newton used upper case A, B, C, D, etc. to describe the position of the surfaces, and lower case a, b, c, d, etc. to describe the velocity of those surfaces.

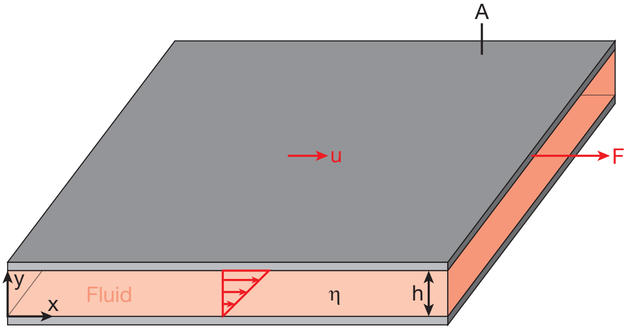

Figure 1.6 Simple shear flow with Cartesian coordinates

As shown in Newton's diagram, his analysis pertained to a rotating cylinder immersed in an infinitely large fluid body. For a more simplified system, such as the simple shear flow generated between two parallel plates presented in Fig. 1.6, Equation 1.2 can be expressed in terms of shear stress, and written as

$$F/A = \eta \frac{u}{h} \tag{1.3}$$

or

$$\tau_{xy} = \eta \dot{\gamma}_{xy} \tag{1.4}$$

where τ_{xy} is the shear stress in the x direction on a plane with its normal direction pointing in the y direction, and $\dot{\gamma}_{xy}$ is the corresponding rate of shear, or rate of deformation. The stress (here τ_{xy}) that leads to the deformation of the fluid contained within the system is also often referred to as the deviatoric stress[4].

The Newtonian model, or the viscous component of a material, is often also represented using a dashpot, shown in Fig. 1.7.

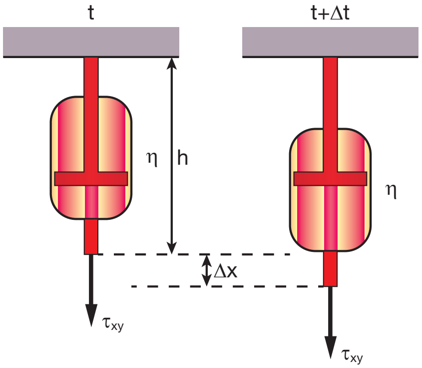

Figure 1.7 The dashpot – a schematic representation of a Newtonian fluid

---

[4] As will be shown in Chapter 2, which covers flow, the total stress, σ, is divided into the deviatoric stress component, τ, which causes deformation, and the hydrostatic stress component, which results from pressure, p.

While the schematic representation in Fig. 1.7 reflects an elongational deformation along the *x*-axis, the dashpot can also be used for shear deformation, which is written as

$$\gamma_{xy} = \frac{\Delta x}{h} \tag{1.5}$$

Figure 1.7 also shows that the deformation is time dependent and, in the case of a Newtonian fluid, the dependence between deformation and time is linear. In terms of shear strain rate, we can write

$$\gamma_{xy} = \dot{\gamma}_{xy}\,\Delta t \tag{1.6}$$

In Fig. 1.8, the strain within a Newtonian fluid, labeled as viscous strain, is presented for the case where a constant stress is applied during a time period from 0 to Δt. Once the load is released at time Δt, the material element remains deformed. This reflects point "C" in the Eisenschitz, Rabinowitsch and Weissenberg triangle, at which all energy is dissipated or lost and the deformation can no longer be recovered.

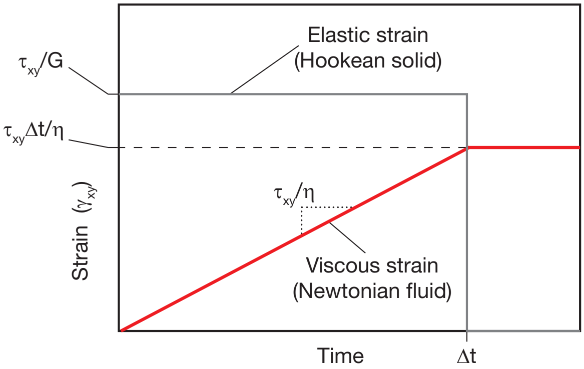

Figure 1.8 Strain response of a Newtonian fluid and a Hookean solid

1.3 Linear Elasticity or the Hookean Spring

Robert Hooke is a relatively unknown English scientist and engineer of the 17th century, who was completely overshadowed by his contemporary, Isaac Newton. In fact, an animosity between the two existed after Hooke claimed that Newton's work on gravitation was based on work he had done. As a result, Newton's obsession was to make sure that Hooke be forgotten; something he almost accomplished. Two years after Hooke's death in 1703, Newton became president of the Royal Society, and in that function made sure that every memory of Hooke was erased from the society, including his portrait and laboratory equipment, which mysteriously disappeared when the Royal Society moved to a new location after 1705.

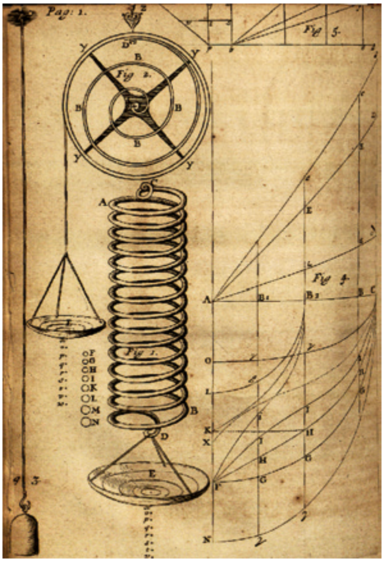

Figure 1.9 Diagram from Hooke's 1678 paper

However, while Hooke is certainly not part of popular culture in the way Newton has become, today his name remains well known among engineers who deal with solid mechanics, thanks to his theory of linear elasticity. Robert Hooke was the first person to find a relation between force and deflection in linear elastic solids, and published that work in his 1678's "*Lectures de Potentia Restitutiva*," or, "Of Spring". The basic theory behind what we today refer to as the Hookean spring (Fig. 1.9) is summarized in Latin by Hooke's words "*Ut tension sic vis*" or "*As the extension, so the force*." More simply stated, we can say that the force, F, is directly proportional to the deflection, Δx. This can be written using

$$F = k\,\Delta x \tag{1.7}$$

where k is the constant of proportionality or the spring constant, also called the stiffness. Hooke's concept was modified in 1727 by Leonhard Euler, who represented the force in terms of stress, F/A, and the displacement in terms of strain, $\Delta x/h$, where h represents the original length. The units in the constant of proportionality can be adjusted by using a modulus of elasticity or stiffness, E, or for a system that is deformed in shear, such as the one depicted in Fig. 1.10, a modulus of rigidity, G,

$$F/A = G\left(\Delta x/h\right) \tag{1.8}$$

In terms of stress and strain the above equation can be written as

$$\tau_{xy} = G\gamma_{xy} \tag{1.9}$$

where τ_{xy} is the shear stress and γ_{xy} the corresponding shear strain.

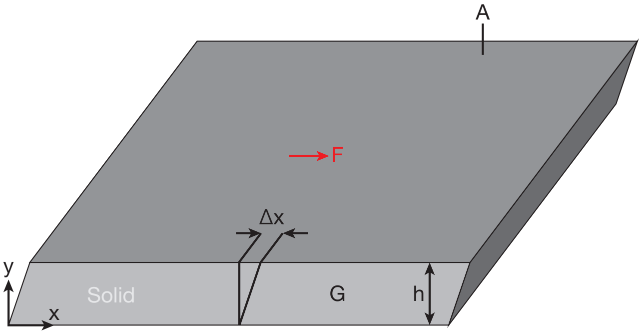

Figure 1.10 Perfectly Hookean solid deformed in shear

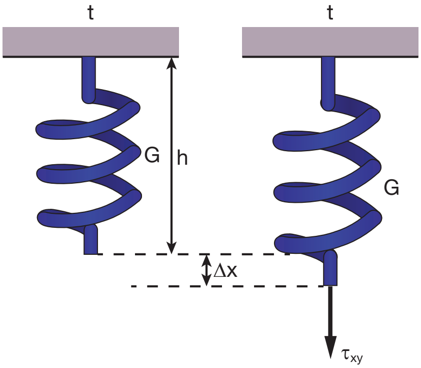

Figure 1.11 The spring – a schematic representation of a Hookean solid

Just like Hooke's approach in 1678, today the elastic component of a material is often represented using a spring, as shown in Fig. 1.11. The spring reflects a stretching body; however, it can also be used to represent shear. In Fig. 1.11 we can see how the spring deforms as soon as the load is applied and remains constant as long as the load remains the same. Once the load is released at time Δt, the material element will almost instantly return to its initial shape. This reflects point "B" in the Eisenschitz, Rabinowitsch and Weissenberg triangle, where the energy is stored and fully recovered.

In his publication, Robert Hooke boldly concluded that the elastic behavior is not only observed in springs, "but in all other springy bodies whatsoever, whether Metal, Wood, Stones, baked Earths, Hair, Horns, Silk, Bones, Sinews, Glass, and the like." His statement may be true for metal, stone, baked earths, and perhaps glass; however, all the other materials have a viscous force component, introducing time dependency when they are deformed, and should therefore be considered as viscoelastic materials.

1.4 Viscoelasticity and the Maxwell Model

After Newton and Hooke proposed their fluid and solid models, the world would have to wait almost two centuries before someone would attempt to model the behavior of a body that has both a viscous and an elastic force component during deformation. In 1867, James Clerk Maxwell (Fig. 1.12) published his paper "On the Dynamical Theory of Gases" [16], in which he presented a model for a system that combines elastic and viscous effects. His model and the resulting linear differential equations that relate stress and strain represent today's Maxwell model, which is graphically depicted by an instantaneous change of the spring and a time-dependent reaction, $t + \Delta t$, of the dash-pot in series, as depicted in Fig. 1.13.

In principle, the model is based on the fact that when a stress τ_{xy} is applied to the system, this stress is the same in both fluid and solid elements, and the total strain is the sum of the elastic strain, γ_{xy}^{G}, and the viscous strain, γ_{xy}^{η}, such that

$$\tau_{xy} = \tau_{xy}^{\eta} = \tau_{xy}^{G} \tag{1.10}$$

and

$$\gamma_{xy} = \gamma_{xy}^{G} + \gamma_{xy}^{\eta} \tag{1.11}$$

which can also be differentiated in time to give a function for total rate of deformation, or rate of strain

$$\dot{\gamma}_{xy} = \dot{\gamma}_{xy}^{G} + \dot{\gamma}_{xy}^{\eta} \tag{1.12}$$

Figure 1.12
James Clerk Maxwell

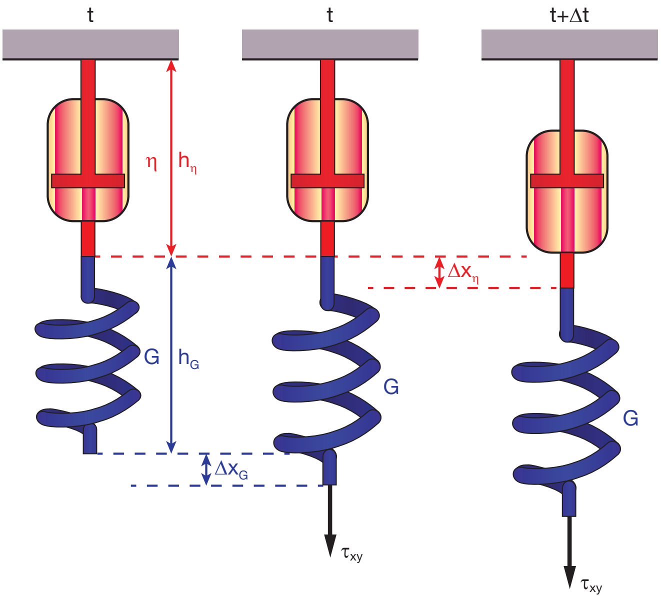

Figure 1.13 Schematic representation of the viscoelastic Maxwell model

Combining Eqs. 1.10–1.12 with the constitutive laws for the dash-pot (Eq. 1.4) and the spring (Eq. 1.9), results in Maxwell's linear differential equation given by

$$\frac{d\tau_{xy}}{dt} = G\frac{d\gamma_{xy}}{dt} - \frac{\tau_{xy}}{\lambda} \tag{1.13}$$

where $\lambda = G/\eta$, which Maxwell called "time of relaxation", and which is now commonly referred to as relaxation time.

In the case of constant stress, Maxwell's linear differential equation is solved for strain

$$\gamma_{xy} = \frac{\tau_{xy}}{\eta}t + \frac{\tau_{xy}}{G} \tag{1.14}$$

which is schematically shown in Fig. 1.14 for the case where the constant stress τ_{xy} is applied from $t = 0$ to $t = \Delta t$. The figure shows how the material element experiences an instant deflection, caused by its elastic component, and continues to deform at a constant rate, caused by its viscous component. The continuous flow experienced by the material under constant load is commonly referred to as creep or retardation. Once the load is released, the stored elastic deformation is recovered, and the viscous deformation remains.

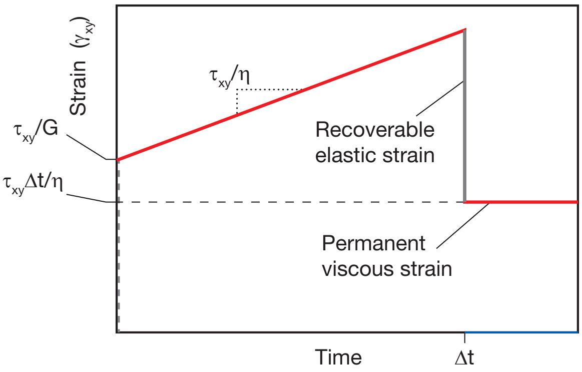

Figure 1.14 Creep in a Maxwell model

In the case of constant strain applied to the Maxwell material model, the linear differential equation is solved for stress

$$\tau_{xy} = G\gamma_{xy}\, e^{-\frac{t}{\lambda}} \tag{1.15}$$

which is schematically depicted in Fig. 1.15 for a case where G = 100 MPa, λ = 1 s and the imposed strain γ_{xy} = 1. Here, we see a gradual reduction in stress, a phenomenon commonly referred to as stress relaxation, which is represented by the line BC on the Eisenschitz, Rabinowitsch and Weissenberg triangle (see Fig. 1.3). At point B in their triangle, the relaxation time λ is infinite, reflecting a Hookean solid, while at position C it is zero, which reflects a Newtonian fluid.

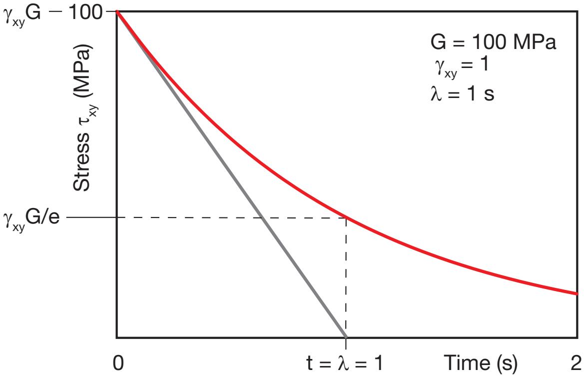

Figure 1.15 Stress relaxation in a Maxwell model

1.5 Time Scale and the Deborah Number

As Maxwell's model easily demonstrates, relaxation time is a property characteristic of a specific material, and the relaxation time limits of zero and infinite frame the field of rheology, ranging from a solid to a liquid. However, when studying a material we need to consider not only its relaxation time, but also the time scale of the process to which the material is subjected under specific circumstances. For example, how fast or how slowly is the material being deformed, or the length of the residence time of a polymer inside an extrusion die.

Returning to Maxwell's model, we can also deform the system at a constant rate of deformation $\dot{\gamma}_{xy}$. For this specific case, Maxwell's model can be solved for stress

$$\tau_{xy} = G\dot{\gamma}_{xy}\left(1 - e^{-\frac{t}{\lambda}}\right) \tag{1.16}$$

Figure 1.16 presents the stress as a function of strain for three different rates of deformation, with G = 100 MPa and λ = 1 s. Each curve is associated with its own time scale. For example, for $\dot{\gamma}_{xy} = 10\ \mathrm{s}^{-1}$, it takes 0.1 s to reach γ_{xy} = 1.0, therefore having a time scale t_p = 0.1 s. For such a small time scale, the material behaves almost like a solid, because there is not sufficient time for the material to relax the stress that built up during deformation. On the other hand, for the material deforming at a much slower rate of 0.1 s^{-1}, the time scale is t_p = 10 s, and there is sufficient time for the stress to relax so that the material behaves more like a fluid. Therefore, while the

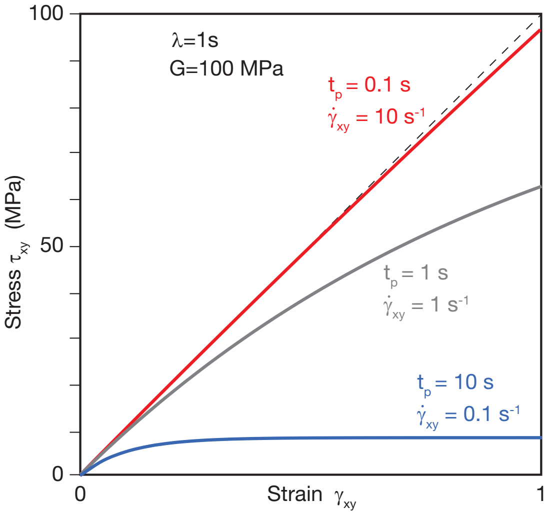

Figure 1.16 Stress as a function of strain for a Maxwell model at various rates of deformation

spring-dashpot system represented in Fig. 1.13, and its response shown in Fig. 1.16, have a fixed relaxation time of 1 s and clearly represent a viscoelastic material, the material's behavior is bound between an elastic solid (straight diagonal line in the diagram), when the process time is zero, and a viscous liquid (horizontal line that represents the strain axis), when the process time is infinite.

While Maxwell explained the viscoelastic behavior of materials using conceptual spring and dashpot elements, it wasn't until polymers became of age for further understanding of viscoelastic behavior of materials to become of extreme importance. Of course, today it is well known that because of their molecular structure, polymers represent the quintessential viscoelastic material. However, it took until 1955 for the concept of stress relaxation and relaxation time, and their relation to molecular structure, to be explained by John Ferry and his coworkers Malcolm Williams and Robert Landel. Williams, Landel, and Ferry directly related stress relaxation time of polymers to the materials' temperature. In their classic paper "The Temperature Dependence of Relaxation Mechanisms in Amorphous Polymers and Other Glass-forming Liquids" [53], Ferry and his coworkers explained how, in order to relax stresses, polymer molecules slide past each other when subjected to a stress. In addition, they demonstrated how a temperature increase accelerates stress relaxation. This effect can be explained by the increase in free volume between the molecules, allowing these molecules to move with more ease, and consequently reducing the relaxation time. Hence, Ferry presented a basic relation between relaxation time and temperature, which today is referred to as time-temperature superposition principle, or often abbreviated as the WLF equation. We shall take a look at Ferry's work in more detail in Chapter 2 of this book.

But lets go back again to the question of whether a material, and particularly a polymeric material, should be considered a solid, a liquid, or a viscoelastic material. Here, we must consider the material's behavior in the context of its specific situation or process. This dilemma was solved in 1964 by Marcus Reiner, of the Technion in Haifa, who introduced the Deborah number (*De*), a dimensionless number that best captures the effect of process time scale on a material's deformational behavior [5]. He chose the name after the Song of Deborah, Judges 5:5, which states "*The mountains flowed before the Lord.*" (Fig. 1.17), which he interpreted to mean that even mountains can appear to flow given a sufficiently large time scale.

The Deborah number is defined by

$$De = \frac{\lambda}{t_\mathrm{p}} \tag{1.17}$$

A Deborah number of zero represents a viscous fluid and a Deborah number of ∞ an elastic solid. For the cases presented in Fig. 1.16, the Deborah number varies between 0.1, for the low rate of deformation, and 10, for the high deformation rate.

Figure 1.17 "The mountains flowed before the Lord." Coyote Buttes North 1 Second Wave, Arizona. Courtesy of Wolfgang Cohnen (© 1998)

1.6 Deformation, Rate of Deformation, and the Deviatoric Stress Tensors

Rheology is concerned with the behavior of fluids undergoing deformation. This deformation can be shear, elongation, or a combination of deformations such as those occuring in the complex flow field within a mixer. If the upper plate in the simple shear flow experiment shown in Fig. 1.6 had a constant speed u_0, it would move a distance D_x in a small time interval Δt. Hence, the shear deformation, which in the *xy*-plane is defined by

$$\gamma_{xy} = \frac{\partial D_x}{\partial y} + \frac{\partial D_y}{\partial x} \tag{1.18}$$

becomes $\gamma_{xy} = D_x / h$ or $\gamma_{xy} = u_0 \, \Delta t / h$.

In the stretching process depicted in Fig. 1.18, assuming a linear increase in velocity from $u_x = u_0$ at $x = 0$, to $u_x = D_R u_0$ at $x = L$, the deformation the material undergoes between those two points is $\gamma_{xx} = \left(D_R u_0 - u_0\right) \Delta t / L$, where D_R is referred to as the draw-down ratio. In addition, the material is also deforming in the *y*-direction by the amount $\gamma_{yy} = -\gamma_{xx}$. Similar to the flow depicted in Fig. 1.18, in polymer processing and rheometry the deformation is a combination of shear and stretching similar to that at the entrance of the capillary in a capillary rheometer. Thus, a more general representation of the deformation is given in tensor form, written as

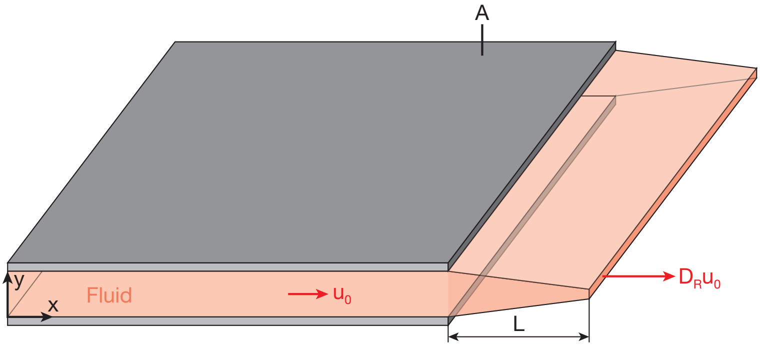

Figure 1.18 Schematic of stretching flow

$$\underline{\underline{\gamma}} = \gamma_{ij} = \begin{bmatrix} \gamma_{xx} & \gamma_{xy} & \gamma_{xz} \\ \gamma_{yx} & \gamma_{yy} & \gamma_{yz} \\ \gamma_{zx} & \gamma_{zy} & \gamma_{zz} \end{bmatrix} \tag{1.19}$$

The rate of deformation tensor can be computed by taking the time derivative of the deformation tensor as

$$\frac{\partial \underline{\underline{\gamma}}}{\partial t} = \underline{\underline{\dot{\gamma}}} = \begin{bmatrix} \dot{\gamma}_{xx} & \dot{\gamma}_{xy} & \dot{\gamma}_{xz} \\ \dot{\gamma}_{yx} & \dot{\gamma}_{yy} & \dot{\gamma}_{yz} \\ \dot{\gamma}_{zx} & \dot{\gamma}_{zy} & \dot{\gamma}_{zz} \end{bmatrix} \tag{1.20}$$

which can also be written as

$$\underline{\underline{\dot{\gamma}}} = \nabla \underline{u} + \nabla \underline{u}^T \tag{1.21}$$

where the velocity gradient $\nabla \underline{u}$ is represented by

$$\nabla \underline{u} = \begin{bmatrix} \frac{\partial u_x}{\partial x} & \frac{\partial u_x}{\partial y} & \frac{\partial u_x}{\partial z} \\ \frac{\partial u_y}{\partial x} & \frac{\partial u_y}{\partial y} & \frac{\partial u_y}{\partial z} \\ \frac{\partial u_z}{\partial x} & \frac{\partial u_z}{\partial y} & \frac{\partial u_z}{\partial z} \end{bmatrix} \tag{1.22}$$

Similar to the definition of the deviatoric shear stress component of Eq. 1.4, we can define the deviatoric stress tensor using

$$\underline{\underline{\tau}} = \eta \underline{\underline{\dot{\gamma}}} \tag{1.23}$$

where $\underline{\underline{\tau}}$ is written as

$$\underline{\underline{\tau}} = \tau_{ij} = \begin{bmatrix} \tau_{xx} & \tau_{xy} & \tau_{xz} \\ \tau_{yx} & \tau_{yy} & \tau_{yz} \\ \tau_{zx} & \tau_{zy} & \tau_{zz} \end{bmatrix} \tag{1.24}$$

1.7 Guide to the Book

The content of this book can be fitted into an Eisenschitz, Rabinowitsch and Weissenberg triangle. Because plastics are extremely viscous, with a viscosity one million times higher than that of water, the first simplification we can make is to eliminate the effects of inertia. That leaves us with only the behavior represented by line BC in Fig. 1.19. While the fundamentals of polymer flow during processing (Chapter 2), their modeling (Chapter 4), and their measurement (Chapter 6) are more related to the molten, liquid-like behavior around vertex C, the behavior of the material during rapid deformation and solidification (Chapter 5) is related to its structure (Chapter 2) and will therefore be discussed in terms of viscoelasticity.

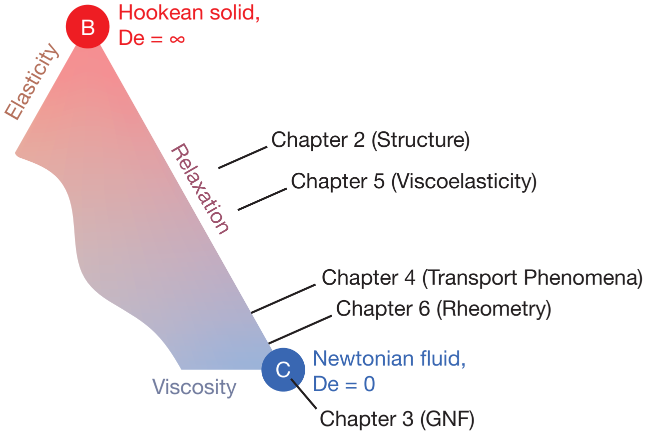

Figure 1.19 The Eisenschitz, Rabinowitsch and Weissenberg triangle and its significance for this book

Problems

1.1 Please retrieve Rabinowitsch's 1929 paper on the capillary viscometer correction factor and write a short essay and presentation summarizing the paper.

1.2 Please retrieve the Bernstein, Kearsley and Zapas paper on the non-linear integral viscoelastic model and write a short essay and presentation summarizing the paper.

1.3 Compare the Cross and Carreau models from their 1965 and 1968 publications.

1.4 Compare the 1923 de Waele model to Ostwald's 1925 model.

1.5 Please retrieve Einstein's 1905 paper on filled fluids and compare the model with Guth and Simha's model from their 1936 paper.

1.6 Please retrieve Williams, Landel and Ferry's 1955 paper on the time-temperature superposition principle and write a short essay and presentation summarizing the paper.

1.7 Choose a paper from the references and write a short essay and presentation summarizing the paper.

References

[1] Bingham, E. C., *Fluidity and Plasticity*, McGraw Hill Book Company, New York, (1922).

[2] Pascal, B., "*Traites de l'equilibre des liqueres et de la pesanteur de la masse de l'air*," Paris, (1663).

[3] Hooke, R., Lectures de Potentia Restitutiva or of Spring. Explaining the Power of Springing Bodies, (1678).

[4] Newton, I., Philosophiæ Naturalis Principia Mathematica, S. Pepys, Reg. Soc. Præs, London, (1686).

[5] Reiner, M., Deformation, strain and flow, Lewis, London, (1960).

[6] Young, T., A course of lectures on natural philosophy and the mechanical arts, Volume 1, Taylor and Walton, (1845).

[7] Gordon. J. E., The Science of Structures and Materials, The Scientific American Library, New York, (1988).

[8] Poisson, S. D., Mémoire sur l'équilibre et le movement des corps élastiques, *Mém. de l'Acad. Sci., 8*, 357, (1829).

[9] Hagen, G. H. L., *Annalen der Physik, 46*, 423, (1839).

[10] Poiseuille, L. J., *Comptes Rendus, 11*, 961, (1840).

[11] Stokes, G. G., *Trans. Camb. Phil. Soc., 8*, 287, (1845).

[12] Stokes, G. G., On the variation of gravity on the surface of the Earth, *Transactions of the Cambridge Philosophical Society, 8*, 672–695, (1849).

[13] Elias, H. G., Große Moleküle, Springer, Berlin, (1985).

[14] Weipert, D., Tscheuschner, H. D., Windhab, E., Rheologie der Lebensmittel, Behr's, Hamburg, (1993).

[15] Graham, T., *Phil. Trans. Roy. Soc., 151*, 183, 184, 206, 207, 220, 221, (1861).

[16] Maxwell, J. C., "On the Dynamical Theory of Gases," *Phil. Trans. R. Soc. Lond., 157*, 49, (1867).

[17] Van der Waals, J. D., Over de Continuiteit van den Gas- en Vloeistoftoestand (on the continuity of the gas and liquid state), PhD thesis (excerpt), Leiden, Netherlands, (1873).

[18] Boltzmann, L., Zur Theorie der elastischen Nachwirkung, *Wiener Berichte, 70*, 275–306, (1874).

[19] Boltzmann, L., Theorie der elastischen Nachwirkung, *Ann. Phys., 7*, Ergänzungsband, 624–625, (1876).

[20] Margules, M., *Wien. Sitzungsber (2A), 83*, 588; *84*, 49, (1881).

[21] Couette, M., *Ann. de Chim., 21*, 433, (1890).

[22] Couette, M., *Compt. Rend., 107*, 388, (1888).

[23] Voigt, W., *Abhandl. Ges. Wiss. Göttingen, 36*, (1890).

[24] Finger, J., *Sitzungsberichte Acad. Wiss. Wien, (IIa), 103*, 163, (1894).

[25] Trouton, F. T., *Proc. Roy. Soc., A77*, (1906).

[26] Einstein, A., *Ann. Physik, 19*, 549, (1906).

[27] Bingham, E. C., *Bur. Stand. Sci. Paps., 13*, 309, (1916).

[28] Staudinger, H., *Chem. Ber., 53*, 1073, (1920).

[29] Bingham, E. C., Fluidity and Plasticity, McGraw-Hill Book Co., New York, (1922).

[30] de Waele, A., *Oil and Color Chem. Assoc. Journal, 6*, 33, (1923).

[31] Ostwald, W., *Kolloid-Z., 36*, 99, (1925).

[32] Hatschek, E., The Viscosity of Liquids, G. Bell and Sons, LTD., London, (1928).

[33] Wassermann, L., Von Heraklit bis W. Scott Blair. J. Rheology, (1991).

[34] Eisenschitz, R., Rabinowitsch, B., Weissenberg, K., Zur Analyse des Formänderungswiderstandes, *Mitt. d. Staatl. Mat. Pruef Amts, 9*, 117, (1929).

[35] Rabinowitsch, B., *Z. Phys. Chem., 145*, 1, (1929).

[36] Jeffreys, H., The Earth, Its Origin, History and Physical Constitution, Cambridge University Press, (1924).

[37] Nadai, A., Wahl, A. M., Plasticity; a mechanics of the plastic state of matter, New York, McGraw-Hill Book Co., (1931).

[38] Mooney, M., *Ind. Eng. Chem., Anal. Ed., 6*, 147, (1934).

[39] Mooney, M., Ewart, R. H., The conicylindrical viscometer. *Physics* 5:350–354; 350, (1934).

[40] Freundlich, H., Trixotropy, Paris, Hermann, (1935).

[41] Burgers, J. M., First Report on Viscosity and Plasticity, Amsterdam, Nordemann Publisher, (1935).

[42] Guth, E., Simha, R., *Kolloid-Zeitschrift, 74*, 266, (1936).

[43] Blair, G. W. S., An introduction to industrial rheology, Philadelphia, Blakiston, (1938).

[44] Mooney, M., *J. Appl. Phys., 11*, 582, (1940).

[45] Reiner, M., Rheological Systematics, Rheology Bulletin, *The Society of Rheology, Vol. 16, 3*, 53–68, (1945).

[46] Mezger, T., Das Rheologie Handbuch, Hannover, Vincentz-Verlag, (2000).

[47] Green, M. S., Tobolsky, V., A New Approach to the Theory of Relaxing Polymeric Media, *J. Chem. Phys., 14*, 80–92, (1946).

[48] Russell, R. J., The determination of the basic rheological constants governing the flow of pseudoplastic substances, Ph. D. Thesis, London University, (1946).

[49] Weissenberg, K., A continuum theory of rheological phenomena, *Nature, 159*, 310–311, (1947).

[50] Rivlin, R. S., *Phil. Trans. R. Soc. A, 240*, 459–490, (1948).

[51] Blair, G. W. S., First International Congress on Rheology, (1948).

[52] Rouse, P. E., A Theory of the Linear Viscoelastic Properties of Dilute Solutions of Coiling Polymers, *J. Chem. Phys., 21*, 1272–1280, (1953).

[53] Williams, M. L., Landel, R. F., Ferry, J. D., *J. Amer. Chem. Soc., 77*, 370, (1955).

[54] Zimm, B. H., Dynamics of Polymer Molecules in Dilute Solution: Viscoelasticity, Flow Birefringence and Dielectric Loss, *Journal of Chemical Physics, 24*, 269–278, (1956).

[55] Lodge, A., A network theory of flow birefringence and stress in concentrated polymer solutions. *Trans. Faraday Soc., 52*, 120–130, (1956).

[56] Eirich, F. R., Rheoloy: Theory and Applications. Volume I, Academic Press, New York, (1956).

[57] Bagley, E. B., *J. Apply. Phys., 28*, 624, (1957).

[58] Cox, W. P., Merz, E. H., *J. Polym. Sci., 28*, 619, (1958).

[59] Bird, R. B., Stewart, W. E., Lightfoot, E. N., Transport Phenomena, John Wiley and Sons, (1960).

[60] Lodge, A. S., Elastic Liquids, Academic Press, London, (1960).

[61] Reiner, M., Deformation, Strain and Flow, London, Lewis Publishers, (1960).

[62] Kaye, A., Non-Newtonian Flow in Incompressible Fluids, CoA Note No. 134, The College of Aeronautics, Cranfield, (1962).

[63] Bernstein, B., Kearsley, E., Zapas, L., *Trans. Soc. Rheol., 7*, 391, (1963).

[64] Cross, M. M., *J. Colloid Sci., 20*, 417, (1965).

[65] Giesekus, H., *Rheol. Acta, 5*, 239, (1966).

[66] Edwards, S. F., *Proc. Soc. London, 92*, 9, (1967).

[67] Carreau, P. J., Ph.D. Thesis, University of Wisconsin-Madison, USA, (1968).

[68] Meissner, J., *Rheologica Acta, 8*, 78, (1968).

[69] De Gennes, P. G., Reptation of a polymer chain in the presence of fixed obstacles. *J. Chem. Phys., 55*, 572–579, (1971).

[70] Bird, R. B., Armstrong, R. C., Hassager, O., Dynamics of polymeric liquids: Fluid Mechanics, New York. Wiley, (1977).

[71] Bird, R. B., Armstrong, R. C., Curtiss, C. F., Dynamics of polymeric liquids: Kinetic theory, New York, Wiley, (1977).

[72] Dealy, J. M., Rheometers for Molten Plastics, New York, Van Nostrand Reinhold Company, (1982).

[73] Doi, M., Edwards, S. F., The Theory of Polymer Dynamics, Clarendon Press, (1986).

[74] Dealy, J. M., Wissbrun, K. F., Melt Rheology and Its Role in Plastics Processing, New York, Van Nostrand, (1990).

[75] Macosko, C. W., Rheology: Principles, Measurements and Applications, New York – Heidelberg, VCH-Wiley, (1994).

[76] Carreau, P. J., De Kee, D. C. R., Chhabra, R. P., Rheology of Polymeric Systems, Munich, Hanser Publishers, (1997).

[77] Beris, A. N., Giacomin, A. J., “Πάντα ῥεῖ: Everything Flows,” Rheology Research Center Report 207, University of Wisconsin-Madison, (2013).

[78] Heraclitos, Complete Works (Απαντα); Series on Ancient Authors (Ἀρχαίίοι Συγγραφεῖς) Vol. 8, T. Falcos, Arvanitakis (translator). Thessaloniki, Greece, Zitros Publishing, (1999).

[79] Peters, F. E., Greek Philosophical Terms, A Historical Lexicon, New York, New York University Press, (1967).

[80] Barnes, J., The Presocratic Philosophers, Vol. 1., Londond, Routledge and Kegan Paul Publishers, (1979).

[81] Graham, D. W., The Texts of Early Greek Philosophy, Part 1, translated (and edited) from Ancient Greek into English by author, Cambridge UK, Cambridge University Press, (2010).

2 Structure and Properties of Deforming Polymers

Because of their molecular structure, polymers are by far the most complex fluids engineers will encounter. Therefore, what seems trivial when dealing with Newtonian fluids, is a complex experimental and mathematical exercise for a rheologist dealing with polymeric melts. An important aspect of any rheologist's work is to find relations between deformation and stresses for various well defined conditions, such as transient shear flows, step strain, creep, and oscillatory shear flow, to name a few. These relations, also called material functions, are determined using different types of rheometric techniques. This chapter will introduce the reader to the causes of the various phenomena only observed with plastics and the relation of these effects to the molecular architecture of polymer melts.

2.1 Molecular Structure of Polymers

Polymers are macromolecular structures that are typically generated synthetically but sometimes also through natural processes. These macromolecules start as monomers, such as ethylene, schematically represented in Fig. 2.1. Once these mono-

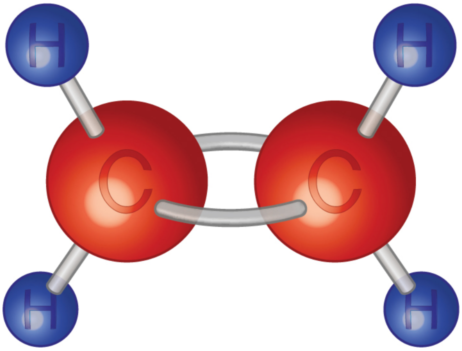

Figure 2.1 Schematic representation of an ethylene monomer

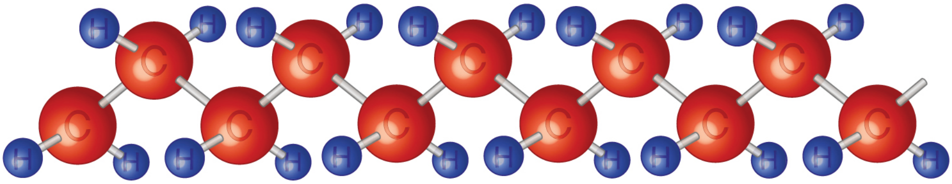

Figure 2.2 Schematic representation of a polyethylene molecule

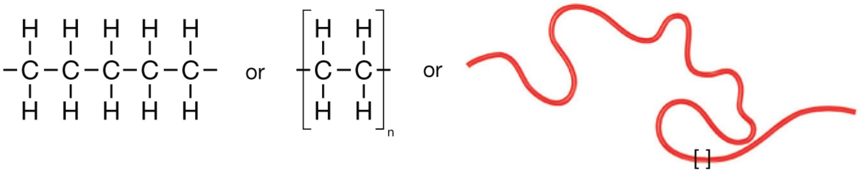

Figure 2.3 Symbolic representation and cartoon of a polyethylene molecule

mers are polymerized, they take the form of long polymer chains with thousands of repeating units. The ethylene of Fig. 2.1 becomes polyethylene, as schematically depicted in Fig. 2.2. Polymer molecules may also be represented symbolically or by using a cartoon as depicted in Fig. 2.3.

Several forces hold a polymeric material together on the molecular level. The most basic acting forces are covalent bonds that hold together the backbone of a polymer molecule, such as the C–C bond. The energy holding together two carbon atoms amounts to approx. 350 kJ/mol, which is equivalent to a polymer component strength between 14 and 19 GPa and a stiffness of up to 300 GPa. However, because the long polymer chains are typically not aligned, the strength of polymers ranges only between 10 and 100 MPa and their stiffness is approx. 1 GPa.

The comparatively low strength found in polymer components indicates that the forces holding a polymer component together do not originate from the C–C bonds but are intermolecular forces, or so-called Van-der-Waals forces. The energy that generates the intermolecular attraction between two polymeric molecules increases with decreasing distance of the molecules as described by Eq. 2.1

$$\varepsilon \sim \frac{1}{r^6} \tag{2.1}$$

where $\varepsilon < 10$ kJ/mol and r is the distance between the molecules. Thus, it becomes clear that as a polymer sample is heated, and the distance between the molecules increases with increasing vibration amplitude of the molecules, the intramolecular forces diminish. This increase in free volume allows the molecules to move more freely, enabling the material to flow at the macroscopic level. An increase in free

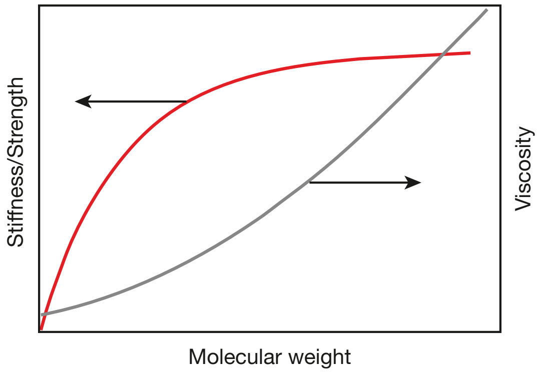

Figure 2.4 Influence of molecular weight on rheological and mechanical properties

volume, and consequently more ease of movement, can also be achieved by introducing solvents or plasticizers between the molecules. As these low molecular weight plasticizers wedge themselves between the molecules, they generate free volume, just as an increase in temperature would.

The properties of polymeric materials are strongly linked to the number of repeat units, n, in the molecular chain, or the molecular weight of the polymer, as shown schematically in Fig. 2.4. A polymer, such as polystyrene, is stiff and brittle at room temperature with a degree of polymerization of 1000, or $n = 1000$. At a degree of polymerization of 10, polystyrene is sticky and soft at room temperature. While the stiffness properties reach an asymptotic maximum, the viscosity increases steadily with molecular weight.

Some thermoplastics, such as some polyamide 11 resins, increase in molecular weight during processing. This leads to a rise in viscosity and may reduce sag once the polymer emerges from the extrusion die. The same is true for thermosets as they cure, or cross-link, during processing. As the curing progresses, the molecular weight increases, causing the viscosity to increase until the gel point is reached, at which point the material is considered a solid. The field studying these effects is referred to as chemorheology, and is covered in more detail in Chapter 3.

Figure 2.5 shows the relationships between molecular weight, temperature, and properties of a typical polymeric material. The glass transition temperature region increases with molecular weight. Therefore, the temperature range at which the polymer can flow (processing temperature), which for most polymers is 45 to 100 K above the glass transition, also increases with molecular weight. On the other hand, the degradation temperature steadily decreases with increasing molecular weight. Hence, it is necessary to find the molecular weight that renders ideal material properties for the finished polymer product, while providing flow properties that make it easy to shape the material during the manufacturing process. It is important to note

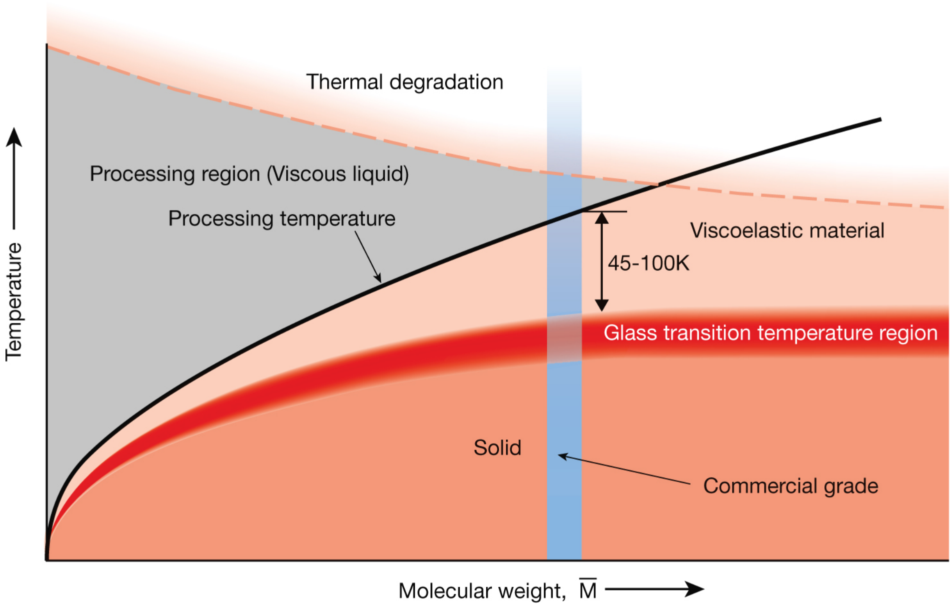

Figure 2.5 Diagram representing the relation between molecular weight, temperature, and properties of a typical thermoplastic

that the temperature scale in Fig. 2.5 corresponds to a specific time scale, e.g., time required for a polymer molecule to flow through an extrusion die. If the time scale is reduced (e.g., by increasing the extruder throughput), the molecules do not have enough time to relax, or get used to the shape of the die. Now a somewhat higher temperature is required to assure flow. In fact, at a specific temperature, a polymer melt may behave like a solid when the time scale is reduced sufficiently. Hence, for this new time scale the stiffness properties and flow temperature curves must be shifted upward on the temperature scale. A limiting factor is the fact that the thermal degradation curve remains fixed, forcing processing conditions to remain above certain time scales.

With the exception of some naturally occurring polymers, most polymers exhibit a molecular weight distribution, in other words, they are composed of molecules of different length, as shown in Fig. 2.6. There are various ways to compute an average molecular weight for such a molecular weight distribution. The number average, $\overline{M}_n$, simply adds all the molecular weights of all the molecules and divides it by the total number of molecules. This is written as

$$\overline{M}_n = \frac{\sum m_i}{\sum n_i} = \frac{\sum n_i M_i}{\sum n_i} \tag{2.2}$$

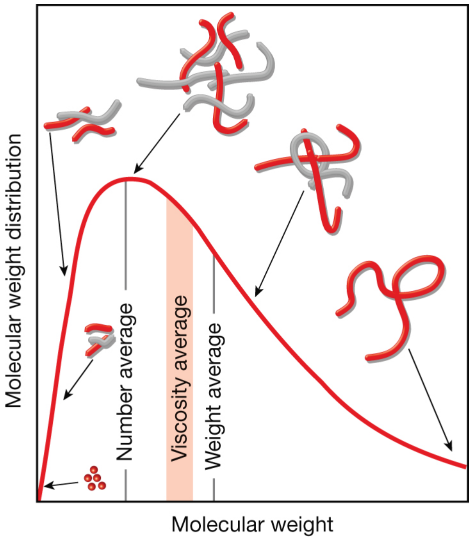

Figure 2.6 Molecular weight distribution of a typical thermoplastic

where m_i is the weight, M_i the molecular weight, and n_i the number of molecules with i repeat units. This gives the short chains, that contribute little to the total performance and weight of the material, equal importance as the long chains. To avoid this, one can take a weighted average, where before adding up all the molecules, the number of molecules with a specific molecular weight is multiplied by the molecular weight of those chains, and instead of dividing this sum by the total number of chains, the total molecular weight of the sample is used. This is represented as

$$\bar{M}_W = \frac{\sum m_i M_i}{\sum m_i} = \frac{\sum n_i M_i^2}{\sum n_i M_i} \tag{2.3}$$

Another form of molecular weight average is the viscosity average, M_v, which is calculated using

$$[\eta] = k \bar{M}_v^{\alpha} \tag{2.4}$$

where $[\eta]$ is the intrinsic viscosity and, α and k are material-dependent parameters. This relation is sometimes referred to as the Mark-Houwink relation. Figure 2.7 [1] schematically presents the viscosity of a typical polymer as a function of molecular weight. The figure shows how the viscosity changes from a linear (α = 1) to a power dependence (α = 3.4) at some critical molecular weight. The linear relationship is sometimes referred to as Staudinger's rule [2] and applies to a perfectly monodispersed polymer of relatively low molecular weight[1]. This linear relationship is a

---

[1] A monodispersed polymer is composed of a single molecular weight species.

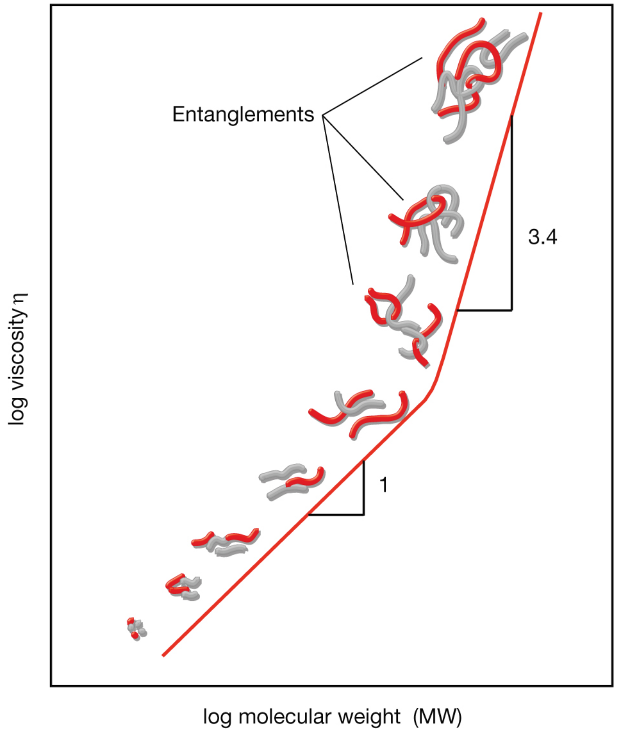

Figure 2.7 Schematic of zero shear rate viscosity for polymers as a function of weight average molecular weight

result of the intramolecular friction, which increases proportionally to the length of the molecules. As the molecular weight increases with increasing length of the molecules, the molecules tend to entangle, causing a power relation between molecular weight and viscosity, or $\alpha = 3.4$.

The broadness of a molecular weigth distribution is related to the polydispersity of the molecular chains. A monodispersed polymer is described by

$$\bar{M}_w = \bar{M}_n = \bar{M}_v \tag{2.5}$$

while in a polydispersed polymer

$$\bar{M}_w > \bar{M}_v > \bar{M}_n \tag{2.6}$$

Hence, a measure of the broadness of a polymer's molecular weight distribution is the polydispersity index defined by

$$PI = \frac{\bar{M}_w}{\bar{M}_n} \tag{2.7}$$

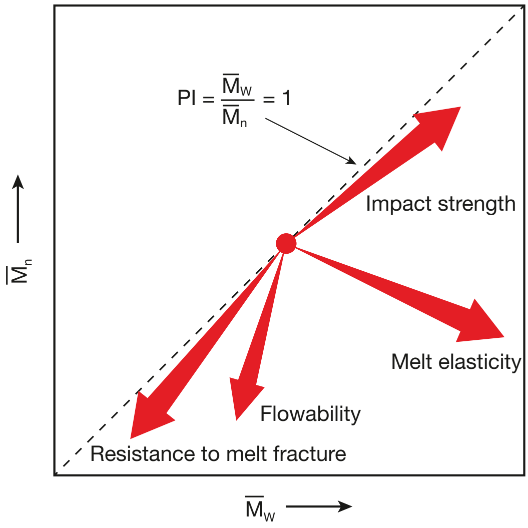

Figure 2.8 Influence of molecular weight number average and weight average on properties of thermoplastic polymers

Here, *PI* = 1 represents a polymer, in which all molecules have the same chain length. However, *PI* varies with the type of polymerization and the polymer itself. For step growth polymerized plastics, such as polyamides, polycarbonates and epoxies, to name a few, the polydispersity index $PI \approx 2$. For chain polymerized plastics, such as polyolefines, polystyrenes, polyacetal, etc., *PI* = 1.01 ... 50, where branched polymers exhibit a polydispersity index ranging between 20 and 50.

Figure 2.8 is a graphical representation of the relationship between number average and weight average and its influence on the properties of polymers. The arrows in the diagram indicate an increase in a specific property.

Branching of the polymer chains also influences the final structure, crystallinity, and properties of the polymeric material. Figure 2.9 shows the molecular architecture of high density (PE-HD), low density (PE-LD), and linear low density polyethylenes (PE-LLD).

The PE-HD has between 5 and 10 short branches for every 1000 carbon atoms. The PE-LD has the same number of branches as PE-LD; however, they are much longer and are themselves usually branched. The PE-LLD has between 10 and 35 short chains for every 1000 carbon atoms. Polymer chains with fewer and shorter branches can crystallize with more ease, resulting in higher density.

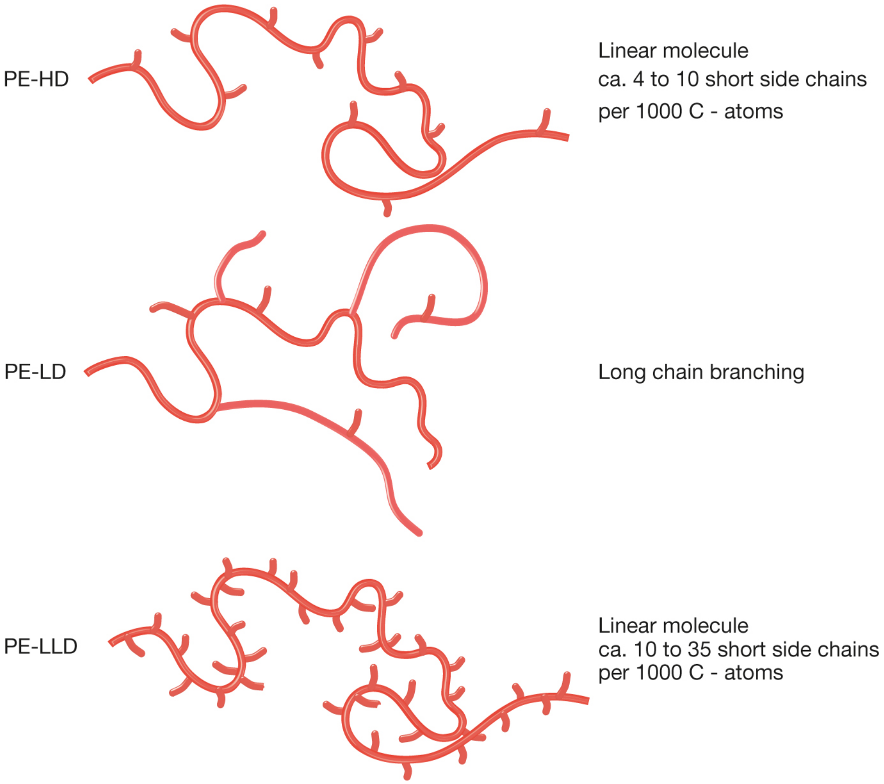

Figure 2.9 Schematic of the molecular structure of different polyethylenes

2.2 Stress Relaxation Behavior

The most basic phenomenon in polymer melts and solids is stress relaxation. Because polymers are composed of macromolecules, and these large molecules have the ability to slide past each other, hindered only by intramolecular forces and molecular entanglements, they tend to relax stresses that arise when subjected to a deformation. Hence, as a mass of polymer is subjected to a stress, the molecules tend to move in an effort to relax those stresses. If these stresses are caused by a constant strain, the initial stress caused by this deformation relaxes in a given time interval, sometimes referred to as relaxation time, λ.

In a stress relaxation test, a polymer test specimen undergoes a fixed deformation, ε_0, and the stress required to hold this amount of deformation is recorded over time. This test is very cumbersome to perform, so design engineers and material scientists tend to ignore it. In fact, the standard relaxation test ASTM D2991 was dropped from the standards in 1990. However, rheologists have been consistently using the stress relaxation test to interpret the viscoelastic behavior of polymers.

Figure 2.10 [3] presents the stress relaxation modulus of polyisobutylene[2] measured at various temperatures. Here, the stress relaxation modulus is defined by

$$E_r(t) = \frac{\sigma(t)}{\varepsilon_0} \tag{2.8}$$

where ε_0 is the applied strain and $\sigma(t)$ is the stress being measured. From the test results it is clear that stress relaxation is time and temperature dependent, especially around the glass transition temperature, where the slope of the curve reaches a maximum. In the case of the polyisobutylene shown in Fig. 2.10, the glass transition temperature is about −70 °C. The measurements were completed in an experimental time window between a few seconds and one day. The tests performed at lower temperatures were used to record the initial relaxation, while the tests performed at higher temperatures only captured the end of relaxation of the rapidly decaying stresses.

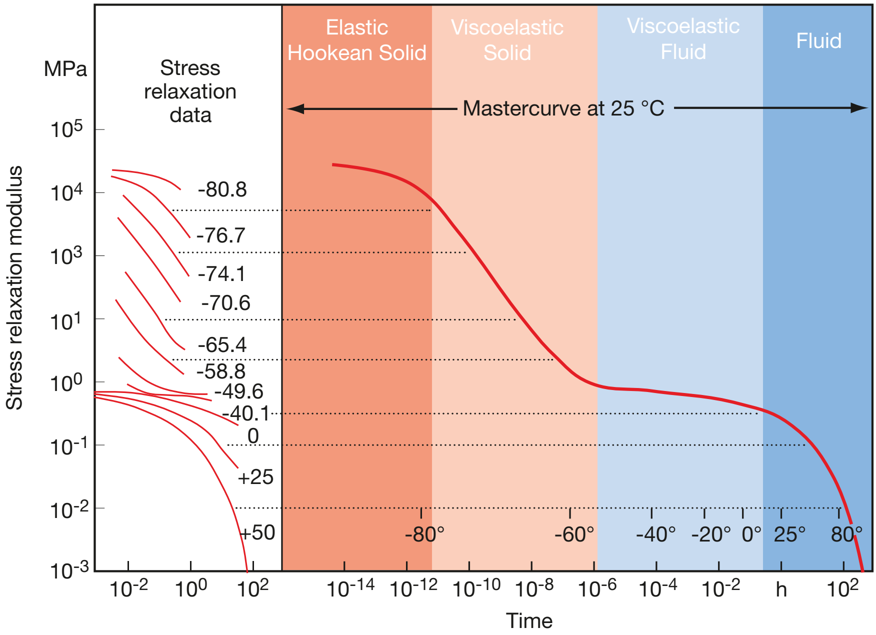

Figure 2.10 Relaxation modulus curves for polyisobutylene at various temperatures and corresponding master curve at 25 °C

---

[2] Better known as chewing gum.

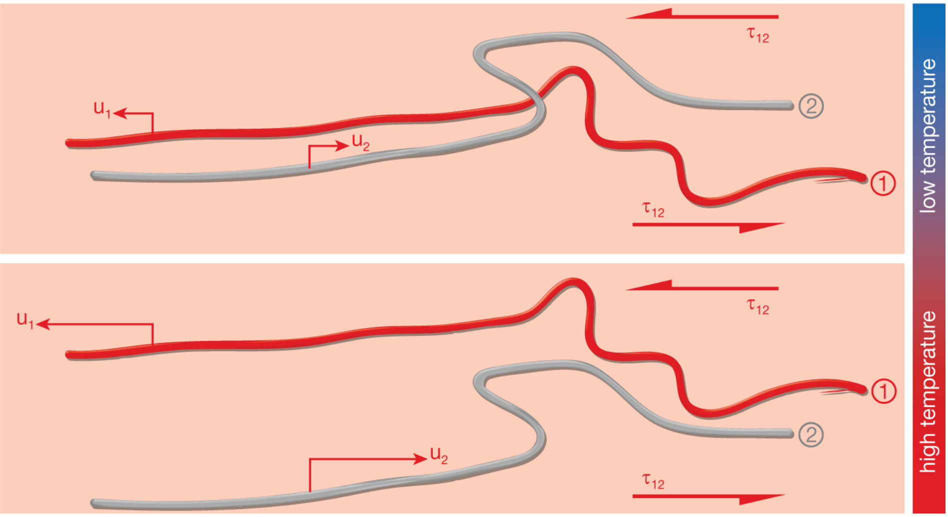

Figure 2.11 Schematic of stress relaxation on a molecular level at low (top) and high (bottom) temperatures

It is well known that high temperatures lead to short molecular relaxation times[3] and low temperatures lead to long relaxation times. This is caused by the fact that at low temperatures the free volume between the molecules is small, restricting or slowing down their movement, as schematically shown in Fig. 2.11. At high temperatures, the free volume is larger and the molecules can move with more ease. When changing temperature, the shape of creep[4] or relaxation test results remains the same, except that they are horizontally shifted to the left or right, which represents lower or higher response times, respectively.

The same behavior observed for varying temperatures can be seen when the pressure is varied. As the pressure is increased, the free volume between the molecules is reduced, slowing down molecular movement. Here, an increase in pressure is equivalent to a decrease in temperature. Hence, it is clear that in the melt state, the viscosity of a polymer increases with pressure. Figure 2.12 [4] illustrates the effect of pressure on stress relaxation.

The time-temperature equivalence seen in stress relaxation test results can be used to reduce data at various temperatures to one general master curve for a reference temperature, T_0. To generate a master curve at the reference temperature, the curves shown on the left of Fig. 2.10 must be shifted horizontally, maintaining the reference curve stationary. Density changes are usually small and can be neglected, eliminating the need to perform tedious corrections. The master curve for the data in Fig. 2.10 is shown on the right side of the figure. Each curve was shifted horizontally until

---

[3] Relaxation time usually refers to the time it takes for applied stresses to relax within a material.

[4] In a creep test the polymer specimen is loaded to a constant stress, and the strain response is recorded in time.

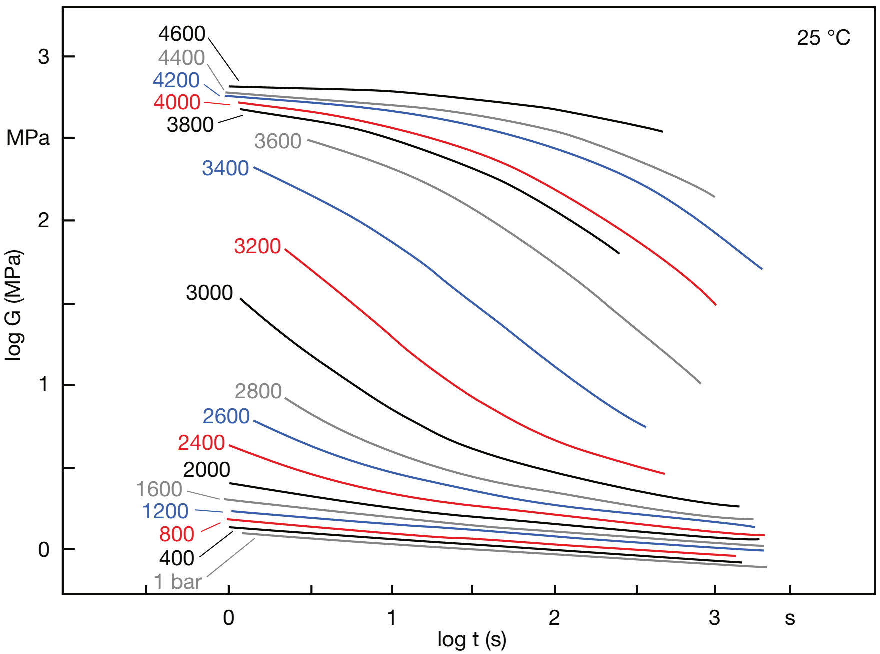

Figure 2.12 Shear relaxation modulus for a chlorosulfonated polyethylene at various pressures

the ends of all the curves became superimposed. The amount by which each curve was shifted can be plotted with respect to the temperature difference taken from the reference temperature, T_0. For the data in Fig. 2.10 the shift factor is shown in the plot in Fig. 2.13. The amounts by which the curves where shifted, $\log a_T$, are represented by

$$\log T - \log T_0 = \log\left(\frac{T}{T_o}\right) = \log a_T \tag{2.9}$$

where T is the temperature of the measurement and T_0 the reference temperature. This shift will be explained in more detail in Chapter 3.

Although the results in Figure 2.13 where shifted to a reference temperature of 298 K (25 °C), Williams, Landel and Ferry (WLF) [5] chose T_0 = 243 K, or 45 K above the glass transition temperature. This temperature is often chosen because for most amorphous polymers it coincides with a typical processing temperature, where the measureable elastic effects are smaller than the viscous effects during deformation. The shift, or time-temperature superposition, is given in general form by

$$\log a_T = -\frac{C_1\left(T - T_0\right)}{C_2 + \left(T - T_0\right)} \tag{2.10}$$

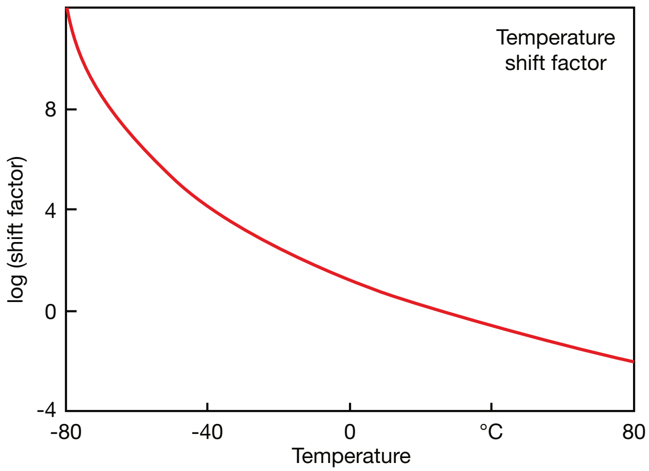

Figure 2.13 Plot of the shift factor as a function of temperature used to generate the master curve plotted in Figure 2.10

where C_1 and C_2 are material dependent constants. Equation 2.10 is often referred to as WLF-equation. Master curves of stress relaxation tests are important because the polymer's behavior can be traced over much longer periods of time than can be determined experimentally. The WLF equation and its use is covered in detail in Chapter 3.

Example 2.1 Relaxation Time Measurement

Using a blow molding grade high density polyethylene, determine the relaxation time for standard processing temperatures.

A sliding plate rheometer can be used to measure relaxation time. In a sliding plate rheometer, two parallel plates separated by a small gap move parallel to one another. The advantage of using a sliding plate rheometer is that a constant stress and strain field is generated between the gap, as the material deforms in simple shear[5]. For a relaxation time measurement, a step strain is imposed by rapidly moving one of the plates a certain distance. This causes the shear to rapidly increase to its maximum value τ_{max}. Because the systems remains stationary after applying the step strain, the stress decreases over time. Typically, the relaxation time, λ, is the time it takes for the maximum stress to decrease to 1% of its initial value. Figure 2.14 presents the stress as a function of time for a blow molding grade PE-HD[6] (MFI = 1.2 g/10 min) tested at 190 °C. The imposed strain was $\gamma = 20$, applied to a 2 mm thick sample using rate of shear of 2 s^{-1}. The instant the plates stopped moving, the shear stress reached 90 kPa. The plot presented in Figure 2.14 shows that it took about 1.2 s for this stress to relax to 1% of its initial value.

---

[5] The sliding plate rheometer is discussed in detail in Chapter 6.

[6] NOVA Chemicals Sclair® 19G Homopolymer HDPE Film Resin.

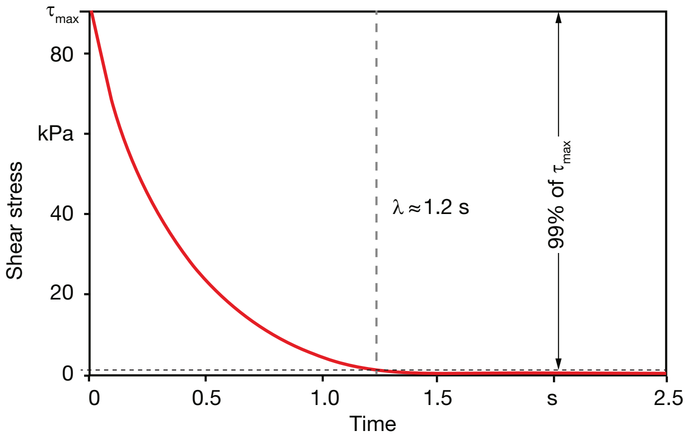

Figure 2.14 Stress as a function of time after imposing a step strain, measured using a sliding plate rheometer and a blow molding grade PE-HD.

2.3 Shear Thinning Behavior

To illustrate shear thinning behavior, picture the randomly oriented entangled macromolecules depicted in Fig. 2.15. At low rates of deformation, the entangled molecules have a hard time sliding past each other, resulting in a relatively high viscosity. Polymer melts exhibit this behavior over a range of small rates of deformation. This constant high viscosity is referred to as a Newtonian plateau, depicted in Fig. 2.16. However, as the rate of deformation increases, the corresponding increased shear stress is sufficiently high to disentangle and unravel the molecules. The disentangled molecules can slide past their neighbors with more ease, resulting in an overall lower melt viscosity. This phenomenon is referred to as shear thinning behavior, pseudoplasticity, or structural viscosity. Eventually, the molecules can no longer stretch out any further. This point is seen in a second Newtonian plateau at higher rates of deformation, reflecting the lowest possible viscosity.

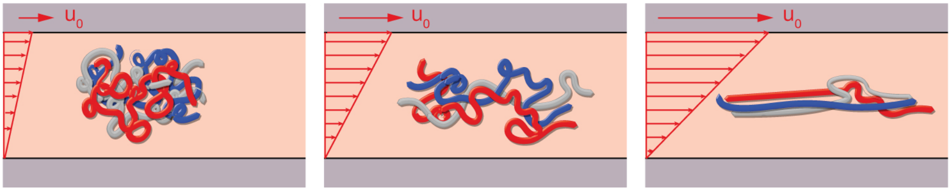

Figure 2.15 Molecular structure with increasing shear

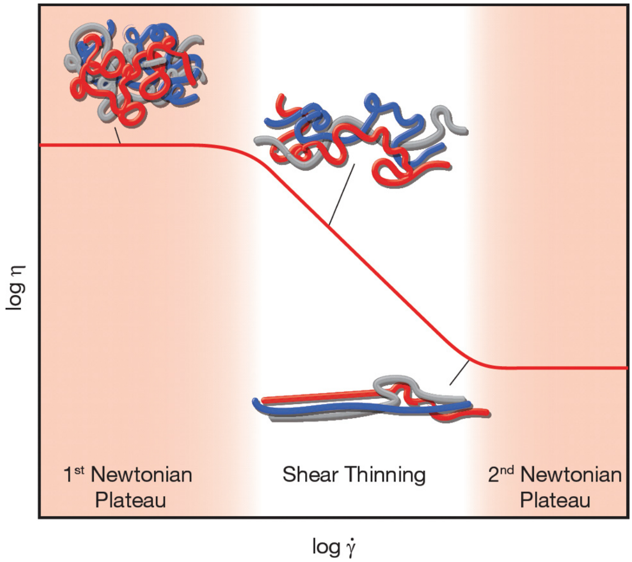

Figure 2.16 Shear thinning behavior or pseudoplasticity

The same effect depicted for shear in Fig. 2.15 occurs in elongation flows as well as in combined deformation flows of various levels of shear and elongation. Therefore, the viscosity of a polymer is a function of the magnitude of the rate of deformation tensor

$$\tau_{xy} = \eta(\dot{\gamma}, T)\,\dot{\gamma}_{xy} \tag{2.11}$$

Because the free volume between the molecules increases with temperature, the intra-molecular friction decreases, resulting in an overall lower viscosity as shown in Fig. 2.16 for various polymers. Figure 2.17 also presents the range of rate of deformation experienced by polymer melts when using various processing techniques.

Figure 2.18 shows the effect of molecular weight variations on the shear thinning behavior of thermoplastics. The shear rate independent plateau is shifted to higher viscosity values with increasing molecular weight as the friction between chains increases. Side branching leads to lower viscosity (shear thinning) caused by the lubrication effect of the side group chains. With increasing width of the molecular weight distribution, shear thinning sets in at higher shear rates, which can be attributed to the smaller shear thinning effect of short chains.

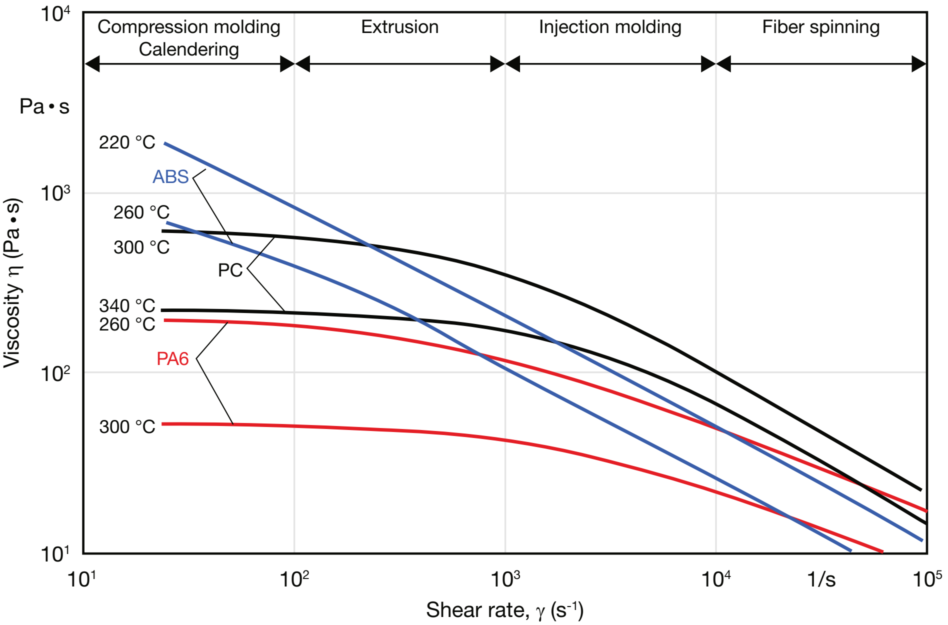

Figure 2.17 Viscosity curves for various polymers at different temperatures

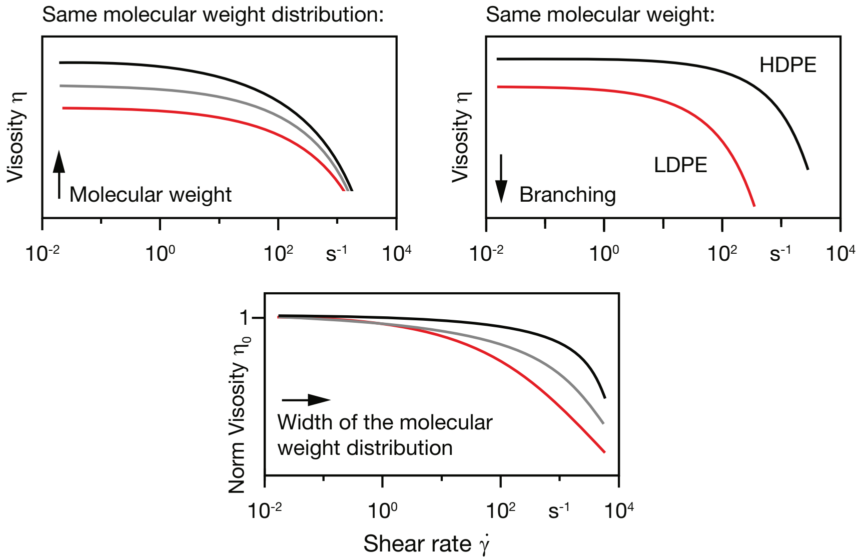

Figure 2.18 Schematic representation of the influence of molecular weight, branching, and molecular weight distribution on the shear rate dependent viscosity of polyolefins [6]

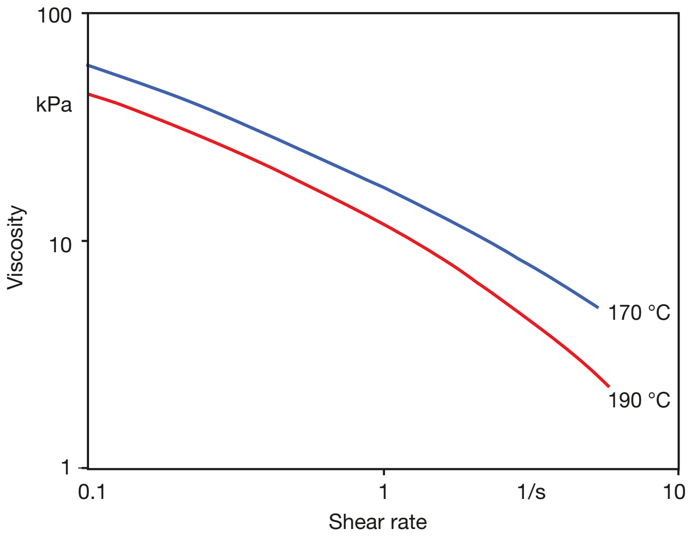

Figure 2.19 Viscosity as a function of rate of deformation for two different temperatures, measured using a sliding plate rheometer and a blow molding grade PE-HD.

Example 2.2 Shear Thinning Behavior Measurement

Using the same extrusion blow molding grade high density polyethylene as in Example 2.1, measure the viscosity as function of rate of deformation for two processing temperatures.

The same sliding plate rheometer used in the stress relaxation experiment of Example 2.1 was used to measure the viscosity of the molding grade polyethylene for rates of deformation between 0.1 and 10 s^{-1}. The measurements were done for test temperatures of 170 °C and 190 °C. Figure 2.19 presents the results. The figure clearly reveals fairly high viscosities at relatively low rates of deformation. From the results it is obvious that this material is not appropriate for injection molding applications. Furthermore, because during the test high shear stresses are generated, tests at higher rates of deformation resulted in surface slip conditions between resin and rheometer surface.

2.4 Normal Stresses in Shear Flow

The tendency of polymer molecules to "curl-up" while they are being stretched in shear flow results in normal stresses in the fluid. For example, in a shear flow that exhibits a deviatoric stress defined by Eq. 1.4 or 2.11, a measurable reaction from the molecular structure is perceived in the form of normal stresses and defined as normal stress differences, $N_1 = \tau_{xx} - \tau_{yy}$ and $N_2 = \tau_{yy} - \tau_{zz}$. This effect is schematically depicted in Fig. 2.20, where stress differences, referred to as the first and second normal stress differences, are shown. An experimental set-up illustrating normal stress difference effects is the so-called rod-climbing experiment, or the Weissenberg effect, shown in Fig. 2.21. In this experiment, a rotating shaft causes the polymeric solution to move towards the shaft and not away from it as seen with Newtonian fluids. As a result, the polymer starts to move up the rotating shaft. Figure 2.22 is a schematic explanation of this effect. As the polymer molecules are stretched by the Couette devices's shear stresses, normal stresses arise. Because the stretched molecules are aligned along the curvilinear streamline, they tend to migrate toward the rotating shaft, leading to the rod-climbing phenomenon.

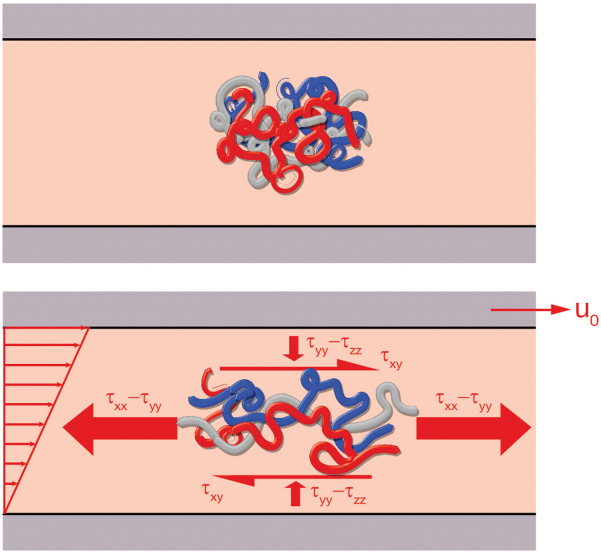

Figure 2.20 Schematic diagram of melt at rest and normal stress reactions during shear flow

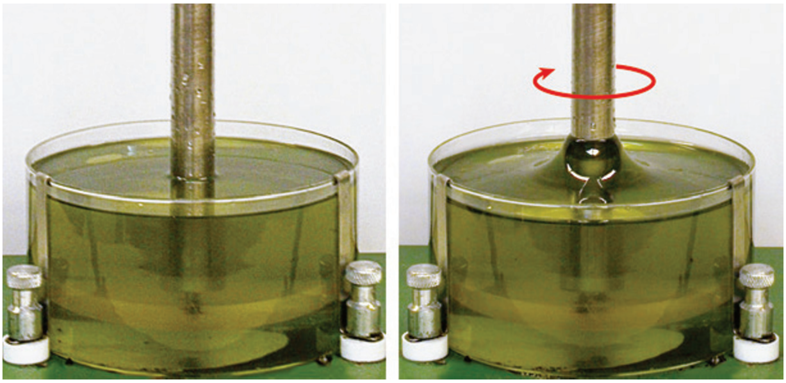

Figure 2.21 The rod-climbing or Weissenberg effect

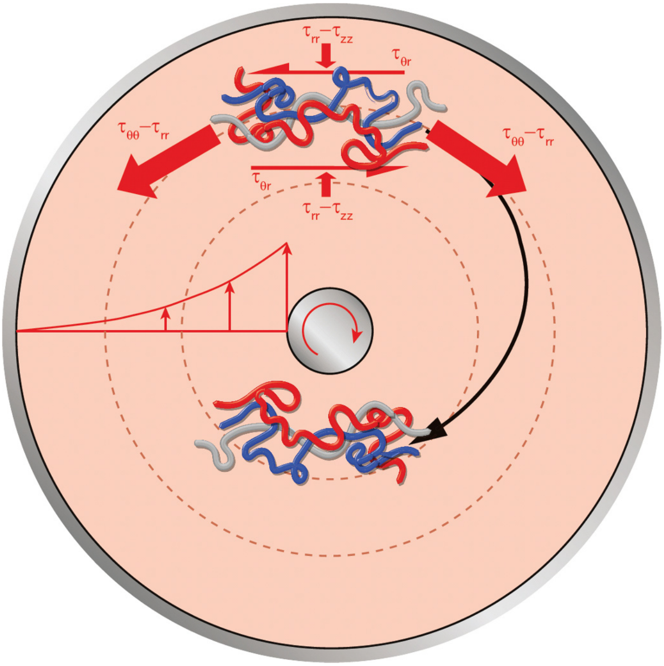

Figure 2.22 Schematic representation of normal stresses in a Couette flow

Just like viscosity, the first and second normal stress differences are material dependent and are defined by

$$N_1 = \tau_{xx} - \tau_{yy} = \psi_1(\dot{\gamma}, T)\,\dot{\gamma}_{xy}^2 \tag{2.12}$$

$$N_2 = \tau_{yy} - \tau_{zz} = \psi_2(\dot{\gamma}, T)\,\dot{\gamma}_{xy}^2 \tag{2.13}$$

where ψ_1 and ψ_2 are material functions called the primary and secondary normal stress coefficients. These material properties are also functions of the strain rate tensor magnitude and the temperature. Also, similar to viscosity, the first and second normal stress differences do not change in sign when the direction of the strain rate changes, clearly reflected in Eqs. 2.12 and 2.13. Figure 2.23 [7] presents the first normal stress difference coefficient for the low density polyethylene melt shown in Fig. 3.2 in Chapter 3 at a reference temperature of 150 °C. Second normal stress differences are more difficult to measure and therefore the data are often approximated by

$$\psi_2(\dot{\gamma}) \approx -0.1\,\psi_1(\dot{\gamma}) \tag{2.14}$$

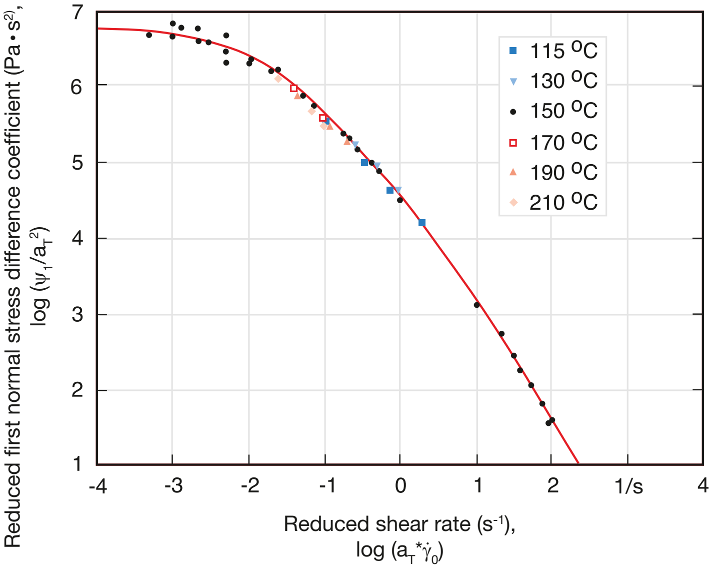

Figure 2.23 Reduced first normal stress difference coefficient for a low density polyethylene melt at a reference temperature of 150 °C

Example 2.3 Normal Stress Measurements

Using the same extrusion blow molding grade high density polyethylene as in Example 2.1, measure the first normal stress difference coefficient as a function of rate of deformation for two processing temperatures.

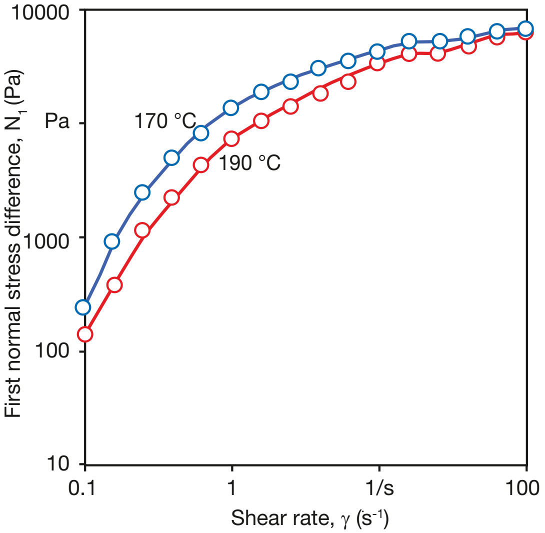

Figure 2.24 First normal stress difference of blow molding grade PE-HD as a function of shear rate and temperature

The first normal stress difference, N_1, was measured for test temperatures of 170 °C and 190 °C, using the same sliding plate rheometer employed in Examples 2.1 and 2.2. As expected, a clear increase in normal stress but a reduction in growth was observed with increased rate of deformation (Fig. 2.24). Furthermore, a reduction in normal stress difference was seen with increase in temperature.

2.5 Stress Overshoot during Start-up Flow

When a polymer sample that is initially at rest is suddenly subjected to a deformation rate, its stress response presents a slight stress overshoot, to a maximum value of τ_{max}, before decreasing and reaching a steady state value. Figure 2.25 schematically depicts this phenomenon. It has been suggested by many researchers [8] that the cause for this stress overshoot is the polymer melt's initial higher resistance to deformation resulting from molecular entanglements. Once the polymer deformation exceeds a certain value, the molecules begin to disentangle, reducing the resistance to deformation, causing the stresses to relax to a steady state value in a time typically shorter than the relaxation time of the melt.

When the flow is restarted after a short rest time, the maximum overshoot stress will be lower than the one experienced during the first start-up. However, if the rest time is sufficiently long, the maximum stress reached during overshoot will approach the value reached during the first start-up, τ_{max}. The rest time that the polymer needs to recover to its original state is based on the time it takes for molecular reentanglement. This time is longer than the characteristic stress relaxation time, λ.

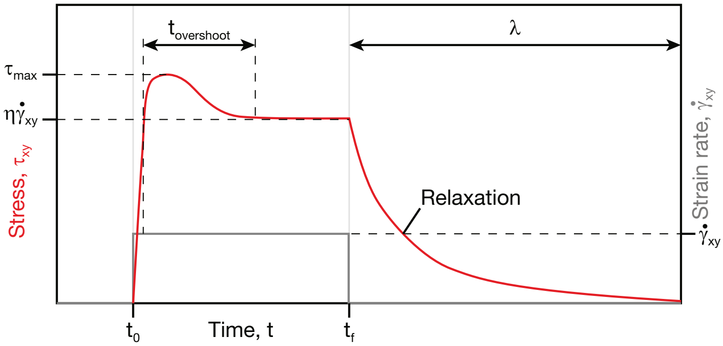

Figure 2.25 Schematic of stress overshoot during start-up flow

Example 2.4 Stress Overshoot Measurement

Using the same extrusion blow molding grade high density polyethylene as in Example 2.1, introduce a constant shear and assess the stress overshoot effect.

To capture the stress overshoot using the same sliding plate rheometer and blow molding grade PE-HD used in the previous three examples, a 2 mm sample was subjected to a constant shear rate of 2 s^{-1}. As can be seen, the shear stress first jumped to a value above 80 kPa, and eventually settled at a stress about half that value (Fig. 2.26). The material was tested at 190 °C.

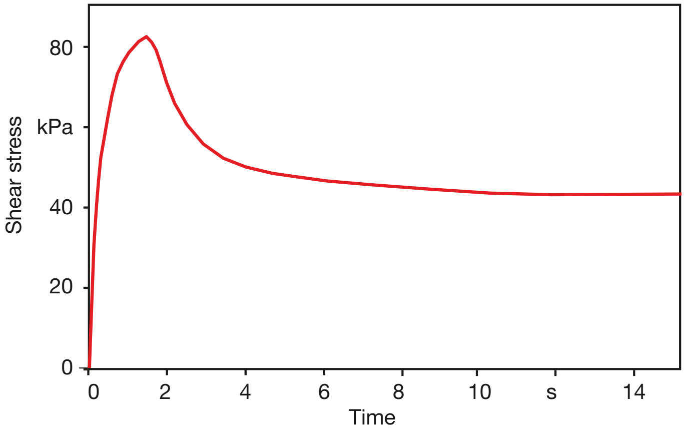

Figure 2.26 Measured stress overshoot at a constant shear rate of 2 s^{-1}

2.6 Melt Strength or Melt Fracture

When a polymer is forced to deform and move at speeds that result in processing times shorter than the relaxation time of the polymer, the stresses will build up until they exceed the melt strength, leading to so called melt fracture. Depending on the process, this phenomenon will present itself in different forms. For example, waves in the extrudate may appear as a result of high speeds during extrusion, where the polymer is not allowed to relax within the extrusion die. This phenomenon is generally referred to as shark skin shown in Fig. 2.27 a [9] for a high density polyethylene.

It is possible to extrude at such high speeds that an intermittent separation of melt and inner die walls is caused, as shown in Fig. 2.27 b.

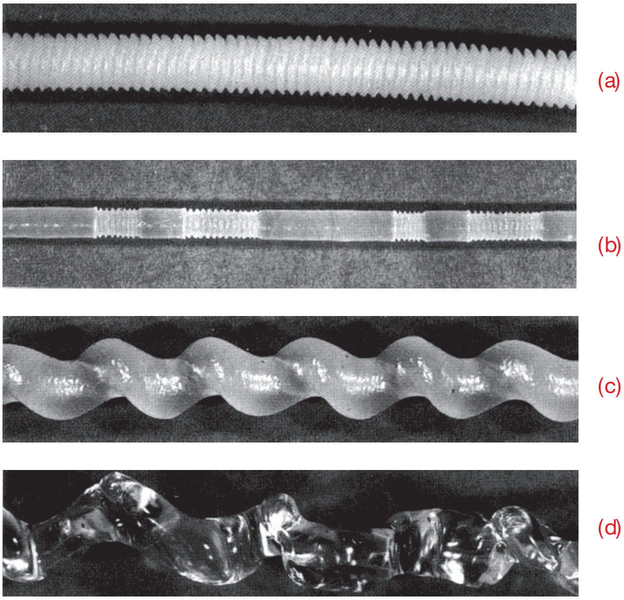

Figure 2.27 Melt fracture during extrusion of a polymer strand

This phenomenon is often referred to as the stick-slip effect or spurt flow and is attributed to high shear stresses between the polymer and the die wall. It occurs when the shear stress is near a critical value of 0.1 MPa [10–12]. However, it is influenced by the molecular weight of the polymer, as schematically shown in Figure 2.28. As the figure shows, a high molecular weight polymer molecule has more contact points with the surface of the mold or the rheometer. Hence, a higher molecular weight polymer exhibits better resistance to melt fracture than a lower molecular weight polymer. It was reported that the critical shear stress of 0.1 MPa is inversely proportional to the weight average molecular weight [11, 13]. However, Vinogradov et al. [10] presented results indicating that the critical stress was independent of molecular weight, except for low molecular weights. The interested reader is referred to the extensive overview of Koopmans et al. [14].

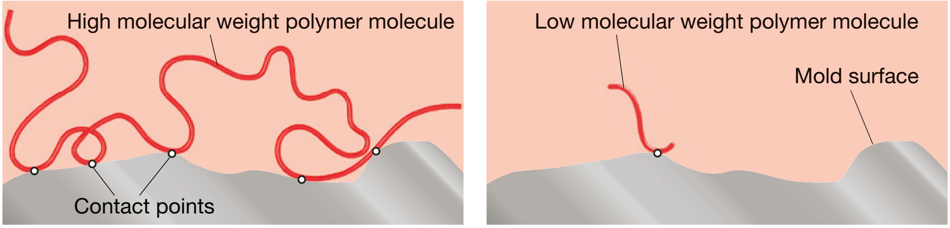

Figure 2.28 Influence of molecular weight on the slip between polymer and tool surface

If the speed is further increased, a helical geometry is extruded, as shown for a polypropylene extrudate in Fig. 2.27 c. Eventually, the speeds are so high that a chaotic pattern develops, such as the one shown in Fig. 2.27 d. This well known phenomenon is called melt fracture. The shark skin effect is frequently absent and spurt flow seems to occur only with linear polymers.

Another form of melt fracture may occur during elongational deformation, for example during fiber spinning. Here, when the drawing speed is too high, the stresses build up before having a chance to relax, until the thread rips, or fractures. We can observe the same effect when stretching silly putty at high speeds.

Although the molecular weight is lower in injection molding grades, these flow instabilities can also occur during mold filling, e.g., with polyacetal or high density polyethylene. These instabilities result in surface defects on the finished part that may take the form of matte surfaces, regular helices, or irregularly spaced ripples.

Production guidelines often recommend a reduction of injection velocity or extrusion speed, an increase of mold and melt temperature, or an increase of the gate diameter to eliminate melt fracture.

2.7 Dynamic Response

In an oscillatory test, a sample is excited with a low frequency stress or strain input which is recorded along with the strain or stress response. Figure 2.29 presents schematic diagrams of a shear strain input, γ_{xy}, and shear stress response, τ_{xy}, for a perfectly elastic solid, an ideal viscous fluid, and a viscoelastic fluid with a linear viscoelastic response.

If the sample in an oscillatory test is perfectly elastic, or a Hookean solid, the strain input and stress response can be described as follows:

$$\gamma_{xy}(t) = \gamma_0 \sin \omega t \tag{2.15}$$

$$\tau_{xy}(t) = \tau_0 \sin \omega t \tag{2.16}$$

where t is time and $\omega = 2\pi f$ with f being the frequency of strain oscillation. As expected, the stress response is in phase with the strain input. Hence, when computing the shear modulus, the transient effects cancel out, and an elastic modulus, G, results as

$$G = \frac{\tau_0 \sin \omega t}{\gamma_0 \sin \omega t} = \frac{\tau_0}{\gamma_0} \tag{2.17}$$

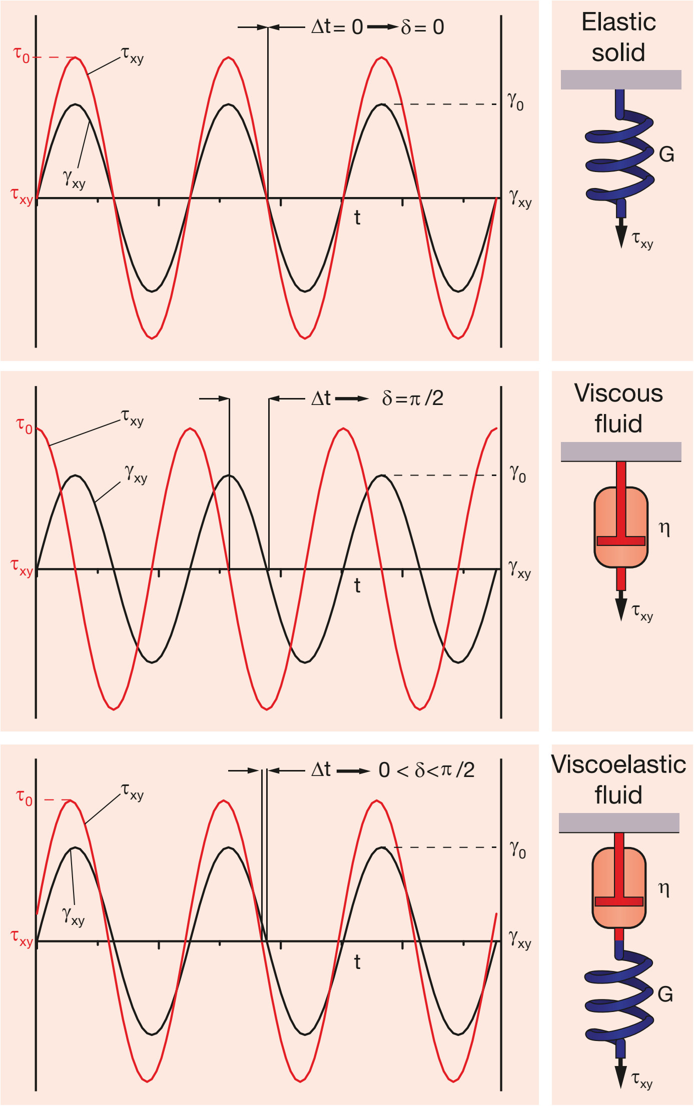

Figure 2.29 Oscillatory shear experiments for an elastic solid, a viscous fluid, and a viscoelastic fluid

On the other hand, if an ideal viscous fluid is subjected to an oscillatory strain, the stress response is proportional to the strain rate, $\gamma_0 \omega \cos \omega t$, which can also be interpreted as a lag of $\pi/2$ radians behind the strain input:

$$\gamma_{xy}(t) = \gamma_0 \sin \omega t \tag{2.18}$$

$$\dot{\gamma}_{xy}(t) = \dot{\gamma}_0 \cos \omega t \tag{2.19}$$

$$\tau_{xy}(t) = \tau_0 \cos\omega t = \tau_0 \sin\left(\omega t - \frac{\pi}{2}\right) \tag{2.20}$$

where $\dot{\gamma}_0 = \gamma_0 \omega$. Using the above equations we can compute the viscosity using the definition of a Newtonian fluid as

$$\eta = \frac{\tau_0 \cos\omega t}{\dot{\gamma}_0 \cos\omega t} = \frac{\tau_0}{\dot{\gamma}_0} \tag{2.21}$$

We can see that here, too, the transient effects cancel each other out, resulting in a constant viscosity.

However, viscoelastic materials, such as polymers, behave somewhere in between the perfectly elastic and the perfectly viscous materials, depending on the time scale. Their response can be described by

$$\gamma_{xy}(t) = \gamma_0 \sin\omega t \quad \text{and} \tag{2.22}$$

$$\tau_{xy}(t) = \tau_0 \sin(\omega t - \delta) \tag{2.23}$$

showing that the stress response lags δ radians behind the strain input, see Fig. 2.29. The shear modulus, computed using the ratio of stress to strain, takes a complex form with real and imaginary terms

$$G^* = \frac{\tau_{xy}(t)}{\gamma_{xy}(t)} = \frac{\tau_0 e^{i\delta}}{\gamma_0} = \frac{\tau_0}{\gamma_0}(\cos\delta + i\sin\delta) = G' + iG'' \tag{2.24}$$

which is graphically represented in Fig. 2.30, and referred to as complex modulus. The length of each vector represents the absolute value of the parameter. Therefore, G^* is the resulting vectorial sum. G' is usually referred to as storage modulus and is represented by

$$G' = \frac{\tau_0}{\gamma_0}\cos\delta \tag{2.25}$$

It is a measure for the stored energy, e.g., during a shearing process. Upon release this energy can be used completely for the recovery of the deformation, which makes it reversible. G'' is referred to as loss modulus and can be computed using

$$G'' = \frac{\tau_0}{\gamma_0}\sin\delta \tag{2.26}$$

It is a measure for the lost energy dissipated, e.g., as heat or used for structural changes of the material. Thus, ideal viscous materials are changed by deformation, which makes the process irreversible. The ratio of loss modulus to storage modulus is referred to as loss factor or loss tangent:

$$\tan\delta = \frac{G''}{G'} \tag{2.27}$$

In an elastic solid, $\delta = 0$ or $\tan\delta = 0$ as G' dominates G'' completely. However, in a viscous fluid, $\delta = 90°$ or $\tan\delta = \infty$ as G'' dominates G' completely. In viscoelastic materials, $0 \le \tan\delta \le \infty$, depending on the time scale and temperature. When the viscous and the elastic behavior are equal to $\delta = 45°$ or $\tan\delta = 1$, the material is making a transition from liquid to solid or vice versa. For example, this occurs during curing of thermosets when the system reaches its gel point. In the liquid state, $\tan\delta > 1$ as $G'' > G'$, and after gelation, $\tan\delta < 1$ as $G' > G''$. As can be seen in Fig. 2.30, the loss factor can be calculated using the dimensions of the resulting right angled triangle.

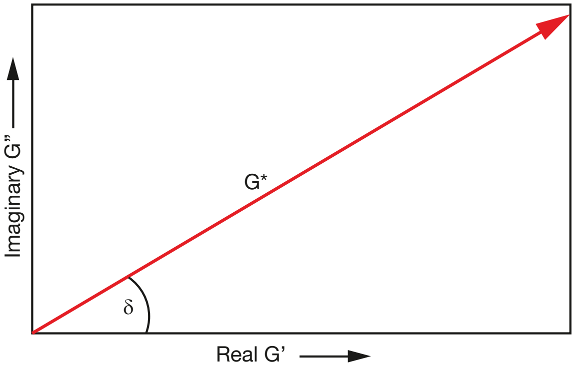

Figure 2.30 Vector representation of the complex shear modulus

Similarly, when the test is regarded from a rheological point of view, a complex viscosity can be computed using the ratio of stress to rate of deformation.

$$\eta^* = \frac{\tau_{xy}(t)}{\dot{\gamma}_{xy}(t)} = \eta' + \eta'' \tag{2.28}$$

where η' is the viscous component of the complex viscosity, also referred to as the dynamic viscosity, and η'' is the elastic component, also referred to as the out-of-phase component of the complex viscosity. The relation between the complex modulus and complex viscosity components can be described by

$$\eta'' = \frac{G'}{\omega} \tag{2.29}$$

$$\eta' = \frac{G''}{\omega} \tag{2.30}$$

with η'' representing the elastic and η' the viscous behavior. This complex modulus representation is often used in industrial testing.

In 1958, Cox and Merz [15] observed that there is an equivalence between viscosity measured during oscillatory tests at low frequencies and the viscosity measured using a steady shear device at low rates of deformation. The equivalence can be expressed as

$$\eta'(\omega)\Big|_{\omega\to 0} = \eta(\dot{\gamma})\Big|_{\dot{\gamma}\to 0} \tag{2.31}$$

In 1992, Al-Hadithi, Barnes, and Walters [16] defined a similar rule to Cox and Merz's rule, where they related the storage modulus measured by oscillatory tests to the first normal stress difference measured by a steady shear rheometer. Using

$$\left.\frac{G'(\omega)}{\omega^2}\right|_{\omega\to 0} = \left.\frac{N_1(\dot{\gamma})}{2\dot{\gamma}^2}\right|_{\dot{\gamma}\to 0} \tag{2.32}$$

and trial-and-error, Al-Hadithi et al. established the following relationship

$$N_1(\dot{\gamma}) \approx 2G'(\omega)\left[1 + \frac{(\eta_0 + \eta')\,G'(\omega)}{2\omega\eta'^2}\right]^{1/2} \tag{2.33}$$

where η_0 is the zero shear rate viscosity. However, in most cases the simple Cox-Merz rule (Eq. 2.31) can be used as long as the test is performed within the linear viscoelastic range, also referred to as small amplitude oscillatory shear (SAOS) test. The linear viscoelastic domain is valid for most polymers when the deformation stays below 10% strain.

Recalling the definition of the Deborah number from Chapter 1, $De = \lambda/t_\mathrm{p}$, we recognize that in an oscillatory test the characteristic time can be defined by $1/\omega$, resulting in $De = \lambda\omega$. However, deformation, γ_0, in conjunction with the Deborah number results in a Weissenberg number, $We = \gamma_0\lambda\omega$, which is a dimensionless number similar to the Deborah number that includes deformation in addition to time scale and relaxation time. Hence, a small Weissenberg number represents a process in the linear viscoelastic domain.

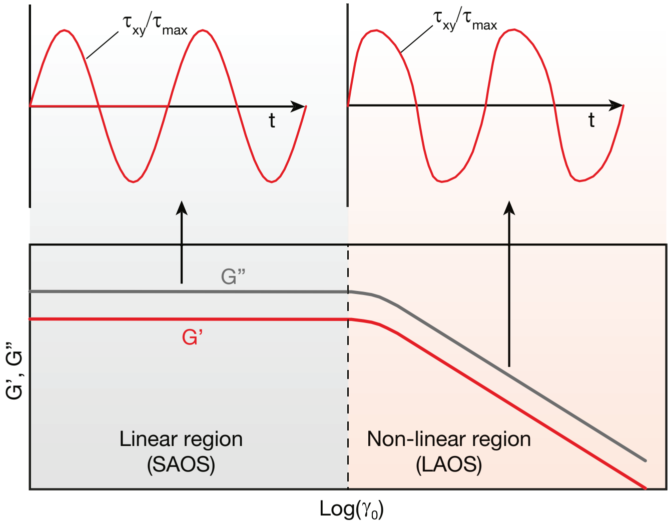

Figure 2.31 Schematic diagram of strain magnitude sweep at a constant test frequency, with visible linear (SAOS) and non-linear (LAOS) viscoelastic responses and their corresponding stress responses.

Once the deformations are large, e.g., *We* > 1, such as those polymer melts are subjected to during processing, the stress response starts exhibiting a non-sinusoidal response, where higher harmonics become evident (Fig. 2.31) [17]. In these cases, the stress reponse can be represented using

$$\tau_{xy}(t) = \tau_1 \sin(\omega t + \delta_1) + \tau_3 \sin(3\omega t + \delta_3) + \tau_5 \sin(5\omega t + \delta_5)\ldots \tag{2.34}$$

A fast Fourier transform of the stress response can be used to determine the contribution of each frequency on the compound stress response. Often, the first two terms, the first and third harmonic, are sufficient to represent the stress wave.

At large deformations, material properties such as storage and loss shear modulus start to exhibit a deformation-dependent behavior caused by molecular disentanglement and molecular orientation. Oscillatory shear tests are referred to as large amplitude oscillatory shear (LAOS). Large deformations are more realistic when analyzing polymer melts because strains that are felt by the material during processing flows can be of several 100%. Figure 2.31 shows a schematic of polymer responses under oscillatory shear caused by small to large deformations.

Example 2.5 Storage and Loss Modulus Measurements Using Oscillatory Shear Tests

Using the same extrusion blow molding grade high density polyethylene as in Example 2.1, measure the storage and loss moduli as functions of frequency and temperature.

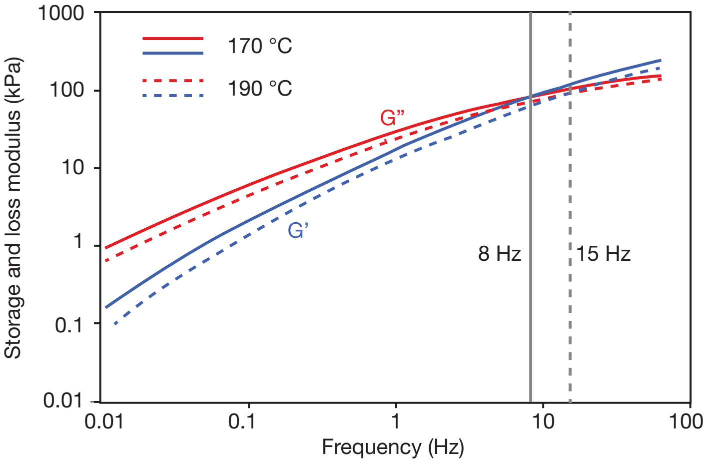

Figure 2.32 Storage and loss moduli for a blow molding grade PE-HD as functions of frequency and temperature.

The storage and loss moduli were measured using a parallel plate rheometer (see Chapter 6) in the linear strain domain, with an applied strain amplitude of 2%. A frequency scan from 0.1 to 70 Hz was performed at 170 °C and 190 °C. The disc size was 25 mm with a distance between the plates of 2 mm. Figure 2.32 shows the results.

Example 2.6 Small and Large Amplitude Oscillatory Shear Tests

Using the same extrusion blow molding grade high density polyethylene as in Example 2.1, measure the stress response when imposing an oscillatory strain input. Repeat the experiment for various shear rates and strain amplitudes.

The same samples used in the previous examples within this chapter where used to impose an oscillatory shear strain for small to large amplitudes, covering the linear and non-linear viscoelastic regimes. Figure 2.33 presents the stress response for a frequency of 7.5 rad/s and a strain amplitude of 0.5. The graph reflects a sinusoidal response, representing a linear behavior. When plotting the stress response as a function of strain input, an elliptical Lissajous curve is generated (Fig. 2.34). The elliptical shape also reflects a linear behavior. It should be noted that the area inside the closed loop represents the volume-specific energy dissipated during one cycle. On the other hand, Fig. 2.35 presents the stress response at a frequency of 10 rad/s and a large strain amplitude of 10. The figure clearly shows a stress response that is not sinusoidal, revealing higher harmonics, as described in Eq. 2.34. Furthermore, the Lissajous loop shown in Fig. 2.36 is no longer elliptical, also reflecting the non-linear behavior at larger strain amplitudes. A full Pipkin diagram (see Chapter 5) is presented in Fig. 2.37, where the linear and nonlinear responses are visible.

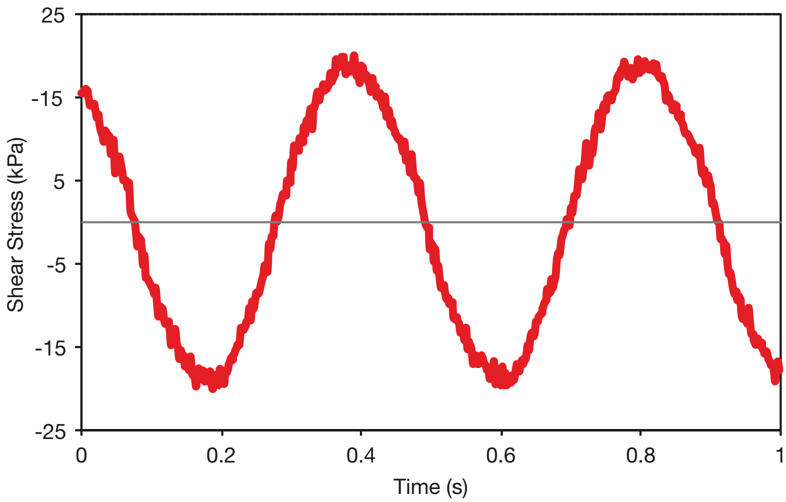

Figure 2.33 Stress response for small amplitude (0.5 strain) deformations and a frequency of 7.5 rad/s of a blow molding grade PE-HD.

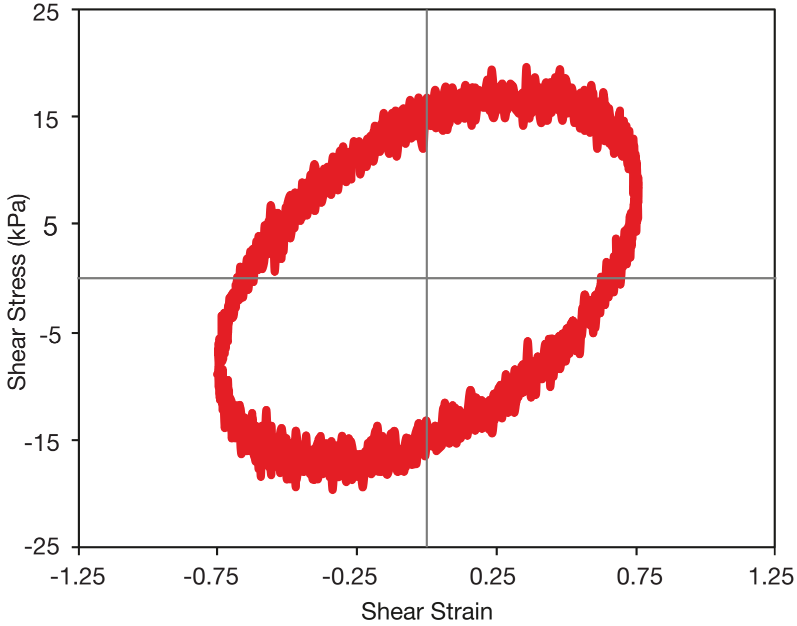

Figure 2.34 Lissajous loop for small amplitude (0.5 strain) deformation and a frequency of 7.5 rad/s of a blow molding grade PE-HD.

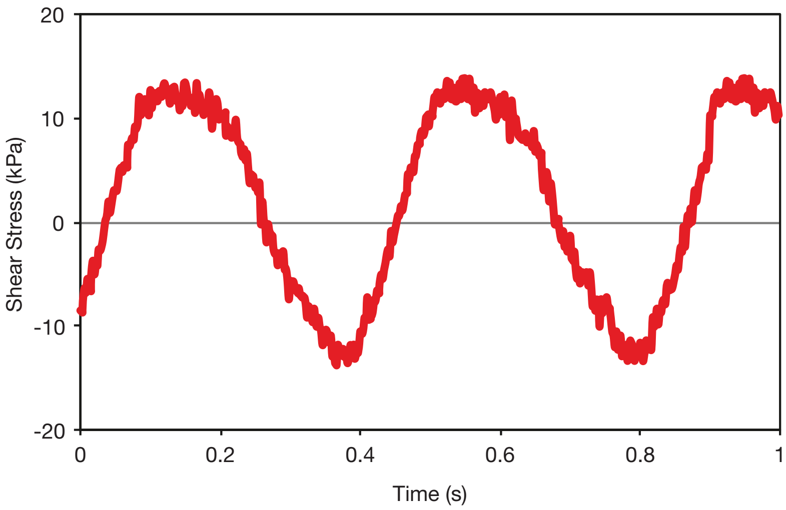

Figure 2.35 Stress response for large amplitude (10 strain) deformations and a frequency of 10 rad/s of a blow molding grade PE-HD.

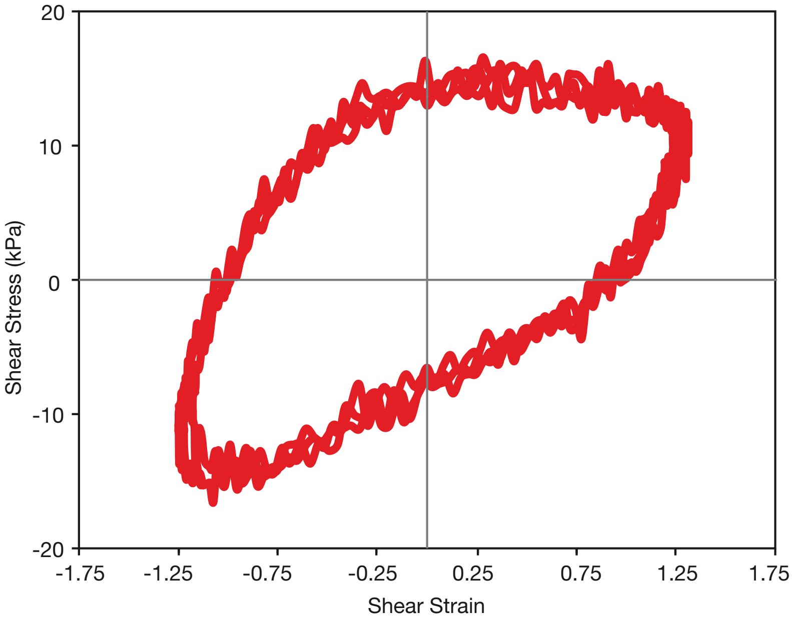

Figure 2.36 Lissajous loop for large amplitude (10 strain) deformations and a frequency of 10 rad/s of a blow molding grade PE-HD.

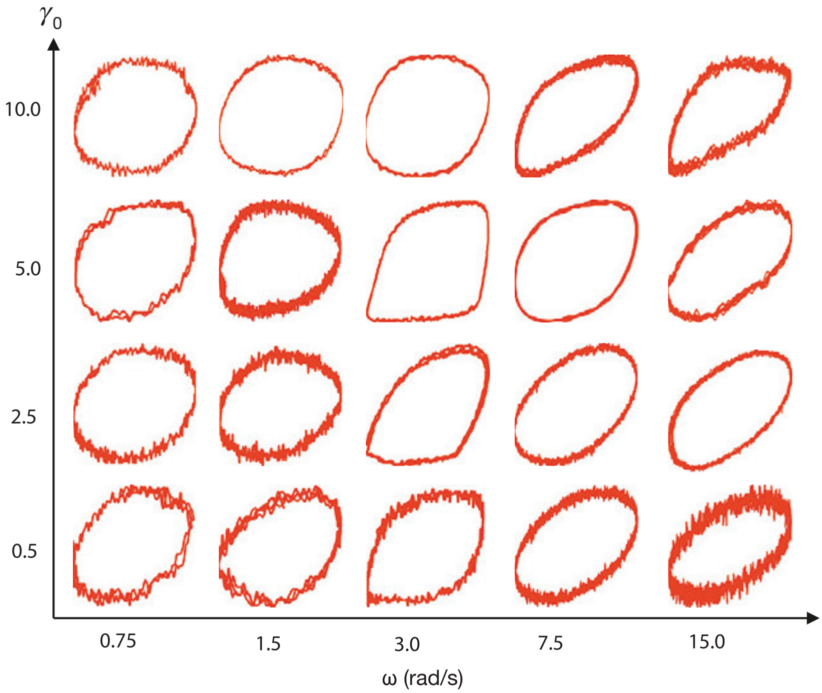

Figure 2.37 Pipkin space for a blow molding grade PE-HD.

Problems

2.1 Compare the Maxwell model presented in Chapter 1 to the experimental data from the step strain step test presented in Example 2.1. How does the Maxwell model's relaxation time, λ, compare to the measured 99% decay value?

2.2 Generate a plot of the first normal stress difference coefficient, ψ_1, for the graphs given in Example 2.2.

2.3 Generate a plot of the first normal stress difference coefficient, ψ_1, using the information given in Figure 10 of the following paper: Baird, D. G., *J. Non-Newtonian Fluid Mech.*, *148*, 13–23, (2008).

2.4 Compare the results of the stress relaxation test of Example 2.1 and the stress overshoot test of Example 2.4.

2.5 Find a function of the form presented in Eq. 2.34 to fit the nonlinear stress response of Example 2.5. Use the first two terms of the equation.

2.6 A sliding plate rheometer was used to perform a stress overshoot and relaxation test on a 4 MFI polypropylene copolymer at 190 °C (Fig. 2.38). The relative speed between the two plates was 4.15 mm/s and the separation between the plates was 2.3 mm. At what shear rate was the test performed? What is the viscosity at the given rate of deformation? Compare the time it took to reach a steady state shear stress and the relaxation time after the plates stopped moving. What can you conclude?

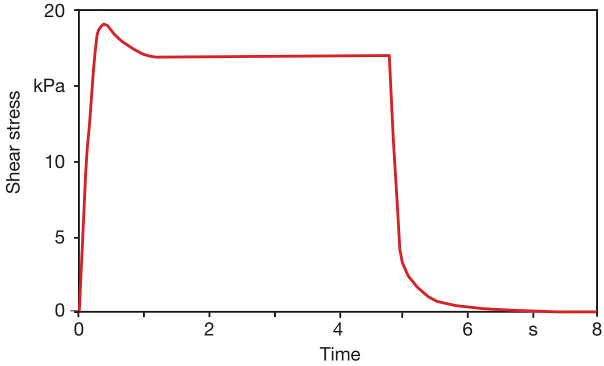

Figure 2.38 Sliding plate rheometer test of a PP copolymer.

2.7 Compare the loss modulus measured in Example 2.5 to the viscosity measured in Example 2.2. Use Eq. 2.30 for your comparison.

2.8 Use the storage and loss moduli graphs presented in Example 2.5 to discuss the significance of the point where the two graphs cross. How does temperature affect this cross-over point?

References

[1] Berry, G. C., Fox, T. G., *Adv. Polymer Sci., 5*, 261, (1968).

[2] Staudinger, H., Huer, W., *Ber. der Deutsch. Chem Gesell., 63*, 222, (1930).

[3] Castiff, E., Tobolsky, A. V. J., *Colloid Sci., 10*, 375, (1955).

[4] Fillers, R. W., Tschoegl, N. W., *Trans. Soc. Rheol., 21*, 51, (1977).

[5] Williams, M. L., Landel, R. F., Ferry, J. D., *J. Amer. Chem. Soc., 77*, 3701, (1955).

[6] Ehrenstein, G. W., Polymeric Materials – Structure, Properties, Applications, Hanser Publishers, Munich, (2001).

[7] Laun, H. M., *Rheol. Acta, 17*, 1, (1978).

[8] Dealy, J. M., Tsang, W. K.-W., *J. Appl. Polym. Sci., 26*, 1149–1158, (1981).

[9] Agassant, J.-F., Avenas, P., Sergent, J.-Ph., Carreau, P. J., Polymer Processing: Principles and Modeling, Hanser Publishers, Munich, (1991).

[10] Vinogradov, G. V., Malkin, A. Y., Yanovskii, Y. G., Borisenkova, E. K., Yarlykov, B. V., Berezhnaya, G. V., *J. Polym. Sci. Part A-2, 10*, 1061, (1972).

[11] Vlachopoulos, J., Alam, M., *Polym. Eng. Sci., 12*, 184, (1972).

[12] Hatzikiriakos, S. G., Dealy, J. M., *ANTEC Tech. Papers, 37*, 2311, (1991).

[13] Spencer, R. S., Dillon, R. D., *J. Colloid Inter. Sci., 3*, 163, (1947).

[14] Koopmans, R., den Doelder, J., Molenaar, J., Polymer Melt Fracture, CRC Press, Boca Raton, FL, (2011).

[15] Cox, W. P., Merz, E. H., *J. Polym. Sci., 28*, 619, (1958).

[16] Al-Hadithi, T. S. R., Barnes, Walters, K., *Colloid and Polymer Science, 270*, 40, (1992).

[17] Hyun, K., Wilhelm, M., Klien, C. O., Cho, K. S., Nam, J. G., Ahn, K. H., Lee, S. J., Ewoldt, R. H., McKinley, G. H., *Progress in Polymer Science, 36*, 1697–1753, (2011).

3 Generalized Newtonian Fluid (GNF) Models

As discussed in Chapter 2, most polymers exhibit *shear thinning*, temperature and pressure dependent viscosities. The shear thinning effect is defined as the reduction in viscosity at high rates of deformation. This phenomenon is explained by the fact that the molecular chains are disentangled and stretched out at high rates of deformation and can therefore slide past each other with more ease, which in turn lowers the bulk viscosity of the melt. Figure 3.1 clearly shows the shear thinning behavior and temperature dependence of the viscosity of a general purpose polystyrene.

To take these *non-Newtonian effects* into consideration while neglecting the viscoelastic effects[1], it is common to define the viscosity η as a function of the strain rate and temperature. To calculate the deviatoric stress tensor in the momentum balance (see Chapter 4), we can then write

$$\underline{\underline{\tau}} = \eta\left(\dot{\gamma}, T\right)\underline{\underline{\dot{\gamma}}} \tag{3.1}$$

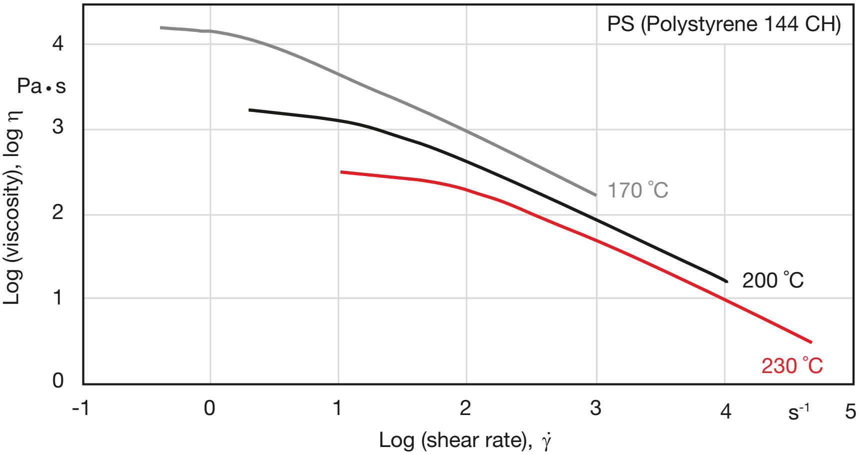

Figure 3.1 Viscosity curves for a polystyrene

---

[1] The Deborah number, Eq. 1.16, defined as the product $De = \lambda\omega$, reflects the degree of viscoelasticity. Newtonian behavior is characterized by low *De* values.

This equation is often referred to as the *Generalized Newtonian Fluid* model. Here, $\underline{\underline{\dot{\gamma}}}$ is the *strain rate* or *rate of deformation tensor* defined by

$$\underline{\underline{\dot{\gamma}}} = \nabla \underline{u} + \nabla \underline{u}^t \tag{3.2}$$

where $\nabla \underline{u}$ represents the velocity gradient tensor, defined in Chapter 1.

Constitutive equations based on generalized Newtonian fluid models differ in their shear thinning expression, but they all require that the non-Newtonian viscosity $\eta(\dot{\gamma})$ is a function of the three scalar invariants of the strain rate tensor. Because of the incompressibility of polymer melts, the first invariant, defined by the sum of the diagonal terms of the tensor, equals zero (I = 0), and assuming steady shear flow, the third invariant, defined by the determinant of the tensor, also equals zero (III = 0). Therefore, $\eta(\dot{\gamma})$ is only a function of the second invariant, II. This is expressed by the magnitude of $\dot{\gamma}$ and can be written as

$$\dot{\gamma} = \sqrt{\frac{1}{2}\mathrm{II}} \tag{3.3}$$

where $\dot{\gamma}$ is the magnitude of the strain rate tensor in Eq. 3.1. The second invariant of the strain rate tensor is defined as

$$\mathrm{II} = \sum_i \sum_j \dot{\gamma}_{ij}\,\dot{\gamma}_{ji} \tag{3.4}$$

The strain rate tensor components in Eq. 3.4 are defined by

$$\dot{\gamma}_{ij} = \frac{\partial u_i}{\partial x_j} + \frac{\partial u_j}{\partial x_i} \tag{3.5}$$

Numerous models describe the shear thinning, temperature and pressure dependence of polymer viscosity. Most are similar and based on the same assumptions; however, the different nomenclatures used make it difficult to distinguish between them. To add to the confusion, different names or combination of names are used. In this chapter, the most common models are presented and the connections to other models are highlighted. The temperature dependence is typically modeled in two different ways and these two approaches are explained in a general form in the following section. Due to the recent need for high pressure injection molding of thin products, a relatively new research area in the field of rheology is the pressure dependence of the viscosity. This topic will be addressed separately after the introduction of the viscous flow models. The description of the modeling of filled (Section 3.4) as well as cross-linking polymers (Section 3.5) will be expanded separately at the end of the chapter with more general comments that pertain to these systems.

3.1 Temperature Dependence of Viscosity

In addition to the strain rate dependence, the temperature dependence of the viscosity is expressed as a function separate from the rate of deformation dependence. This can be written as

$$\eta(T,\dot{\gamma}) = f(T)\,\eta(\dot{\gamma}) \tag{3.6}$$

where for small variations in temperature, $f(T)$ is often approximated using an exponential function such as

$$f(T) = \exp\left[-a\left(T - T_0\right)\right] \tag{3.7}$$

In the above equation, a is the temperature sensitivity of the viscosity, T is the temperature at which the viscosity is sought, and T_0 is a reference temperature, at which the viscosity is known. However, as mentioned in Chapter 2, a variation in temperature corresponds to a shift in the time scale when determining characteristic relaxation times within the polymer melt. There are two additional models that can be used, depending on the specific material processed and the desired temperature range: the Arrhenius shift and the WLF shift. The Arrhenius shift [1], which applies to semi-crystalline polymers, is written as

$$a_T(T) = \frac{\eta_0(T)}{\eta_0(T_0)} = \exp\left[\frac{E_0}{R}\left(\frac{1}{T} - \frac{1}{T_0}\right)\right] \tag{3.8}$$

where E_0 is the activation energy, T_0 a reference temperature, and R the gas constant. Using this shift, the viscosity curves measured at different temperatures can be used to generate a master curve at a specific temperature. Figure 3.2 [2] shows the viscosity of a low density polyethylene, for which the measured values were shifted to a reference temperature of 150 °C. For the shift in Figure 3.2, an activation energy of E_0 = 54 kJ/mol was used.

For amorphous thermoplastics, the Arrhenius shift is valid for temperatures $T > T_g + 100$ K. Below this temperature, free volume effects dominate the behavior. Hence, for lower temperatures, the temperature dependence of the viscosity of amorphous thermoplastics is best described by the Williams-Landel-Ferry (WLF) equation [3, 4]. This equation describes the viscosity η of the polymer at any given temperature, T, in relation to a reference viscosity at a reference temperature, T_s

$$\log a_T(T) = \log\frac{\eta_0(T)}{\eta_0(T_s)} = \frac{-C_1\left(T - T_s\right)}{C_2 + T - T_s} \tag{3.9}$$

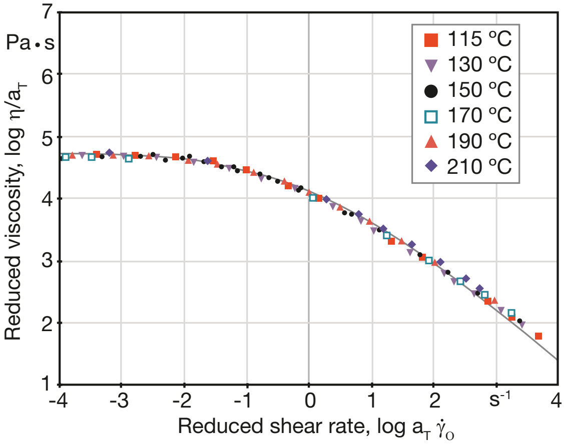

Figure 3.2 Reduced viscosity curve for a low density polyethylene (LDPE) at a reference temperature of 150 °C.

For polymers, this equation holds true only in the zero shear viscosity region. Because T_g is a widely used temperature, it is often chosen as the reference temperature T_s with $C_1 = 17.44$ and $C_2 = 51.6$ K. T_g is much lower than typical processing temperatures, therefore, van Krevelen [5] proposed a better alternative for T_s using $T_s = T_g + 43$ K, resulting in $C_1 = 8.86$ and $C_2 = 101.6$ K. Usually, the viscosity is not known at the reference temperature T_s, but at a temperature in the processing temperature range T^*, so that a second shift between measurement or processing temperature T^* and the reference temperature T_s is required. Equation 3.10 presents the relation between viscosity at T^* and at the actual temperature T

$$\log \frac{\eta_0(T)}{\eta_0(T^*)} = \frac{8.86\,(T^* - T_s)}{101.6 + T^* - T_s} - \frac{8.86\,(T - T_s)}{101.6 + T - T_s} \tag{3.10}$$

where the first term represents the shift between the measurement temperature T^* and the reference temperature T_s, and the second term represents the shift described above in Eq. 3.9, between the desired temperature T and the reference temperature T_s.

Table 3.1 gives an overview of the temperature differences between the glass transition or melting temperature and the processing temperatures T_{process} of amorphous and semi-crystalline thermoplastics, respectively.

Table 3.1 Difference between Common Reference Temperatures and Processing Temperatures for Common Thermoplastics

Polymer	T_g / T_m (°C)	T_{process} (°C)	ΔT (K)
Polystyrene	90–100	200–240	100–150
High density polyethylene	125–135	180–250	45–125
Low density polyethylene	100–110	150–310	40–210
Polypropylene	160–165	200–250	35–90
Polyamide 66	255–265	295–310	30–55
Polycarbonate	140–150	280–320	130–170
Polyvinyl chloride	−70–80	165–200	85–270

Example 3.1 WLF Shift

Compute the temperature shift factors for the given polycarbonate data using the WLF equation.

The shear dependent viscosity data are given for four different temperatures in the processing temperature range: 260, 280, 300 and 320 °C. In Figure 3.3 the logarithmic viscosity is plotted over the logarithmic shear rate. Calculate the temperature shift factors a_T for every single curve using T_s = 320 °C.

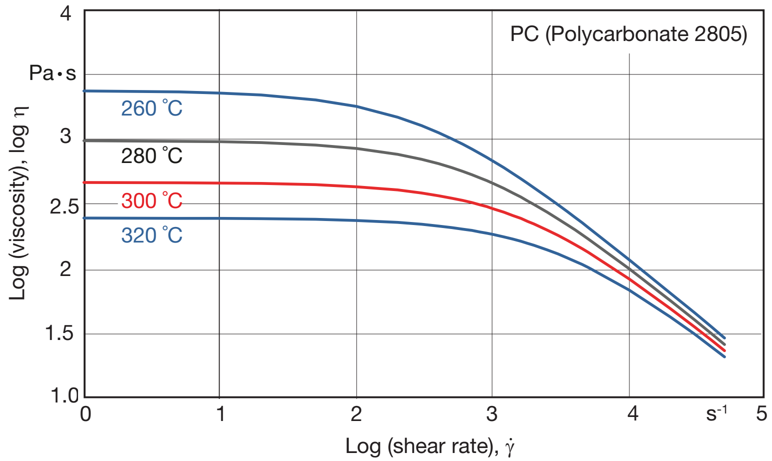

Figure 3.3 Viscosity curves for a polycarbonate

Table 3.2 Logarithmic Zero Shear (0 s^{-1}) and Shear Dependent (2, 3.5 s^{-1}) Viscosity for Different Temperatures

Log shear rate (s^{-1})	logη (260 °C)	logη (280 °C)	logη (300 °C)	logη (320 °C)
0	3.371	2.988	2.666	2.392
2	3.252	2.929	2.634	2.374
3.5	2.495	2.387	2.259	2.116

The shift factors are calculated with the zero shear viscosity data of Table 3.2 using Eq. 3.9. The results are given in Table 3.3:

Table 3.3 Shift Factors and ΔT

T (°C)	$\Delta T = T - T_s = (T - 320\ °C)$	$\log a_T$ (@ 1 s^{-1})	$[-(T - T_s)] / \log a_T$
260	−60	1.409	42.583
280	−40	1.249	32.026
300	−20	1.115	17.937
320	0	1	0

Now plot the WLF diagram using these shift factors with $\left[-\left(T-T_s\right)\right]/\log a_T$ as the y-axis and $\left(T-T_s\right)$ as the x-axis.

The determined linear equation $Y = -0.709\ \Delta T + 1.861$ can be used to calculate the viscosity at any temperature above T_g.

In order to calculate the viscosity at a processing temperature of, e.g., $T = 272$ °C, the temperature difference $\Delta T = 272\ °C - 320\ °C = -48\ °C$ is needed. Therefore, solving the equation yields a Y-value

$$Y = -0.709 \cdot \left(-48\right) + 1.861 = 35.893$$

Together with the temperature difference ΔT, the shift factor can be calculated using

$$\log a_T = \frac{-T - T_0}{Y} = \frac{48}{35.893} = 1.337$$

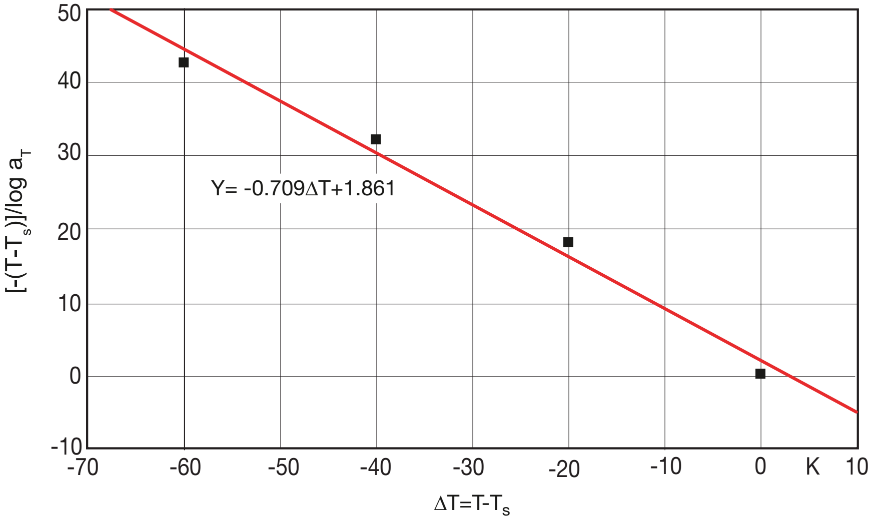

Figure 3.4 WLF diagram for linear regression to determine the constants C_1 and C_2

Now the $\log\eta$ at 272 °C can be obtained by adding the $\log\eta$ at the reference temperature, 320 °C,

$$\log\eta(272\ °\mathrm{C}) = \log a_T + \log\eta(320\ °\mathrm{C}) = 1.337 + 2.392 = 3.729$$

The viscosity is calculated as

$$\eta(272\ °\mathrm{C}) = 10^{3.729} = 5357\ \mathrm{Pa\ s}$$

3.2 Viscous Flow Models

Several models that comply with the *Generalized Newtonian Fluid* assumptions have been proposed in the literature. They vary in their form and in the number of parameters required to fit them to experimental results. These models have two general purposes: to obtain analytical solutions for different flow scenarios encountered in polymer processing, and to allow storage of the measured data with a minimum number of parameters [6]. The flow behavior of different fluids requires usage of different models; some fluids may be shear thinning, others may be fluids that experience a yield stress, and exhibit both behaviors (Fig. 3.5).

A rheologist's task is to find the model, represented in Eq. 3.1, that best fits the measured viscosity data, and at the same time is appropriate for the specific application (process) and type of flow. Complex models that better represent the rheological behavior of the polymer can add significant difficulty to the analysis of a flow field.

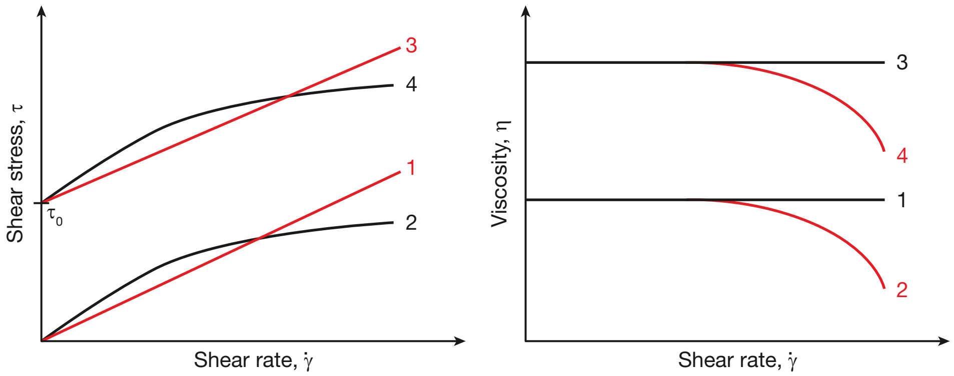

Figure 3.5 Stress curves (left) and viscosity curves (right) for different fluids; (1) Newtonian fluid, (2) shear thinning fluid, (3) Newtonian fluid with yield stress τ_0, (4) shear thinning fluid with yield stress τ_0

However, such models also increase the accuracy of the results and will require numerical solutions. Some of the models used on a day-to-day basis to represent the viscosity of industrial polymers are presented in the following sections.

3.2.1 The Power Law Model

The Power Law model proposed by Ostwald [7] and de Waele [8] is a simple model that accurately represents the shear thinning region in the viscosity versus shear rate curve, but neglects the Newtonian plateau observed at small strain rates, see Fig. 3.6. The Power Law model can be written as:

$$\eta = m(T)\,\dot{\gamma}^{n-1} \tag{3.11}$$

where m is often referred to as the consistency index and n as the Power Law or flow index. The Power Law index represents the shear thinning behavior of the polymer melt for $n < 1$. The consistency index may include the temperature dependence of the viscosity such as represented in Eq. 3.7. The temperature dependence of the consistency index can be represented using the relations given in Section 3.1. For example, one can use

$$m(T) = m_0 \cdot \exp\left[-a\left(T - T_0\right)\right] \tag{3.12}$$

where a is the temperature dependence or sensitivity parameter.

Figure 3.7 presents normalized velocity distributions inside a tube for fluids with various Power Law indices calculated using the Power Law model. It can be seen that a Power Law index of n = 1 represents Newtonian behavior and n = 0 represents plug flow.

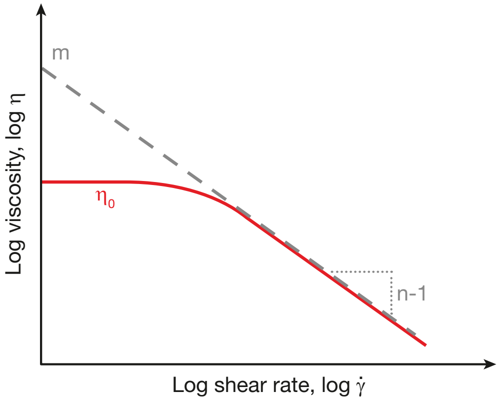

Figure 3.6 Viscosity curve (solid line) and approximation by the Power Law model (dashed line) in Eq. 3.11

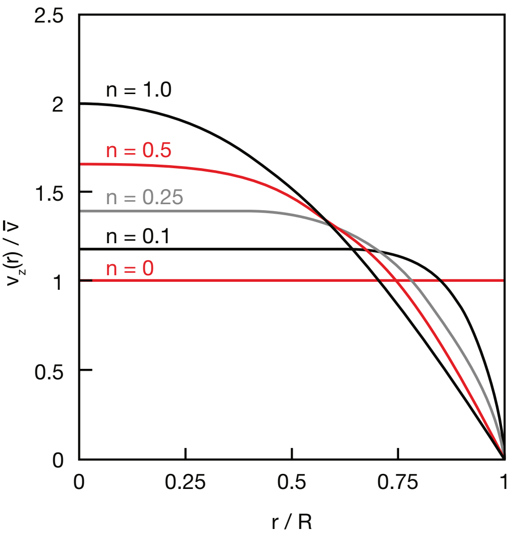

Figure 3.7 Pressure flow velocity distributions inside a tube for fluids with various Power Law indices

Table 3.4 Power Law *n*, Consistency Indices *m*, and Temperature Dependence Constants *a* for Common Thermoplastics

Polymer	m (Pa·s^n)	n	a (°C^{-1})	T (°C)
Polystyrene	2.80×10^4	0.28	−0.025	170
High density polyethylene	2.00×10^4	0.41	−0.002	180
Low density polyethylene	6.00×10^3	0.39	−0.013	160
Polypropylene	7.50×10^3	0.38	−0.004	200
Polyamide 66	6.00×10^2	0.66	−0.016	290
Polycarbonate	6.00×10^2	0.98	−0.015	300
Polyvinyl chloride	1.70×10^4	0.26	−0.019	180

Table 3.4 presents a list of typical Power Law and consistency indices as well as temperature dependence parameters for common thermoplastics. These parameters will vary significantly from grade to grade of the same type of polymer because of the variations in molecular weight, side groups, as well as flowing agents and other processing additives, to name a few. Therefore, the coefficients presented here should be used only as a guideline, and are not recommended for design purposes.

The Power Law model has the following limits:

$$\begin{aligned} &\eta \rightarrow 0 \quad \text{as} \quad \dot{\gamma} \rightarrow \infty \quad \text{and} \\ &\eta \rightarrow \infty \quad \text{as} \quad \dot{\gamma} \rightarrow 0 \end{aligned}$$

The infinite viscosity at zero strain rate $\dot{\gamma}$ leads to an erroneous result when a region of zero shear rate is encountered, e.g., for flow in a tube or slit. Here, the shear rate is high at the walls, but low near the center and zero at the center itself. Neglecting the zero shear viscosity values in the center would result in an over-prediction of the viscosity in this area. Therefore, the predicted velocity distribution would be flatter at the center than the experimental profile.

Another example is the filling of a cavity at high flow rates in the beginning of the filling process and at a low flow rate towards the end of filling. Here, the viscosity at the end of filling would be too high, leading to over-predicted injection molding pressure requirements.

Computer simulation of polymer flows overcome this problem by using a truncated model, such as

$$\eta = m_0(T)\,\dot{\gamma}^{n-1} \quad \text{for} \quad \dot{\gamma} > \dot{\gamma}_0 \quad \text{and} \tag{3.13}$$

$$\eta = m_0(T) \quad \text{for} \quad \dot{\gamma} \le \dot{\gamma}_0 \tag{3.14}$$

where m_0 represents a zero shear rate viscosity and $\dot{\gamma}_0$ the shear rate where the Newtonian plateau ends and shear thinning starts to manifest itself.

3.2.2 The Bird-Carreau-Yasuda Model

Bird, Carreau [9] and Yasuda [10] developed a model that accounts for the observed Newtonian plateaus and fits a wide range of strain rates; it contains five parameters:

$$\frac{\eta_{\dot{\gamma}} - \eta_\infty}{\eta_0 - \eta_\infty} = \left(1 + \left|\lambda\dot{\gamma}\right|^a\right)^{\frac{(n-1)}{a}} \tag{3.15}$$

where η_0 is the zero shear rate viscosity, η_∞ is an infinite shear rate viscosity of the second Newtonian plateau, λ is a time constant, and n is the Power Law index, which accounts for the shear thinning behavior, see Fig. 3.8. The parameter a accounts for the width of the transition region between the zero shear viscosity and the Power Law region, which in the original Bird-Carreau model equaled 2. In the literature this model is referred to by different combinations of the collaborators' names, although Carreau model and Bird-Carreau model are commonly used.

In many cases, the infinite shear rate viscosity is negligible, reducing Eq. 3.15 to a three-parameter model:

$$\eta(\dot{\gamma}) = \frac{\eta_0}{\left(1 + \left|\lambda\dot{\gamma}\right|^a\right)^{\frac{(n-1)}{a}}} \tag{3.16}$$

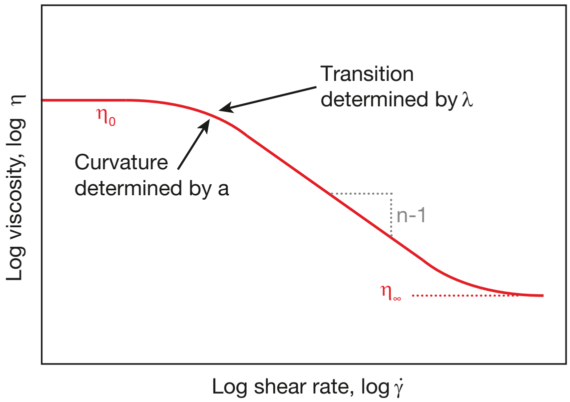

Figure 3.8 Viscosity approximation using the Bird-Carreau-Yasuda model in Eq. 3.15

Equation 3.16 was modified by Menges, Wortberg, and Michaeli [11] to include a temperature dependence using a WLF relation. The modified model, which is often used in commercial polymer data bases, is written as

$$\eta = \frac{k_1 \cdot a_T}{\left(1 + k_2\,\dot{\gamma}\,a_T\right)^{k_3}} \tag{3.17}$$

where the shift factor a_T applies well for amorphous thermoplastics and is written as

$$\log a_T = \frac{8.86\,(k_4 - k_5)}{101.6 + k_4 - k_5} - \frac{8.86\,(T - k_5)}{101.6 + T - k_5} \tag{3.18}$$

The above equation is comparable to Eq. 3.10 and for semi-crystalline thermoplastics with the Arrhenius shift given in Eq. 3.8.

Table 3.5 presents constants for the Carreau-WLF (amorphous) and Carreau-Arrhenius models (semi-crystalline) for various common thermoplastics.

Table 3.5 Constants for Carreau-WLF (Amorphous) and Carreau-Arrhenius (Semi-Crystalline) Models for Various Common Thermoplastics

Polymer	k_1 (Pa s)	k_2 (s)	k_3	k_4 (°C)	k_5 (°C)	T_0 (°C)	E_0 (J/mol)
Polystyrene	1777	0.064	0.73	200	123	–	–
High density polyethylene	24198	1.38	0.60	–	–	200	22272
Low density polyethylene	317	0.015	0.61	–	–	189	43694
Polypropylene	1386	0.091	0.68	–	–	220	427198
Polyamide 66	44	0.00059	0.40	–	–	300	123058
Polycarbonate	305	0.00046	0.48	320	153	–	–
Polyvinyl chloride	1786	0.054	0.73	185	88	–	–

3.2.3 The Cross-WLF Model

This 6-parameter model considers the effects of shear rate and temperature on the viscosity. Similar to the Bird-Carreau model, this model describes both Newtonian and shear thinning behavior. The shear thinning part is modeled by the general Cross equation [12], which is a popular and earlier alternative to the Bird-Carreau-Yasuda model:

$$\frac{\eta_{\dot{\gamma}} - \eta_\infty}{\eta_0 - \eta_\infty} = \frac{1}{1 + \left(K \cdot \dot{\gamma}\right)^{1-n}} \tag{3.19}$$

where η_0 is the zero shear rate viscosity, η_∞ is an infinite shear rate viscosity, K is a time constant such as k_2 in Table 3.5, and n is the Power Law index, which accounts for the shear thinning behavior. For $\eta_{\dot{\gamma}} \ll \eta_0$ and $\eta_{\dot{\gamma}} \gg \eta_\infty$, the Cross model reduces to the Power Law model. If the infinite shear rate viscosity is negligible, the well-known form of the Cross model can be written as

$$\eta\left(\dot{\gamma}\right) = \frac{\eta_0}{1 + \left(\dfrac{\eta_0\,\dot{\gamma}}{\tau^*}\right)^{1-n}} \tag{3.20}$$

Here, τ^* is the critical shear stress at the transition from the Newtonian plateau, with $K = \eta_0 / \tau^*$, and n is the Power Law index, see Fig. 3.9. If the model is used to fit the data prior to making the Weissenberg-Rabinowitsch correction (see Eq. 6.19 in Chapter 6), the apparent shear stress can be shifted [13] by setting

$$\tau^* = \left(\frac{4n}{3n+1}\right)^{\frac{n}{1-n}} \tag{3.21}$$

In this case, the remaining model parameters remain unchanged.

The zero shear viscosity is modeled with the WLF equation

$$\eta_0\left(T\right) = D_1 \cdot \exp\left[\frac{A_1\left(T - D_2\right)}{A_2 + T - D_2}\right] \tag{3.22}$$

where D_1 is the viscosity at a reference temperature D_2 and A_1 and A_2 describe the temperature dependency, which is comparable to the temperature shift factor described in Eq. 3.9.

The Cross-WLF model is the most common model used by injection molding simulation software, because it offers the best fit to most viscosity data [14]. Table 3.6 presents constants for various common thermoplastics.

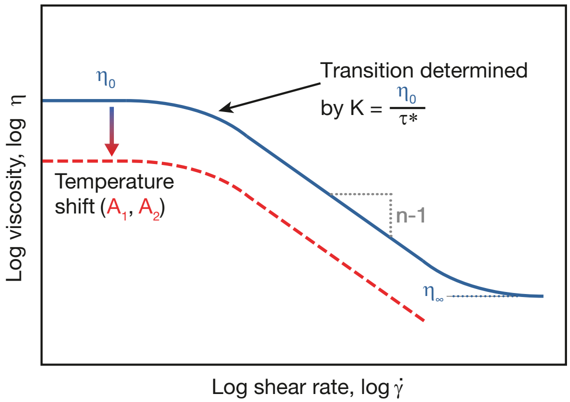

Figure 3.9 Viscosity approximation with the Cross-WLF model in Eq. 3.20 and Eq. 3.22

Table 3.6 Constants for the Cross-WLF Model for Various Common Thermoplastics [15, 16]

Polymer	τ (Pa)	n	D_1 (Pa s)	D_2 (K)	A_1	A_2 (K)
Polystyrene	31,200	0.243	1223	503	6.5	158.2
High density polyethylene	75,700	0.342	7×10^{12}	153	26.3	51.6
Low density polyethylene	34,515	0.315	3.1×10^{14}	233	34.6	51.6
Polypropylene	32,477	0.251	564	493	2803.3	165,097.1
Polyamide 66	151,905	0.347	144	573	256,999.6	11,235,949
Polycarbonate	8,437,056	0.116	462	573	8.4	246.8
Polyvinyl chloride	46,070	0.399	3.2×10^{16}	353	42.9	51.6

3.2.4 The Bingham Model

The Bingham model is an empirical two-parameter model that represents the rheological behavior of materials that exhibit yield stresses τ_0, below which the material does not flow. Typical examples of Bingham fluids are polymer emulsions and slurries. In the flow range, above the yield stress, a Bingham fluid behaves like a Newtonian liquid and can therefore be represented as

$$\eta = \infty \quad \text{or} \quad \dot{\gamma} = 0 \quad \text{for} \quad \tau \leq \tau_0 \tag{3.23}$$

$$\eta = \mu_0 + \frac{\tau_0}{\dot{\gamma}} \quad \text{for} \quad \tau > \tau_0 \tag{3.24}$$

Here, τ is the magnitude of the deviatoric stress tensor and μ_0 is the Newtonian viscosity for vanishing yield stress. The model shows that a critical level of stress must be attained in order to initiate flow.

3.2.5 The Herschel-Bulkley Model

The Herschel-Bulkley model is widely used to represent the behavior of fluids that have a yield stress, such as the Bingham fluid, but that otherwise exhibit shear thinning behavior. The model is represented as

$$\tau = \tau_0 + m \cdot \dot{\gamma}^n \tag{3.25}$$

$$\eta = \frac{\tau_0}{\dot{\gamma}} + m \cdot \dot{\gamma}^{n-1} \quad \text{for} \quad \tau > \tau_0 \tag{3.26}$$

where τ_0 is the yield stress, m the consistency index, and n the Power Law or flow index. As with the Bingham model, this model also requires that a critical level of stress must be attained to initiate flow. Below this critical stress τ_0, the material behaves like a solid, allowing it to sustain stress without flow, but above the critical stress, the material flows like a Power Law fluid. Similar to the Power Law model, $n < 1$ represents shear thinning, $n > 1$ shear thickening, and $n = 1$ reduces the model to the Bingham model and represents Newtonian flow above the critical yield stress.

Table 3.7 shows that all models discussed so far can be derived from one base equation. While the Power Law model is the simplest model that can be used when the shear rate is high, the Cross-WLF model is the most common model in numerical simulations because it fits the viscosity data of a wide range of materials. In terms of practical applications, it is closely followed by the Bird-Carreau-Yasuda model.

Table 3.7 Overview of Viscous Flow Models

	Power Law	Bird-Carreau-Yasuda	Cross-WLF	Bingham
Base equation	$\frac{\eta - \eta_\infty}{\eta_0 - \eta_\infty} = \frac{1}{\left[1 + (K\dot{\gamma})^a\right]^{\frac{(1-n)}{a}}}$			
Assumptions	$\eta \ll \eta_0$, $\eta \gg \eta_\infty$, $\eta_\infty = 0$, $a = 1$, $K = m$	$\eta_\infty = 0$, $K = \lambda$	$\eta_\infty = 0$, $a = 1$, $K = \frac{\eta_0}{\tau^*}$	$\eta \ll \eta_0$, $\eta \ll \mu_0$, $K = \tau_Y$, $n = 0$
Model	$\eta = m \cdot \dot{\gamma}^{n-1}$	$\eta = \frac{\eta_0}{\left(1 + \lvert\lambda\dot{\gamma}\rvert^a\right)^{\frac{(1-n)}{a}}}$	$\eta = \frac{\eta_0}{1 + \left(\frac{\eta_0 \dot{\gamma}}{\tau^*}\right)^{1-n}}$	$\eta = \mu_0 + \frac{\tau_Y}{\dot{\gamma}}$

3.2.6 Accounting for Pressure Dependence in Viscous Flow Models

Although the effect of pressure on viscosity is well known, few research groups have focused on this topic. However, using some experimental values in conjunction with theoretical considerations, pressure effects have been incorporated into existing models. These are discussed in the following sections.

3.2.6.1 Power Law

The Power Law model, Eq. 3.11, may also include a dimensionless temperature sensitivity factor, a or α, Eq. 3.7, as well as a dimensionless pressure sensitivity factor, b or β, proposed by Barus [17], respectively,

$$\eta\left(T,\dot{\gamma},p\right)=m_0\cdot\exp\left[-a\left(T-T\right)_0\right]\cdot\exp\left[b\left(p-p_0\right)\right]\cdot\dot{\gamma}^{n-1} \tag{3.27}$$

The opposing signs of the sensitivity factors a and b reflect their effect on viscosity, due to the fact that viscosity increases with decreasing temperature and increasing pressure. The terms in the above equation can be expressed in terms of a temperature shift factor

$$a_T\left(T\right)=\frac{\eta_0\left(T\right)}{\eta_0\left(T_0\right)}=\exp\left[-a\left(T-T_0\right)\right] \tag{3.28}$$

and a pressure shift factor

$$a_p\left(p\right)=\frac{\eta_0\left(p\right)}{\eta_0\left(p_0\right)}=\exp\left[b\left(p-p_0\right)\right] \tag{3.29}$$

This model neglects the Newtonian plateau, or shear independent behavior, observed with polymers at low shear rates. However, the exponential form of the viscosity shifts make it easy to represent the sensitivity to temperature and pressure during measurements and processing.

3.2.6.2 Carreau-WLF

Cogswell [18] related a viscosity change to a change in density, because a temperature reduction and an increase in pressure will increase both density and viscosity. Based on this assumption, Menges et al. [11] introduced the pressure shift in the WLF-temperature shift, Eq. 3.10, in combination with the Bird-Carreau-Yasuda model, Eq. 3.17. For their shift $T_s\left(p\right)$ they used the glass transition temperature T_g from pressure-volume-temperature (pvT) measurements [19, 20] at 1 bar, and a correction that included the pressure dependence of T_g

$$T_s(p) = T_g + 43\,\mathrm{K} = T_{g\,(1\,\mathrm{bar})} + (P_1 \cdot p) + 43\,\mathrm{K} \tag{3.30}$$

with P_1 being the pressure dependence of the glass transition and p the absolute pressure. P_1 ranges from 0.02 to 0.03 K/bar, depending on the polymer. Introducing Eq. 3.30 into Eq. 3.18 results in

$$\log \eta(T,p) = \log \eta_0 + \frac{8.86\,(T^* - T_s)}{101.6 + T^* - T_s} - \frac{8.86\,(T - T_s - P_1 \cdot p)}{101.6 + T - T_s - P_1 \cdot p} \tag{3.31}$$

In the above equation, the first term represents a shift between the measured temperature T^* and the reference temperature T_s. The second term represents the temperature and pressure shifts between the actual temperature and the reference temperature, as well as between 1 bar and the actual pressure. Hence, in the above model a rise in pressure is equivalent to a drop in temperature. Menges et al. [11] proposed that P_1 = 0.02 K/bar, which provides a good approximation in case *pvT*-data are not available.

3.2.6.3 Cross-WLF

Incorporating the pressure dependence in the Cross-WLF equation leaves the shear thinning part unchanged. It is modeled by the general Cross equation

$$\eta(\dot{\gamma}) = \frac{\eta_0}{1 + \left(\dfrac{\eta_0\,\dot{\gamma}}{\tau^*}\right)^{n-1}} \tag{3.20}$$

where τ^* is the critical shear stress at the transition from the Newtonian plateau, η_0, to the Power Law regime, and n denotes the Power Law index.

The zero shear viscosity is modeled with the WLF equation

$$\eta_0(T,p) = D_1 \cdot \exp\left[\frac{A_1\,(T - T_c)}{A_2 + T - T_c}\right] \tag{3.32}$$

with $T_c = D_2 + D_3 \cdot p$ and $A_2 = \tilde{A}_2 + D_3 \cdot p$. In addition to the parameters in Eq. 3.25, D_3 denotes the pressure dependency, while p is the pressure acting on the melt. Because of the added parameters, the model is sometimes referred to as the 7-parameter model. D_1 reflects the initial level of viscosity at reference conditions, D_2 is typically taken as the glass transition temperature T_g, and A_1 and $\tilde{A}_2$ are temperature dependent factors. Other than P_1 in Eq. 3.31, D_3 also corrects the reference temperature D_2. If pressure dependent viscosity data are not available, *pvT*-data are used to account for the pressure dependence of the glass transition temperature. Equation 3.32 is often written as

$$\eta_0(T,p) = D_1 \cdot \exp\left[\frac{A_1(T - D_2 - D_3 \cdot p)}{\tilde{A}_2 + T - D_2}\right] \tag{3.33}$$

Typical values for the pressure sensitivity for different polymers are listed in Table 3.8.

Table 3.8 Pressure Shift Factors of Viscosity for Various Common Polymers

Polymer	*b* or *β* (bar^{-1}) Power Law	Reference	D_3 (K bar^{-1}) Cross-WLF	Reference
Polystyrene	0.004345 0.00568, 0.0029	21, 22, 23	0.1	24
High density polyethylene	0.001036 0.0015, 0.001 0.001	21, 22, 23 25	0.012	26
Low density polyethylene	0.00183 0.00147 0.00165, 0.0016	21, 23, 25		
Polypropylene	0.002091, 0.00282, 0.0022 0.0023	21, 22, 23, 25	0.0205, 0.014	24, 27
Polycarbonate	0.003112	21	0.03, 0.018	26, 27
Polymethyl methacrylate	0.004357 0.0024	21, 23	0.023	14

The differences between the shift factors for one material reported by different research groups underline the difficulty of the measurement. Therefore, different measurement methods for the pressure influence on viscosity are described in more detail in Chapter 6.

3.2.6.4 Universal Temperature and Pressure Invariant Viscosity Function

Because the viscosity behavior of a specific thermoplastic is very similar from grade to grade one can predict its full behavior based on one single function. This allows the use of single point data, such as measured with an MFI, to predict the viscosity of a given material as a function of pressure and temperature. This “universal” behavior was recognized in the early polymer research days and is reflected in the WLF shift. Different research groups have investigated this temperature and pressure invariant representation of viscosity [28, 29, 30, 31, 32, 33]. Reference viscosity curves, such as the one presented for polycarbonate in Fig. 3.10, can then be used as a reference, if no multipoint data are available. To generate such a curve, the shear dependent viscosity is divided by the shear independent viscosity, η_0, for each given temperature and pressure. This is followed by multiplying the shear rate by η_0. By doing this, the “universal” curve approaches a slope of −1, or a 45° angle in a log-log scale.

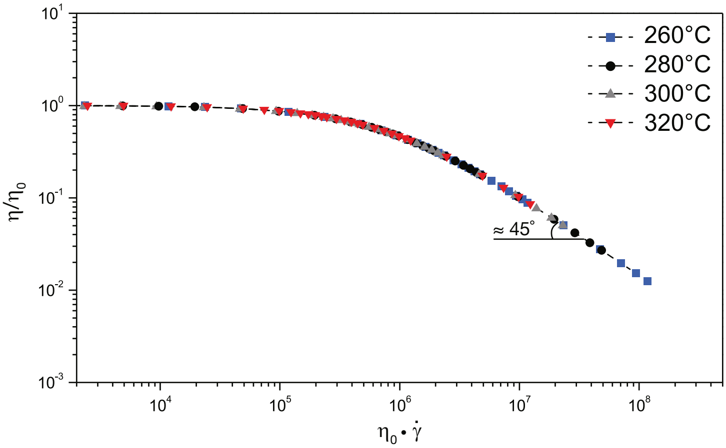

Figure 3.10 Master curve for polycarbonate (Makrolon 2805) as obtained as a function of zero shear viscosity

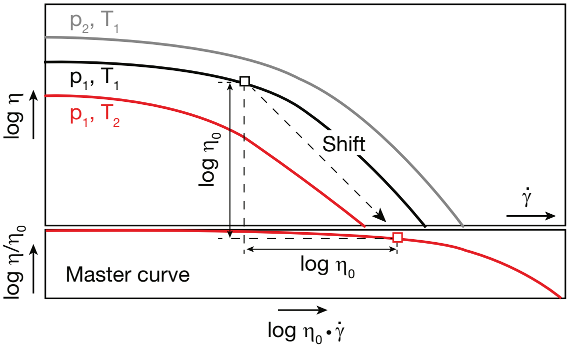

Figure 3.11 Measured viscosity at different temperatures and pressures as a function of shear rate and shift into general viscosity function (master curve)

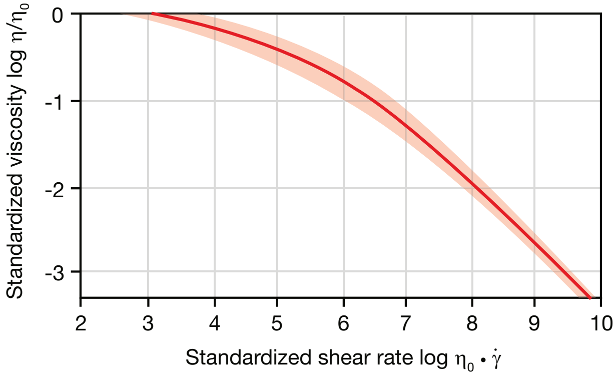

Figure 3.12 Universal temperature-independent viscosity characteristic of polymer melts

Vinogradov and Malkin [34] discovered that the viscosity curves for several structurally different materials, such as polyethylene, polypropylene, polystyrene, and unvulcanized natural rubber, could be reduced to a narrow band of viscosity curves if plotted as $\log \eta/\eta_0 = f\left(\eta_0 \cdot \dot{\gamma}\right)$ as shown in Fig. 3.12.

Figure 3.11 shows schematically how the master curve is generated from shear dependent viscosity data.

Dividing the viscosity by the zero shear viscosity gives a dimensionless number, $\log \eta/\eta_0$, which becomes zero when the viscosity approaches the shear independent viscosity at the Newtonian plateau, and is negative in the shear thinning region, see Fig. 3.12.

The centerline in Fig. 3.12 represents the universal, temperature invariant viscosity function or master curve. The band width shows how close the master curves align for the investigated materials [34]. As the pressure dependence can be converted into a temperature dependence, this master curve can also be used for a pressure and temperature independent presentation [35]. The master curve can be described by a general viscosity function in the form

$$\eta(\dot{\gamma},T,p) = \eta_0 \left[1 + A_1\left(\eta_0\,\dot{\gamma}\right)^{\alpha} + A_2\left(\eta_0\,\dot{\gamma}\right)^{2\alpha}\right]^{-1} \tag{3.34}$$

where η_0 is the zero shear viscosity as a function of temperature and pressure as well as shear rate $\dot{\gamma}$. A_1, A_2 and α are constants with $A_1 = 6.12 \cdot 10^{-3}$, $A_2 = 2.85 \cdot 10^{-4}$, and $\alpha = 0.355$ [34]. Rewriting the constants $\tau_1 = A_1^{-1/\alpha}$ and $\tau_2 = A_2^{-1/2\alpha}$ and assuming $\alpha = n - 1$, a function very similar to the Cross model, Eq. 3.20, is obtained

$$\eta(\dot{\gamma},T,p) = \frac{\eta_0}{1 + \left(\dfrac{\eta_0\,\dot{\gamma}}{\tau_1}\right)^{\alpha} + \left(\dfrac{\eta_0\,\dot{\gamma}}{\tau_2}\right)^{2\alpha}} \tag{3.35}$$

where τ_1 = 1,715,943 Pa and τ_2 = 98,441 Pa. Menges et al. [35] showed that this universal viscosity function allows the use of single-point viscosity data to predict rate dependent flow behavior. Of course, the use of multi-point data is always recommended. However, in case only single-point data such as MFI is available, this approach can be used to estimate the shear rate dependent behavior. An example for this estimation is given in the following.

Example 3.2 Vinogradov's Universal Viscosity Approach

For injection molding experiments with HDPE, the following single-point material properties are known from the material datasheet:

- MFI: 20 g/10 min measured at 190 °C and 2.16 kg weight
- Density at room temperature ρ_{T_0}: 0.948 g/cm^3
- Linear thermal expansion coefficient α: $6.9 \cdot 10^{-4}\ \mathrm{K}^{-1}$

In order to obtain shear dependent viscosity data, the single-point MFI value can be used. For this approach the testing conditions and geometry of the die must also be known. For MFI data, the geometry of the ASTM standard D1234 [36] can be used; the standard utilizes a capillary with 2.095 mm diameter (R = 1.0475 mm) and 8 mm length.

The melt flow index (MFI) is converted into the melt volume flow rate (MVR) Q by

$$Q = \mathrm{MVR} = \frac{\mathrm{MFI}}{\rho(T^*)} = \frac{20\ \mathrm{g} \cdot \mathrm{cm}^3}{0.704\ \mathrm{g} \cdot 10\ \mathrm{min}} = 28.39\,\frac{\mathrm{cm}^3}{10\ \mathrm{min}}$$

where the density ρ at the measurement temperature T^* of 190 °C is calculated by

$$\rho(T) = \rho_{T_0}\,\frac{1}{1+\alpha\left(T^* - T_0\right)} = 0.948\,\frac{\mathrm{g}}{\mathrm{cm}^3} \cdot \frac{1}{1+3 \cdot 6.9 \cdot 10^{-4}\ \mathrm{K}^{-1}\left(190\ ^\circ\mathrm{C} - 23\ ^\circ\mathrm{C}\right)}$$

$$= 0.704\,\frac{\mathrm{g}}{\mathrm{cm}^3}$$

where T_0 is room temperature, and α is the linear thermal expansion coefficient, which has to be multiplied by 3 to obtain the required volume expansion coefficient.

Because the flow within the capillary can be represented by the Hagen-Poiseuille equation (Chapter 4), the shear rate at the wall of the capillary can be easily calculated. Using Schümmer's assumption [37], which is explained in more detail in Section 6.4.2, that the intersection of the velocity distribution of the Newtonian and the shear thinning fluid coincides at the same position for all polymers, the true shear rate $\dot{\gamma}_\mathrm{w}$ (Eq. 6.28) and shear stress τ_w (Eq. 6.29) at the wall can be computed for the melt flow indexer measurement using

$$\dot{\gamma}_\mathrm{w} = \frac{Q}{R^3} = \frac{28.39\ \mathrm{cm}^3}{\left(0.10475\ \mathrm{cm}\right)^3 \cdot 600\ \mathrm{s}} = 41.17\ \mathrm{s}^{-1}$$

and

$$\tau_\mathrm{w} = \frac{R \cdot \pi \cdot \partial p/\partial z}{8} = \frac{0.0010475\ \mathrm{m} \cdot \pi \cdot 768.12\ \mathrm{MPa}}{8 \cdot \mathrm{m}} = 0.32\ \mathrm{MPa}$$

where $\partial p/\partial z$ is the pressure gradient along the capillary over the length L, given by

$$\partial p/\partial z = \frac{F}{R^2 \cdot \pi \cdot L} = \frac{21.18\ \mathrm{N}}{\left(0.0010475\ \mathrm{m}\right)^2 \cdot \pi \cdot 0.008\ \mathrm{m}} = 768.12\,\frac{\mathrm{MPa}}{\mathrm{m}}$$

where F is the piston load of the MFI (2.16 kg · 9.81 m/s^2) and L is the die length. The radius of the piston should be used for the pressure calculation; however, for simplification the radius of the die R is used here.

The viscosity under MFI measurement conditions is then

$$\eta\left(\dot{\gamma}_{\mathrm{w}}, T^*, p^*\right) = \frac{\tau_{\mathrm{w}}}{\dot{\gamma}_{\mathrm{w}}} = \frac{0.32\ \mathrm{MPa}}{41.17\ \mathrm{s}^{-1}} = 7675.15\ \mathrm{Pa\ s}$$

Because the shear rate experienced by the material inside the melt flow indexer is very small (< 100 s^{-1}), the resulting viscosity value of 7,675.15 Pa s can be considered as the zero shear viscosity $\eta_0\left(T^*, p^*\right)$. To assure that this assumption is correct, the MFI should be measured using small loads, allowing the presented calculation of $\dot{\gamma}_{\mathrm{w}}$ and τ_{w}.

In order to obtain the zero shear viscosity at a given temperature and pressure, first the pressure at the entrance of the MFI measurement die, p^*, has to be calculated using

$$p^* = \frac{\partial p/\partial z \cdot L}{2} = \frac{768.12\ \mathrm{MPa} \cdot 0.008\ \mathrm{m}}{2 \cdot \mathrm{m}} = 3.07\ \mathrm{MPa} = 30.72\ \mathrm{bar}$$

Now the viscosity under typical processing conditions of HDPE, e.g., 210 °C at 1 bar and at 1000 bar, should be measured. Therefore, the temperature and pressure shifts of the modified Carreau-WLF model, Eq. 3.31, have to be used

$$\eta_0\left(T, p\right) = \eta_0\left(T^*, p^*\right) \cdot 10^{\frac{8.86\left(T^* - T_{\mathrm{s}}\right)}{101.6 + T^* - T_{\mathrm{s}}} - \frac{8.86\left(T - T_{\mathrm{s}} + P_1 \cdot p\right)}{101.6 + T - T_{\mathrm{s}} + P_1 \cdot p}}$$

where T^* = 190 °C, p^* = 30.72 bar, and P_1 = 0.02 K/bar. For T = 210 °C, p = 1 bar and T_{s} = −150 °C + 43 °C = −107 °C. The zero shear viscosity is

$$\begin{aligned}\eta_0\left(T, p\right) &= \eta_0\left(T^*, p^*\right) \cdot 10^{\frac{8.86\left(190\,^\circ\mathrm{C} + 107\,^\circ\mathrm{C}\right)}{101.6\,^\circ\mathrm{C} + 190\,^\circ\mathrm{C} + 107\,^\circ\mathrm{C}} - \frac{8.86\left(210\,^\circ\mathrm{C} + 107\,^\circ\mathrm{C} + 0.61\,^\circ\mathrm{C}\right)}{101.6\,^\circ\mathrm{C} + 210\,^\circ\mathrm{C} + 107\,^\circ\mathrm{C} + 0.61\,^\circ\mathrm{C}}} \\ &= 7675.15\ \mathrm{Pa\ s} \cdot 10^{-0.111029} = 5943.72\ \mathrm{Pa\ s}\end{aligned}$$

For T = 210 °C, p = 1000 bar and T_{s} = −150 °C + 43 °C = −107 °C, the zero shear viscosity is

$$\begin{aligned}\eta_0\left(T, p\right) &= \eta_0\left(T, 1000\ \mathrm{bar}\right) \cdot 10^{\frac{8.86\left(210\,^\circ\mathrm{C} + 107\,^\circ\mathrm{C}\right)}{101.6\,^\circ\mathrm{C} + 210\,^\circ\mathrm{C} + 107\,^\circ\mathrm{C}} - \frac{8.86\left(210\,^\circ\mathrm{C} + 107\,^\circ\mathrm{C} - 20\,^\circ\mathrm{C}\right)}{101.6\,^\circ\mathrm{C} + 210\,^\circ\mathrm{C} + 107\,^\circ\mathrm{C} - 20\,^\circ\mathrm{C}}} \\ &= 5943.72\ \mathrm{Pa}\ s \cdot 10^{0.1079000} = 7620.05\ \mathrm{Pa\ s}\end{aligned}$$

In addition, the shear rate dependent viscosity can now be calculated with the universal Eq. 3.34 for T = 210 °C, p_1 = 1 bar, and p_2 = 1000 bar so that the following Table 3.9 can be generated.

Table 3.9 Shear Rate Dependent Viscosity Data of HDPE at 210 °C and 1 and 1000 bar Using the Vinogradov Approach (Eq. 3.34)

Shear rate (s^{-1})	1	40	80	200	400	1000	3000	5000
1 bar	4680	1770	1270	768	507	284	137	97
1000 bar	5820	2260	1620	984	650	364	176	124

3.3 Elongational Viscosity

In polymer processes such as fiber spinning, blow molding, thermoforming, foaming, certain extrusion die flows, and compression molding with specific processing conditions, the major mode of deformation is elongational.

To illustrate elongational flows, consider the fiber spinning process shown in Figure 3.13.

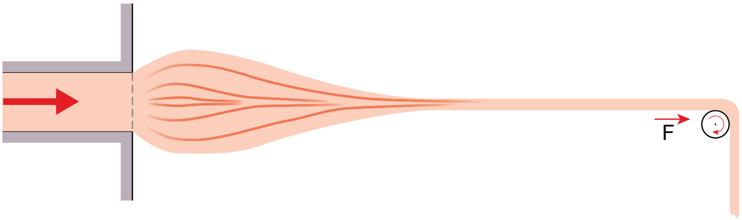

Figure 3.13 Schematic diagram of a fiber spinning process

As the filament is stretched, a simple elongational flow develops with the following components of the rate of deformation:

$$\dot{\gamma}_{11} = -\dot{\varepsilon} \tag{3.36}$$

$$\dot{\gamma}_{22} = -\dot{\varepsilon} \tag{3.37}$$

$$\dot{\gamma}_{33} = -2\dot{\varepsilon} \tag{3.38}$$

where $\dot{\varepsilon}$ is the elongation rate, and the non-diagonal terms of $\dot{\gamma}_{ij}$ are all zero. The diagonal terms of the total stress tensor can be written as

$$\sigma_{11} = -p - \eta\dot{\varepsilon} \tag{3.39}$$

$$\sigma_{22} = -p - \eta\dot{\varepsilon} \tag{3.40}$$

$$\sigma_{33} = -p + 2\eta\dot{\varepsilon} \tag{3.41}$$

Because the only outside forces acting on the fiber are in the axial or 3-direction, for the Newtonian case, σ_{11} and σ_{12} must be zero. Hence,

$$p = -\eta\dot{\varepsilon} \tag{3.42}$$

$$\sigma_{33} = 3\eta\dot{\varepsilon} = \overline{\eta}\dot{\varepsilon} \tag{3.43}$$

which is known as *elongational viscosity or Trouton viscosity* [38]. This is analogous to elasticity with the following relation between elastic modulus, *E*, and shear modulus, *G*:

$$\frac{E}{G} = 2\left(1+\nu\right) \tag{3.44}$$

where ν is Poisson's ratio. For the incompressibility case, where $\nu = 0.5$, Eq. 3.44 reduces to

$$\frac{E}{G} = 3 \tag{3.45}$$

Figure 3.14 [39] shows shear and elongational viscosities of polystyrene. In the region of the Newtonian plateau, the limit of 3, shown in Eq. 3.43, is quite clear.

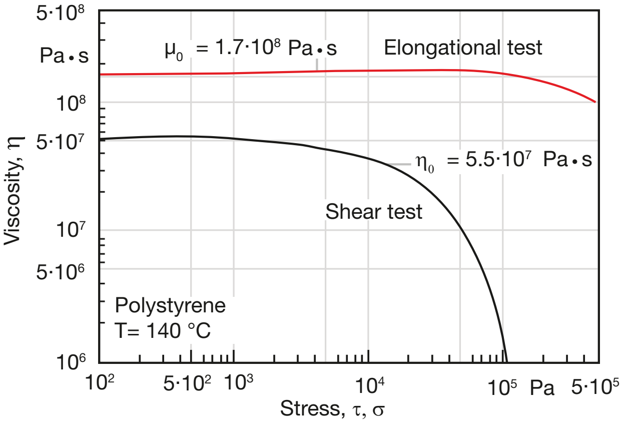

Figure 3.14 Shear and elongational viscosity curves of polystyrene

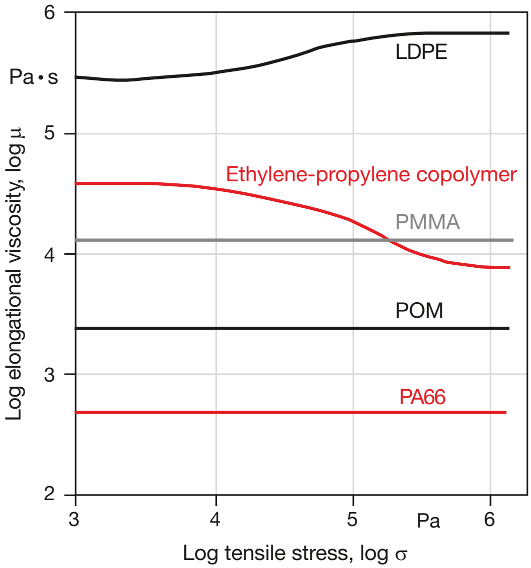

Figure 3.15 Elongational viscosity curves as functions of tensile stress for several thermoplastics

Figure 3.15 [40] shows plots of elongational viscosities at common processing conditions as functions of stress for various thermoplastics. Measuring elongational or extensional viscosity is an extremely difficult task, because maintaining a constant strain rate is challenging. For example, the specimen must be deformed uniformly exponentially. Different common measurement techniques are explained in more detail in Chapter 6 and additional examples are provided.

3.4 Suspension Rheology

Particles suspended in a material, such as in reinforced or filled polymers, have a direct effect on the properties of the final component and on the viscosity during processing. Today, polymer materials are seldom used in their pure form. Instead various filler particles are used to enhance mechanical properties, increase the resistance to wear, improve thermal or electrical conductivity, add magnetic properties, and much more. In addition, the use of polymers as binders during ceramic processing is another growing market. The shape of those particles can vary from rod-like particles in fiber suspensions to spherical particles or flakes. The viscosity of a fluid filled with particles is higher than that of the neat polymer. The viscosity of the filled system depends on the volume fraction of the particles, the particle shape, the average particle size and the size distribution, the shear rate, and the interaction between particles as well as between particles and the polymer matrix [41]. A volume fraction between 20 to 40% is considered low filler loading range, whereas 40 to 60% is referred to as high filler loading range. The higher the volume fraction and the larger the aspect ratio (fiber > platelet > sphere) of the particle, the higher the viscosity increase compared to the neat polymer.

Depending on whether the matrix system is a thermoplastic or a thermoset, the flow is shear thinning or Newtonian, respectively [42]. However, during flow particles may agglomerate. The shape of these clusters is dependent on the shear rate and directly related to a change in viscosity [43, 44]. Another effect that accompanies agglomeration or filler size in general is thixotropy [43]. During shearing, the initial formation of the particles begins to change until a final structure has formed [45]. This change is accompanied by an initial decrease in viscosity until a steady-state Newtonian plateau is reached. Both effects are directly proportional to the volume fraction and size of the filler.

However, viscosity measurements of filled polymers are more difficult than those of neat polymers, because the no-slip condition at the wall cannot be readily assumed. Furthermore, shearing occurs not only at the wall but also between the particles. For measurements in capillary rheometers, problems occur at the inlet of the die. First, the inlet pressure drop is larger and sometimes instable. Second, phase separation can occur with filled polymers and therefore impede the development of steady flow.

For example, magnetic particles, such as strontium ferrite, distributed in a polymer matrix are used to manufacture permanent magnets. These particles tend to agglomerate, as seen in Fig. 3.16. An extensive study on single-point viscosity values, such as the melt volume rate (MVR) and shear rate and temperature dependent viscosity data, revealed the influence of particle content on flow behavior [46].

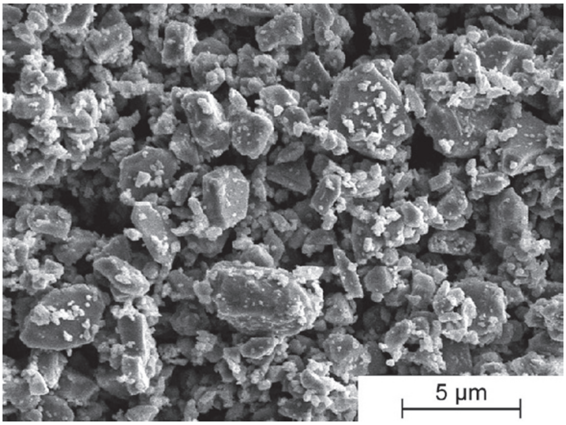

Figure 3.16 SEM of strontium ferrite particles

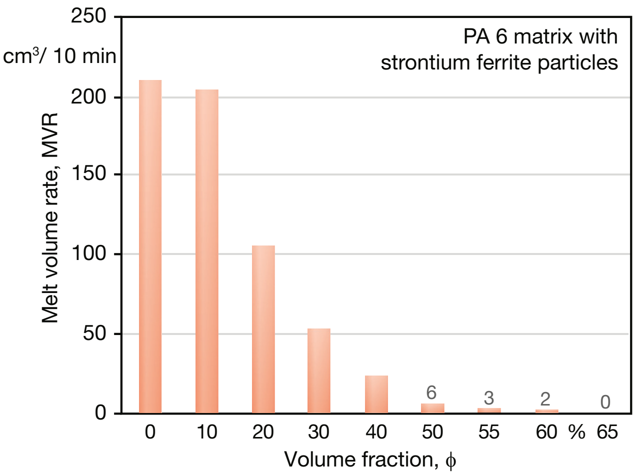

Figure 3.17 Dependence of melt volume rate (MVR) on volume fraction of strontium ferrite in a PA 6 matrix

The influence of different volume fractions of strontium ferrite on the MVR is shown in Fig. 3.17.

Figures 3.18 and 3.19 present the effect of increasing filler volume fraction on the shear rate and temperature dependence, respectively.

The viscosity shifted to higher values with increasing filler content. In the shear rate range from $10^3 - 10^4$ s^{-1} the viscosity shifted from 10^2 to $5 \cdot 10^2$ Pa s for neat PA, and to $5 \cdot 10^3$ to 10^4 Pa s for 60 vol.-% filler. Referring to Fig. 3.17, we can see that because of the higher apparent viscosity during the measurements using higher filler

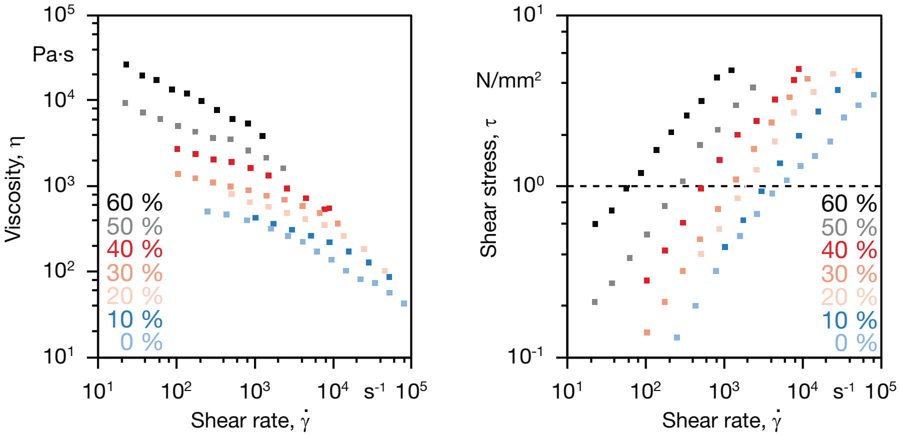

Figure 3.18 Effect of volume fractions of strontium ferrite in PA 6 at 280 °C;
Left: shear rate dependent viscosity; Right: shear rate dependent stress

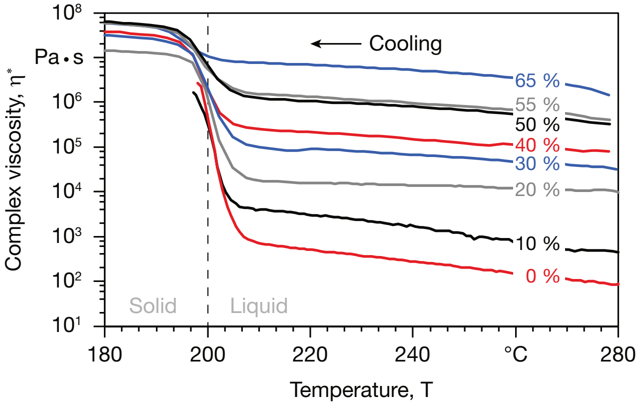

Figure 3.19 Temperature dependence of the complex viscosity of PA 6 filled with strontium ferrite; frequency: 1 Hz, cooling rate: 5 K/min

content, lower shear rates were achieved. A conversion of the shear rate dependent viscosity and the corresponding shear stress shows a linear dependence of the shear stress on the shear rate when plotted on a logarithmic scale. Therefore, only the viscosity level, but not the shear rate dependence is affected by the filler content.

The temperature dependence of the zero shear viscosity is measured in a parallel plate rheometer. The drop once the crystallization temperature is reached decreases with increasing filler content and almost vanishes for 65 vol.-% filler content. Therefore, the influence of filler content is strong in the melt and weaker in the solid material.

Numerous models have been proposed to predict the viscosity of filled liquids [47, 48, 49, 50, 51], and most take the form of a power series of the volume fraction ϕ:

$$\frac{\eta_f}{\eta_0} = 1 + a_1\,\phi + a_2\,\phi^2 + a_3\,\phi^3 + \ldots \tag{3.46}$$

The linear term in Eq. 3.46 represents the reduction of the flow passage caused by the fillers that are dragged by the fluid and are not deformed, as shown in Fig. 3.20.

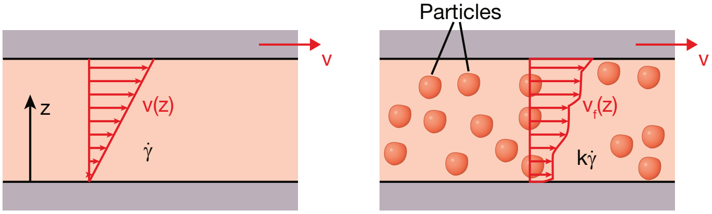

Figure 3.20 Schematic diagram of strain rate increase in a filled system

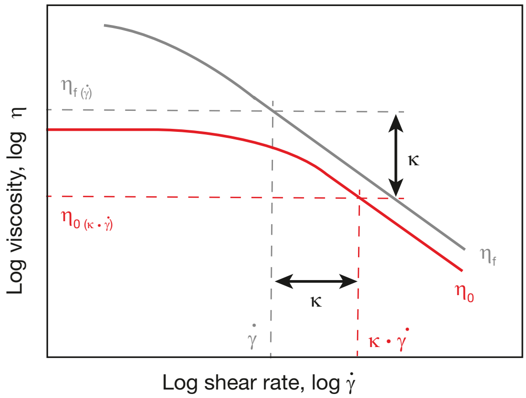

Figure 3.21 Viscosity approximation using the Geisbüsch Model in Eq. 3.49

For instance, Einstein's model for viscosity of a filled liquid only includes the linear term with $a_1 = 2.5$. He derived his equation based on a viscous dissipation balance. The quadratic term in the equation represents the effects related to the interaction between the filler particles. For small volume fractions (< 10 vol.-%), Eq. 3.46 can be simplified to

$$\frac{\eta_\mathrm{f}}{\eta_0} = 1 + \phi^2 \tag{3.47}$$

Geisbüsch suggested a model that included a yield stress, and in which the strain rate of the melt increases by a factor κ as

$$\eta_\mathrm{f}\left(\dot{\gamma}\right) = \frac{\tau_0}{\dot{\gamma}} + \kappa \cdot \eta_0\left(\kappa\dot{\gamma}\right) \tag{3.48}$$

where η_f is the viscosity of the filled polymer, τ_0 is the yield stress, $\dot{\gamma}$ is the shear rate, and η_0 is the viscosity of the neat polymer, see Fig. 3.21. For high deformation stresses, as typically found in polymer processing, the yield stress in the filled polymer melt can be neglected, resulting in the following, simplified expression

$$\eta_\mathrm{f}\left(\dot{\gamma}\right) \approx \kappa \cdot \eta_0\left(\kappa\dot{\gamma}\right) \tag{3.49}$$

Figure 3.22 compares Geisbüsch's experimental data to the results from Eq. 3.46 using the coefficients $a_1 = 2.5$ and $a_2 = 14.1$ as derived by Guth [49]. The data and Guth's model seem to agree well. A comprehensive survey of particulate suspensions was given by Gupta [52], and on short-fiber suspensions by Milliken and Powell [53].

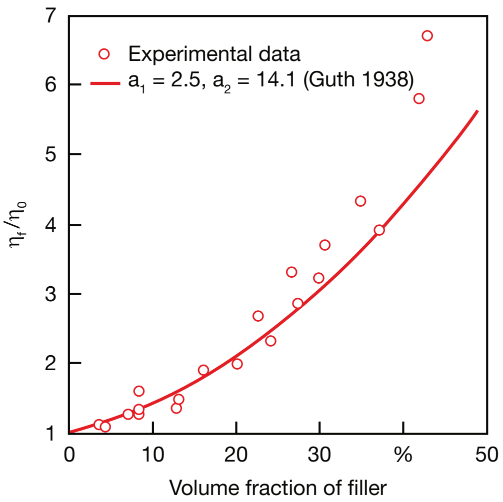

Figure 3.22 Viscosity increase as a function of volume fraction of filler for polystyrene and low density polyethylene containing spherical glass particles with diameters ranging from 36 µm to 99.8 µm

3.5 Chemo-Rheology

Chemo-rheology is used to describe the rheological behavior of cross-linking polymers during chemical reactions such as curing or vulcanization. The changes in flow behavior of cross-linking polymers is captured using rheological measurement during the curing reaction and can be used for material evaluation, process design, and process simulation. The rheological measurements also provide the most direct form of monitoring cure and capturing the gel point. Thermosets or cross-linked polymers are widely used in composites together with fiber reinforcement. They are used to manufacture structural parts in aerospace and automotive applications. Knowledge about the flow behavior of the resin within the heated mold through the fiber bed until the gel point is reached is crucial for the design and production of such parts. Thermoset rubbers such as liquid silicone rubbers (LSR) are used increasingly in the medical, automotive, and consumer markets. Part and process design require knowledge of the curing and related flow.

Figure 3.23 shows the viscosity change during curing at room temperature, the so-called cold curing. This process is used for large parts that cannot be accommodated by curing ovens. As soon as the two components are mixed, the curing process begins. The formation of chemical bonds releases heat which causes an increase in temperature. This, in turn, causes a decrease in viscosity, which eases processing of the resin, allows the exhaustion of air bubbles, and improves wetting of fillers.

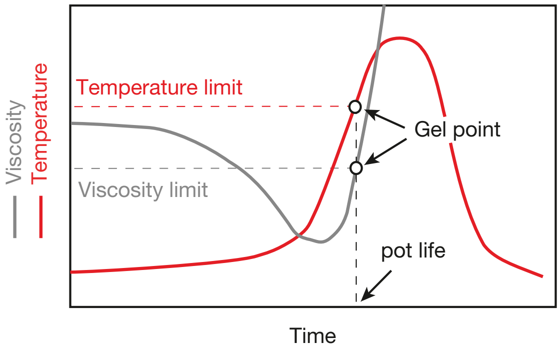

Figure 3.23 Temperature and viscosity change during cold curing [54]

As curing progresses, the viscosity increases due to the increase in molecular weight of the reacting polymers. The effect of curing eventually counteracts the decrease in viscosity caused by temperature rise, leading to a rapid rise in viscosity. As soon as the *gel point* is reached, the resin loses its ability to flow. On the time scale this point is often referred to as the pot life of the resin. The gel point is reached when the molecules are interconnected, or an infinite network is formed. After the gel point is reached, the curing reaction continues as the temperature rises until a fully cured state is reached. The chemical conversion at which the gel point is reached varies according to the molecular structure of the resin.

As an illustration of curing rates as a function of temperature, the isothermal curing history of a vinyl ester is presented in Fig. 3.24. At lower temperatures the curing starts later compared to the higher temperatures and the curing rate is slower (slope). Additionally, a lower final degree of cure is reached. The viscosity shows a comparable behavior, with a lower final viscosity value at lower temperatures, see Fig. 3.25 [55].

Rotational rheometers (see Chapter 6) have proven to be the most useful devices for investigating curing reactions of thermosetting materials, because they can capture the transitions from liquid to solid. Among these, the cone-plate and the parallel-plate systems are the most common ones, simply because they are more easily cleaned. However, some modifications are necessary to accommodate the large variations in viscosity. Just before solidification it is cumbersome to distinguish between permanent viscous deformations and recoverable contributions [56]. Therefore, it is helpful to obtain calorimetric measurements such as differential scanning calorimetry, under the same conditions.

The gel point is commonly determined by isothermal dynamic tests according to ASTM D4473 [57]. The storage (G') and loss modulus (G'') are measured at a fixed low frequency and fixed strain over a period of time. The crossover of G' and G'' is defined as the gel point as the elastic response starts to govern the viscous behavior. This point is equivalent to the point where the loss tangent reaches unity, $\tan\delta = G'/G'' = 1$.

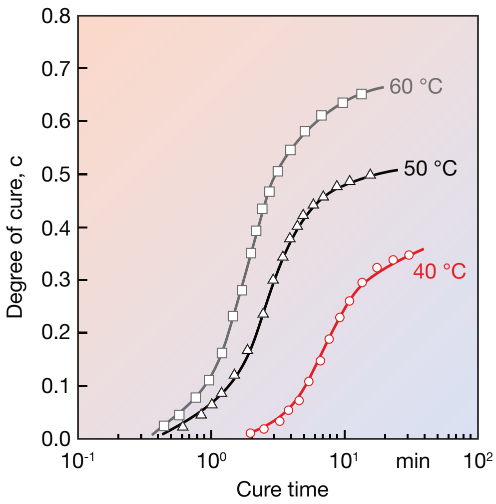

Figure 3.24 Degree of cure as a function of time for a vinyl ester at various isothermal cure temperatures

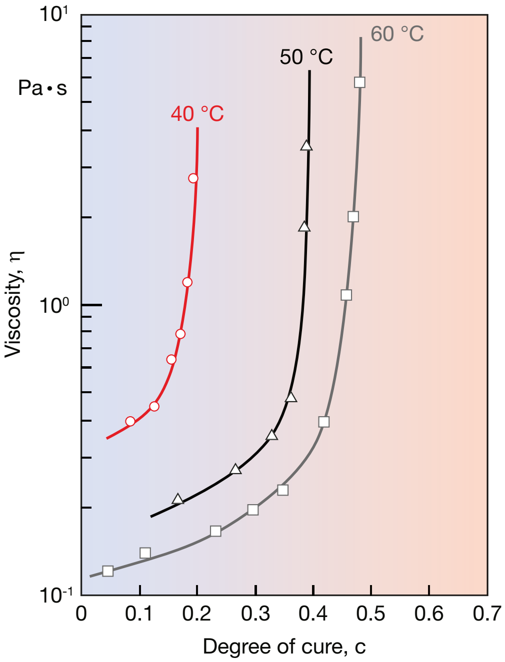

Figure 3.25 Viscosity as a function of degree of cure for a vinyl ester at various isothermal cure temperatures

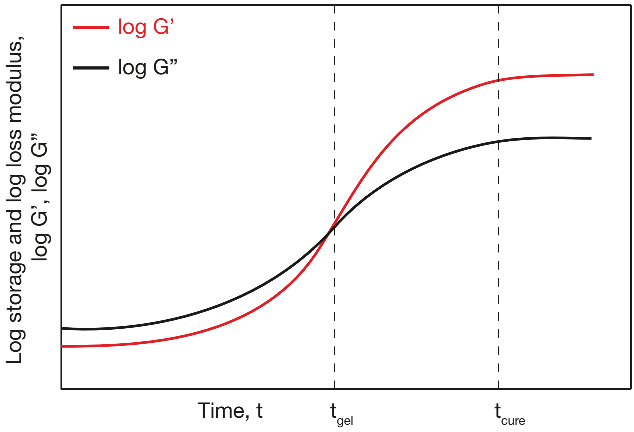

Figure 3.26 Determination of gel point by isothermal dynamic tests during cure [58]

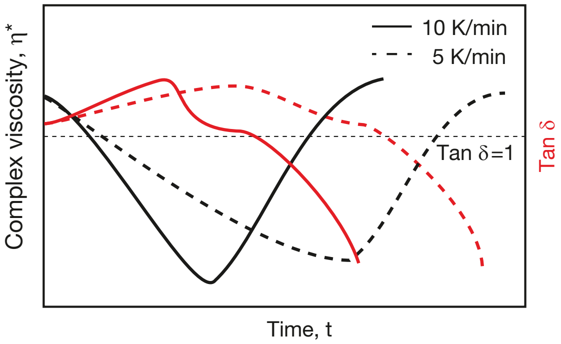

Figure 3.27 Complex viscosity and loss tangent as a function of time for different heating rates [57]

The time to reach the gel point is called the gel time, and the time at which the storage modulus levels out to a constant value is called the cure time, see Fig. 3.26. The influence of heating rate on the loss tangent and therefore the gel point as well as the complex viscosity can be seen in Fig. 3.27. At higher heating rates the gel point is reached faster.

For neat resins, the temperature corresponding to a complex viscosity η^* value of 100 Pa s after the initial heating, flowing, and onset of cure, has been suggested as the dynamic gel temperature [57].

In the first stage of injection or transfer molding processes, the effect of shear rate on viscosity is of interest. Therefore, it is often measured on the uncured resin. The strain rate dependence is dependent on the resin type. While EP and PF show shear thinning behavior, UP and PU exhibit Newtonian, strain rate independent flow behavior [59, 60]. Some measurements, especially those done without initiators, are performed with capillary rheometers. However, as already mentioned, the most common rheometers for curing resins are rotational rheometers.

Investigations regarding the effects of fillers on the viscosity of thermosets are still in their infancy. The viscosity of the unfilled resin, the fiber content, fiber length and orientation, as well as the coupling agents influence the viscosity of the whole system [61].

A complete model for viscosity of a reacting polymer must contain the effects of temperature, T, pressure, p, strain rate, $\dot{\gamma}$, degree of cure, c, and filler properties, F [62]:

$$\eta = \eta(T, p, \dot{\gamma}, c, F) \tag{3.50}$$

There are no generalized models that include all these variables for thermosetting polymers. The different models focus either on one or two effects or on a specific material system [56]. The most common shear rate model for thermosets is the Power Law model, although the Cross model and the Newtonian models have also been used.

The effect of temperature and time are often included in form of models for cure kinetics. Extensive work has been done on the viscosity of polyurethanes [63, 64]. An empirical relation that models the viscosity of these mixing-activated polymers as a function of temperature and degree of cure, the Castro-Macosko-model, is written as

$$\eta = \eta_0 \cdot \exp\left(\frac{E}{RT}\right) \cdot \left(\frac{c_g}{c_g - c}\right)^{c_1 + c_2 c} \tag{3.51}$$

where E is the activation energy of the polymer, R is the ideal gas constant, T is the temperature, c_g is the conversion at the gel point, c the conversion, and c_1 and c_2 are constants that fit the experimental data. The most salient feature of the right term of the equation is that the viscosity increases rapidly as curing proceeds, and becomes unbound as the extent of cure approaches the extent of cure at gelation. The diffusion controlled regime after gelation is not incorporated. The fitting constants c_1 and c_2 are determined by experiments in which the viscosity is measured as a function of extent of cure at constant temperature and decreasing strain rate. Thereby, the first term on the right hand side of the equation represents the temperature dependence of the viscosity using an Arrhenius relation. In order to incorporate the shear thinning behavior of the curing polymer, a model such as the Cross model, Eq. 3.20, could be incorporated; this can be represented as

$$\eta = \frac{\eta_0(T)}{1 + \left[\dfrac{\eta_0(T)\,\dot{\gamma}}{\tau^*}\right]^{1-n}} \cdot \left(\frac{c_g}{c_g - c}\right)^{c_1 + c_2 c} \tag{3.52}$$

where τ^* is the critical shear stress at the transition from the Newtonian plateau η_0 to the Power Law regime, $\eta_0\left(T\right)$ the temperature dependent zero shear viscosity, and n the Power Law index.

Figure 3.28 shows the viscosity as a function of time and temperature for a polyurethane. At lower temperatures, the viscosity is initially higher, but increases more slowly because of the slower reaction rate. In the early stages of the reaction the viscosity is mainly affected by temperature.

Figure 3.29 shows the viscosity as a function of degree of cure. The Castro- Macosko model is a good fit for the described material system. It can be seen that the predicted viscosity approaches a finite value at the gel point.

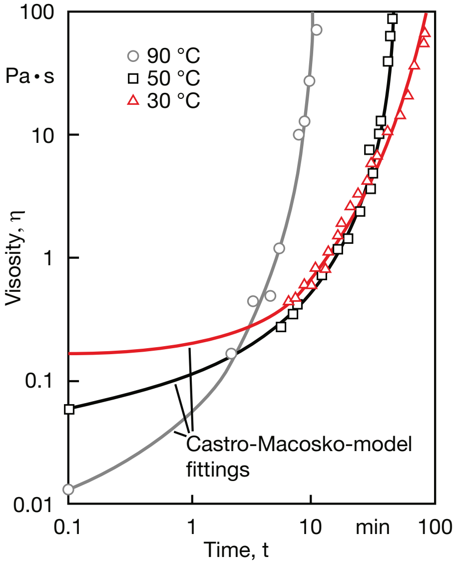

Figure 3.28
Viscosity as a function of time for a polyurethane at various isothermal cure temperatures

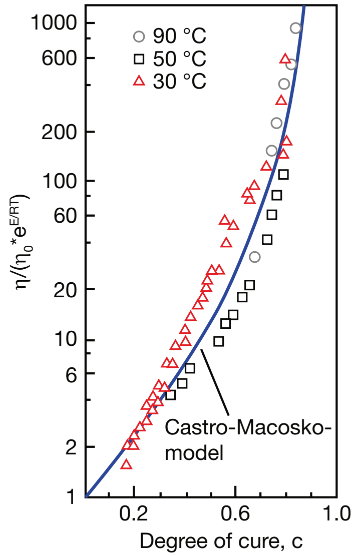

Figure 3.29
Reduced viscosity as a function of degree of cure for a polyurethane at various isothermal cure temperatures

Example 3.3 Castro-Macosko Viscosity Model

In reaction injection molding processes (RIM), polymeric parts are made directly from low viscosity (less than 10 Pa s) reactants, which cure and solidify inside the mold. For polyurethanes, the polymerization is initiated by mixing the two highly reactive components, isocyanate and polyol, inside the mold. Because the monomers are highly reactive during RIM, the mold cavity walls are maintained at low temperatures. To simulate mold filling, the rheological properties have to be known. Experiments provided the following constants [64]:

- η_0: $10.3 \cdot 10^{-8}$ Pa s
- E: 41.3 J/mol
- R (ideal gas constant): 8.3144621 J/mol K
- c_g: 0.65
- c_1: 1.5
- c_2: 1.0

In order to obtain the viscosity at 50 °C as a function of the degree of cure, the following calculation (Eq. 3.51) has to be performed for different conversion rates c, ranging from 0 to $c_g = 0.65$, which is shown here for a conversion of 0.1

$$\eta = 10.3 \cdot 10^{-8}\ \text{Pa s} \cdot \exp\left(\frac{41.3\ \text{J/mol}}{8.314\ \text{J/mol K} \cdot 323\ \text{K}}\right) \cdot \left(\frac{0.65}{0.65 - 0.1}\right)^{1.5+1.0 \cdot 0.1}$$

$$= 2.97 \cdot 10^{-8}\ \text{Pa s}$$

Calculating for all degrees of cure provides the result shown left in Figure 3.30:

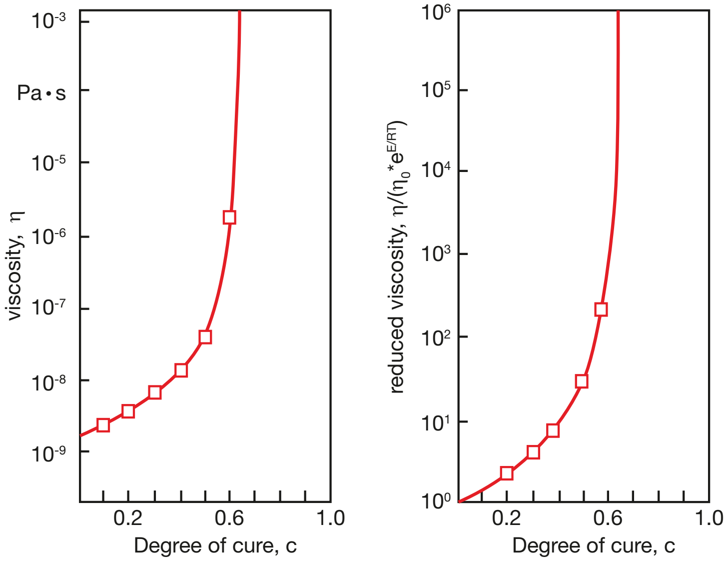

Figure 3.30 Calculated viscosity (right) and reduced viscosity (left) as functions of degree of cure for a polyurethane

Above the gel point, which here occurs at 65% cure, the right term in Eq. 3.51 cannot be solved because the base becomes negative and the exponent is not a natural number. Often, the reduced viscosity is given as a function of the degree of cure, right in Fig. 3.30, which is calculated using

$$\frac{\eta}{\eta_0 \cdot \exp\left(\frac{E}{RT}\right)} = \left(\frac{c_g}{c_g - c}\right)^{c_1 + c_2 c} \tag{3.53}$$

Example 3.4 Castro-Macosko Viscosity Model (Shear rate dependent)

For the production of flip chip packages, the so called moldable underfill (MUF) technique is used to electrically connect the die to the package carrier. The package carrier then provides the connection from the die to the exterior of the package. MUF are normally 1-component epoxies, which have to flow through a very narrow gap of 0.1 mm. In the transfer molding process, flow and heat transfer are dynamically coupled with the curing reaction. The kinetics of the curing reaction not only affect the degree of conversion of the molding compound, but also control the stresses on the overmolded structures during flow, as the viscosity increases due to the progression in degree of cure. Viscosity is influenced primarily by temperature and shear rate. Therefore, the rheological behavior of the used resins is of fundamental importance for the molding process. In order to obtain viscosity values at specific shear rates, temperatures, and conversion, the following data are needed to solve Eq. 3.52 [65]:

- n: $9.683 \cdot 10^{-3}$
- τ^*: 200 Pa
- B: $6.263 \cdot 10^{-44}$ Pa s
- T_b: $4.937 \cdot 10^{4}$ K
- c_g: 0.25
- c_1: 1.818
- c_2: −5.521

The temperature dependence of the viscosity is commonly calculated by

$$\eta_0(T) = B \cdot \exp\left(\frac{T_b}{T}\right) \tag{3.54}$$

$$\eta_0(T) = 6.263 \cdot 10^{-44}\ \text{Pa s} \cdot \exp\left(\frac{49370\ \text{K}}{423\ \text{K}}\right) = 3.05 \cdot 10^{7}\ \text{Pa s}$$

where B and T_b are constants. For example, the zero shear viscosity at 160 °C and a conversion of 0.1 and at a shear rate of 100 s^{-1} can be calculated as

$$\eta = \frac{3.05\cdot 10^{7}\ \text{Pa s}}{1+\left(\dfrac{3.05\cdot 10^{7}\ \text{Pa s}\cdot 100\ \text{s}^{-1}}{200\ \text{Pa}}\right)^{1-n}}\cdot\left(\frac{0.25}{0.25-0.1}\right)^{1.818-5.521\cdot 0.1} = 18.945\ \text{Pa s}$$

Calculating the viscosity for conversions of 0.05, 0.1, and 0.2 and for temperatures of 100, 150 and 200 °C as a function of shear rate gives the following results, Fig. 3.31:

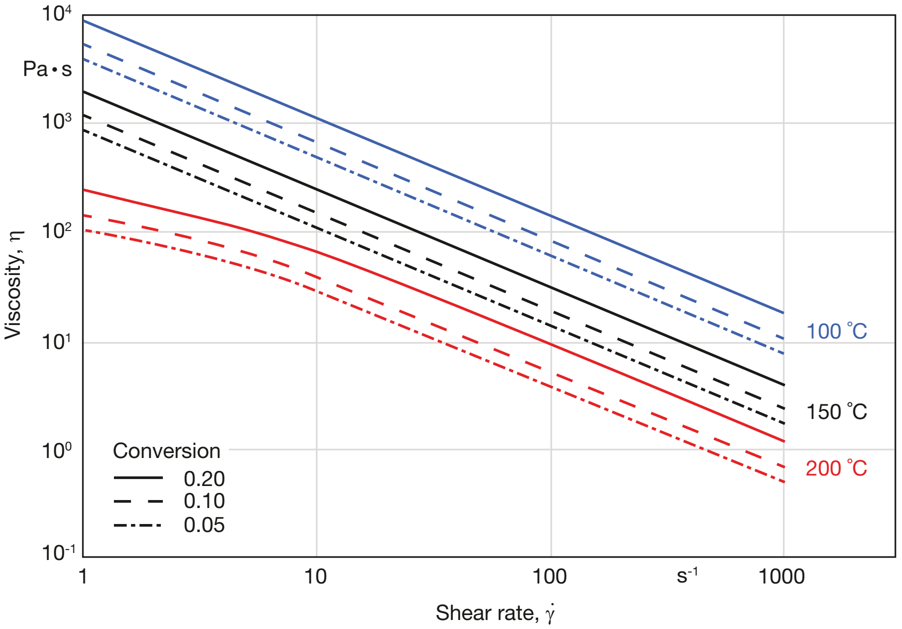

Figure 3.31 Calculated viscosity at different temperatures and degrees of cure as a function of shear rate for an epoxy (MUF)

Problems

3.1 Use the Power Law model and an exponential viscosity dependence to best fit the viscosity measurement data presented in Example 2.2.

3.2 Use the Bird-Carreau model and an Arrhenius temperature dependence to best fit the viscosity measurement data presented in Example 2.2.

3.3 Use the Cross-WLF model to best fit the viscosity measurement data presented in Example 2.2.

3.4 Use the Power Law model with a pressure shift factor $b = 0.003$ (see Table 3.8) to calculate the pressure dependent viscosity of PC for all given temperatures and shear rates at pressures of 100, 200, 500 and 1000 bar. What can be concluded for low shear rates?

3.5 Use the Carreau-WLF model and the parameters for PS in Table 3.5 to plot the viscosity at temperatures of 180, 200 and 220 °C and shear rates from 1 to 1,000 s^{-1}. Extend the temperature dependence with the pressure dependence using $P_1 = 0.02$ K/bar and a glass transition temperature $T_g = 80$ °C. Calculate the viscosity for pressures of 200, 400, 800 and 1200 bar.

3.6 Use Eq. 3.46 and the shear rate dependent viscosity shown in Fig. 3.18 to calculate constants a_1 and a_2. Then, using Eq. 3.48, calculate κ from the right hand side of Fig. 3.18 at a stress of 1 N/mm^2 and plot it as a function of filler volume fraction. Finally, calculate the viscosity as a function of shear rate for various volume fractions of filler and compare the calculated values with the measured values on the left hand side of Fig. 3.18. Which model works best for the shear rate dependence?

3.7 Use the parameters given in Example 3.3 to calculate the viscosity as well as the reduced viscosity as a function of degree of cure for temperatures of 30 and 90 °C and plot them in two separate diagrams. In case of multiple reactions taking place at once, the conversion will occur at a faster rate. For such a case a second order polynomial is necessary to represent the higher degree of conversion. Rewrite the right term of Eq. 3.51 to incorporate the faster degree of conversion. Using the additional constant $c_3 = 2$, recalculate the viscosity for temperatures of 30, 50 and 90 °C. How does the second order polynomial affect the resulting graphs compared to the previously used linear form?

3.8 Use a first order reaction model given by

$$\frac{\mathrm{d}c}{\mathrm{d}t} = a\,\mathrm{e}^{-\frac{E}{RT}}(1-c)$$

to approximate the reaction presented in Fig. 3.24. How would you improve the model?

3.9 Using the Castro-Macosko viscosity model and a first order reaction given by

$$\frac{\mathrm{d}c}{\mathrm{d}t} = a\,\mathrm{e}^{-\frac{E}{RT}}(1-c)$$

fit the viscosity data presented in Fig. 3.25.

References

[1] Arrhenius, S., The viscosity of pure liquids, Meddelanden Från K. Vetenskapsakademiens Nobelinstitut, 3, 1–40, (1916).

[2] Laun, H. M., *Rheol. Acta, 17*, 1, (1978).

[3] Williams, M. L., Landel, R. F., Ferry, J. D., The temperature dependence of relaxation mechanisms in amorphous polymers and other glass-forming liquids, *J. Am. Chem. Soc., 77*, 3701–3707, (1955).

[4] Ferry, J. D., Viscoelastic properties of polymers, 3rd ed., Wiley, NY (1980).

[5] Van Krevelen, D. W., Properties of Polymers, 2nd ed., Elsevier, Amsterdam (1976).

[6] Tadmor, Z., Costas, G. G., Principles of polymer processing, John Wiley & Sons, Inc, Hoboken (2006).

[7] Ostwald, W., *Kolloid-Z.*, 36, 99, (1925).

[8] de Waele, A., *Oil and Color Chem. Assoc. Journal, 6*, 33, (1923).

[9] Carreau, P. J., Ph.D. Thesis, University of Wisconsin-Madison, USA, (1968).

[10] Yasuda, K., Armstrong, R. C., Cohen, R. E., *Rheol. Acta, 20*, 163, (1981).

[11] Menges, G., Wortberg, F., Michaeli, W., *Kunststoffe, 68*, 71, (1978).

[12] Cross, M. M., Rheology of non-newtonian fluids: a new flow equation for pseudoplastic systems, *Journal of Colloid Science, 20*, 417–437, (1965).

[13] Isayev, A. I., Injection molding and compression molding fundamentals, Marcel Decker, New York (1987).

[14] Hieber, C. A., Chiang, H. H., Shear-rate-dependence modeling of polymer melt viscosity, *Polymer Engineering & Science, 32*, 931, (1992).

[15] Fetecau, C., Dobrea, D. V., Postolche, I., Overmolding injection molding simulation of tensile test specimen, *International Journal of Modern Manufacturing Technologies, 2*, p. 45–51, (2010).

[16] Garcia, J. L., Koelling, K. W., Summers, J. W., Computational prediction of PVC degradation during injection molding in rectangular channel, *Polymer Engineering & Science, 44*, 1295–1312, (2004).

[17] Barus, C., Isothermals, isopiestics and isometrics relative to viscosity. *Am. J. Sci., 45*, 87–96 (1883).

[18] Cogswell, F. N., Polymer Melt Rheology, John Wiley & Sons, New York (1981).

[19] Menges, G., Thienel, P., Wübken, G., *Kunststoffe, 60*, 42–48, (1976).

[20] Hellwege, K. H., Knappe, W., Lehmann, P., *Kolloid-Z. u. Z. Polymere, 183*, 110–119, (1962).

[21] Sedlacek, T., Zatloukal, M., Filip, P., Boldizar, A., Saha, P., *Polym. Eng. Sci., 44*, 1328, (2004).

[22] Son, Y., *J. Polym. Res., 16*, 667–671, (2009).

[23] Couch, M. A., Binding, D. M., *Polymer, 41*, 6323, (2000).

[24] Kadijk, S. E., van den Brule, B. H. A. A., On the pressure dependence of the viscosity of molten polymers, *Polym. Eng. & Sci., 34*, p. 1535–1547, (1994).

[25] Sedlacek, T., Zatloukal, M. , Lengalova, A. , Filip, P. , Saha, P., SPE ANTEC, 3748–3752, Nashville, Tennessee (2003).

[26] Amano, O., Pressure Dependent Viscosity of Polymer Melts, Proceedings of ANTEC 2000, Orlando, FL (2000).

[27] Mahishi, M., Proceedings of ANTEC 1986, Boston, MA, 547–551, (1986).

[28] Ferry, J. D., Viscoelastic properties of Polymers, Wiley, New York (1961).

[29] Bischoff, J., Catsiff, E., Tobolsky, A. V., *J. Am. Chem. Soc., 74*, 3378, (1952).

[30] Bischoff, J., Catsiff, E., Tobolsky, A. V., *J. App. Phys., 25*, 1092, (1954).

[31] Ito, K., *J. Appl. Phys., 32*, 1743, (1961).

[32] Schott, H., Kaghan, W. S., *J. Appl. Polymer Sci., 5*, 175, (1961).

[33] Vinogradov, G. V., Malkin, A. Y., *J. Polymer Sci., Part A, 2*, 2357–2372, (1964).

[34] Vinogradov, G. H., Malkin, A. Y., *J. Polymer Sci., Part A-2, 4*, 135–154, (1966).

[35] Menges, G., Wortberg, J., Michaeli, W., *Kunststoffe, 68*, 47–50, (1978).

[36] ASTM, 8.01, Plastics (I), ASTM, Philadelphia, (1994).

[37] Schümmer, P., Worthoff, R. H., *Chem. Eng. Sci., 38*, 759, (1978).

[38] Trouton, F. T., *Proc. Roy. Soc., A77*, (1906).

[39] Münstedt, H., *Rheologica Acta, 14,* 1077, (1975).

[40] Powell, P. C., Housz, A. J. I., Engineering with Polymers, CRC Press (1998).

[41] Gleißle, W., Hochgefüllte Kunststoffe, special publ. Springer-VDI Verlag, Düsseldorf, 108, (2002).

[42] Laun, H. M., Rheological properties of aqueous polymer dispersions, *Die Angewandte Makromolekulare Chemie, 123*, 335, (1984).

[43] Freundlich, H., The colloidal state: I Thixotropy, Hermann, Paris (1935).

[44] Starov, V., Zhdanov, V., Meireles, M., Molle, C., Viscosity of concentrated suspensions: influence of cluster formation, *Advances in Colloid and Interface Science, 96*, 279, (2002).

[45] Stokes, J. R., Telford, J. H., Measuring the yield behavior of structured fluids, In: *J. Non-Newtonian Fluid Mech., 124*, 137, (2004).

[46] Drummer, D., Ph.D. Thesis, LKT, University of Erlangen-Nuremberg, Germany (2004).

[47] Einstein, A., *Ann. Physik, 19*, 549, (1906).

[48] Guth, E., Simha, R., *Kolloid-Zeitschrift, 74*, 266, (1936).

[49] Guth, E., *Proceedings of the American Physical Society*, (1937); *Physical Review, 53*, 321, (1938).

[50] Batchelor, G. K., *Annu. Rev. Fluid Mech., 6*, 227, (1974).

[51] Geisbüsch, P., Ph.D. Thesis, IKV, RWTH-Aachen, Germany, (1980).

[52] Gupta, R. K., Flow and Rheology in Polymer Composites Manufacturing, Ed. S. G. Advani, Elsevier, Amsterdam, (1994).

[53] Milliken, W. J., Powell, R. L., Flow and Rheology in Polymer Composites Manufacturing, Ed. S. G. Advani, Elsevier, Amsterdam, (1994).

[54] Ehrenstein, G. W., Polymeric Materials, Hanser Publisher, Cincinatti (2004).

[55] Han, C. D., Lem, K. W., *J. Appl. Polym. Sci., 29*, 1879, (1984).

[56] Halley, P. J., Mackay, M. E., Chemorheology of Thermosets – An Overview, *Polym. Eng. Sci., 36*, 593, (1996).

[57] ASTM D4473, Plastics (I), Dynamic Mechanical Properties: Cure Behavior, ASTM, Philadelphia, (2008).

[58] Mezger, T., Das Rheologie Handbuch, Vincentz, Hannover (2000).

[59] Sundstrom, D. W., Burkett, S. J., *Polym. Eng. Sci., 21*, 1108, (1981).

[60] Hartley, M. D., Williams, H. L., *Polym. Eng. Sci., 21*, 135, (1981).

[61] Han, C. D., Multiphase Flow in Polymer Processing, Academic Press, New York (1981).

[62] Ryan, M. E., *Polym. Eng. Sci., 24*, 358, (1984).

[63] Castro, J. M., Macosko, C. W., *AIChe J., 28*, 250, (1982).

[64] Castro, J. M., Perry, S. J., Macosko, C. W., *Polymer Comm., 25*, 82, (1984).

[65] Tamil, J., Ore, S. H., Gan, K. Y., Bo, Y. Y., Ng, G., Wah, P. T., Suthiwongsunthorn, N., Chungpaiboonpatana, S., *Journal Micro. and Elect. Pack., 9*, 19, (2012).

4

Transport Phenomena

The field of transport phenomena provides the basis for modeling in plastics rheology and processing. Modeling of a system, whether it is a rheometer or an actual process, often begins with a dimensional analysis of the system, which provides insight into the meaningful parameters that govern the system or process. The resulting dimensionless groups or numbers, in conjunction with experiments and models, can help the engineer determine significant conditions or effects, such as inertia, viscous heating, and if dealing with a process, scale a pilot or model of the process to industrial dimensions. While the dimensionless numbers give insight into a system, modeling of the system requires that mass, force, and energy flux within the system are balanced, using the appropriate material models or constitutive equations. This chapter presents the most important dimensionless groups relevant in plastics rheology and processing. This is followed by the derivation of the balance equations, in combination with simple constitutive and rheological models that allow the modeling of rheometric flows and polymer processes. The chapter also presents ways to simplify the complex equations in order to model basic systems, such as flow in a tube (Hagen-Poiseuille flow), pressure flow between parallel plates, flow between two rotating concentric cylinders (Couette flow), and many more. These simple systems, or their combinations, can be used to model and analyze rheometers, and of course, processes in order to optimize them.

4.1 Dimensionless Groups

Dimensional analysis and dimensionless groups or numbers are used by engineers to gain insight into a problem by presenting theoretical and experimental results in a compact manner. This is done by reducing the number of variables in a system, by lumping them into meaningful dimensionless numbers. For example, if a flow system is dominated by the fluid's inertia as well as by the viscous effects, it may be best to present the pressure requirements in terms of the Reynolds number, which is the ratio of both effects. When checking the order of these dimensionless numbers and comparing them to one another, it is possible to distinguish the most important parameters, such as process conditions and material properties. Many researchers also use dimensional analysis in theoretical studies, which in combination with experiments often reveal fundamental relations governing a process.

The classic techniques to determine dimensionless numbers are the so-called Buckingham Pi-Theorem and Pawlowski's matrix transformation technique [1]. For detailed information about these widely used methods in polymer rheology and processing the reader is encouraged to consult the literature [2–7]. Table 4.1 lists some dimensionless numbers, useful in plastics rheology and processing.

Example 4.1 Flow in a tube

Consider the classical problem of pressure drop during flow in a smooth straight pipe, ignoring the inlet effects. In such a system, the relevant parameters are pressure drop Δp, tube diameter D, tube length L, viscosity of the fluid η, density of the fluid ρ, and average fluid velocity u. Such a system is governed by three dimensionless numbers:

$$\begin{aligned} &Eu = \frac{\Delta p}{u^2 \rho} \quad \text{(Euler number)} \\ &\text{Tube aspect ratio} = \frac{L}{D} \\ &Re = \frac{D u \rho}{\eta} \quad \text{(Reynolds number)} \end{aligned} \tag{4.1}$$

which can be put in relationship by the following function

$$f\left(Eu, Re, \frac{L}{D}\right) = 0 \tag{4.2}$$

Table 4.1 Dimensionless Groups in Plastics Rheology and Polymer Processing

Name	Symbol	Definition	Meaning
Biot	Bi	$\frac{hL}{k}$	$\frac{\text{Convection from surface}}{\text{Conduction through body}}$
Brinkman	Br	$\frac{\eta u^2}{k\,\Delta T}$	$\frac{\text{Viscous heating}}{\text{Conduction}}$
Capillary	Ca	$\frac{\tau R}{\sigma_s}$	$\frac{\text{Deviatoric stresses}}{\text{Surface tension stresses}}$
Damköhler	Da	$\frac{c\,\Delta H_r}{\rho C_p T_0}$	$\frac{\text{Reaction energy}}{\text{Internal energy}}$
Deborah	De	$\frac{\lambda}{t}$ or $\lambda\omega$	$\frac{\text{Relaxation time}}{\text{Process time}}$
Fourier	Fo	$\frac{\alpha t}{L^2}$	$\frac{\text{Process time}}{\text{Thermal diffusion time}}$
Giacomin	G_n	$(De + i\,We)$	Measure of non-Newtonianness
Graetz	Gz	$\frac{uL}{\alpha}\left(\frac{d}{L}\right)$	$\frac{\text{Lengthwise convection}}{\text{Transverse conduction}}$
Manas-Zloczower	M_z	$\frac{\dot{\gamma}}{\dot{\gamma}+\omega}$	$M_z = 0.0 -$ No deformation $M_z = 0.5 -$ Shear flow $M_z = 1.0 -$ Elongational flow
Nahme-Griffith	Na	$a\,\Delta T\,Br$	Effect of viscous heating on flow
Nusselt	Nu	$\frac{hL}{k_{\text{fluid}}}$	$\frac{\text{Convective heat transfer}}{\text{Conductive heat transfer}}$
Péclet	Pe	$\frac{UL}{\alpha}$	$\frac{\text{Rate of advective heat transfer}}{\text{Rate of diffusion heat transfer}}$
Prandtl	Pr	$\frac{\nu}{\alpha}$	$\frac{\text{Momentum diffusivity}}{\text{Thermal diffusivity}}$
Reynolds	Re	$\frac{\rho u L}{\eta}$	$\frac{\text{Inertia forces}}{\text{Viscous forces}}$
Schmidt	Sc	$\frac{\nu}{D}$	$\frac{\text{Mechanical mixing}}{\text{Diffusion mixing}}$
Weissenberg	We	$\lambda\dot{\gamma}$ or $\frac{N_1}{\tau}$ or $\lambda\gamma_0\omega$	$\frac{\text{Elastic stresses}}{\text{Viscous stresses}}$

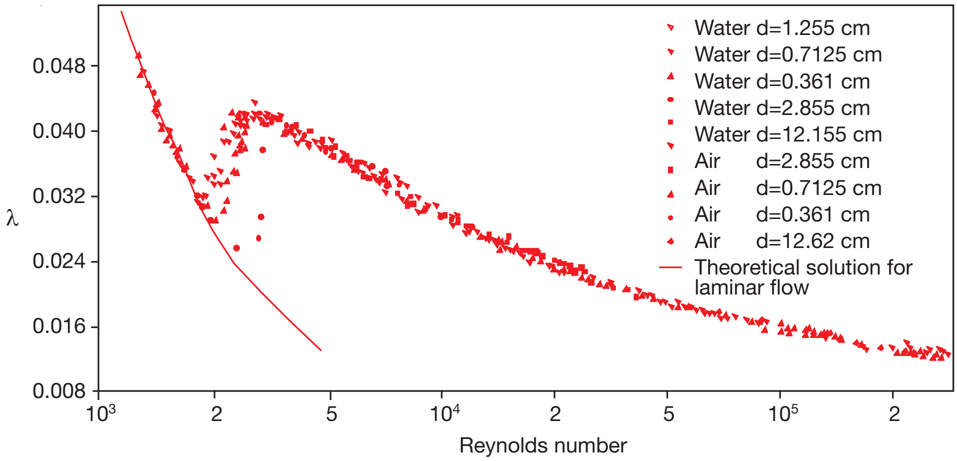

Figure 4.1 Pressure drop characteristic of a straight smooth tube

Although this does not explain the nature of the relation, the form of the function *f* can be generated experimentally. Figure 4.1 presents results from such experiments performed by Stanton and Pannell [8], where they plotted $\lambda = 2\,Eu\,D/L$ as a function of *Re*. This figure clearly demonstrates the usefulness of dimensionless numbers. In the figure, note the line that denotes laminar flow, which is represented by pressure flow in a tube, derived in this chapter.

Example 4.2 Significance of viscous dissipation in a sliding plate rheometer

A sliding plate rheometer is used to perform large oscillatory shear experiments at 230 °C with a 1 mm thick low density polyethylene sample with a strain defined by

$$\gamma_{xy}(t) = \gamma_0 \sin \omega t \tag{4.3}$$

where the maximum strain γ_0 = 1.00 and the frequency ω = 2 π rad/s. The quickest way to assess the significance of viscous dissipation is to compute the Brinkman number

$$Br = \frac{\eta u^2}{k\,\Delta T} \tag{4.4}$$

The given frequency of 1 Hz means that a whole oscillation cycle is completed in 1 second. Hence, since we know that a 1 mm thick sample must travel 1 mm in the positive and negative direction to achieve a maximum strain of 1.00, a characteristic velocity *u* and rate of deformation can be computed as

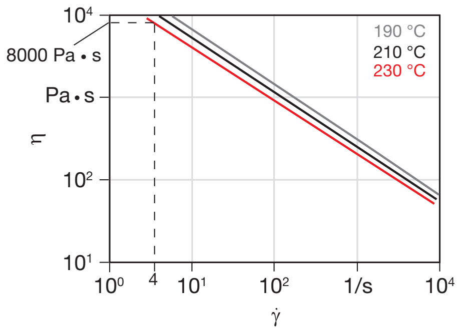

Figure 4.2 Viscosity curve for a PE-LD

$$u = \frac{0.002\ \mathrm{m}}{0.5\ \mathrm{s}} = 0.004\ \mathrm{m/s} \quad \text{and} \quad \dot{\gamma} = \frac{0.004\ \mathrm{m/s}}{0.001\ \mathrm{m}} = 4\ \mathrm{s}^{-1} \tag{4.5}$$

Using the viscosity curve for a PE-LD given in Fig. 4.2, the viscosity at the given temperature and rate of deformation can be estimated to be 8000 Pa s. If we assume that a 1 K temperature rise affects the viscosity measurements, we can use $\Delta T = 1$ K and with thermal conductivity for PE-LD of 0.33 W/m K [9], we can compute the Brinkman number as

$$Br = \frac{8000\ \mathrm{Pa\ s} \cdot (0.004\ \mathrm{m/s})^2}{\left(0.33\ \frac{\mathrm{W}}{\mathrm{m\,K}}\right)(1\ \mathrm{K})} = 0.39 \tag{4.6}$$

This means that here viscous dissipation does not play a significant role because the heat generated at these low speeds is conducted out faster than it is generated by a factor of almost 3. While the Brinkman number only provides a general estimate of the effects of viscous heating, the actual temperature in this widely accepted rheometer has not been measured to this date. Recently, Giacomin et al. [10] presented an analytical model that predicts viscous heating in large amplitude oscillatory shear tests using a viscoelastic corotational Maxwell model. They showed various boundary conditions, representing different scenarios, and determined for insulated walls (adiabatic case) that the temperature rise is not limited. For such a case, the effect of viscous heating is significant and will affect the measurements as time progresses.

4.2 Balance Equations

When solving flow and heat transfer problems in polymer processing, we must satisfy conservation of mass, forces or momentum, and energy. Momentum and energy balances, in combination with material properties through constitutive relations, sometimes result in governing equations that are highly non-linear. This chapter presents the balance equations, utilizing the constitutive relations presented in Chapter 3 of this book.

4.2.1 The Mass Balance or Continuity Equation

The most basic aspect of modeling polymer processing is to satisfy the conservation of mass. When modeling the flow of polymers we can assume incompressibility[1], making a volume balance equivalent to a mass balance. The resulting equation is referred to as the continuity equation. In order to derive the continuity equation, we place an imaginary wire frame of dimensions $\Delta x \times \Delta y \times \Delta z$ inside a flowing system, as schematically depicted in Fig. 4.3.

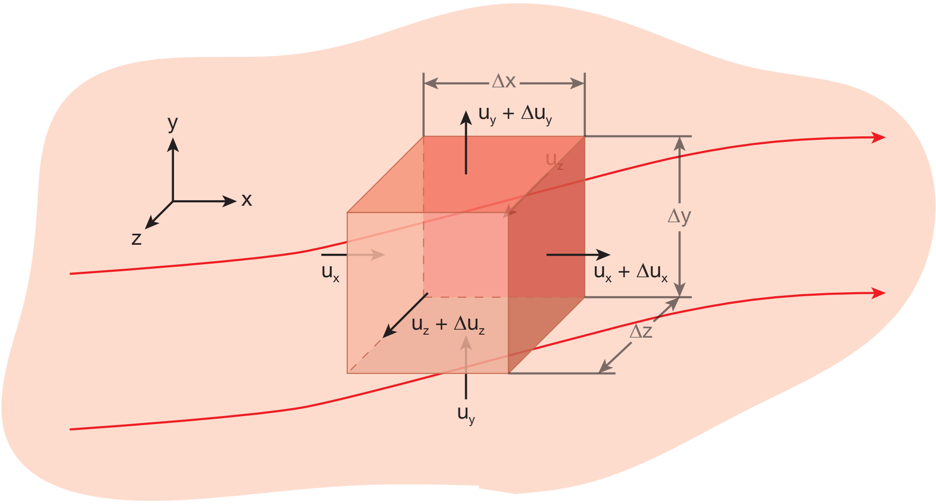

Figure 4.3 Differential frame immersed in a flow and fixed in space

---

[1] From the *pvT* behavior of a polymer melt we know that, in principle, a polymer is not an incompressible fluid. However, the changes of volume with respect to pressure variations within a process are not significant enough to affect the flow field.

Using the notation introduced in Fig. 4.3 we can perform a volumetric balance, in and out of the differential element, in a volume-specific form by dividing the balance by the element's volume $\Delta x \times \Delta y \times \Delta z$,

$$\frac{\Delta u_z}{\Delta z} + \frac{\Delta u_y}{\Delta y} + \frac{\Delta u_x}{\Delta x} = 0 \tag{4.7}$$

Letting the size of the differential element go to zero results in

$$\frac{\partial u_z}{\partial z} + \frac{\partial u_y}{\partial y} + \frac{\partial u_x}{\partial x} = \frac{\partial u_i}{\partial x_i} = 0 \tag{4.8}$$

which states that the divergence of the velocity vector must equal zero when the mass or the volume is conserved. We can also write this equation as

$$\nabla \cdot u = 0 \tag{4.9}$$

When the flow is compressible, variable density has to be taken into account and the continuity equation must be written as

$$\nabla \cdot (\rho u) = 0 \tag{4.10}$$

Table 4.2 presents the continuity equation in Cartesian and cylindrical coordinate systems. Note that in most cases the density ρ is constant and can be dropped from the equation.

Table 4.2 Continuity Equation

Cartesian Coordinates (x, y, z):
$\frac{\partial}{\partial x}(\rho u_x) + \frac{\partial}{\partial y}(\rho u_y) + \frac{\partial}{\partial z}(\rho u_z) = 0$
Cylindrical Coordinates (r, θ, z):
$\frac{1}{r}\frac{\partial}{\partial r}(\rho r u_r) + \frac{1}{r}\frac{\partial}{\partial \theta}(\rho u_\theta) + \frac{\partial}{\partial z}(\rho u_z) = 0$

4.2.2 The Material or Substantial Derivative

It is possible to describe a flowing system from a fixed or moving observation point. A fixed observer, such as described in Fig. 4.4, feels the transient effects; changes in the variables during the time before the system reached steady state.

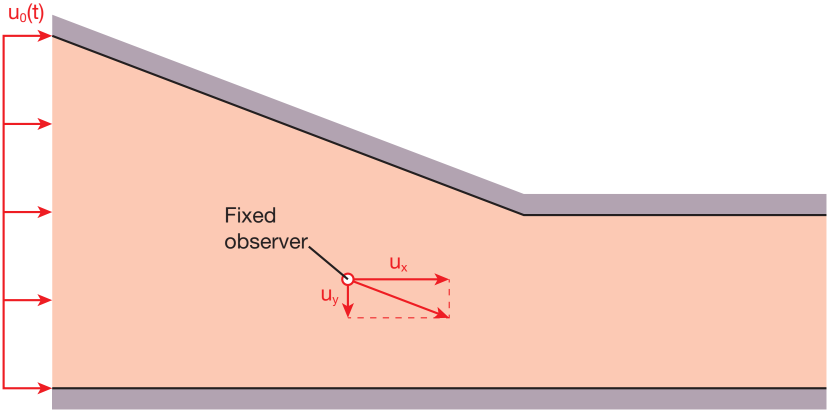

Figure 4.4 Flow system with a fixed observer

In a non-isothermal flow, a fixed observer feels

$$\frac{\partial u_z}{\partial t}, \frac{\partial u_y}{\partial t}, \frac{\partial u_x}{\partial t}, \frac{\partial T}{\partial t}, \quad \text{etc.} \tag{4.11}$$

Once the system reaches steady state, the fixed observer feels a constant velocity, temperature, and other field variables.

On the other hand, a moving observer, such as the one shown in Fig. 4.5, not only feels the transient effects, but also the changes that the variables undergo as the material element travels through a gradient of velocity, temperature, concentration, etc.

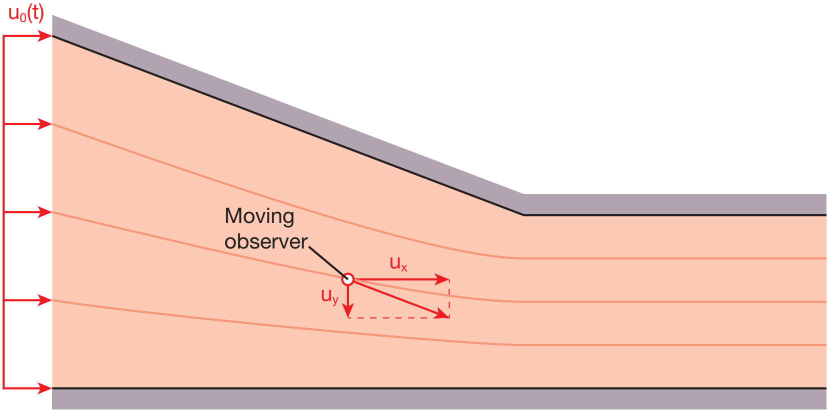

Figure 4.5 Flow system with an observer moving with a fluid particle on a given streamline

The moving observer, described by a fluid particle, feels

$$\frac{\partial u_x}{\partial t} + u_x \frac{\partial u_x}{\partial x} + u_y \frac{\partial u_x}{\partial y} + u_z \frac{\partial u_x}{\partial z} = \frac{\partial u_i}{\partial t} + u_j \frac{\partial u_i}{\partial x_j} \tag{4.12}$$

as the change of u_x. Equation 4.12 is often written in short form as $\mathrm{D}u_x/\mathrm{D}t$ and is referred to as the *material derivative* or the *substantial derivative*.

4.2.3 The Momentum Balance or Equation of Motion

For a momentum balance, we take the same flow system as presented in Fig. 4.3 but instead of submerging an imaginary frame into the melt, we take an actual fluid element of dimensions $\Delta x \times \Delta y \times \Delta z$ (Fig. 4.6) and perform a force balance with the forces acting on its surfaces.

The force balance can be written as

$$\sum f = m\boldsymbol{a} \tag{4.13}$$

where the terms in the equation define force, f, mass, m, and acceleration, $\boldsymbol{a}$, respectively. For simplicity, here we will only show the balance of forces in the x-direction. The balance in the y- and z-directions are left to the reader as a short exercise. The forces acting in the x-direction on a small fluid element are described in Fig. 4.6.

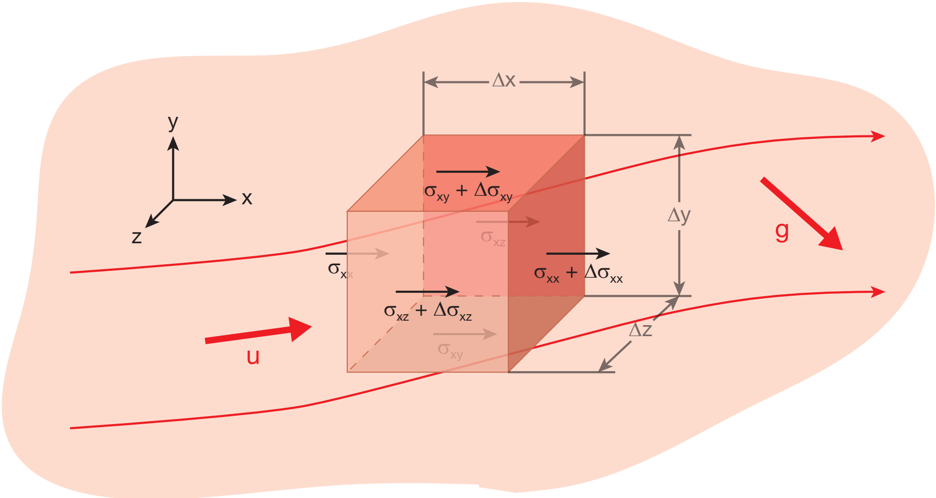

Figure 4.6 Differential fluid element traveling along its streamline x-direction and forces that act on its surfaces

Because the element in Fig. 4.6 is a fluid particle that moves with the flow, the change of its velocity components is described by the material derivative. Hence, the force balance in the x-direction is given by

$$\sum f = m\frac{\mathrm{D}u_x}{\mathrm{D}t} \tag{4.14}$$

where $m = \rho\, \Delta x \times \Delta y \times \Delta z$.

After adding the forces, dividing by the element's volume, and letting the volume go to zero, the force balance in the x-direction results in

$$\rho\frac{\mathrm{D}u_x}{\mathrm{D}t} = \frac{\partial \sigma_{xx}}{\partial x} + \frac{\partial \sigma_{yx}}{\partial y} + \frac{\partial \sigma_{zx}}{\partial z} + \rho g_x \tag{4.15}$$

which for all three directions can be written as

$$\begin{aligned} \rho\frac{\mathrm{D}u_i}{\mathrm{D}t} &= \frac{\partial \sigma_{ij}}{\partial x_j} + \rho g_i \\ \rho\frac{\mathrm{D}\boldsymbol{u}}{\mathrm{D}t} &= \nabla \cdot \boldsymbol{\sigma} + \rho \boldsymbol{g} \end{aligned} \tag{4.16}$$

In fluid flow, however, it is necessary to split the total stress, σ_{ij}, into a deviatoric stress, τ_{ij}, and a hydrostatic stress, σ_{H}. The deviatoric stress causes deformation (Fig. 4.7) and the hydrostatic stress is described by pressure (Fig. 4.8).

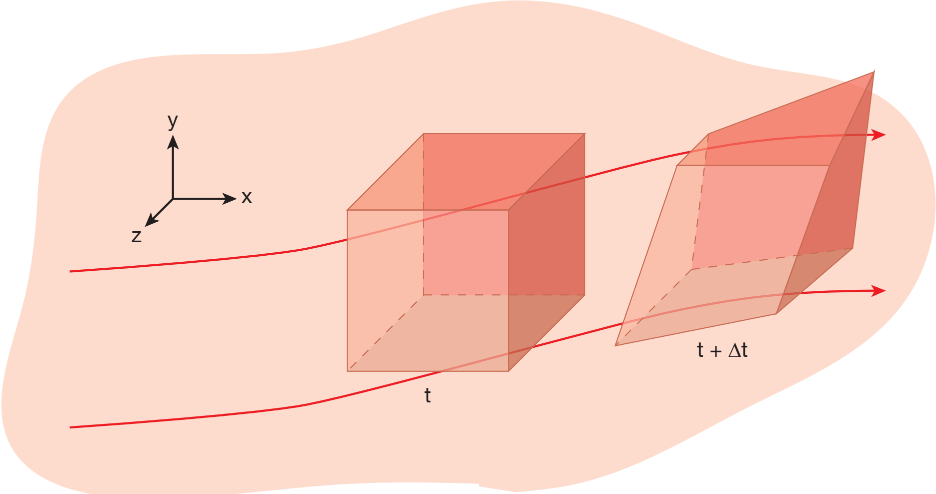

Figure 4.7 Effect of deviatoric stresses as the fluid element travels along its streamline

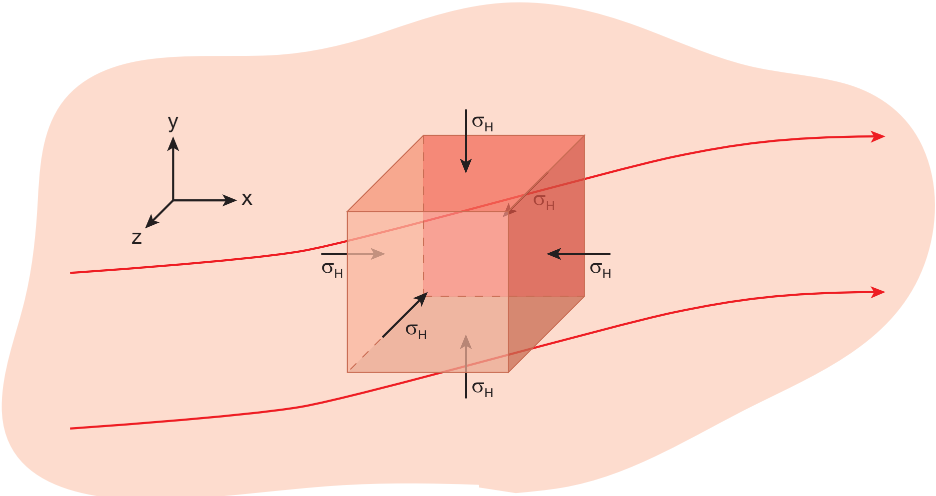

Figure 4.8 Hydrostatic stresses acting on a differential element

We can write

$$\sigma_{ij} = \sigma_{\mathrm{H}} \delta_{ij} + \tau_{ij} \tag{4.17}$$

where δ_{ij} is the Kronecker delta. As the above equation reveals, the hydrostatic stress can only act in the normal direction of a surface and it is equal in all three directions. Hence, we can write

$$\sigma_{\mathrm{H}} = -p \tag{4.18}$$

where p defines the pressure. The negative pressure reflects the fact that a positive pressure causes a compressive stress. The total stress can be written as

$$\sigma_{ij} = -p\,\delta_{ij} + \tau_{ij} \tag{4.19}$$

Using the definition of total stress given above, the momentum balance can now be written as

$$\begin{gathered}\rho \frac{\mathrm{D}u_i}{\mathrm{D}t} = -\frac{\partial p}{\partial x_i} + \frac{\partial \tau_{ij}}{\partial x_j} + \rho\, g_i \\ \rho \frac{\mathrm{D}\boldsymbol{u}}{\mathrm{D}t} = -\nabla p + \nabla \cdot \boldsymbol{\tau} + \rho\, \boldsymbol{g}\end{gathered} \tag{4.20}$$

Table 4.3 presents the momentum balance in terms of deviatoric stress in Cartesian and cylindrical coordinate systems.

Table 4.3 Momentum Equations in Terms of $\boldsymbol{\tau}$

Cartesian Coordinates (x, y, z):
$\rho\left(\frac{\partial u_x}{\partial t}+u_x\frac{\partial u_x}{\partial x}+u_y\frac{\partial u_x}{\partial y}+u_z\frac{\partial u_x}{\partial z}\right)=-\frac{\partial p}{\partial x}+\left(\frac{\partial \tau_{xx}}{\partial x}+\frac{\partial \tau_{yx}}{\partial y}+\frac{\partial \tau_{zx}}{\partial z}\right)+\rho g_x$
$\rho\left(\frac{\partial u_y}{\partial t}+u_x\frac{\partial u_y}{\partial x}+u_y\frac{\partial u_y}{\partial y}+u_z\frac{\partial u_y}{\partial z}\right)=-\frac{\partial p}{\partial y}+\left(\frac{\partial \tau_{xy}}{\partial x}+\frac{\partial \tau_{yy}}{\partial y}+\frac{\partial \tau_{zy}}{\partial z}\right)+\rho g_y$
$\rho\left(\frac{\partial u_z}{\partial t}+u_x\frac{\partial u_z}{\partial x}+u_y\frac{\partial u_z}{\partial y}+u_z\frac{\partial u_z}{\partial z}\right)=-\frac{\partial p}{\partial z}+\left(\frac{\partial \tau_{xz}}{\partial x}+\frac{\partial \tau_{yz}}{\partial y}+\frac{\partial \tau_{zz}}{\partial z}\right)+\rho g_z$
Cylindrical Coordinates (r, θ, z):
$\rho\left(\frac{\partial u_r}{\partial t}+u_r\frac{\partial u_r}{\partial r}+\frac{u_\theta}{r}\frac{\partial u_r}{\partial \theta}-\frac{u_\theta^2}{r}+u_z\frac{\partial u_r}{\partial z}\right)=-\frac{\partial p}{\partial r}+\left(\frac{1}{r}\frac{\partial}{\partial r}(r\tau_{rr})+\frac{1}{r}\frac{\partial \tau_{r\theta}}{\partial \theta}-\frac{\tau_{\theta\theta}}{r}+\frac{\partial \tau_{rz}}{\partial z}\right)+\rho g_r$
$\rho\left(\frac{\partial u_\theta}{\partial t}+u_r\frac{\partial u_\theta}{\partial r}+\frac{u_\theta}{r}\frac{\partial u_\theta}{\partial \theta}+\frac{u_r u_\theta}{r}+u_z\frac{\partial u_\theta}{\partial z}\right)=-\frac{1}{r}\frac{\partial p}{\partial \theta}+\left(\frac{1}{r^2}\frac{\partial}{\partial r}\left(r^2\tau_{r\theta}\right)+\frac{1}{r}\frac{\partial \tau_{\theta\theta}}{\partial \theta}+\frac{\partial \tau_{\theta z}}{\partial z}\right)+\rho g_\theta$
$\rho\left(\frac{\partial u_z}{\partial t}+u_r\frac{\partial u_z}{\partial r}+\frac{u_\theta}{r}\frac{\partial u_z}{\partial \theta}+u_z\frac{\partial u_z}{\partial z}\right)=-\frac{\partial p}{\partial z}+\left(\frac{1}{r}\frac{\partial}{\partial r}(r\tau_{rz})+\frac{1}{r}\frac{\partial \tau_{\theta z}}{\partial \theta}+\frac{\partial \tau_{zz}}{\partial z}\right)+\rho g_z$

These forms of the equation of motion are commonly called *the Cauchy momentum equations*. For generalized Newtonian fluids we can define the terms of the deviatoric stress tensor as a function of a generalized Newtonian viscosity, η, and the components of the rate of deformation tensor, as described in Chapter 1 and Table 4.4.

In fluid mechanics, one common description of the deviatoric stress tensor is the Newtonian model given by

$$\tau_{ij}=\mu\dot{\gamma}_{ij} \tag{4.21}$$

which reduces the Cauchy momentum equations to

$$\begin{aligned}\rho\frac{\mathrm{D}u_i}{\mathrm{D}t}&=-\frac{\partial p}{\partial x_i}+\mu\frac{\partial^2 u_i}{\partial x_j\,\partial x_j}+\rho g_i\\ \rho\frac{\mathrm{D}\boldsymbol{u}}{\mathrm{D}t}&=-\nabla p+\mu\nabla^2\boldsymbol{u}+\rho\boldsymbol{g}\end{aligned} \tag{4.22}$$

Table 4.4 Stress Tensor Definition for a Generalized Newtonian Fluid

Cartesian Coordinates (x, y, z):		
$\tau_{xx} = 2\eta \frac{\partial u_x}{\partial x}$	$\tau_{xy} = \eta \left(\frac{\partial u_x}{\partial y} + \frac{\partial u_y}{\partial x} \right)$	
$\tau_{xz} = \eta \left(\frac{\partial u_x}{\partial z} + \frac{\partial u_z}{\partial x} \right)$		
$\tau_{yx} = \eta \left(\frac{\partial u_y}{\partial x} + \frac{\partial u_x}{\partial y} \right) = \tau_{xy}$	$\tau_{yy} = 2\eta \frac{\partial u_y}{\partial y}$	
$\tau_{yz} = \eta \left(\frac{\partial u_y}{\partial z} + \frac{\partial u_z}{\partial y} \right)$		
$\tau_{zx} = \eta \left(\frac{\partial u_z}{\partial x} + \frac{\partial u_x}{\partial z} \right) = \tau_{xz}$	$\tau_{zy} = \eta \left(\frac{\partial u_z}{\partial y} + \frac{\partial u_y}{\partial z} \right) = \tau_{yz}$	$\tau_{zz} = 2\eta \frac{\partial u_z}{\partial z}$
Cylindrical Coordinates (r, θ, z):		
$\tau_{rr} = 2\eta \frac{\partial u_r}{\partial r}$	$\tau_{r\theta} = \eta \left[r \frac{\partial}{\partial r} \left(\frac{u_\theta}{r} \right) + \frac{1}{r} \frac{\partial u_r}{\partial \theta} \right]$	
$\tau_{rz} = \eta \left(\frac{\partial u_r}{\partial z} + \frac{\partial u_z}{\partial r} \right)$		
$\tau_{\theta r} = \eta \left[\frac{1}{r} \frac{\partial u_r}{\partial \theta} + r \frac{\partial}{\partial r} \left(\frac{u_\theta}{r} \right) \right] = \tau_{r\theta}$	$\tau_{\theta\theta} = 2\eta \left(\frac{1}{r} \frac{\partial u_\theta}{\partial \theta} + \frac{u_r}{r} \right)$	
$\tau_{\theta z} = \eta \left(\frac{1}{r} \frac{\partial u_z}{\partial \theta} + \frac{\partial u_\theta}{\partial z} \right)$		
$\tau_{zr} = \eta \left(\frac{\partial u_z}{\partial r} + \frac{\partial u_r}{\partial z} \right) = \tau_{rz}$	$\tau_{z\theta} = \eta \left(\frac{\partial u_\theta}{\partial z} + \frac{1}{r} \frac{\partial u_z}{\partial \theta} \right) = \tau_{\theta z}$	$\tau_{zz} = 2\eta \frac{\partial u_z}{\partial z}$

These equations are often referred to as the *Navier-Stokes equations*. Table 4.5 presents the full form of the Navier-Stokes equations.

With a few exceptions one can say that a flowing polymer melt does not follow the model presented in Eq. 4.22. To properly model the flow of a polymer we must take into account the effects of rate of deformation, temperature, and often time, making the partial differential equations that govern a system non-linear.

Table 4.5 Navier-Stokes Equations

Cartesian Coordinates (x, y, z):
$\rho\left(\frac{\partial u_x}{\partial t}+u_x\frac{\partial u_x}{\partial x}+u_y\frac{\partial u_x}{\partial y}+u_z\frac{\partial u_x}{\partial z}\right)=-\frac{\partial p}{\partial x}+\mu\left(\frac{\partial^2 u_x}{\partial x^2}+\frac{\partial^2 u_x}{\partial y^2}+\frac{\partial^2 u_x}{\partial z^2}\right)+\rho g_x$
$\rho\left(\frac{\partial u_y}{\partial t}+u_x\frac{\partial u_y}{\partial x}+u_y\frac{\partial u_y}{\partial y}+u_z\frac{\partial u_y}{\partial z}\right)=-\frac{\partial p}{\partial y}+\mu\left(\frac{\partial^2 u_y}{\partial x^2}+\frac{\partial^2 u_y}{\partial y^2}+\frac{\partial^2 u_y}{\partial z^2}\right)+\rho g_y$
$\rho\left(\frac{\partial u_z}{\partial t}+u_x\frac{\partial u_z}{\partial x}+u_y\frac{\partial u_z}{\partial y}+u_z\frac{\partial u_z}{\partial z}\right)=-\frac{\partial p}{\partial z}+\mu\left(\frac{\partial^2 u_z}{\partial x^2}+\frac{\partial^2 u_z}{\partial y^2}+\frac{\partial^2 u_z}{\partial z^2}\right)+\rho g_z$
Cylindrical Coordinates (r, θ, z):
$\rho\left(\frac{\partial u_r}{\partial t}+u_r\frac{\partial u_r}{\partial r}+\frac{u_\theta}{r}\frac{\partial u_r}{\partial \theta}+u_z\frac{\partial u_r}{\partial z}-\frac{u_\theta^2}{r}\right)$ $=-\frac{\partial p}{\partial r}+\mu\left\{\frac{\partial}{\partial r}\left[\frac{1}{r}\frac{\partial}{\partial r}\left(r u_r\right)\right]+\frac{1}{r^2}\frac{\partial^2 u_r}{\partial \theta^2}+\frac{\partial^2 u_r}{\partial z^2}-\frac{2}{r^2}\frac{\partial u_\theta}{\partial \theta}\right\}+\rho g_r$
$\rho\left(\frac{\partial u_\theta}{\partial t}+u_r\frac{\partial u_\theta}{\partial r}+\frac{u_\theta}{r}\frac{\partial u_\theta}{\partial \theta}+\frac{u_r u_\theta}{r}+u_z\frac{\partial u_\theta}{\partial z}\right)$ $=-\frac{1}{r}\frac{\partial p}{\partial \theta}+\mu\left\{\frac{\partial}{\partial r}\left[\frac{1}{r}\frac{\partial}{\partial r}\left(r u_\theta\right)\right]+\frac{1}{r^2}\frac{\partial^2 u_\theta}{\partial \theta^2}+\frac{\partial^2 u_\theta}{\partial z^2}-\frac{2}{r^2}\frac{\partial u_r}{\partial \theta}\right\}+\rho g_\theta$
$\rho\left(\frac{\partial u_z}{\partial t}+u_r\frac{\partial u_z}{\partial r}+\frac{u_\theta}{r}\frac{\partial u_z}{\partial \theta}+u_z\frac{\partial u_z}{\partial z}\right)=-\frac{\partial p}{\partial z}+\mu\left\{\frac{\partial}{\partial r}\left[\frac{1}{r}\frac{\partial}{\partial r}\left(r u_z\right)\right]+\frac{1}{r^2}\frac{\partial^2 u_z}{\partial \theta^2}+\frac{\partial^2 u_z}{\partial z^2}\right\}+\rho g_z$

4.2.4 The Energy Balance or Equation of Energy

Using Fourier's law for heat conduction

$$q_i=-k_i\frac{\partial T}{\partial x_i} \tag{4.23}$$

and assuming an isotropic material, $k_x = k_y = k_z = k$, an energy balance around a moving fluid element, as shown in Fig. 4.9, can be written as

$$\rho C_p\frac{\mathrm{D}T}{\mathrm{D}t}=k\left(\frac{\partial^2 T}{\partial x^2}+\frac{\partial^2 T}{\partial y^2}+\frac{\partial^2 T}{\partial z^2}\right)+\dot{Q}+\dot{Q}_{\text{viscous eating}} \tag{4.24}$$

where an arbitrary heat source $\dot{Q}$, and viscous dissipation $\dot{Q}_{\text{viscous heating}}$ terms were included.

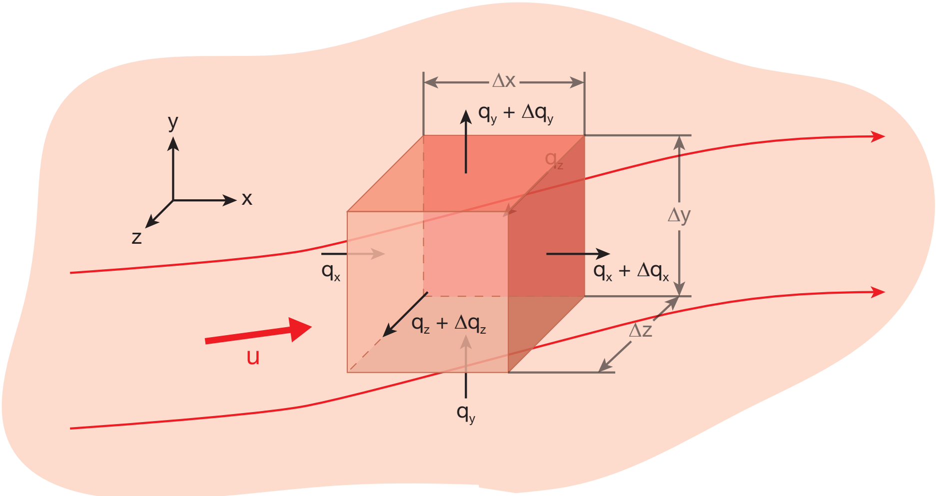

Figure 4.9 Heat flux across a differential fluid element during flow

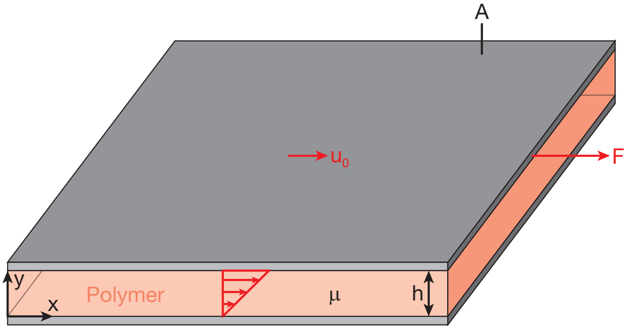

Figure 4.10 Schematic of a simple shear flow system used to illustrate viscous dissipation terms in the energy balance

As an illustration, we will derive the viscous dissipation terms in the energy balance using a simple shear flow system, such as the one shown in Fig. 4.10.

Here, the stresses within the system can be calculated using

$$\tau_{yx} = \mu \frac{\partial u_x}{\partial y} \tag{4.25}$$

which in terms of the parameters depicted in Fig. 4.10, such as force, F, area, A, gap height, h, and plate speed, u_0, can be written as

$$\frac{F}{A} = \mu \frac{u_0}{h} \tag{4.26}$$

Table 4.6 Energy Equation for a Newtonian Fluid

Cartesian Coordinates (x, y, z):

$$\rho C_p\left(\frac{\partial T}{\partial t}+u_x\frac{\partial T}{\partial x}+u_y\frac{\partial T}{\partial y}+u_z\frac{\partial T}{\partial z}\right)=k\left(\frac{\partial^2 T}{\partial x^2}+\frac{\partial^2 T}{\partial y^2}+\frac{\partial^2 T}{\partial z^2}\right)+2\mu\left[\left(\frac{\partial u_x}{\partial x}\right)^2+\left(\frac{\partial u_y}{\partial y}\right)^2+\left(\frac{\partial u_z}{\partial z}\right)^2\right]$$
$$+\mu\left[\left(\frac{\partial u_x}{\partial y}+\frac{\partial u_y}{\partial x}\right)^2+\left(\frac{\partial u_x}{\partial z}+\frac{\partial u_z}{\partial x}\right)^2+\left(\frac{\partial u_y}{\partial z}+\frac{\partial u_z}{\partial y}\right)^2\right]+\dot{Q}$$

Cylindrical Coordinates (r, θ, z):

$$\rho C_p\left(\frac{\partial T}{\partial t}+u_r\frac{\partial T}{\partial r}+\frac{u_\theta}{r}\frac{\partial T}{\partial \theta}+u_z\frac{\partial T}{\partial z}\right)=k\left[\frac{1}{r}\frac{\partial}{\partial r}\left(r\frac{\partial T}{\partial r}\right)+\frac{1}{r^2}\frac{\partial^2 T}{\partial \theta^2}+\frac{\partial^2 T}{\partial z^2}\right]$$
$$+2\mu\left[\left(\frac{\partial u_r}{\partial r}\right)^2+\left(\frac{1}{r}\frac{\partial u_\theta}{\partial \theta}+\frac{u_r}{r}\right)^2+\left(\frac{\partial u_z}{\partial z}\right)^2\right]$$
$$+\mu\left\{\left(\frac{\partial u_\theta}{\partial z}+\frac{1}{r}\frac{\partial u_z}{\partial \theta}\right)^2+\left(\frac{\partial u_z}{\partial r}+\frac{\partial u_r}{\partial z}\right)^2+\left[\frac{1}{r}\frac{\partial u_r}{\partial \theta}+r\frac{\partial}{\partial r}\left(\frac{u_\theta}{r}\right)\right]^2\right\}+\dot{Q}$$

In the system, the *rate of energy input* is given by

$$Fu_0=\mu\frac{u_0}{h}Au_0 \tag{4.27}$$

and by dividing the above equation by the volume of the polymer, Ah, the rate of energy input per unit volume is represented by

$$\frac{Fu_0}{Ah}=\mu\left(\frac{u_0}{h}\right)\left(\frac{u_0}{h}\right) \tag{4.28}$$

or

$$\dot{Q}_{\text{viscous heating}}=\mu\left(\frac{\partial u_x}{\partial y}\right)\left(\frac{\partial u_x}{\partial y}\right) \tag{4.29}$$

From the above equation, we can deduce that for a Newtonian fluid, the general term for viscous dissipation is given by $\mu(\dot{\gamma}:\dot{\gamma})$, where

$$\dot{\gamma}:\dot{\gamma}=\sum_{i=1}^{3}\sum_{j=1}^{3}\dot{\gamma}_{ij}\,\dot{\gamma}_{ji} \tag{4.30}$$

and for a non-Newtonian material, the viscous heating is written as $\tau:\dot{\gamma}$. Hence, the energy balance becomes

$$\rho C_p \frac{\partial T}{\partial t} + \rho C_p u_j \frac{\partial T}{\partial x_j} = \frac{\partial}{\partial x_j} k \frac{\partial T}{\partial x_j} + \tau_{ij} \dot{\gamma}_{ji} + \dot{Q} \tag{4.31}$$

$$\rho C_p \frac{\partial T}{\partial t} + \rho C_p \boldsymbol{u} \cdot \nabla T = \nabla \cdot k \, \nabla T + \tau : \dot{\gamma} + \dot{Q}$$

Table 4.6 presents the energy equation in Cartesian and cylindrical coordinate systems for a Newtonian fluid.

4.3 Model Simplification

In order to obtain analytical solutions we must first simplify the balance equations. Although the balance equations are fundamental and rigorous, they are nonlinear, non-unique, complex, and difficult to solve. In other words, they do not have a general solution and so far, only particular solutions for special problems have been found.

Therefore, the balance equations must be simplified sufficiently in order to arrive at an analytical solution of the problem under consideration. The simplifications of a system are typically based on the scale of the variables, an estimate of its maximum order of magnitude. As discussed in the previous section, scaling is the process of identifying the correct order of magnitude of the various unknowns. These magnitudes are often referred to as characteristic values, i.e., characteristic times, characteristic length, etc. When a variable is scaled with respect to its characteristic magnitude (scale), the new dimensionless variable will be of order 1, i.e., $(\sim O(1))$. For example, if we scale the x-velocity field, u_x, within a system, with respect to a characteristic velocity, U_0, we can generate a dimensionless velocity, or scaled velocity, given by

$$\hat{u}_x = \frac{u_x}{U_0} \tag{4.32}$$

Using the above relation, the original variable can be expressed in terms of the dimensionless variable and its characteristic value as

$$u_x = U_0 \, \hat{u}_x \tag{4.33}$$

By substituting the new variables into the original equations we will acquire information that allows the simplification of a specific model. Length and time scales, for example, can lead to geometrical simplifications, such as a reduction in dimensionality.

Example 4.3 Object submerged in a fluid

Consider an object with a characteristic length L and a thermal conductivity k that is submerged in a fluid of constant temperature T_∞ and convection coefficient h (see Fig. 4.11). If a heat balance is made on the surface of the object, it must be equivalent to the heat by conduction:

$$-k\left.\frac{\partial T}{\partial n}\right|_{\mathrm{S}} = h\left(T_{\mathrm{S}} - T_\infty\right) \tag{4.34}$$

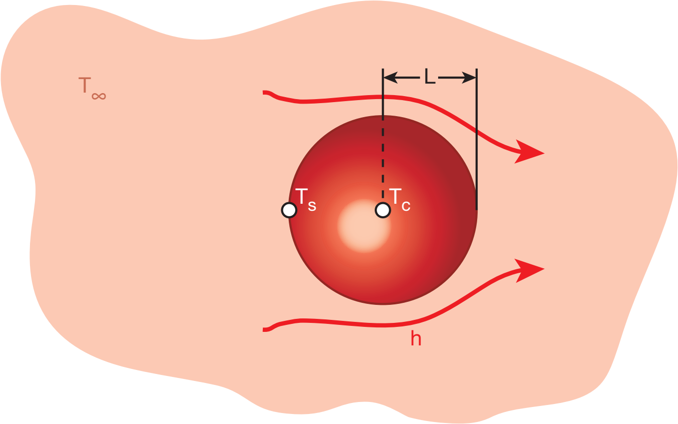

Figure 4.11 Schematic of a body submerged in a fluid

The maximum value possible for the temperature gradient must be the difference between the central temperature, T_{c}, and the surface temperature, T_{S},

$$\Delta T \sim T_{\mathrm{c}} - T_{\mathrm{S}} \tag{4.35}$$

which provides a characteristic temperature difference[2]. Here, the length variable is the normal distance Δn and has a characteristic length L. We can now approach the scaling in two ways. The first and quickest is to simply substitute the variables into the original equations, often referred to an *order of magnitude analysis*. The second is to express the original equations in terms of dimensionless variables. The order of magnitude analysis results in a scaled conduction given by

$$k\left.\frac{\partial T}{\partial n}\right|_{\mathrm{S}} \sim k\,\frac{T_{\mathrm{c}} - T_{\mathrm{S}}}{L} \tag{4.36}$$

---

[2] Characteristic temperatures are always given in terms of temperature differences. For example, the characteristic temperature of the melt of an amorphous polymer in an extrusion operation is $\Delta T = \left(T_{\mathrm{h}} - T_{\mathrm{g}}\right)$, which is the difference between the heater temperature and the glass transition temperature of the polymer.

reducing the problem to

$$k\frac{T_c - T_S}{L} \sim h\left(T_S - T_\infty\right) \tag{4.37}$$

or in a more convenient way

$$Bi = \frac{hL}{k} \sim \frac{T_c - T_S}{T_S - T_\infty} \tag{4.38}$$

where *Bi* is the *Biot number*.

When $Bi \ll 1$, the solid can be considered isothermal, which means that we *reduced the dimensionality* of the problem from (x, y, z), to a zero dimensional or *lumped model* [11]. On the other hand, if $Bi \gg 1$, the fluid can be considered non-isothermal and $T_S = T_\infty$, which changes the convection boundary condition to a thermal equilibrium condition.

The same can be deduced when we scale the problem by expressing the governing equations in dimensionless form. Again, we choose the same characteristic values for normal distance and temperature, allowing us to generate dimensionless variables as

$$\hat{T} = \frac{T}{T_c - T_S}, \quad \hat{n} = \frac{n}{L} \tag{4.39}$$

which can be solved to give

$$T = \left(T_c - T_S\right)\hat{T}, \quad n = L\hat{n} \tag{4.40}$$

Substituting these into the original equations results in

$$-\frac{k}{Lh}\frac{\partial\hat{T}}{\partial\hat{n}} = \frac{T_S - T_\infty}{T_c - T_S} \tag{4.41}$$

or

$$Bi\frac{\partial\hat{T}}{\partial\hat{n}} = \Theta \tag{4.42}$$

Again, because $\partial\hat{T}/\partial\hat{n}$ is of order one, the same analysis done above applies here.

4.3.1 Reduction in Dimensionality

The number of special coordinates, or the dimensionality of a problem, can be reduced using three basic strategies: symmetry, aspect ratio, and series resistances.

Symmetry is the easiest strategy to apply. It is based on the correct selection of the coordinate system for a given problem. For example, a temperature field with circular symmetry can be described using just the coordinates (r, z), instead of (x, y, z). In addition, symmetry can help to get rid of special variables that are not required by the conservation equations and interfacial conditions. For example, the velocity field in a tube, according to the Navier-Stokes and continuity equations, can have the functional form $u_z(r)$.

The ratio of two linear dimensions of an object is called the *aspect ratio*. There are a number of possible simplifications when the aspect ratio of an object or region is large (or small). For example, for the classical *fin approximation*, the thickness of the fin is small compared with the length, therefore the temperature will be assumed to change in the direction of the length only.

For example in problems where $Bi \ll 1$, convection controls the cooling process and conduction is so fast that the solid is considered isothermal, reducing the dimensionality from (x, y, z) to a zero dimensional problem or lumped mass method.

Characteristic times are a key factor in formulating conduction or diffusion models, because they determine how fast a system can respond to changes imposed at a boundary. In other words, if the temperature or concentration is perturbed at some location, it is important to estimate the finite time required for the temperature or concentration changes to be noticed at a given distance from the original perturbation. The time involved in a stagnant medium is the characteristic time for conduction or diffusion, therefore this is the most widely used characteristic time in transport models [11, 12].

Example 4.4 Temperature development in a simple shear flow

In this example, we illustrate the reduction in dimensionality of the energy equation to find an equation that would reveal the change in temperature of a polymer melt confined between two solid surfaces, set at different temperatures, T_1 and T_2, that are sliding past one another, as schematically depicted in Fig. 4.12. The lower plate is fixed and the upper one is moving at a velocity u_{2x}. To simplify the problem, we assume constant properties and a Newtonian viscosity.

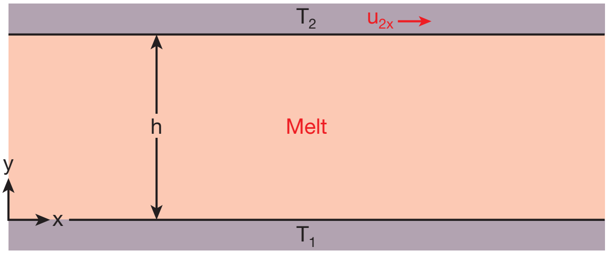

Figure 4.12 Schematic diagram of the non-isothermal simple shear flow set-up

The thickness of the melt is small compared to the dimensions of the plates, which indicates that a reduction in dimensionality can be performed. Here, it can be assumed that the velocity field is unidirectional, i.e., $u_x(y)$. The energy equation is then reduced to

$$\rho C_p u_x \frac{\partial T}{\partial t} = k\left(\frac{\partial^2 T}{dx^2} + \frac{\partial^2 T}{\partial y^2}\right) + \mu\left(\frac{\partial u_x}{\partial y}\right)^2 \tag{4.43}$$

By choosing characteristic variables for temperatures, velocities, and lengths we can reduce the dimensionality even further. The temperature is scaled based on the temperature difference $T_2 - T_1$, the length with the gap thickness, h, and plate size, L, and the velocity with the velocity of the moving surface, u_{2x},

$$\begin{aligned} \theta &= \frac{T - T_1}{T_2 - T_1} \qquad & \eta &= \frac{y}{h} \\ \xi &= \frac{x}{L} \qquad & \bar{u} &= \frac{u_x}{u_{2x}} \end{aligned} \tag{4.44}$$

Using these dimensionless variables, the energy equation becomes,

$$\rho C_p u_{2x} \frac{h^2}{L} \bar{u} \frac{\partial \theta}{\partial \xi} = \frac{h^2}{L^2}\frac{\partial^2 \theta}{\partial \xi^2} + \frac{\partial^2 \theta}{\partial \eta^2} + \frac{\mu u_{2x}^2}{k\left(T_2 - T_1\right)}\left(\frac{\partial \bar{u}}{\partial \eta}\right)^2 \tag{4.45}$$

which indicates that for small aspect ratios, h/L, two extra terms can be neglected: the conduction and convection in the x-direction,

$$\frac{\partial^2 \theta}{\partial \eta^2} + \frac{\mu u_{2x}^2}{k\left(T_2 - T\right)_1}\left(\frac{\partial \bar{u}}{\partial \eta}\right)^2 = 0 \tag{4.46}$$

The last step is to compare the two remaining terms: conduction and viscous dissipation. The two derivatives, according to the scaling parameter, are of order 1. The remaining term, $Br = \mu u_{2x}^2 / k\left(T_2 - T_1\right)$, is the Brinkman number, which indicates whether the viscous dissipation is important or not. For $Br \ll 1$, the conduction is dominant, while for $Br > 1$, the viscous dissipation has to be included, which is the case for many rheometers and is true in most polymer processing operations.

When the viscous dissipation term is negligible, the temperature distribution between the plates is linear

$$\Theta = \eta \quad \text{or} \quad \Theta = \Theta_{21}\,\eta \tag{4.47}$$

where $\Theta_{21} = T_2 - T_1$ and $\Theta = T - T_1$.

For this problem, the equation of motion reduces to

$$0 = \frac{\partial \tau_{xy}}{\partial y} \tag{4.48}$$

which after integration gives

$$\tau_{xy} = C_1 \tag{4.49}$$

To include the temperature dependence of the polymer, a commonly used model is

$$\eta = \eta_0 \, \mathrm{e}^{-a\Theta} \tag{4.50}$$

combining the constitutive equation and the above equation for shear stress, we can write

$$\tau_{xy} = C_1 = \eta_0 \, \mathrm{e}^{-a\Theta} \frac{\mathrm{d}u_x}{\mathrm{d}y} \quad \text{or} \quad \frac{\mathrm{d}u_x}{\mathrm{d}y} = C_1 \, \eta_0 \, \mathrm{e}^{a\Theta} \tag{4.51}$$

which after integration results in

$$u_x / u_{2x} = \left(\frac{1 - \mathrm{e}^{\Theta_{21} \eta}}{1 - \mathrm{e}^{\Theta_{21}}} \right) \tag{4.52}$$

which is represented in Fig. 4.13 for various thermal imbalances between the plates.

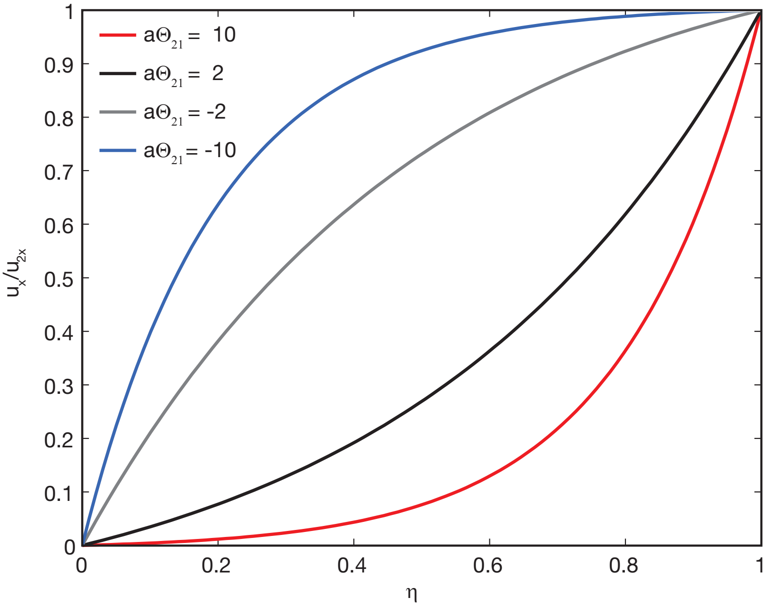

Figure 4.13 Velocity distribution in shear flow for various thermal imbalances

4.3.2 Lubrication Approximation

Liquid flows in long, narrow channels or thin films often are nearly unidirectional and dominated by viscous stresses. This means, flows in which a second component and the inertial effects are nearly zero.

The steady, two-dimensional flow in a thin channel or a narrow gap between solid objects is schematically represented in Fig. 4.14. The channel height or gap width varies with the position, and there may be a relative motion between the solid surfaces. This type of flow is very common for the oil between bearings. The original solution came from the field of tribology and is therefore often referred to as the *lubrication approximation*.

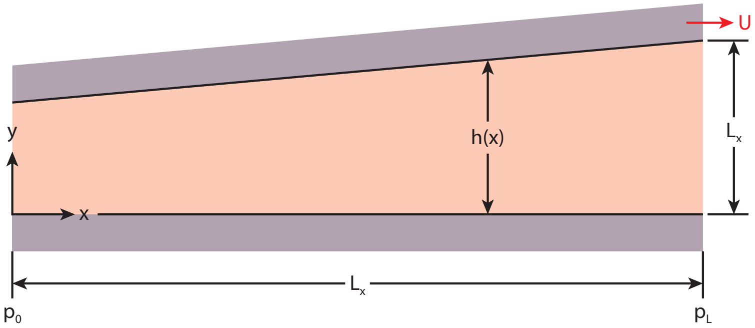

Figure 4.14 Schematic diagram of the lubrication problem

For this type of flow, the momentum equations (for a Newtonian fluid) are reduced to the steady Navier-Stokes equations, i.e.,

$$\frac{\partial u_x}{\partial x}+\frac{\partial u_y}{\partial y}=0 \tag{4.53}$$

$$\rho\left(u_x\frac{\partial u_x}{\partial x}+u_y\frac{\partial u_x}{\partial y}\right)=-\frac{\partial p}{\partial x}+\mu\left(\frac{\partial^2 u_x}{\partial x^2}+\frac{\partial^2 u_x}{\partial y^2}\right) \tag{4.54}$$

$$\rho\left(u_x\frac{\partial u_y}{\partial x}+u_y\frac{\partial u_y}{\partial y}\right)=-\frac{\partial p}{\partial y}+\mu\left(\frac{\partial^2 u_y}{\partial x^2}+\frac{\partial^2 u_y}{\partial y^2}\right) \tag{4.55}$$

The lubrication approximation depends on two basic conditions, one *geometric* and one *dynamic*. The geometric requirement is revealed by the continuity equation. If L_x and L_y represent the length scales for the velocity variations in the x- and y-directions, respectively, and let U and V be the respective scales for u_z and u_y. From the continuity equation we obtain

$$\frac{V}{U} \sim \frac{L_y}{L_x} \tag{4.56}$$

In order to neglect pressure variation in the y-direction, all the terms in the y-momentum equation must be small, in other words $V/U \ll 1$. The continuity scale analysis reveals that the geometric requirement is

$$\frac{L_y}{L_x} \ll 1 \tag{4.57}$$

which holds for thin films and channels. The consequences of this geometric constrain are reflected in the Navier-Stokes equations as

$$\frac{\partial p}{\partial y} \ll \frac{\partial p}{\partial x} \quad \text{and} \quad \frac{\partial^2 u_x}{\partial x^2} \ll \frac{\partial^2 u_x}{\partial y^2} \tag{4.58}$$

In addition, the continuity equation also tells us that the two inertia terms in the x-momentum equation are of similar magnitude, i.e.,

$$u_y \frac{\partial u_x}{\partial y} \sim \frac{VU}{L_y} \sim \frac{U^2}{L_x} \sim u_x \frac{\partial u_x}{\partial x} \tag{4.59}$$

These inertia effects can be neglected, i.e.,

$$\rho u_x \frac{\partial u_x}{\partial x} \ll \mu \frac{\partial^2 u_x}{\partial y^2} \quad \text{and} \quad \rho u_y \frac{\partial u_x}{\partial x} \ll \mu \frac{\partial^2 u_x}{\partial y^2} \tag{4.60}$$

only if $\rho U^2 / L_x \ll \mu U / L_y^2$ or

$$\left(\frac{\rho U L_y}{\mu}\right)\left(\frac{L_y}{L_x}\right) = Re\left(\frac{L_y}{L_x}\right) \ll 1 \tag{4.61}$$

which is the dynamic requirement for the lubrication approximation. The x-momentum (Navier-Stokes) equation is then reduced to

$$\frac{\partial^2 u_x}{\partial y^2} = \frac{1}{\mu}\frac{\mathrm{d}p}{\mathrm{d}x} \tag{4.62}$$

for $p = p(x)$ only.

4.4 Viscometric Flows

There are only a few exact or analytical solutions of the momentum balance equations, and most of them are for situations in which the flow is unidirectional; that is, the flow has only one non-zero velocity component. Some of these are illustrated in the following.

4.4.1 Pressure Driven Flow of a Newtonian Fluid through a Slit

One of the most common flows in polymer processing is the pressure driven flow between two parallel plates. This is also very important for slit rheometers or inline measurements inside cavities. When deriving the equations that govern *slit flow*, we use the notation presented in Fig. 4.15 and consider a steady, fully developed flow, i.e., a flow where the entrance effects are ignored.

This flow is unidirectional, which means there is only one non-zero velocity component. The continuity for an incompressible flow is reduced to

$$\frac{\partial u_z}{\partial z} = 0 \tag{4.63}$$

The z-momentum equation for a Newtonian, incompressible flow (Navier-Stokes equations) is

$$-\frac{\partial p}{\partial z} + \mu \frac{\partial^2 u_z}{\partial y^2} = 0 \tag{4.64}$$

and the x- and y-components of the equations of motion are reduced to

$$-\frac{\partial p}{\partial x} = -\frac{\partial p}{\partial y} = 0 \tag{4.65}$$

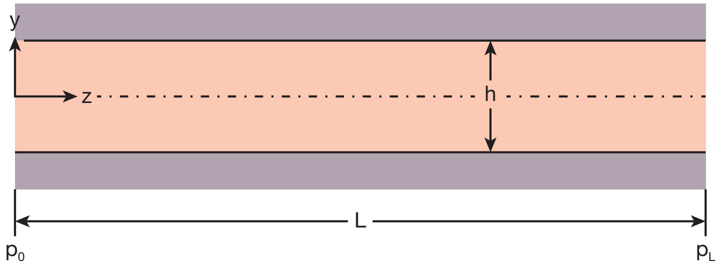

Figure 4.15 Schematic diagram of pressure flow through a slit

This relation indicates that for this fully developed flow, the total pressure is a function of z alone. Additionally, because u does not vary with z, the pressure gradient, $\partial p/\partial z$, must be a constant. Therefore,

$$\frac{\partial p}{\partial z} = \frac{\Delta p}{L} = 0 \tag{4.66}$$

where $\Delta p = p_L - p_0$. The momentum equation can now be written as

$$\frac{1}{u}\frac{\Delta p}{L} = \frac{\partial^2 u_z}{\partial y^2} \tag{4.67}$$

As boundary conditions, two no-slip conditions given by $u_z(\pm h/2) = 0$ are used in this problem. Integrating twice and evaluating the two integration constants with the boundary conditions gives

$$u_z(y) = \frac{h^2}{8\mu}\frac{\mathrm{d}p}{\mathrm{d}z}\left[1 - \left(\frac{2y}{h}\right)^2\right] = \frac{h^2}{8\mu}\frac{\Delta p}{L}\left[1 - \left(\frac{2y}{h}\right)^2\right] \tag{4.68}$$

Also note that the same profile will result, if one of the non-slip boundary conditions is replaced by a symmetry condition at $y = 0$, namely $\mathrm{d}u_z/\mathrm{d}y = 0$. The mean velocity in the channel is obtained integrating the above equation

$$\bar{u}_z = \frac{1}{h}\int_0^h u_z(y)\,\mathrm{d}y = \frac{h^2}{12\mu}\frac{\mathrm{d}p}{\mathrm{d}z} \tag{4.69}$$

and the volumetric flow rate is

$$Q = hW\bar{u}_z = \frac{Wh^3}{12\mu}\frac{\Delta p}{L} \tag{4.70}$$

where W is the width of the channel.

4.4.2 Flow of a Power Law Fluid in a Straight Circular Tube (Hagen-Poiseuille Equation)

Tube flow is encountered in several polymer processes, such as in extrusion dies and sprue and runner systems inside injection molds, as well as in capillary rheometers. When deriving the equations for pressure driven flow in tubes, also known as Hagen-Poiseuille flow, we assume that the flow is steady, fully developed, with no entrance effects, and axis-symmetric (see Fig. 4.16).

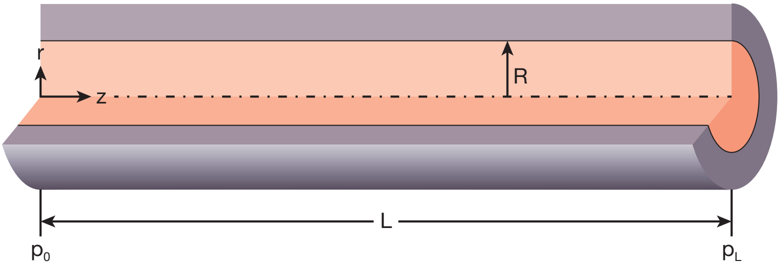

Figure 4.16 Schematic diagram of pressure flow through a tube

Thus, we have $u_z = u_z(r)$, $u_r = u_\theta = 0$ and $p = p(z)$. With this type of velocity field, the only non-vanishing component of the rate-of-deformation tensor is the *zr*-component. It follows that for the generalized Newtonian flow, τ_{zr} is the only non-zero component of the viscous stress and that $\tau_{zr} = \tau_{zr}(t)$. The *z*-momentum equation is then reduced to

$$\frac{1}{r}\frac{\mathrm{d}}{\mathrm{d}r}\left(r\tau_{zr}\right) = \frac{\mathrm{d}p}{\mathrm{d}z} \tag{4.71}$$

However, because $p = p(z)$ and $\tau_{zr} = \tau_{zr}(r)$, the above equation is satisfied only if both sides are constant and can be integrated to obtain

$$r\tau_{zr} = \frac{\mathrm{d}p}{\mathrm{d}z}\frac{r^2}{2} + c_1 \tag{4.72}$$

At this point, a symmetry argument at $r = 0$ leads to the conclusion that $\tau_{zr} = 0$ because the stress must be finite. Hence, we must satisfy $c_1 = 0$. For a Power Law fluid (Section 3.2.1) it is found that

$$\tau_{zr} = -m\left|\frac{\mathrm{d}u_z}{\mathrm{d}r}\right|^n \tag{4.73}$$

The minus sign in this equation is required because the pressure flow is in the direction of the flow $(\mathrm{d}p/\mathrm{d}z < 0)$, indicating that $\tau_{zr} \leq 0$. Combining the above equations and solving for the velocity gradient gives

$$\frac{\mathrm{d}u_z}{\mathrm{d}r} = -\left(-\frac{1}{2m}\frac{\mathrm{d}p}{\mathrm{d}z}\right)^{1/n} r^{1/n} \tag{4.74}$$

Integrating this equation and using the no-slip condition, at $r = R$, to evaluate the integration constant, the velocity as a function of r is obtained

$$u_z(r) = \left(\frac{3n+1}{n+1}\right)\left[1-\left(\frac{r}{R}\right)^{(n+1)/n}\right]\bar{u}_z \tag{4.75}$$

where the mean velocity, $\bar{u}_z = 0$, is defined as

$$\bar{u}_z = \frac{2}{R^2}\int_0^R u_z\, r\, \mathrm{d}r = \left(\frac{n}{3n+1}\right)\left[-\frac{R^{n+1}}{2m}\frac{\mathrm{d}p}{\mathrm{d}z}\right]^{1/n} \tag{4.76}$$

Finally, the volumetric flow rate is given by

$$Q = \pi R^2 \bar{u}_z = \left(\frac{n\pi}{3n+1}\right)\left[-\frac{R^{3n+1}}{2m}\frac{\mathrm{d}p}{\mathrm{d}z}\right]^{1/n} = \left(\frac{n\pi}{3n+1}\right)\left[-\frac{R^{3n+1}}{2m}\frac{\Delta p}{L}\right]^{1/n} \tag{4.77}$$

Example 4.5 Velocity distribution in a tube for shear thinning fluids

In this example, we illustrate the effect of the Power Law index on the velocity distribution of a shear thinning polymer in a 100 mm long, 2 mm diameter tube. Using Eq. 4.75, the velocity distribution for a Power Law fluid with a consistency index *m* of 100 Pa s and Power Law indices *n* of 1, 0.75, 0.5 and 0.25 were computed. Figure 4.17 presents the four velocity distributions, each normalized to their maximum velocity at the center of the tube.

In addition, Eq. 4.77 was used to plot the volumetric throughput in the tube as a function of pressure for the four different Power Law indices.

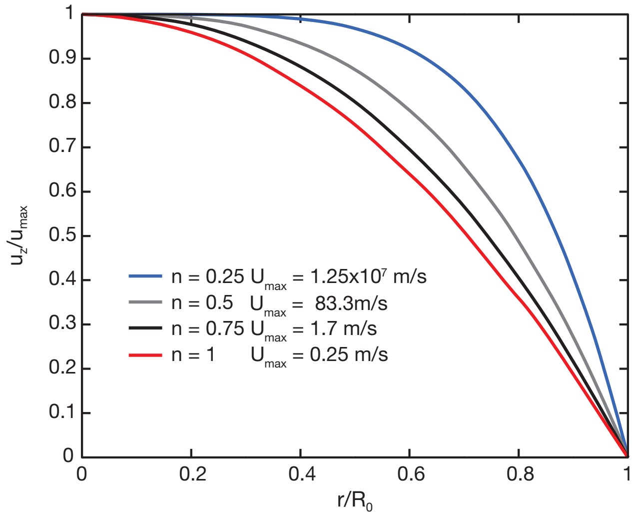

Figure 4.17 Velocity distribution within a tube for various power-law indices using a Power Law model

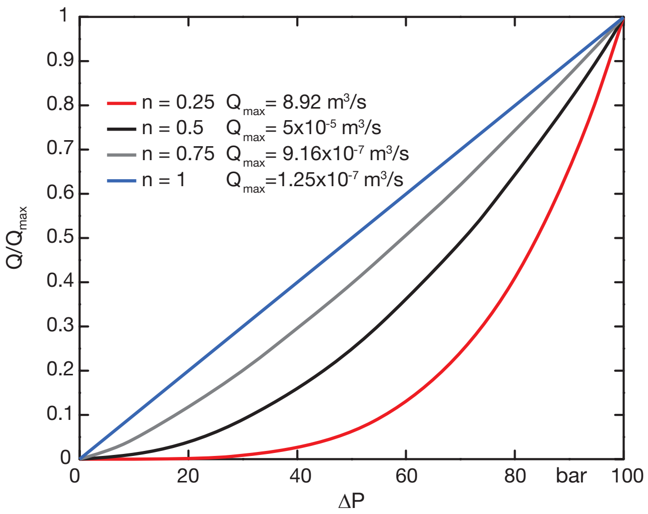

Figure 4.18 Volumetric throughput through a tube for various Power Law indices computed using a Power Law model

4.4.3 Volumetric Flow Rate of a Power Law Fluid in Axial Annular Flow

Annular flow is encountered in pipe extrusion dies, wire coating dies, and film blowing dies. In the problem under consideration, a Power Law fluid is flowing through an annular gap between two coaxial cylinders of radius κR and R, with $\kappa < 1$, as schematically depicted in Fig. 4.19. The maximum in the velocity profile is located at $r = \beta R$, where β is a constant to be determined. Considering the geometrical characteristics and ignoring entrance effects, the flow is unidirectional, i.e., $\boldsymbol{u} = \left(u_r, u_\theta, u_z\right) = \left(0, 0, u_{z(r)}\right)$.

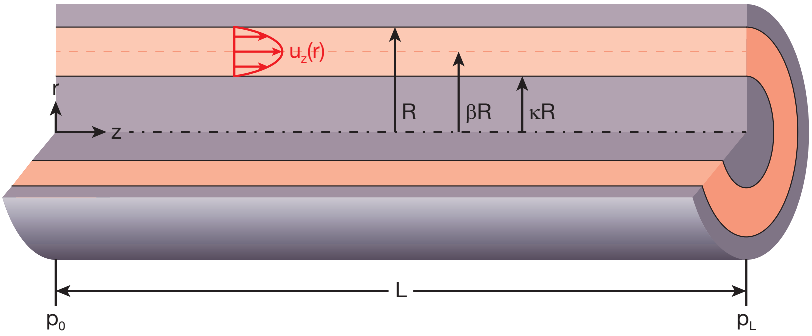

Figure 4.19 Schematic diagram of pressure flow through an annulus

The z-momentum equation is then reduced to

$$\frac{1}{r}\frac{\mathrm{d}}{\mathrm{d}r}\left(r\tau_{zr}\right)=\frac{\mathrm{d}p}{\mathrm{d}z} \tag{4.78}$$

Integrating this equation we obtain

$$r\tau_{zr}=\frac{\mathrm{d}p}{\mathrm{d}z}\frac{r^2}{2}+c_1 \tag{4.79}$$

The constant c_1 cannot be set to zero, because $\kappa R \le r \le R$. However, β can be used rather than c_1,

$$r\tau_{zr}=\frac{\Delta p\,R}{2L}\left(\frac{r}{R}-\beta^2\frac{R}{r}\right) \tag{4.80}$$

which makes β the new integration constant. The Power Law expression for the shear stress is given by

$$\begin{aligned}\tau_{zr}&=-m\left(\frac{\mathrm{d}u_z}{\mathrm{d}r}\right)^n &&\text{if}\quad \kappa R\le r\le \beta R\\ \tau_{zr}&=m\left(-\frac{\mathrm{d}u_z}{\mathrm{d}r}\right)^n &&\text{if}\quad \beta R\le r\le R\end{aligned} \tag{4.81}$$

Substitution of these expressions into the momentum equation leads to differential equations for the velocity distribution in the two regions. Integrating these equations with boundary conditions, $u_z = 0$ at $r = \kappa R$ and at $r = R$, leads to

$$\begin{aligned}u_z&=R\left[\frac{\Delta p\,R}{2mL}\right]^{1/n}\int_{\kappa}^{\xi}\left(\frac{\beta^2}{\xi'}-\xi'\right)^{1/n}\mathrm{d}\xi' &&\text{if}\quad \kappa\le\xi\le\beta\\ u_z&=R\left[\frac{\Delta p\,R}{2mL}\right]^{1/n}\int_{\xi}^{1}\left(\xi'-\frac{\beta^2}{\xi'}\right)^{1/n}\mathrm{d}\xi' &&\text{if}\quad \beta\le\xi\le 1\end{aligned} \tag{4.82}$$

where $\xi = r/R$. In order to find the parameter β, the above equations must match at the location of the maximum velocity,

$$\int_{\kappa}^{\xi}\left(\frac{\beta^2}{\xi'}-\xi'\right)^{1/n}\mathrm{d}\xi=\int_{\xi}^{1}\left(\xi'-\frac{\beta^2}{\xi}\right)^{1/n}\mathrm{d}\xi' \tag{4.83}$$

This equation is a relation between β, the geometrical parameter κ, and the Power Law exponent n. The volumetric flow rate in the annulus becomes

$$
\begin{aligned}
Q &= 2\pi \int_{\kappa R}^{R} u_z \, r \, \mathrm{d}r = \pi R^3 \left[\frac{\Delta p R}{2mL}\right]^{1/n} \int_{\kappa}^{1} \left|\beta^2 - \xi'^2\right|^{1/n+1} \xi'^{-1/n} \, \mathrm{d}\xi' \\
&= \frac{\pi R^{3+1/n}}{1/n+3} \left[\frac{\Delta p R}{2mL}\right]^{1/n} \left[\left(1-\beta^2\right)^{1+1/n} - \kappa^{1-1/n} \left(\beta^2-\kappa^2\right)^{1+1/n}\right]
\end{aligned}
\tag{4.84}
$$

4.4.4 Circular Annular Couette Flow of a Power Law Fluid

Circular annular Couette flow is a drag-induced flow between two concentric cylinders with one cylinder rotating relative to the other. Couette flow or circular annular Couette flow, as schematically depicted in Fig. 4.20, is commonly encountered in rheometry and polymer processing [1]. This is a two-dimensional analysis that is most easily solved using cylindrical coordinates (r, θ, z) as shown in Fig. 4.20. When solving this problem, an isothermal flow with negligible viscous dissipation is assumed.

In a laminar flow, with perfect, concentric cylinders, it is intuitive to assume that $u_r = 0$. In addition, it can safely be assumed that there is no flow in the axial or z-direction, $u_z = 0$. The only velocity component left is u_θ, which only varies in the radial direction, r. Hence, the velocity field can be represented using

$$u = \left(0, u_\theta\left(r, 0, 0\right), 0\right) \tag{4.85}$$

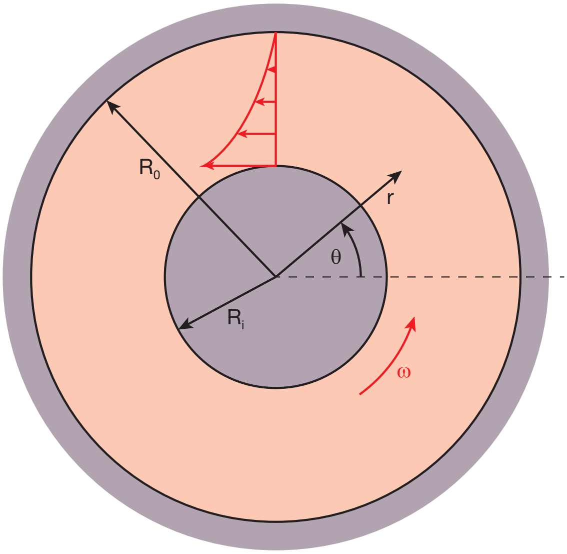

Figure 4.20 Schematic diagram of circular annular Couette flow

With the above flow field the continuity equation for an incompressible flow reduces to

$$\frac{\partial u_\theta}{\partial \theta} = 0 \tag{4.86}$$

This supports the initial assumption by showing that u_θ is not a function of θ.

Creeping flow, characteristic in polymeric melts, was considered, with the understanding that inertia effects are negligible in comparison to the viscous effects (Reynolds number, $Re \ll 1$). Gravity forces are also much smaller than viscous forces (Poiseuille number $Ps \ll 1$), and are therefore neglected. For a polymeric melt, the pressure gradient does not play a role, because gravity forces and inertial forces are insignificant (for the Newtonian case, the pressure gradient is a function of the centrifugal force and the gravity force, $p(r,z)$) [2]. The velocity field is generated by the drag flow caused by rotation of the inner boundary. No pressure is imposed on the system. The θ component of the equations of motion gives insight into the velocity field, and the r component provides information on the pressure gradient. For a 2D approach, only the θ component is used,

$$r\text{-component} \qquad 0 = -\frac{\partial p}{\partial r} \tag{4.87}$$

$$\theta\text{-component} \qquad 0 = \left[\frac{1}{r^2}\frac{\partial}{\partial r}\left(r^2 \tau_{r\theta}\right)\right] \tag{4.88}$$

The rate of deformation tensor components are derived using the assumptions about the velocity, Eq. 4.85 and Eq. 4.86,

$$\dot{\gamma} = \dot{\gamma}_{r\theta} = \dot{\gamma}_{\theta r} = r\frac{\partial}{\partial r}\left(\frac{u_\theta}{r}\right) \tag{4.89}$$

A constitutive equation that couples the θ component of the equations of motion, Eq. 4.88, and the $r\theta$ component of the rate of deformation tensor, Eq. 4.89, is needed. The Power Law model is used as the constitutive model for the non-Newtonian behavior of the polymer melt

$$\tau = \eta\dot{\gamma} \tag{4.90}$$

$$\eta = m\dot{\gamma}^{(n-1)} \tag{4.91}$$

The fact that the only component left of the rate of deformation tensor is the $r\theta$ component (Eq. 4.89) assures that the $\tau_{r\theta}$ term is the only component left in the θ-component of the equations of motion (Eq. 4.88). After integrating this term with respect to r, the equation of motions is reduced to

$$\tau_{r\theta} = \frac{A}{r^2} \tag{4.92}$$

where A is a constant of integration.

Substituting the $r\theta$ component of the rate of deformation tensor, $\dot{\gamma}_{r\theta}$ (Eq. 4.89), into the Power Law model (Eq. 4.91), the shear stress tensor becomes

$$\tau_{r\theta} = m\left[-r\frac{\mathrm{d}}{\mathrm{d}r}\left(\frac{u_\theta}{r}\right)\right]^n \tag{4.93}$$

The partial derivatives were changed to regular derivatives because the unknown parameters are only a function of r. Equating Eqs. 4.92 and 4.93 and solving for the velocity field by integrating the equation one time results in

$$\frac{u_\theta}{r} = B\frac{n}{2}(r)^{-\frac{2}{n}} + C \tag{4.94}$$

where $B = (A/m)^{1/n}$. In order to fully account for the velocity field, the constants A and B must be solved by using the given boundary conditions for the inner and outer cylinders,

$$u_\theta = 0 \qquad \text{if} \quad r = R_\mathrm{o} \tag{4.95}$$

$$u_\theta = R_\mathrm{i}\,\omega \qquad \text{if} \quad r = R_\mathrm{i} \tag{4.96}$$

It is possible now to solve the system with two unknowns, A and C, and two equations. Substituting the boundary conditions, Eq. 4.95 and Eq. 4.96, into Eq. 4.94, the velocity field, u_θ, is obtained

$$u_\theta(r) = \omega r \frac{\left[1-\left(\frac{r}{R_\mathrm{o}}\right)^{-\frac{2}{n}}\right]}{\left[1-\left(\frac{R_\mathrm{i}}{R_\mathrm{o}}\right)^{-\frac{2}{n}}\right]} \tag{4.97}$$

Example 4.6 Velocity distribution within a Couette device containing shear thinning fluids

In this example, we illustrate the effect of the Power Law index on the velocity distribution of a shear thinning polymer within a Couette device. For a Couette device with an inner radius R_i = 3 cm and outer radius R_o = 6 cm, and in conjunction with

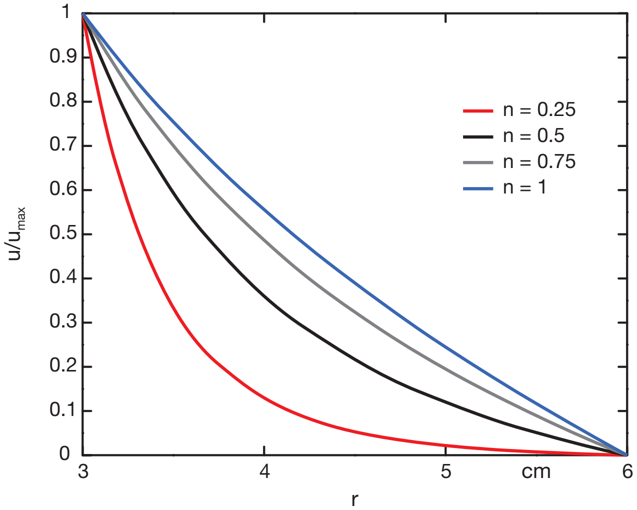

Figure 4.21 Velocity distribution within a Couette device for Power Law indices computed using a Power Law model

Eq. 4.75, the velocity profile was computed using Power Law indices *n* of 1, 0.75, 0.5 and 0.25.

4.4.5 Squeezing Flow of a Newtonian Fluid between Two Parallel Circular Discs

Squeezing flow between two parallel discs results when two parallel surfaces approach each other, displacing the fluid out from between the plates. This is a two-dimensional analysis that is most easily solved using cylindrical coordinates (r, θ, z) [13] as shown in the Fig. 4.22.

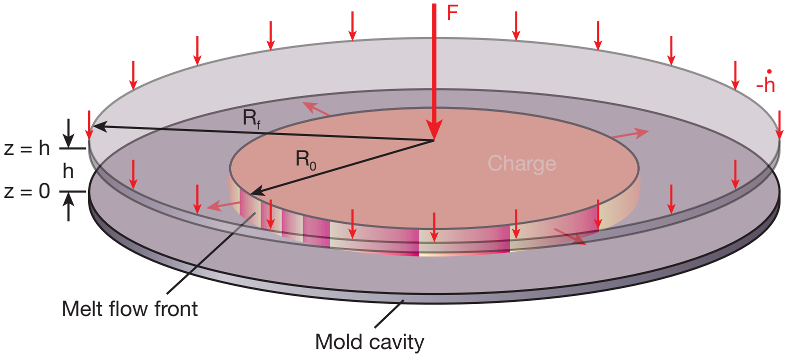

Figure 4.22 Schematic diagram of squeezing flow between two parallel discs

The first assumption one can make is that there is no velocity component in the θ-direction because the plates do not rotate. In addition, because the z-dimension (h) is reduced over time by $\dot{h} = \mathrm{d}h/\mathrm{d}t$, the two remaining velocity components, u_r and u_z, are functions of space and time. The radial velocity component, u_r, changes along the radius and across the distance between the plates, or in the z-direction. Additionally, u_z changes in the z-direction but is not a function of r.

$$\boldsymbol{u} = \left[u_r\left(r,0,z,t\right),0,u_z\left(0,0,z,t\right)\right] \tag{4.98}$$

For an incompressible fluid, the continuity equation reduces to

$$\frac{1}{r}\frac{\partial}{\partial r}\left(r\,u_r\right)+\frac{\partial u_z}{\partial z}=0 \tag{4.99}$$

Assuming a quasi-steady condition and negligible inertia effects, the left hand side of the equation of motion is neglected. This assumption implies that the radial profile of the flow can be assumed to be in a hydrodynamic steady-state. Additionally, because inertial effects are negligible, the body force terms can be dropped. With $R_0 \gg h$, two assumptions can be made

$$u_z \ll u_r \quad \text{and} \quad \frac{\partial u_r}{\partial r} \ll \frac{\partial u_r}{\partial z} \tag{4.100}$$

which reduces the equations of motion for a Newtonian fluid to

$$r\text{-component} \qquad 0 = -\frac{\partial p}{\partial r} + \mu\,\frac{\partial^2 u_r}{\partial z^2} \tag{4.101}$$

$$z\text{-component} \qquad 0 = -\frac{\partial p}{\partial z} \tag{4.102}$$

An analysis of the components of the rate of deformation tensor leads to

$$\dot{\gamma}_{rr} = \frac{\partial u_r}{\partial r} \tag{4.103}$$

$$\dot{\gamma}_{rz} = \dot{\gamma}_{zr} = \frac{1}{2}\left(\frac{\partial u_z}{\partial r}+\frac{\partial u_r}{\partial z}\right) \tag{4.104}$$

$$\dot{\gamma}_{\theta\theta} = \frac{u_r}{r} \tag{4.105}$$

$$\dot{\gamma}_{zz} = \frac{\partial u_z}{\partial z} \tag{4.106}$$

The continuity equation and the equation of motion now form a system of 3 equations and 3 unknowns, u_r, u_θ and ΔP. Before proceeding to solve this system of equations, they can be simplified using known relationships. In order to fulfill the continuity equation (Eq. 4.99) u_r must have a particular shape, namely,

$$u_r = r\,f(z,t) \tag{4.107}$$

The z-component of the equation of motion, Eq. 4.102, shows that p is not a function of z but r. By substituting u_r into the r-component of the equation of motion, p becomes

$$p = p_\text{o} + p_2 r^2 \tag{4.108}$$

Using these three relationships, the continuity equation and the equation of motion can now be written as

$$2f + \frac{\partial u_z}{\partial z} = 0 \tag{4.109}$$

$$-2p_2 + \mu\frac{\partial^2 f}{\partial z^2} = 0 \tag{4.110}$$

which is a system of 2 equations and 2 unknowns. To solve the above system of equations, the following boundary conditions are used

$$\frac{\partial f}{\partial z} = 0 \qquad \text{at} \quad z = 0 \tag{4.111}$$

$$f = 0 \qquad \text{at} \quad z = h/2 \tag{4.112}$$

$$u_z = 0 \qquad \text{at} \quad z = 0 \tag{4.113}$$

$$u_z = \dot{h}/2 \qquad \text{at} \quad z = h/2 \tag{4.114}$$

$$p = p_\text{a} \qquad \text{at} \quad r = R_0 \tag{4.115}$$

With these conditions we can solve Eq. 4.109 and 4.110 as

$$u_r = r\,f = \frac{3}{4}\frac{(-\dot{h})}{h}\,r\left[1-\left(\frac{z}{2h}\right)^2\right] \tag{4.116}$$

$$u_z = \frac{3}{4}\dot{h}\left[\left(\frac{z}{2h}\right)-\frac{1}{3}\left(\frac{z}{2h}\right)^3\right] \tag{4.117}$$

$$p = p_a + 3\frac{(-\dot{h})}{h^3}\mu R_0^2\left[1-\left(\frac{r}{R_o}\right)^2\right] \tag{4.118}$$

With the resulting pressure distribution and the knowledge that $\tau_{zz} = 0$ on the discs, the force on a disc surface can be determined using

$$F = \int_0^{2\pi}\int_0^{R_0}\left(p - p_a + \tau_{zz}\right)_{z=h} r\,\mathrm{d}r\,\mathrm{d}\theta \tag{4.119}$$

$$F = 2\pi R_0^2\int_0^1 \left(p - p_a\right)\left(\frac{r}{R_0}\right)d\left(\frac{r}{R_0}\right) \tag{4.120}$$

$$F = 6\pi R_0^4\,\mu\,\frac{\left(-\dot{h}\right)}{h^3} \tag{4.121}$$

4.4.6 Flow of a Power Law Fluid between Two Parallel Circular Discs

The flow between two rotating parallel circular discs results when one disc is fixed and the other rotates at a rotational speed ω [14]. This is the case in the parallel plate rheometer. The necessary two-dimensional analysis is most easily solved using cylindrical coordinates (r, θ, z) as shown in Fig. 4.23. The geometric restrictions of circular discs set-up reduces the velocity to

$$u = \left(0, u_\theta\left(r, 0, z\right), 0\right) \tag{4.122}$$

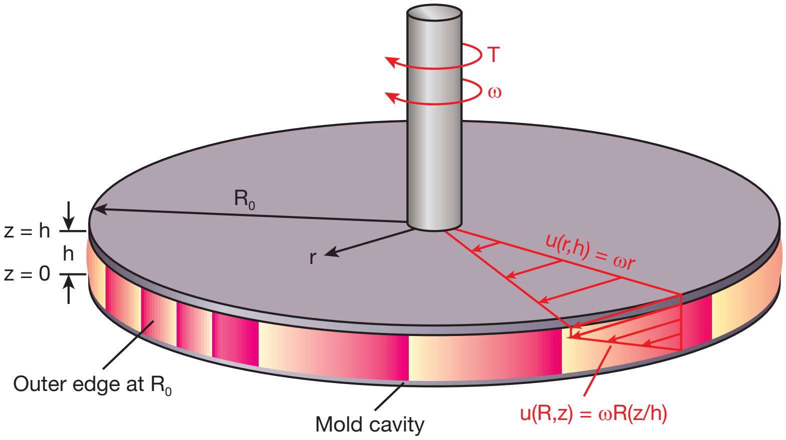

Figure 4.23 Schematic diagram of the flow between two parallel discs

As expected, the continuity equation reveals that u_θ is not a function of θ.

$$\frac{\partial u_\theta}{\partial \theta} = 0 \tag{4.123}$$

Assuming that simple shear flow takes place with a velocity component in the θ-direction and a gradient in the z-direction, we can write

$$u_\theta = A(r)\, z + B(r) \tag{4.124}$$

The respective boundary conditions are:

$$u_\theta = 0 \qquad \text{at} \quad z = 0 \tag{4.125}$$

$$u_\theta = r\,\omega \qquad \text{at} \quad z = h \tag{4.126}$$

These boundary conditions allow to solve for $A(r)$ and $B(r)$, where $B(r)=0$ and $A(r)=r\,\omega\, z/h$. This leads to a velocity profile

$$u_\theta = r\,\omega \frac{z}{h} \tag{4.127}$$

also depicted in Fig. 4.23. Using Eq. 4.122, an evaluation of the components of the rate of deformation tensor leads to

$$\dot\gamma_{z\theta} = \dot\gamma_{\theta z} = \frac{\partial u_\theta}{\partial z} \tag{4.128}$$

$$\dot\gamma_{r\theta} = \dot\gamma_{\theta r} = r \frac{\partial}{\partial r}\left(\frac{u_\theta}{r}\right) \tag{4.129}$$

Substituting the velocity field, Eq. 4.127, the components in the rate of deformation tensor are

$$\dot\gamma_{z\theta} = \dot\gamma_{\theta z} = \frac{r\,\omega}{h} \tag{4.130}$$

$$\dot\gamma_{r\theta} = \dot\gamma_{\theta r} = 0 \tag{4.131}$$

Defining the strain rate as

$$\dot\gamma = \dot\gamma_{r_0} \frac{r}{R_0} \tag{4.132}$$

with the strain rate at the outer edge of the discs given by

$$\dot{\gamma}_{r_0} = \frac{R_0\,\omega}{h} \tag{4.133}$$

With the additional assumption that the pressure stays constant in the θ-direction, the analysis of the θ-component of the equation of motion gives us

$$0 = -\frac{\partial \tau_{z\theta}(z,r)}{\partial z} \tag{4.134}$$

which after integration results in

$$\tau_{z\theta} = C(r) \tag{4.135}$$

In order to determine the shear stress, we must measure and find the viscosity at specific radii. Hence, it is more practical to measure the torque, T, required to turn the upper disk. The torque on the top disk is given by

$$T = \int_0^{R_0} \left(-\tau_{z\theta\, z=h}\right)(r)\left(2\pi r\, \mathrm{d}r\right) \tag{4.136}$$

The viscosity at any position r is given by

$$\eta(r) = \frac{-\tau_{z\theta}(r)}{\dot{\gamma}(r)} \tag{4.137}$$

Substituting Eq. 4.137 into Eq. 4.136 gives

$$T = 2\pi \int_0^{R_0} \eta\dot{\gamma}(r)\, r^2\, \mathrm{d}r \tag{4.138}$$

Using the strain rate defined in Eq. 4.132, it is possible to replace r by $\dot{\gamma}$

$$T = 2\pi \frac{r_0^3}{\dot{\gamma}_{R_0}} \int_0^{\dot{\gamma}_{R_0}} \eta\dot{\gamma}^3\, \mathrm{d}\dot{\gamma} \tag{4.139}$$

and after differentiating both sides of Eq. 4.139 using the Leibnitz rule, we can solve for a viscosity function defined by

$$\eta\left(\dot{\gamma}_{r_0}\right) = \frac{1}{2\pi r_0^3}\,\frac{T}{\dot{\gamma}_{r_0}}\left[3 + \frac{d\ln\left(\dfrac{T}{2\pi r_0^3}\right)}{d\ln\dot{\gamma}_{r_0}}\right] \tag{4.140}$$

Problems

4.1 Rearrange the Lissajous loops in Fig. 2.37 of Example 2.6 in Chapter 2 with *We* instead of γ_0 on the vertical axis. Draw the line where $G_n = 1$. What is the significance of this graph?

4.2 Please retrieve and read the paper by A. J. Giacomin et al., [15]. Write a short essay on the significance of G_n.

4.3 Explain and prove the three different forms presented for the Weissenberg number in Table 4.1.

4.4 Explain and prove the two different forms presented for the Deborah number in Table 4.1.

4.5 The 7 mm diameter piston in a capillary rheometer moves at a speed of 20 mm/s, forcing a blow molding grade PE-HD melt of the examples in Chapter 2 through the 2 mm diameter capillary. The test temperature is190 °C and the thermal conductivity k is 0.2 W/m K. Is viscous dissipation important?

4.6 Derive the equation that describes the pressure flow between parallel plates with a temperature difference between the upper and the lower plates. Follow the same procedure used in Example 4.2.

4.7 Derive the equations that describe the pressure flow through a slit using a Power Law viscosity model. Plot the velocity distribution for various Power Law indices.

4.8 Plot the velocity distribution within a capillary using the Hagen-Poiseuille equation with a Power Law viscosity model, such as used in Example 4.5. What is the smallest Power Law index n you can use?

4.9 Derive the governing equation for a squeeze flow between two parallel plates using a Power Law viscosity model.

4.10 Using the squeeze flow equations between two parallel discs derived for a Newtonian fluid, plot the force F necessary to close the disc as the gap changes from 10 mm to 1 mm at a closing speed of 1 mm/s. The disc diameter is 100 mm and the polymer viscosity 100 Pa s.

4.11 Is viscous heating important in the squeeze flow of Problem 4.10?

References

[1] Pawlowski, J., Die Ähnlichkeitstheorie in der Physikalisch-Technischen Forschung – Grundlagen und Anwendung. Springer-Verlag, Berlin, (1971).

[2] Osswald, T. A., Hernández, J. P., Polymer Processing – Modeling and Simulation. Hanser Publishers, Munich, (2006).

[3] Osswald, T. A., Understanding Polymer Processing, Hanser Publishers, Munich, (2010).

[4] Zlokarnik, M., Scale-up in Chemical Engineering. Wiley-VCH, Weinhein, (2002).

[5] Zlokarnik, M., Eignung von Rührern zum Homogenisieren von Flüssigkeitsgemischen. *Chem.Ing. Tech., 39 (9/10)*, 539, (1967).

[6] Pawlowski, J., *Chemie-Ing. Techn., 38*, 1229, (1966).

[7] Pawlowski, J., *Chemie-Ing. Techn., 39*, 1180, (1967).

[8] Stanton, T. E., Pannell, J. R., Similarity of motion in relation to the surface friction of fluids. *Phil. Trans. Roy. Soc. London, 214*, 199, (1914).

[9] Osswald, T. A., Menges, G., Materials Science of Polymers for Engineers, 3rd ed., Hanser Publishers, (2012).

[10] Giacomin, A. J., Bird, R. B., Aumnate, C., Mertz, A. M., Schmalzer, A. M., Mix, A. W., *Fluids of Physics., 24*, 10, (2012).

[11] Bird, R. B., Steward, W. E., Lightfoot, E. N., Transport Phenomena. John Wiley & Sons, New York, 2nd ed., (2002).

[12] Incropera, F. P., DeWitt, D. P., Fundamentals of Heat and Mass Transfer. John Wiley & Sons, New York, (1996).

[13] Middleman, S., Fundamentals of Polymer Processing, New York, McGraw-Hill, (1977).

[14] Bird, R. B., Curtiss, C. F., Stewart, W. E., *Chem. Eng. Sci., 11*, 114–117, (1959).

[15] Giacomin, A. J., Bird, R. B., Johnson, L. M., Mix, A. W., *J. Non-Newton. Fluid Mech., 166 (19–20)*, 1081–1099, (2011).

5 Viscoelasticity

Although polymers have their distinct transitions and may be considered liquid when above the glass transition or melting temperatures, or solid when below those temperatures, in reality they are neither liquid nor solid, but viscoelastic. In fact, at any temperature, a polymer can be either a liquid or a solid, depending on the time scale or the speed at which its molecules are being deformed.

We can use the Deborah number, $De = \lambda\omega$, first discussed in Chapter 1, and the deformation, γ_0, to summarize how the system can be most accurately modeled. Figure 5.1 helps visualize the relation between time scale, deformation, and applicable material behavior. At small Deborah numbers, the polymer can be modeled as a Newtonian fluid, and at very high Deborah numbers, the material can be modeled as a Hookean solid. Both cases are well understood; the first is extensively covered in Chapters 3 and 4, and the latter within the field of solids mechanics, outside the scope of this book.

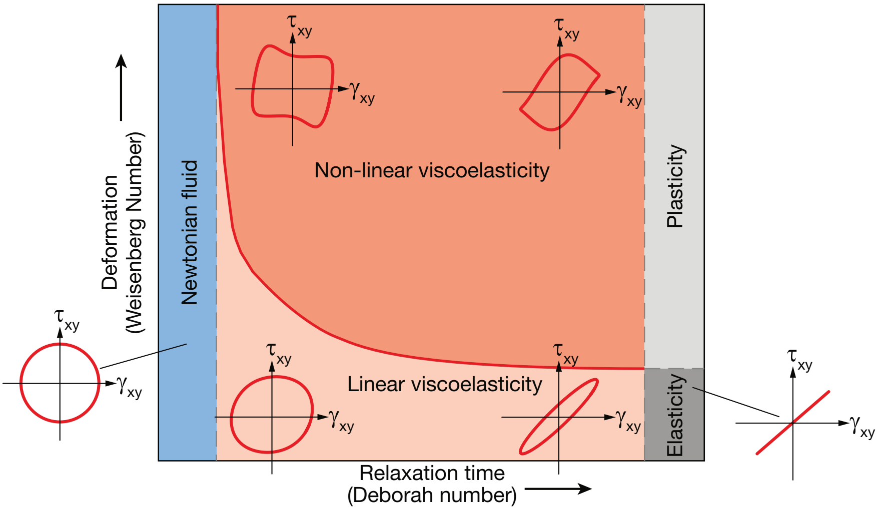

Figure 5.1 Schematic of Newtonian, elastic, linear, and non-linear viscoelastic regimes as a function of deformation and relaxation time during deformation of polymeric materials

The cases that fall between these two situations are covered within this chapter. Here, the viscoelastic region is divided in two: the linear viscoelastic region for small deformations, and the non-linear viscoelastic region for large deformations.

Experimentally, simple laboratory tests are desirable in order to obtain information relevant to actual processing conditions. Experiments that apply small deformations are used to study linear viscoelasticity, revealing information about the molecular structure. Here, the material functions and models are useful for predicting general tendencies and for quality control in production. A comprehensive guide to understanding linear viscoelasticity is given by Ferry [1]. For actual processing-relevant information, however, the more complex, viscoelastic behavior under large deformations must be studied, typically using large amplitude oscillatory shear (LAOS) tests.

The collected data can be displayed in the form of Lissajous loops or they can be presented on a so-called Pipkin diagram, where instead of deformation, the Weissenberg number, $We = \gamma_0 \lambda \omega$, is on the vertical axis

5.1 Linear Viscoelasticity

The well-established field of linear viscoelasticity applies to materials undergoing small deformations, such as the short term deformation of polymer components. The most common, linear viscoelastic model is the Maxwell model presented in Chapter 1. The governing equation for the Maxwell model is given by

$$\tau_{xy} + \lambda \frac{d\tau_{xy}}{dt} = -\eta_0 \dot{\gamma}_{xy} \tag{5.1}$$

Experimentally, linear viscoelasticity is maintained during a dynamic mechanical test (DMA) or oscillatory sliding plate rheometry, where the small deformations leave the molecular structure almost unaffected and the same response is observed in each cycle during testing. The non-linearities arise as soon as the deformation is large enough to alter the structure of the polymer chains. This, of course, is the topic for non-linear viscoelasticity discussed later in this chapter.

5.1.1 Relaxation Modulus

As discussed in Chapter 2, the most basic principle that governs the mechanical and rheological behavior of polymers is the stress relaxation behavior. When a sudden strain is applied at $t = 0$, such as a small amount of shear γ_0, the resulting stress can be measured as a function of time, $\tau(t)$. For non-linear materials, such as polymers, the decaying stress results in a shear modulus that is also a function of strain $G(\gamma_0,t)$, where

$$G(\gamma_0,t)=\tau_{xy}(\gamma_0,t)/\gamma_0 \tag{5.2}$$

Similar to the stress relaxation modulus presented for elongational deformations in Chapter 2, we can assume that for small instantaneous deformations the shear modulus is proportional to strain and is therefore only a function of time

$$G(t)=\tau_{xy}(t)/\gamma_0 \tag{5.3}$$

This linear relation is the basic principle behind linear viscoelasticity.

5.1.2 The Boltzmann Superposition Principle

In addition to the *time-temperature superposition principle (WLF)*, the *Boltzmann superposition principle* is of extreme importance in the theory of linear viscoelasticity. The Boltzmann superposition principle states that the deformation of a polymer component is the sum or superposition of all strains that result from various loads acting on the part at different times. This means that the response of a material to a specific load is independent of already existing loads or strains. That is, if at a particular time t_i a sudden strain $\Delta\gamma(t_i)$ is applied, the resulting stress from this strain can be expressed as

$$\tau_{xy_i}(t)=G(t-t_i)\,\Delta\gamma_{xy_i}(t_i) \tag{5.4}$$

Hence, we can compute the stress within a polymer specimen that is exposed to several strains at different points in time (such as presented in Fig. 5.2) by simply adding all stress responses:

$$\tau_{xy}(t)=G(t-t_1)\,\Delta\gamma_{xy_1}(t_1)+G(t-t_2)\,\Delta\gamma_{xy_2}(t_2)+G(t-t_3)\,\Delta\gamma_{xy_3}(t_3)+\ldots \tag{5.5}$$

or

$$\tau_{xy}(t)=\sum_{i=1}^{n}G(t-t_i)\,\Delta\gamma_{xy_i}(t_i) \tag{5.6}$$

where $t > t_n$. For very small strain intervals that lead to a continuous strain function we can write the above sum in integral form

$$\tau_{xy}(t)=\int_{-\infty}^{t}G(t-t')\,\mathrm{d}\gamma_{xy}(t') \tag{5.7}$$

which can be written in terms of strain rate as

$$\tau(t) = \int_{-\infty}^{t} G(t - t')\,\dot{\gamma}_{xy}(t')\,\mathrm{d}t' \tag{5.8}$$

which in turn can be written in terms of compliance

$$\tau_{xy}(t) = \int_{-\infty}^{t} J(t - t')\,\dot{\tau}_{xy}(t')\,\mathrm{d}t' \tag{5.9}$$

In the case that the polymer component is stress-free at $t = 0$, we can write

$$\tau_{xy}(t) = \int_{0}^{t} G(t - t')\,\dot{\gamma}_{xy}(t')\,\mathrm{d}t' \tag{5.10}$$

Which, for systems with complex three-dimensional stress and strain fields, can be written in tensor form as

$$\underline{\underline{\tau}}(t) = \int_{0}^{t} G(t - t')\,\underline{\underline{\dot{\gamma}}}(t')\,\mathrm{d}t' \tag{5.11}$$

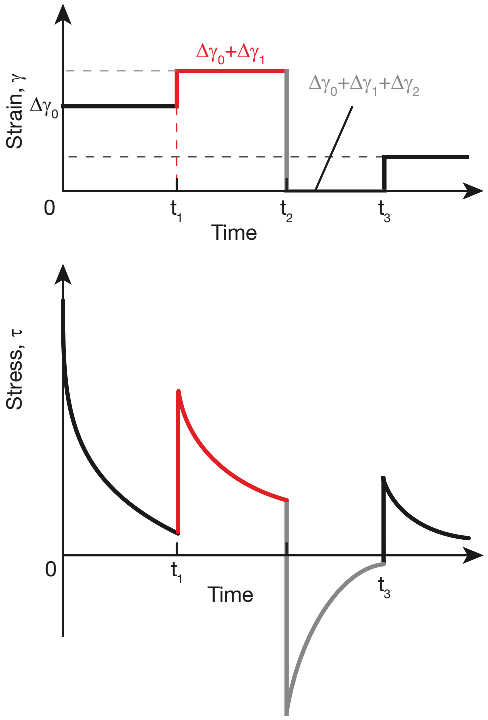

Figure 5.2 Schematic demonstration of Boltzmann's superposition principle

5.1.3 The Maxwell Model – Relaxation

A stress relaxation test consists of monitoring the time-dependent shear stress, τ_{xy}, resulting from a constant shear strain, γ_{xy}. The model to describe the stress relaxation of polymers is the Maxwell model already described in Chapter 1. The spring should be visualized as representing the elastic or energy storage component of the response, while the dashpot represents the conformational, loss or entropic component. Using this model, schematically depicted in Fig. 5.3, only the spring deforms initially, something that in the model happens instantaneously. This is followed by the time-dependent response of the dash-pot, which deforms under the same constant strain. The deformation within the spring is transferred to the dashpot as the stress relaxes to zero; the deformation of the dash-pot is irreversible and leads to a loss of energy.

For a constant strain, the stress is represented by

$$\tau_{xy} = G\gamma_{xy}\,\mathrm{e}^{-\frac{t}{\lambda}} = \left(G\,\mathrm{e}^{-\frac{t}{\lambda}}\right)\gamma_{xy} = G(t)\,\gamma_{xy} \tag{5.12}$$

which in turn can be represented in integral form, using the Boltzmann superposition principle

$$\tau_{xy}(t) = \int_0^t G\,\mathrm{e}^{-\frac{t-t'}{\lambda}}\,\dot{\gamma}_{xy}(t')\,\mathrm{d}t' \tag{5.13}$$

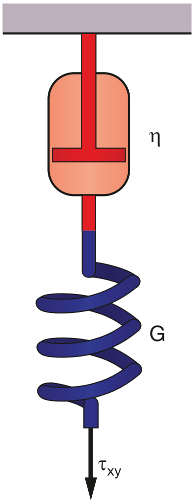

Figure 5.3 Schematic diagram of the Maxwell model

5.1.4 Kelvin Model

Depending on the time scale, the Maxwell model can emulate solids (short time scales) as well as liquids (long time scales), while the Kelvin model can only be used to model viscoelastic solids. The Kelvin model, sometimes also called the Kelvin-Voigt model, is shown in Fig. 5.4. It is the simplest model that can be used to represent the behavior of a solid polymer component at the beginning of loading.

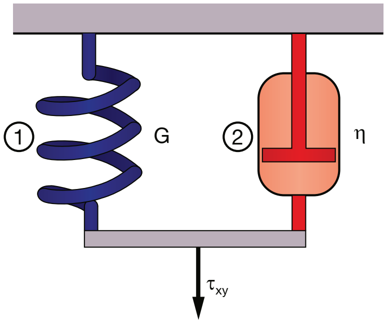

Figure 5.4 Schematic diagram of the Kelvin model

The momentum balance for the Kelvin model is stated as

$$\tau_{xy} = \tau_{xy_1} + \tau_{xy_2} \tag{5.14}$$

and the continuity equation is represented by

$$\gamma_{xy} = \gamma_{xy_1} = \gamma_{xy_2} \tag{5.15}$$

Using Eq. 5.15 with the constitutive relations $\tau_{xy_1} = G\gamma_{xy}$ for the spring, and $\tau_{xy_2} = \eta\dot{\gamma}_{xy}$, for the dashpot, the governing equation, Eq. 5.14, can be rewritten as

$$\tau_{xy} = G\gamma_{xy} + \eta\dot{\gamma}_{xy} \tag{5.16}$$

Using Eq. 5.16, in the Kelvin model, and replacing the ratio (η/G) by λ, the strain in a creep test with constant load τ_0 can be determined by

$$\gamma_{xy}(t) = \frac{\tau_0}{G}\left(1 - \mathrm{e}^{-t/\lambda}\right) \tag{5.17}$$

where λ is the relaxation time. The creep modulus is therefore

$$G_\mathrm{c}(t) = \frac{G}{\left(1 - \mathrm{e}^{-t/\lambda}\right)} \tag{5.18}$$

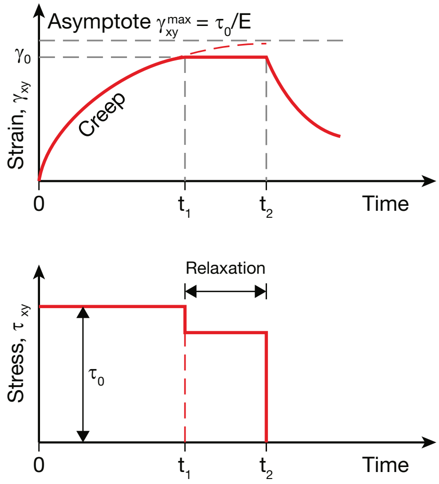

Figure 5.5 Creep, relaxation, and recovery response in the Kelvin model

The creep response of the Kelvin model is shown in Fig. 5.5. Eventually, a maximum strain γ_{xy}^{max} is reached. However, if a constant strain γ_0 is maintained in a Kelvin model, the stress does not relax and remains constant at

$$\tau_{xy} = G\gamma_0 \tag{5.19}$$

In Fig. 5.5, the creep test is stopped at γ_0 before reaching γ_{xy}^{max}, which causes the stress to drop somewhat.

Because the stresses do not relax in a Kelvin model, the full shape of the original component or specimen can be recovered. The strain recovery response can be written as

$$\gamma_{xy}(t) = \gamma_0 \, e^{-t/\lambda} \tag{5.20}$$

and is shown in Fig. 5.5.

We can also consider the response of a Kelvin model subjected to a sinusoidal strain given by

$$\gamma_{xy}(t) = \gamma_0 \sin(\omega t) \tag{5.21}$$

where γ_0 is the strain amplitude and ω is the frequency. Differentiating Eq. 5.21 and substituting into Eq. 5.16 results in

$$\tau_{xy}(t) = G\gamma_0 \sin(\omega t) + \eta\omega\gamma_0 \cos(\omega t) \tag{5.22}$$

Dividing Eq. 5.22 by the strain amplitude results in the *complex modulus*. For the Kelvin model, the two components of the complex modulus are

$$G' = G \tag{5.23}$$

which represents the *storage modulus* and

$$G'' = \eta\omega \tag{5.24}$$

which represents the *loss modulus*. Tests with a sinusoidal strain input, also referred to as the *dynamic tests*, will be discussed in more detail in Section 5.1.8.

5.1.5 Jeffrey's Model

As shown in Fig. 5.6, the Jeffrey model is a Kelvin model with a dashpot. This extra feature ensures that the missing long-term creep behavior is represented in the Kelvin model.

The momentum balance of the Jeffrey model is represented by two equations as

$$\tau_{xy} = \tau_{xy_3} \quad \text{and} \tag{5.25}$$

$$\tau_{xy} = \tau_{xy_1} + \tau_{xy_2} \tag{5.26}$$

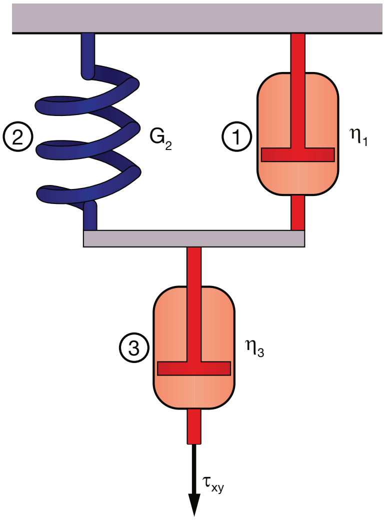

Figure 5.6 Schematic diagram of the Jeffrey model

as is the continuity equation by

$$\gamma_{xy_1} = \gamma_{xy_2} \quad \text{and} \tag{5.27}$$

$$\gamma_{xy} = \gamma_{xy_2} + \gamma_{xy_3} \tag{5.28}$$

Combining Eq. 5.25 with 5.28 and applying the constitutive equations gives

$$\tau_{xy} + \left(\frac{\eta_1 + \eta_3}{G_2}\right)\dot{\tau}_{xy} = \eta_3\,\dot{\gamma}_{xy} + \left(\frac{\eta_3\,\eta_1}{G_2}\right)\ddot{\gamma}_{xy} \tag{5.29}$$

which is sometimes written as

$$\tau_{xy} + \lambda_1\,\dot{\tau}_{xy} = \eta_0\left(\dot{\gamma}_{xy} + \lambda_2\,\ddot{\gamma}_{xy}\right) \tag{5.30}$$

Using Eq. 5.30, the strain in a creep test in the Jeffrey model can be solved for as

$$\gamma_{xy}(t) = \frac{\tau_0}{G}\left(1 - \mathrm{e}^{-t/\lambda_2}\right) + \frac{\tau_0}{\eta_0}\,t \tag{5.31}$$

which is depicted in Fig. 5.7. The creep modulus of the Jeffrey model is written as

$$G_{\mathrm{c}}(t) = \left[\frac{\left(1 - \mathrm{e}^{-t/\lambda_2}\right)}{G} + \frac{t}{\eta_3}\right]^{-1} \tag{5.32}$$

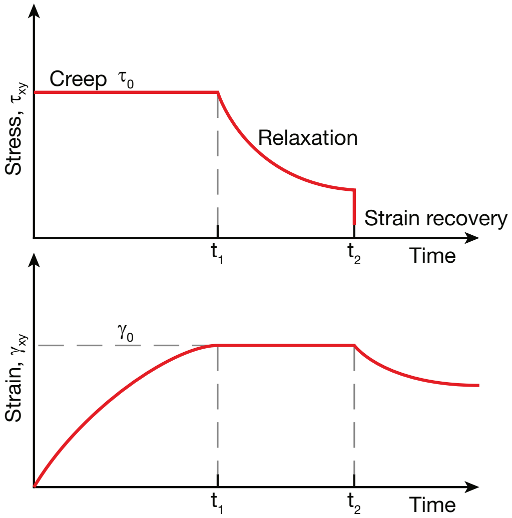

Figure 5.7 Creep, relaxation, and recovery response in the Jeffrey model

The stress relaxation of the Jeffrey model is derived from the governing equation, Eq. 5.30 as

$$\tau_{xy} = \tau_0 \, e^{-t/\lambda_1} \tag{5.33}$$

and is also represented in Fig. 5.7.

The unrelaxed stress is recovered in the same way as in the Kelvin model

$$\gamma_{xy}(t) = \gamma_0 \, e^{-t/\lambda} \tag{5.34}$$

5.1.6 Standard Linear Solid Model

The standard linear solid model, shown in Fig. 5.8, is a commonly used model to simulate the short-term behavior of solid polymer components. The momentum balance of the standard linear solid model is expressed with two equations as

$$\tau_{xy} = \tau_{xy_1} + \tau_{xy_2} \tag{5.35}$$

and

$$\tau_{xy_1} = \tau_{xy_3} \tag{5.36}$$

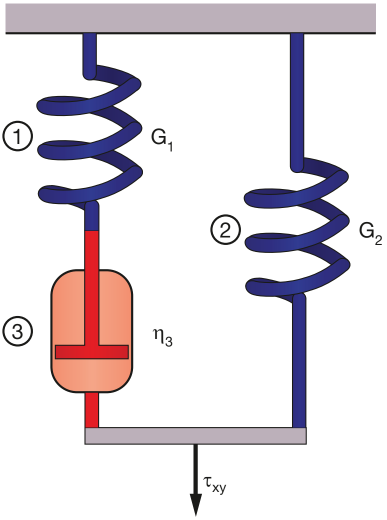

Figure 5.8 Schematic diagram of the standard linear solid model

Continuity and deformation are represented by

$$\gamma_{xy} = \gamma_{xy_1} + \gamma_{xy_3} \tag{5.37}$$

and

$$\gamma_{xy} = \gamma_{xy_2} \tag{5.38}$$

When we combine Eqs. 5.35 to 5.38 and use the constitutive equations for the spring and dashpot elements, we get the governing equation for the standard linear solid model:

$$\eta \dot{\tau}_{xy} + G_1 \tau_{xy} = \eta \left(G_1 + G_2\right) \dot{\gamma}_{xy} + G_1 G_2 \gamma_{xy} \tag{5.39}$$

Using Eq. 5.39, the strain in a creep test in the standard linear solid model can be solved for as

$$\gamma_{xy} = \frac{\tau_0}{G_2} + \left(\frac{\tau_0}{G_1 + G_2} - \frac{\tau_0}{G_2}\right) \mathrm{e}^{-\left[G_1 G_2 / \eta \left(G_1 + G_2\right)\right] t} \tag{5.40}$$

which is plotted in Fig. 5.9.

The stress relaxation in the standard linear solid model can be derived by integrating Eq. 5.39 and is represented by

$$\tau_{xy} = \gamma_0 \left(G_2 + G_1\right) \mathrm{e}^{-\left(G_1/\eta\right) t} \tag{5.41}$$

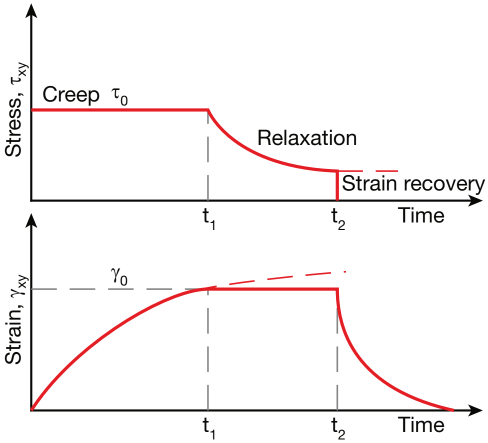

Figure 5.9 Creep, relaxation, and recovery response in the standard linear solid model

5.1.7 The Generalized Maxwell Model

The generalized Maxwell model, also known as the Maxwell-Wiechert model, shown in Fig. 5.10, is a generalized model that consists of an arbitrary number of Maxwell models connected in parallel, allowing to simulate more accurately to fit experimentally generated mechanical behavior.

The momentum balance in the i^{th} Maxwell element of the Maxwell-Wiechert model is expressed as

$$\tau_{xy_1} = \tau_{xy_{i1}} = \tau_{xy_{i2}} \tag{5.42}$$

and the full momentum balance for a model with n elements is written as

$$\tau_{xy} = \sum_{i=1}^{n} \tau_{xy_i} \tag{5.43}$$

Continuity or deformation for the i^{th} Maxwell element is expressed as

$$\gamma_{xy_i} = \gamma_{xy_{i1}} + \gamma_{xy_{i2}} \tag{5.44}$$

and for the full model

$$\gamma_{xy} = \gamma_{xy_1} = \gamma_{xy_2} = \gamma_{xy_i} \cdots \tag{5.45}$$

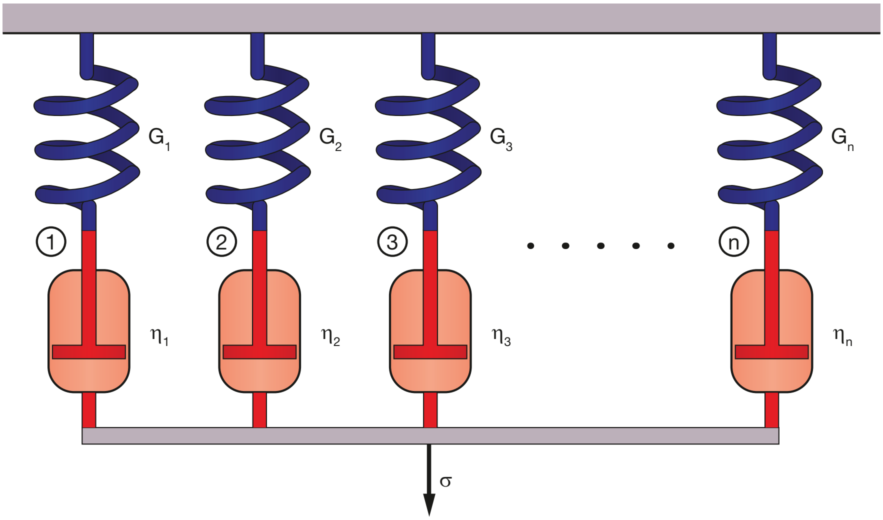

Figure 5.10 Schematic diagram of the Maxwell-Wiechert model

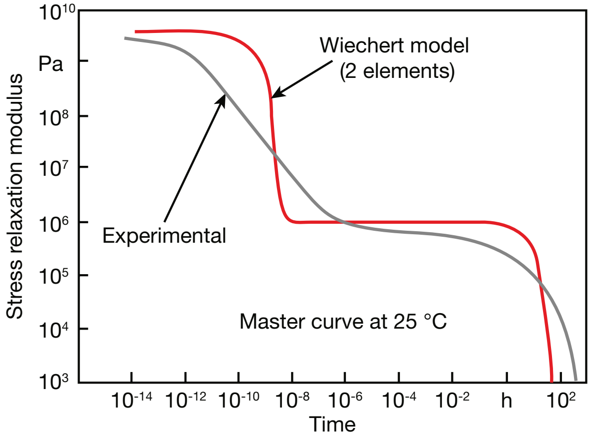

Figure 5.11 Comparison of the experimental stress relaxation for polyisobutylene with a two-component Maxwell-Wiechert model response

The governing equation for the Maxwell-Wiechert model is written as

$$\dot{\gamma}_{xy} = \frac{\dot{\tau}_{xy_i}}{G_i} + \frac{\tau_{xy_i}}{\eta_i} \tag{5.46}$$

The stress relaxation of the Maxwell-Wiechert model can be derived by integrating Eq. 5.46 and substituting the resulting stress into Eq. 5.43. Dividing by the applied strain ε_0 results in an expression for the relaxation model that is written as

$$G(t) = \sum_{i=1}^{n} G_i \, \mathrm{e}^{-(1/\lambda_i)\,t} \tag{5.47}$$

It represents a model with n relaxation times and where $\lambda_i = \eta_i / G_i$.

As an example, we can approximate the relaxation behavior of polyisobutylene by using a Maxwell-Wiechert model having two Maxwell elements with $\lambda_1 = 10^{-8}$ h and $\lambda_2 = 100$ h, and $G_1 = 3 \times 10^9$ Pa and $G_2 = 10^6$ Pa. Figure 5.11 compares the experimental relaxation modulus with the model. It shows that although there are big differences between the two curves, the model with its two relaxation times does, at least qualitatively, represent the experimental values.

For a better fit with experimental data[1] it is common to use several spring-dash pot models in parallel, such as shown in Fig. 5.12 [2]. The curve shown in the figure fits a four-parameter model with experimental relaxation and retardation data for a common polystyrene with a molecular weight of 260,000 g/mole. For this specific

---

[1] Note that the experiments are extensional, that is, ε instead of γ_{xy}.

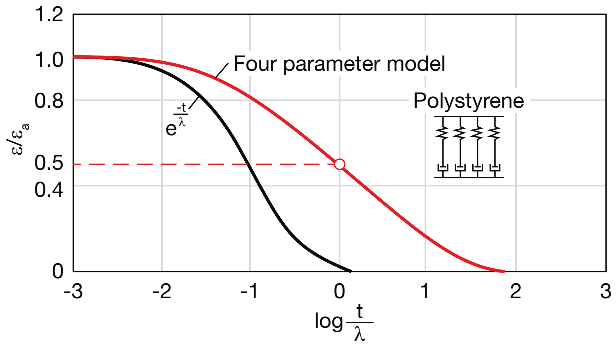

Figure 5.12 Relaxation response of a Maxwell model and a four-parameter Maxwell model

material, the relaxation behavior of the injected melt into a hot cavity, at a reference temperature of 113 °C, is described by

$$\frac{\varepsilon}{\varepsilon_a} = 0.25\left(e^{-8.75t/\lambda} + e^{-1.0t/\lambda} + e^{-0.28t/\lambda} + e^{-0.0583t/\lambda}\right) \tag{5.48}$$

where ε_a is the strain after relaxation defined by

$$\varepsilon_a = \frac{l_a - l_0}{l_0} = \frac{S_0}{1 - S_0} \tag{5.49}$$

Here, l_a and l_0 represent the length of the stretched and relaxed sample, respectively, and S_0 represents the total shrinkage.

The terms $\frac{\lambda}{8.75}, \lambda, \frac{\lambda}{0.28}, \frac{\lambda}{0.0583}$ in Eq. 5.48 represent four individual relaxation times for this specific polystyrene, modeled using the four-parameter model. The relaxation time, λ, correlates with the time it takes for the initial strain to reduce, by relaxation, to one-half of its initial value. This relaxation time is also temperature dependent, as shown for various polymers in Fig. 5.13. Figure 5.13 shows how the shapes of the curves are all similar, but shifted by a certain temperature. It is important to note that the relaxation and retardation behavior of all amorphous thermoplastics is similar.

Wübken [2] performed similar tests with different amorphous thermoplastics, and he found that, indeed, in all cases the measurements showed a correlation between time and temperature such as described by the WLF equation [3]. The data fit by the four-parameter model was generated via two different experiments: a relaxation test inside an injection mold between 100 and 180 °C, and a retardation test outside of the mold between 72 and 100 °C. The measured data are shown in Figs. 5.14 and 5.15 for the relaxation and retardation tests, respectively. The curves shown in both

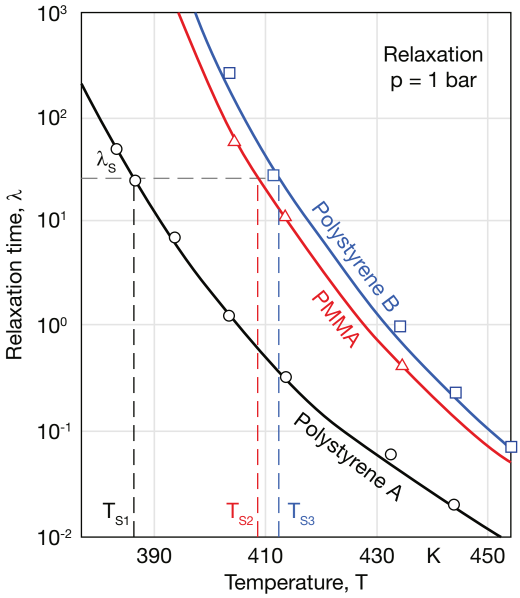

Figure 5.13 Relaxation time as a function of temperature for various thermoplastics

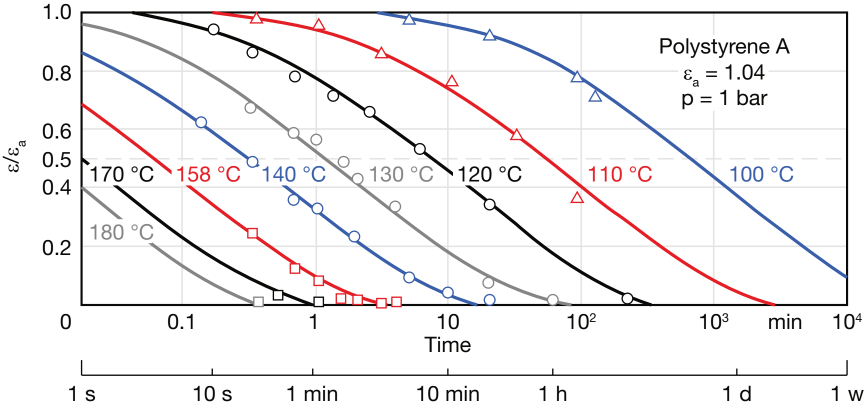

Figure 5.14 Relaxation response, inside an injection mold, of a polystyrene specimen at various temperatures

graphs were shifted horizontally to generate one master curve as shown in Fig. 5.16. The solid line in the figure is the four-parameter fit represented by Eq. 5.48.

Hence, appropriate T_{ref} and λ values must be found. However, the reference temperature is not quite independent of the relaxation behavior of the polymer, but rather related to the material properties. For the polystyrene A in Fig. 5.17, T_{ref} = 113 °C, or about 48 °C above T_g. For example, for the polystyrene A of Fig. 5.17, the relaxation time, λ, can be computed by

Relaxation: $$\log(\lambda)=\log(27)-\frac{8.86\left(T-T_s\right)}{101.6+\left(T-T_s\right)} \tag{5.50}$$

Creep: $$\log(\lambda)=\log(0.0018)-\frac{8.86\left(T-T_s\right)}{101.6+\left(T-T_s\right)} \tag{5.51}$$

where the constants 27 and 0.0018 are the relaxation times, λ, in minutes, at the reference temperature of 113 °C.

As discussed in Chapter 2, similar to the temperature induced shift, there is also a shift caused by pressure. Figure 5.18 shows the influence of pressure on T_g, and we can see that this effect can easily be incorporated into the WLF equation, i.e., there is approximately a 2 °C shift in the glass transition temperature of polystyrene for every 100 bar of pressure increase [4].

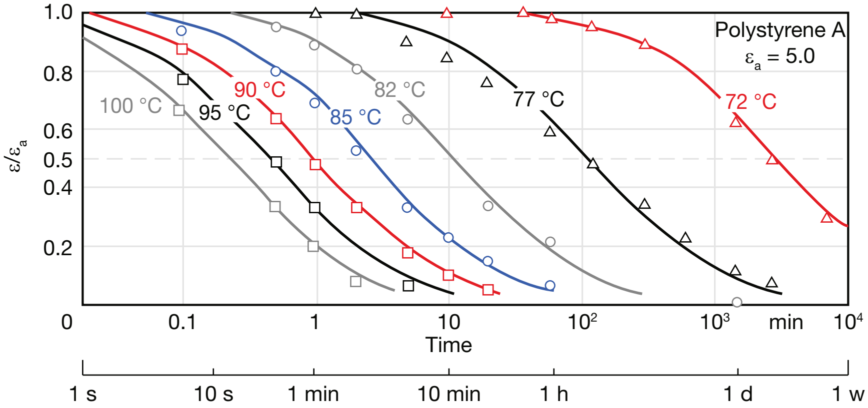

Figure 5.15 Recovery or retardation response after injection molding of a polystyrene specimen at various temperatures

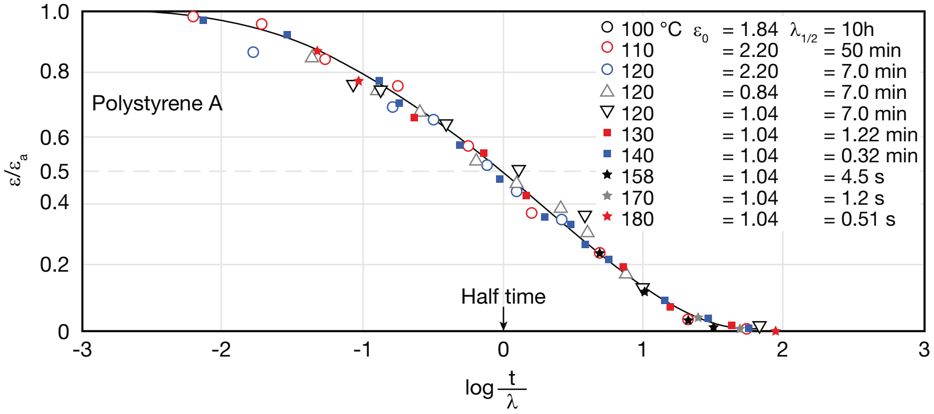

Figure 5.16 Master curve for the relaxation response, inside an injection mold, of a polystyrene specimen at various temperatures

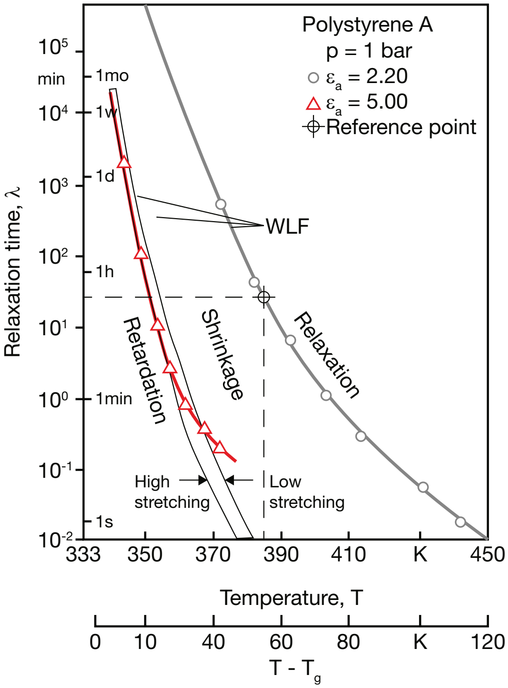

Figure 5.17 Relaxation and retardation times as a function of temperature for a polystyrene

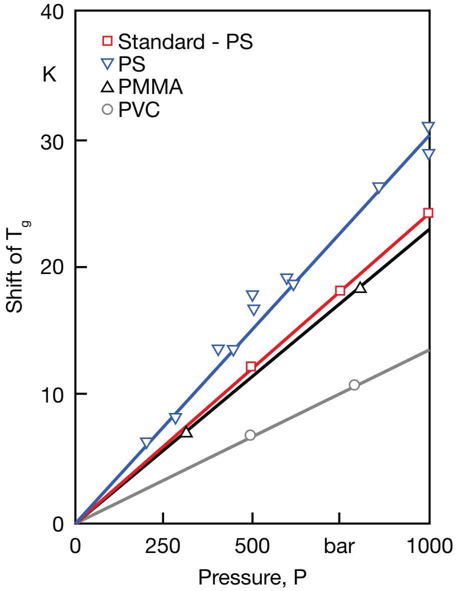

Figure 5.18 Influence of hydrostatic pressure on the glass transition temperature for various amorphous thermoplastics

5.1.8 Dynamic Tests

Stress relaxation and creep or stress retardation tests are convenient to study material responses to long-term loads (minutes to days), but less accurate for short-term loads (seconds and less). Dynamic tests, in which the stress (or strain) resulting from a sinusoidal strain (or stress) is measured are better tools to investigate the short time range of the polymer response. The most common test is in oscillation, which will be described in more detail here.

If the test specimen in a sinusoidal oscillatory test is perfectly elastic, the strain input and stress response would be as follows:

$$\gamma_{xy}(t) = \gamma_0 \sin \omega t \tag{5.52}$$

$$\tau_{xy}(t) = \tau_0 \sin \omega t \tag{5.53}$$

Taking the ratio of stress and strain gives the elastic shear modulus

$$G = \frac{\tau_0 \sin \omega t}{\gamma_0 \sin \omega t} = \frac{\tau_0}{\gamma_0} \tag{5.54}$$

For an ideally viscous test specimen, the stress response would lag $\pi/2$ radians behind the stress input:

$$\gamma_{xy}(t) = \gamma_0 \sin \omega t \tag{5.55}$$

$$\tau_{xy}(t) = \tau_0 \cos \omega t \tag{5.56}$$

$$\tau_{xy}(t) = \tau_0 \sin\left(\omega t + \frac{\pi}{2}\right) \tag{5.57}$$

Taking the ratio of stress and rate of deformation results in the viscosity

$$\eta = \frac{\tau_0 \cos \omega t}{\gamma_0\, \omega \cos \omega t} = \frac{\tau_0}{\dot{\gamma}_0} \tag{5.58}$$

On the other hand, polymers behave somewhere between the perfectly elastic and the perfectly viscous materials. When they are subjected to a sinusoidal varying stress, a steady state will eventually be reached in which the resulting strain is also sinusoidal, having the same angular frequency but retarded in phase by an angle δ; this is analogous to the delayed strain observed in creep experiments. The stress lags the strain by the phase angle, and this is true even if the stress rather than the strain is the controlled variable. This relation is described by

$$\gamma_{xy}(t) = \gamma_0 \sin \omega t \tag{5.59}$$

$$\tau_{xy}(t) = \tau_0 \sin(\omega t + \delta) \tag{5.60}$$

The shear modulus takes a complex form of

$$G^* = \frac{\tau_{xy}(t)}{\gamma_{xy}(t)} = \frac{\tau_0 \, e^{i\delta}}{\gamma_0} = \frac{\tau_0}{\gamma_0}(\cos\delta + i \sin\delta) = G' + iG'' \tag{5.61}$$

which is graphically represented in Fig. 5.19. G' is usually referred to as *storage modulus* and G'' as *loss modulus*. The ratio of loss modulus to storage modulus is referred to as *loss tangent*:

$$\tan\delta = \frac{G''}{G'} \tag{5.62}$$

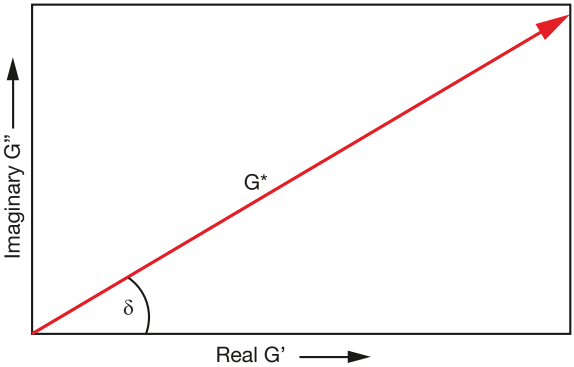

Figure 5.19 Vector representation of the complex shear modulus

Linear viscoelastic models, such as the Maxwell model, can also be used to model the dynamic response of polymers. Using the above oscillatory test in conjunction with the Maxwell model we obtain

$$\tau_{xy} = \left[\frac{G\gamma_0 \omega\lambda}{1+(\omega\lambda)^2}\right]\left[\omega\lambda \sin(\omega t) + \cos(\omega t)\right] \tag{5.63}$$

for a steady state response. Dividing Eq. 5.63 by the amplitude of the strain input results in a complex modulus, which is formed by an elastic component that is in-phase with the strain input and a viscous component. The elastic term is the *storage modulus* and is defined by

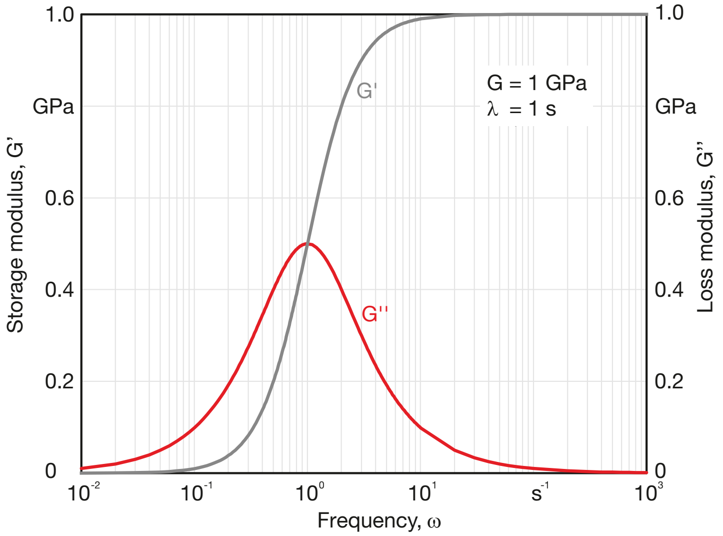

Figure 5.20 Storage modulus and loss modulus of a Maxwell model as a function of frequency

$$G' = \left[\frac{G(\omega\lambda)^2}{1+(\omega\lambda)^2}\right] \tag{5.64}$$

and the viscous term is the *loss modulus*, and is given by

$$G'' = \left[\frac{G\omega\lambda}{1+(\omega\lambda)^2}\right] \tag{5.65}$$

Figure 5.20 presents the storage and loss moduli as a function of frequency for the special case where $\lambda = 1$ s and $G = 1$ GPa, both typical values for polymer melts and solids, respectively. As the graph shows, at low frequencies, representing large time scales, the material responds like a perfect viscous fluid. However, at high frequencies, representing small time scales, the material responds like a perfect Hookean solid. Between these extremes, the material behaves like a viscoelastic material. The point where the loss modulus reaches a maximum represents the frequency at which the test temperature corresponds to the glass transition temperature of the polymer. The point where the loss modulus and the storage modulus cross each other (which for the Maxwell model is the same as the glass transition temperature) is where the test temperature corresponds to the *softening temperature* of the polymer. At frequencies below this crossing point, the material is a viscoelastic liquid. Above these frequencies the material is a viscoelastic solid. For actual material responses, the frequency at which the material undergoes softening is below the frequency at which the material experiences its glass transition, as shown for polyisobutylene in Fig. 5.21 [5].

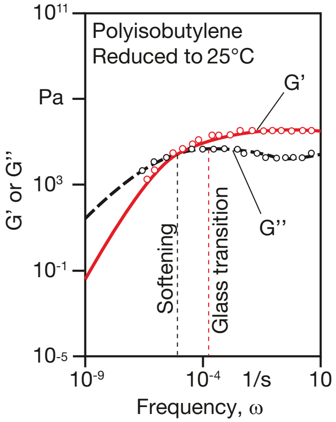

Figure 5.21 Storage modulus and loss modulus for polyisobutylene as a function of frequency

We can also consider the response of a Maxwell-Wiechert model subjected to a sinusoidal strain given by Eq. 5.59. In a similar analysis to that presented for the Kelvin and the Maxwell model, the *storage modulus* is given by

$$G' = \sum_{i=1}^{n} \left[\frac{G_i \left(\omega_i \lambda_i\right)^2}{1 + \left(\omega_i \lambda_i\right)^2} \right] \tag{5.66}$$

and the viscous term or the *loss modulus*, is given by

$$G'' = \sum_{i=1}^{n} \left[\left(\frac{G_i \, \omega_i \, \lambda_i}{1 + \left(\omega_i \lambda_i\right)^2} \right) \right] \tag{5.67}$$

A common way to present the results of dynamic tests is to plot the stress response as a function of strain input. Such diagrams are referred to as Lissajous curves. Figure 5.22 presents normalized Lissajous curves at various frequencies of a Maxwell model. Here, a perfect circle represents a Newtonian fluid and a straight line a perfect Hookean solid.

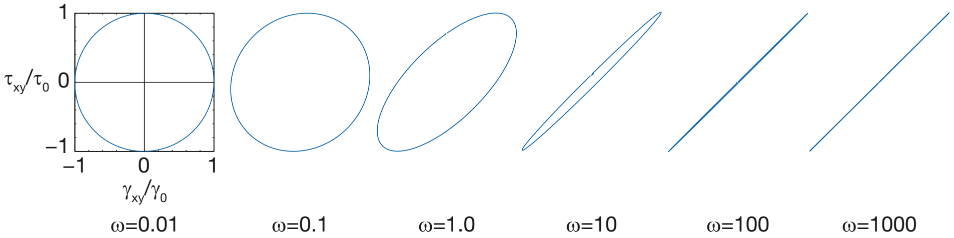

Figure 5.22 Normalized Lissajous curves of a Maxwell model for various frequencies with G = 1 GPa and λ = 1 s.

5.2 Non-Linear Viscoelasticity

As mentioned earlier, a non-linear viscoelastic response in a polymer occurs when the deformation or the rate of deformation is large. In the course of polymer processing operations, large deformations are always imposed on the material, requiring the use of non-linear viscoelastic models.

5.2.1 Objectivity

Before we begin to present non-linear viscoelastic models, we must first introduce the term “objectivity”. A system of equations or a constitutive model is called *objective* when it does not depend on the coordinate system’s movement and orientation. For example, the force exerted on an elastic spring depends on the amount of stretching and its stiffness, but not on the orientation of the spring’s principal axis, such as illustrated in Fig. 5.23.

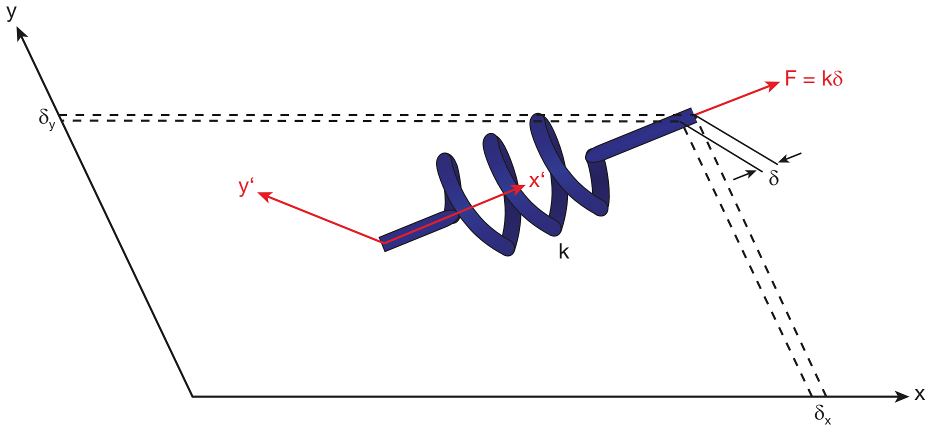

Figure 5.23 Objective spring system

In order to illustrate a non-objective rheological model, let us consider the tensor form of Maxwell’s linear viscoelastic model presented in Chapter 1

$$\underline{\underline{\tau}} + \lambda \frac{\partial}{\partial t} \underline{\underline{\tau}} = -\eta_0 \underline{\underline{\dot{\gamma}}} \tag{5.68}$$

and the experimental set-up depicted in Fig. 5.24. The experiment is composed of a simple shear flow set-up mounted on a rotating disc. The simple shear flow domain has its own coordinate system $x'y'$ that rotates with the disc at an angular speed ω. Within the $x'y'$ coordinate system we can represent the flow field using

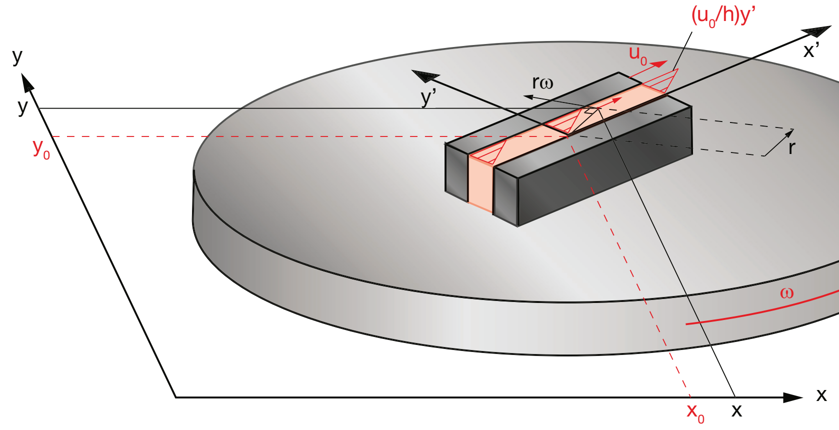

Figure 5.24 Simple shear flow on a rotating disc

$$u\left(y'\right)=\frac{u_0}{h}\,y' \tag{5.69}$$

and the velocity that results from rotation as

$$U=r\,\omega \tag{5.70}$$

Assuming that at $t = 0$ the orientation of the $x'y'$ coordinate system is aligned with the xy coordinate system, we can relate the local $x'y'$ and the global xy coordinates using

$$\begin{pmatrix} x' \\ y' \end{pmatrix}=\begin{pmatrix} \cos\omega t & \sin\omega t \\ -\sin\omega t & \cos\omega t \end{pmatrix}\begin{pmatrix} x-x_0 \\ y-y_0 \end{pmatrix} \tag{5.71}$$

Hence, an observer sitting on the global coordinate system will see a flow field represented by the velocity components

$$\begin{aligned} u_x &=\frac{u_0}{h}\left[-\sin\omega t\cos\omega t\left(x-x_0\right)+\cos^2\omega t\left(y-y_0\right)\right]-\omega\left(y-y_0\right) \\ u_y &=\frac{u_0}{h}\left[-\sin^2\omega t\left(x-x_0\right)+\cos\omega t\sin\omega t\left(y-y_0\right)\right]-\omega\left(x-x_0\right) \end{aligned} \tag{5.72}$$

Using this velocity field, the rate of deformation tensor becomes

$$\underline{\underline{\dot{\gamma}}}=\begin{pmatrix} -\sin 2\omega t & \cos 2\omega t & 0 \\ \cos 2\omega t & \sin 2\omega t & 0 \\ 0 & 0 & 0 \end{pmatrix}\frac{u_0}{h} \tag{5.73}$$

This shows that our rate of deformation tensor depends on the rotational speed of the frame of reference, and is therefore not objective.

Using the above rate of deformation tensor with a general form of the Maxwell model in integral form, we have

$$\underline{\underline{\tau}}(t)=\int_0^t G(t-t')\begin{bmatrix}-\sin 2\omega(t-t') & \cos 2\omega(t-t') & 0\\ \cos 2\omega(t-t') & \sin 2\omega(t-t') & 0\\ 0 & 0 & 0\end{bmatrix}\frac{u_0}{h}\,\mathrm{d}t' \tag{5.74}$$

and, because at $t = 0$ the $x'y'$ coordinate system is aligned with the xy coordinates, we get

$$\tau_{xy}=\int_0^t G(t')\cos 2\omega(t')\,\mathrm{d}t'\,\frac{u_0}{h}=\eta\frac{u_0}{h} \tag{5.75}$$

which means that the viscosity is represented by

$$\eta=\int_0^t G(t')\cos 2\omega(t')\,\mathrm{d}t' \tag{5.76}$$

Hence, according to the above equation, the viscosity depends on the rotational speed ω of the coordinate system $x'y'$, which we know cannot be true. Therefore, we find that the linear viscoelastic Maxwell model *is not objective*. In the following section, we introduce the corotational derivative that eliminates the above effect, making the models objective.

5.2.2 Differential Viscoelastic Models

There are two types of general, non-linear, viscoelastic flow models: the differential type and the integral type. In this chapter we will concentrate primarily on the differential models; however, the integral models will be introduced at the end.

Differential models have traditionally been the tool of choice to describe the viscoelastic behavior of polymers when simulating complex flow systems. Many differential viscoelastic models can be described in the general form

$$\begin{aligned}&Y\underline{\underline{\tau}}+\lambda_0\underline{\underline{\tau}}_{(0)}+\lambda_1\underline{\underline{\tau}}_{(1)}+\lambda_2\left[\underline{\underline{\dot{\gamma}}}\cdot\underline{\underline{\tau}}+\underline{\underline{\tau}}\cdot\underline{\underline{\dot{\gamma}}}\right]+\lambda_3\left[\underline{\underline{\tau}}\cdot\underline{\underline{\tau}}\right]\\&=\eta_0\left[\underline{\underline{\dot{\gamma}}}+\lambda_4\underline{\underline{\dot{\gamma}}}_{(0)}+\lambda_5\underline{\underline{\dot{\gamma}}}_{(1)}\right]\end{aligned} \tag{5.77}$$

where $\underline{\underline{\tau}}_{(0)}$ is the *corotational or Jaumann derivative* of the stress tensor defined by

$$\underline{\underline{\tau}}_{(0)} = \frac{\mathcal{D}}{\mathcal{D}t}\underline{\underline{\tau}} = \frac{\mathrm{D}}{\mathrm{D}t}\underline{\underline{\tau}} + \frac{1}{2}\left\{\underline{\underline{\omega}}\cdot\underline{\underline{\tau}} - \underline{\underline{\tau}}\cdot\underline{\underline{\omega}}\right\} \tag{5.78}$$

and $\mathrm{D}\underline{\underline{\tau}}/\mathrm{D}t$ is the substantial derivative and $\underline{\underline{\omega}}$ is the vorticity tensor given by

$$\underline{\underline{\omega}} = \nabla\underline{u} - \left(\nabla\underline{u}\right)^{\dagger} \tag{5.79}$$

where $\nabla\underline{u}$ is the velocity gradient

$$\nabla\underline{u} = \begin{pmatrix} \dfrac{\partial u_x}{\partial x} & \dfrac{\partial u_y}{\partial x} & \dfrac{\partial u_z}{\partial x} \\ \dfrac{\partial u_x}{\partial y} & \dfrac{\partial u_y}{\partial y} & \dfrac{\partial u_z}{\partial y} \\ \dfrac{\partial u_x}{\partial z} & \dfrac{\partial u_y}{\partial z} & \dfrac{\partial u_z}{\partial z} \end{pmatrix} \tag{5.80}$$

and $\left(\nabla\underline{u}\right)^{\dagger}$ is the transpose of the velocity gradient. $\underline{\underline{\tau}}_{(1)}$ is the *first contravariant convected time derivative* of the deviatoric stress tensor and represents rates of change with respect to a convected coordinate system that moves and deforms with the fluid. The *convected derivative* of the deviatoric stress tensor is defined as

$$\underline{\underline{\tau}}_{(1)} = \frac{\mathrm{D}\underline{\underline{\tau}}}{\mathrm{D}t} - \left[\left(\nabla\underline{u}\right)^{\dagger}\cdot\underline{\underline{\tau}} + \underline{\underline{\tau}}\cdot\left(\nabla\underline{u}\right)\right] \tag{5.81}$$

and similarly, $\underline{\underline{\dot{\gamma}}}_{(0)}$ is the Jaumann derivative of the rate of deformation tensor and $\underline{\underline{\dot{\gamma}}}_{(1)}$ is the *first contravariant convected time derivative* of the rate of deformation tensor. The constants in Eq. 5.77 are defined in Table 5.1 for various viscoelastic models commonly used to simulate polymer flows. A review by Bird and Wiest [6] provides a more complete list of existing viscoelastic models.

The upper convective model and the White-Metzner model are very similar with the exception that the White-Metzner model incorporates the strain rate effects of the relaxation time and the viscosity. Both models provide a first order approximation to flows in which shear rate dependence and memory effects are important. However, both models predict zero second normal stress coefficients. The Giesekus model is molecular-based, non-linear in nature and describes the Power Law region for viscosity and both normal stress coefficients. The Phan-Thien-Tanner models are based on network theory and give non-linear stresses. Both the Giesekus and Phan-Thien-Tanner models have been successfully used to model complex flows.

Table 5.1 Definition of Constants in Eq. 5.77

Constitutive Models	Y	λ_0	λ_1	λ_2	λ_3	λ_4	λ_5
Generalized Newtonian	1	0	0	0	0	0	0
Upper convected Model	1	0	λ_1	0	0	0	0
Corotational Maxwell	1	λ_0	0	0	0	0	0
Convected Jeffrey's	1	0	λ_1	0	0	0	λ_5
Corotational Jeffrey's	1	λ_0	0	0	0	λ_4	0
White-Metzner	1	0	$\lambda_1(\dot{\gamma})$	0	0	0	0
Phan-Thien-Tanner-1	$e^{\left[-\varepsilon(\lambda/\eta_0)tr\tau\right]}$	0	λ	$\frac{\lambda\xi}{2}$	0	0	0
Phan-Thien-Tanner-2	$1-\varepsilon\left(\lambda/\eta_0\right)tr\tau$	0	λ	$\frac{\lambda\xi}{2}$	0	0	0
Giesekus	1	0	λ_1	0	0	$-(\alpha\lambda_1/\eta_0)$	0

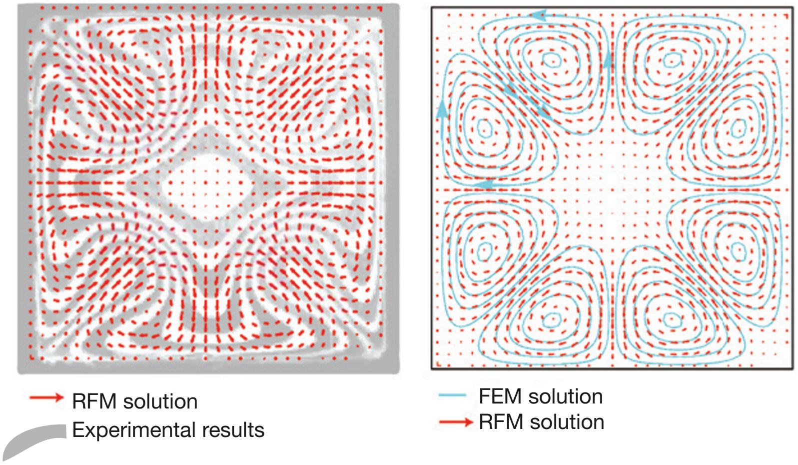

Figure 5.25 Polystyrene strand profile progression in a square die

An overview of numerical simulations of viscoelastic flow systems and an extensive literature review on the subject was given by Keunings [7], and details on numerical implementation of viscoelastic models are given by Crochet et al. [8] and Debbaut et al. [9]. As an example of the application of differential models to predict flow of polymeric liquids, it is worth mentioning work by Dietsche and Dooley [10], who evaluated the White-Metzner, the Phan-Thien-Tanner-1, and the Giesekus models by comparing finite element[2] and experimental results of the flow inside multi-layered coextrusion dies. Figure 5.25 [11] presents the progression of a matrix of colored

---

[2] For their simulation they used the commercially available code POLYFLOW.

circular polystyrene strands flowing in an identical polystyrene matrix down a channel with a square cross section of 0.95×0.95 cm. The cuts in the figure are shown at intervals of 7.6 cm.

The circulation pattern caused by the secondary normal stress differences inside non-circular dies were captured well by the Phan-Thien-Tanner and Giesekus models but, as expected, not by the White-Metzner model. Figure 5.26 presents flow patterns predicted by the Phan-Thien-Tanner model along with the experimental rearrangement of 165 initially horizontal layers of polystyrene in square, rectangular, and tear-drop shaped dies[3]. In all three cases, the shapes of the circulation patterns were predicted accurately. The flow simulation of the square die predicted a velocity on the order of 10 to 5 m/s along the diagonal of the cross section, which was in agreement with the experimental results. Also worth mentioning is work recently done by Baaijens [12], who evaluated the Phan-Thien-Tanner models 1 and 2, and the Giesekus model. He compared finite element results to measured isochromatic birefringence patterns using complex experiments with polymer melts and solutions. His simulation results predicted the general shape of the measured birefringence patterns. He found that at high Deborah numbers, the Phan-Thien-Tanner models converged much more easily than the Giesekus model.

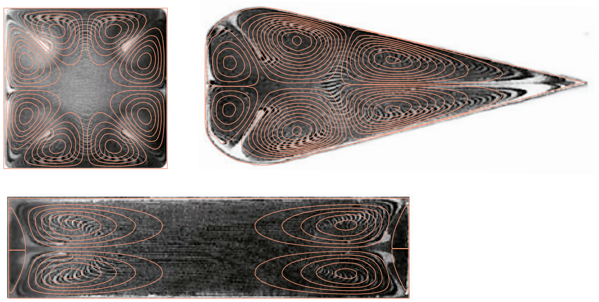

Figure 5.26 Comparison between experimental and predicted flow patterns of polystyrene in square, rectangular, and tear-drop shaped dies

Example 5.1 Corotational Maxwell Model (Simple Shear Flow)

Examine a simple shear flow using the corotational Maxwell model.

The corotational Maxwell model, extensively discussed by Bird et al. [13] and by Giacomin et al. [14], is obtained from the Maxwell model of linear viscoelasticity by replacing the partial time derivative $(\partial/\partial t)$ by the corotational or Jaumann derivative $(\mathcal{D}/\mathcal{D}t)$. This substitution ensures that the model is independent of the instantaneous orientation of the fluid element as it moves through space. The model is written as

---

[3] These geometries are typical for distribution manifolds used in sheeting dies.

$$\underline{\underline{\tau}} + \lambda_0 \frac{\mathcal{D}}{\mathcal{D}t}\underline{\underline{\tau}} = -\eta_0\,\underline{\underline{\dot{\gamma}}} \tag{5.82}$$

To model simple shear flow using the corotational Maxwell model, the velocity gradient of the velocity vector can be defined using

$$\nabla\underline{u} = \begin{pmatrix} 0 & 0 & 0 \\ 1 & 0 & 0 \\ 0 & 0 & 0 \end{pmatrix}(u/h) \tag{5.83}$$

and the vorticity tensor using

$$\underline{\underline{\omega}} = \begin{pmatrix} 0 & -1 & 0 \\ 1 & 0 & 0 \\ 0 & 0 & 0 \end{pmatrix}(u/h) \tag{5.84}$$

For simple shear flows the stress tensor is represented by

$$\underline{\underline{\tau}} = \begin{pmatrix} \tau_{xx} & \tau_{yx} & 0 \\ \tau_{yx} & \tau_{yy} & 0 \\ 0 & 0 & \tau_{zz} \end{pmatrix} \tag{5.85}$$

Using Eqs. 5.84 and 5.85 we can write

$$\frac{1}{2}\left\{\underline{\underline{\omega}}\cdot\underline{\underline{\tau}} - \underline{\underline{\tau}}\cdot\underline{\underline{\omega}}\right\} = \frac{1}{2}\left\{\begin{matrix} -2\tau_{yx} & \tau_{xx}-\tau_{yy} & 0 \\ \tau_{xx}-\tau_{yy} & 2\tau_{yx} & 0 \\ 0 & 0 & 0 \end{matrix}\right\}(u/h) \tag{5.86}$$

For a symmetric stress tensor $\underline{\underline{\tau}}$ we can write

$$\frac{\mathrm{D}}{\mathrm{D}t}\underline{\underline{\tau}} = \frac{\partial}{\partial t}\underline{\underline{\tau}} + \underline{u}\cdot\nabla\underline{\underline{\tau}} \tag{5.87}$$

the corotational derivative of $\underline{\underline{\tau}}$ can be written as

$$\begin{aligned}\frac{\mathcal{D}}{\mathcal{D}t}\underline{\underline{\tau}} = {} & \frac{\partial}{\partial t}\begin{pmatrix} \tau_{xx} & \tau_{yx} & 0 \\ \tau_{yx} & \tau_{yy} & 0 \\ 0 & 0 & \tau_{zz} \end{pmatrix} + \left(u_x\frac{\partial}{\partial x} + u_y\frac{\partial}{\partial y} + u_z\frac{\partial}{dz}\right)\begin{pmatrix} \tau_{xx} & \tau_{yx} & 0 \\ \tau_{yx} & \tau_{yy} & 0 \\ 0 & 0 & \tau_{zz} \end{pmatrix} \\ & + \frac{1}{2}\left\{\begin{matrix} -2\tau_{yx} & \tau_{xx}-\tau_{yy} & 0 \\ \tau_{xx}-\tau_{yy} & 2\tau_{yx} & 0 \\ 0 & 0 & 0 \end{matrix}\right\}(u/h)\end{aligned} \tag{5.88}$$

In shear flow the velocity field is represented using

$$\begin{aligned} u_x &= (u/h)\, y \\ u_y &= 0 \\ u_z &= 0 \end{aligned} \tag{5.89}$$

and

$$\frac{\mathcal{D}}{\mathcal{D}t}\underline{\underline{\tau}} = \frac{\partial}{\partial t}\begin{pmatrix} \tau_{xx} & \tau_{yx} & 0 \\ \tau_{yx} & \tau_{yy} & 0 \\ 0 & 0 & \tau_{zz} \end{pmatrix} + (u/h)\, y\, \frac{\partial}{\partial x}\begin{pmatrix} \tau_{xx} & \tau_{yx} & 0 \\ \tau_{yx} & \tau_{yy} & 0 \\ 0 & 0 & \tau_{zz} \end{pmatrix} + \frac{1}{2}\left\{\begin{matrix} -2\tau_{yx} & \tau_{xx}-\tau_{yy} & 0 \\ \tau_{xx}-\tau_{yy} & 2\tau_{yx} & 0 \\ 0 & 0 & 0 \end{matrix}\right\}(u/h) \tag{5.90}$$

Since for simple shear flows the continuity equation reduces to $\mathrm{d}u_x/\mathrm{d}x = 0$, we can write

$$\frac{\mathrm{d}}{\mathrm{d}x}\underline{\underline{\tau}} = 0 \tag{5.91}$$

and the rate of deformation is defined by

$$\underline{\underline{\dot{\gamma}}} = \begin{pmatrix} 0 & 1 & 0 \\ 1 & 0 & 0 \\ 0 & 0 & 0 \end{pmatrix}(u/h) \tag{5.92}$$

we write

$$\begin{pmatrix} \tau_{xx} & \tau_{yx} & 0 \\ \tau_{yx} & \tau_{yy} & 0 \\ 0 & 0 & \tau_{zz} \end{pmatrix} + \lambda_0 \frac{\partial}{\partial t}\begin{pmatrix} \tau_{xx} & \tau_{yx} & 0 \\ \tau_{yx} & \tau_{yy} & 0 \\ 0 & 0 & \tau_{zz} \end{pmatrix} + \frac{1}{2}\lambda_0\,(u/h)\,\frac{1}{2}\left\{\begin{matrix} -\tau_{xy}-\tau_{yx} & -\tau_{yy}+\tau_{xx} & 0 \\ \tau_{xx}-\tau_{yy} & -\tau_{yx}+\tau_{xy} & 0 \\ 0 & 0 & 0 \end{matrix}\right\} = -\eta_0\begin{pmatrix} 0 & 1 & 0 \\ 1 & 0 & 0 \\ 0 & 0 & 0 \end{pmatrix}(u/h) \tag{5.93}$$

Substituting (u/h) by $\dot{\gamma}$, the corotational Maxwell model for steady-state simple shear flow becomes

$$\tau_{yx} + \frac{1}{2}\lambda_0\,\dot{\gamma}\left(\tau_{xx}-\tau_{yy}\right) = -\eta_0\,\dot{\gamma} \tag{5.94}$$

$$\tau_{xx} - \lambda_0 \dot{\gamma} \tau_{yx} = 0 \tag{5.95}$$

$$\tau_{yy} + \lambda_0 \dot{\gamma} \tau_{yx} = 0 \tag{5.96}$$

$$\tau_{zz} = 0 \tag{5.97}$$

Using Eqs. 5.95 and 5.96 to substitute the normal stresses in Eq. 5.94, we get

$$\tau_{yx} = \frac{\eta_0 \dot{\gamma}}{1 + \lambda_0^2 \dot{\gamma}^2} \tag{5.98}$$

$$\eta(\dot{\gamma}) \equiv \frac{-\tau_{yx}}{\dot{\gamma}} = \frac{\eta_0}{1 + \lambda_0^2 \dot{\gamma}^2} \tag{5.99}$$

Subtracting Eq. 5.96 from Eq. 5.95 results in

$$N_1 = 2\lambda_0 \dot{\gamma} \tau_{yx} \tag{5.100}$$

and substituting Eq. 5.102 into Eq. 5.105 we get

$$N_1 = \frac{-2\eta_0 \lambda_0 \dot{\gamma}^2}{1 + \lambda_0^2 \dot{\gamma}^2} \tag{5.101}$$

or

$$\Psi_1 = \frac{-2\eta_0 \lambda_0}{1 + \lambda_0^2 \dot{\gamma}^2} = 2\lambda_0 \eta(\dot{\gamma}) \tag{5.102}$$

From the above equations we can also say that

$$\Psi_2 = -0.5\Psi_1 \tag{5.103}$$

Hence, we can say that the corotational Maxwell model predicts a shear thinning viscosity with a Newtonian plateau. In addition, the model also exhibits a first and second normal stress difference. The second normal stress difference is about 5 times larger than what we encounter with polymer melts. Figures 5.27 and 5.28 present sample viscosity and first normal stress difference coefficient curves.

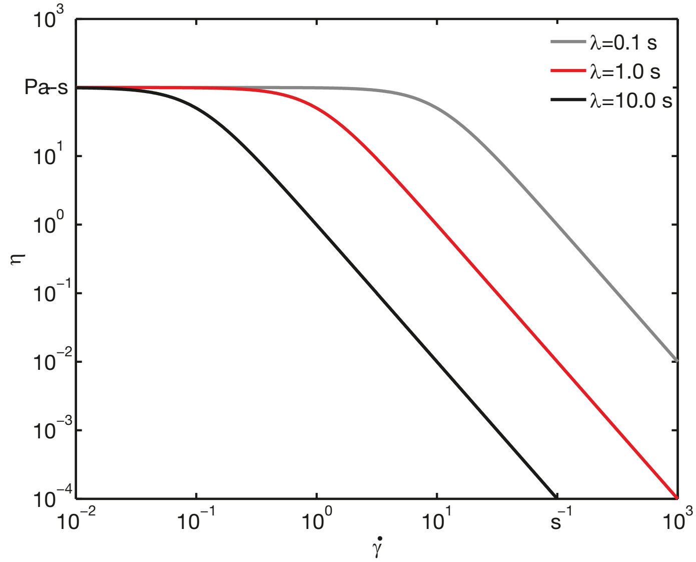

Figure 5.27 Viscosity as a function of rate of deformation for a corotational Maxwell model

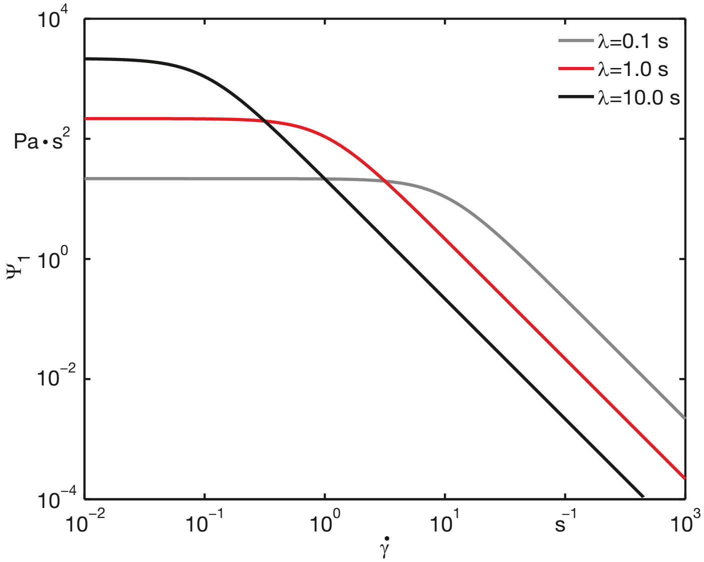

Figure 5.28 First normal stress coefficient as a function of rate of deformation for a corotational Maxwell model

Example 5.2 Corotational Maxwell Model (Elongational Flow)

Examine an elongational flow described in Fig. 3.13 using the corotational Maxwell model.

A typical elongational flow, or stretching flow, is encountered in fiber spinning processes. Other stretching flows exist in film blowing, blow molding, and thermoforming. These types of flows are also referred to as shear-free flows. The velocity gradient for an elongational flow, where stretching occurs in the *z*-direction, is

$$\nabla \underline{u} = \begin{pmatrix} -\frac{1}{2} & 0 & 0 \\ 0 & -\frac{1}{2} & 0 \\ 0 & 0 & 1 \end{pmatrix} \dot{\varepsilon}(t) \tag{5.104}$$

For an elongational flow, the vorticity tensor is

$$\underline{\underline{\omega}} = \nabla \underline{u} - (\nabla \underline{u})^{\dagger} = \underline{\underline{0}} \tag{5.105}$$

Therefore, the Jaumann derivative reduces to the substantial or material derivative

$$\frac{\mathrm{D}}{\mathrm{D}t}\underline{\underline{\tau}} = \frac{\partial}{\partial t}\underline{\underline{\tau}} + \underline{u} \cdot \nabla \underline{\underline{\tau}} \tag{5.106}$$

In Eq. 5.106 the stress tensor is given by

$$\underline{\underline{\tau}} = \begin{pmatrix} \tau_{xx} & 0 & 0 \\ 0 & \tau_{yy} & 0 \\ 0 & 0 & \tau_{zz} \end{pmatrix} \tag{5.107}$$

Thus, the substantial derivative is expanded as

$$\frac{\mathrm{D}}{\mathrm{D}t}\underline{\underline{\tau}} = \frac{\partial}{\partial t}\begin{pmatrix} \tau_{xx} & 0 & 0 \\ 0 & \tau_{yy} & 0 \\ 0 & 0 & \tau_{zz} \end{pmatrix} + \left(u_x \frac{\partial}{\partial x} + u_y \frac{\partial}{\partial y} + u_z \frac{\partial}{dz} \right)\begin{pmatrix} \tau_{xx} & 0 & 0 \\ 0 & \tau_{yy} & 0 \\ 0 & 0 & \tau_{zz} \end{pmatrix} \tag{5.108}$$

The kinematics of shear-free flows is defined by

$$\begin{aligned} u_x &= -\frac{1}{2}\dot{\varepsilon}(t)\, x \\ u_y &= -\frac{1}{2}\dot{\varepsilon}(t)\, y \\ u_z &= +\dot{\varepsilon}(t)\, z \end{aligned} \tag{5.109}$$

In a homogeneous flow field, the spatial derivatives of the stress tensor are all negligible because every fluid element is being subjected the same deformation

$$\begin{aligned}\frac{\partial \tau_{xx}}{\partial x} &= 0\\ \frac{\partial \tau_{yy}}{\partial y} &= 0\\ \frac{\partial \tau_{zz}}{\partial z} &= 0\end{aligned} \tag{5.110}$$

With the rate of deformation tensor defined by

$$\underline{\underline{\dot{\gamma}}} = \begin{pmatrix} -1 & 0 & 0 \\ 0 & -1 & 0 \\ 0 & 0 & 2 \end{pmatrix} \dot{\varepsilon}(t) \tag{5.111}$$

the corotational Maxwell model for a steady state elongational flow field is written as

$$\tau_{xx} = \eta_0\, \dot{\varepsilon} \tag{5.112}$$

$$\tau_{yy} = \eta_0\, \dot{\varepsilon} \tag{5.113}$$

$$\tau_{zz} = -2\eta_0\, \dot{\varepsilon} \tag{5.114}$$

When describing the two normal stress differences, one can define two independent viscosity functions. With the corotational Maxwell model, these functions are

$$\tau_{zz} - \tau_{xx} = -\eta_1\, \dot{\varepsilon} \tag{5.115}$$

$$\eta_1 = \frac{\tau_{xx} - \tau_{zz}}{\dot{\varepsilon}} \tag{5.116}$$

and

$$\tau_{yy} - \tau_{xx} = -\eta_2\, \dot{\varepsilon} \tag{5.117}$$

$$\eta_2 = \frac{\tau_{xx} - \tau_{yy}}{\dot{\varepsilon}} \tag{5.118}$$

Because $\tau_{xx} = \tau_{yy}$, we can write

$$\overline{\eta} = \eta_1 = 3\eta_0 \tag{5.119}$$

and

$$\eta_2 = 0 \tag{5.120}$$

Equation 5.120 shows how the corotational Maxwell model predicts extensional viscosity or "Trouton viscosity" of $3\eta_0$ [15].

Example 5.3 Corotational Maxwell Model (Small and large amplitude oscillatory shear)[4]

Develop normalized Lissajous curves for a corotational Maxwell model for various frequencies and deformations with $G = 1$ GPa and $\lambda = 1$ s using the corotational Maxwell model with a shear strain input of $\dot{\gamma}_{xy} = \dot{\gamma}^0 \cos\omega t$

Using a rate of deformation tensor represented by

$$\underline{\underline{\dot{\gamma}}} = \begin{bmatrix} 0 & 1 & 0 \\ 1 & 0 & 0 \\ 0 & 0 & 0 \end{bmatrix} \dot{\gamma}^0 \cos\omega t \tag{5.121}$$

and implementing it into the corotational Maxwell model, we can write

$$\tau_{yx} + \lambda \frac{\partial}{\partial t}\tau_{yx} + \frac{1}{2}\lambda\dot{\gamma}^0 \cos\omega t\left(\tau_{xx} - \tau_{yy}\right) = -\eta_0\dot{\gamma}^0 \cos\omega t \tag{5.122}$$

$$\tau_{xx} + \lambda \frac{\partial}{\partial t}\tau_{xx} - \tau_{yx}\lambda\dot{\gamma}^0 \cos\omega t = 0 \tag{5.123}$$

$$\tau_{yy} + \lambda \frac{\partial}{\partial t}\tau_{yy} - \tau_{yx}\lambda\dot{\gamma}^0 \cos\omega t = 0 \tag{5.124}$$

$$\tau_{zz} = 0 \tag{5.125}$$

Equation 5.122 can be rewritten as

$$\tau_{yx} + \lambda \frac{\partial}{\partial t}\tau_{yx} + \frac{1}{2}N_1\lambda\dot{\gamma}^0 \cos\omega t = -\eta_0\dot{\gamma}^0 \cos\omega t \tag{5.126}$$

Because all partial derivatives are with respect to time, we can rewrite the equation in dimensionless form as

---

[4] A full derivation is given in [14].

$$\frac{\tau_{yx}}{\eta_0\,\dot{\gamma}^0}+\frac{\lambda}{\eta_0\,\dot{\gamma}^0}\frac{\partial}{\partial t}\tau_{yx}+\frac{1}{2}N_1\frac{\lambda\dot{\gamma}^0}{\eta_0\,\dot{\gamma}^0}\cos\tau=-\frac{\eta_0\,\dot{\gamma}^0}{\eta_0\,\dot{\gamma}^0}\cos\tau \tag{5.127}$$

which can be written as

$$\mathbb{S}+De\frac{\partial}{\partial t}\mathbb{S}+\frac{1}{2}\mathbb{N}_1\,Wi\cos\tau=-\cos\tau \tag{5.128}$$

where the dimensionless terms are defined in Table 5.2. Similarly, subtracting Eq. 5.123 from Eq. 5.122 and writing in dimensionless form gives

$$\frac{N_1}{\eta_0\,\dot{\gamma}^0}+\frac{\lambda}{\eta_0\,\dot{\gamma}^0}\frac{\partial}{\partial t}N_1-\frac{2\tau_{yx}\,\lambda\dot{\gamma}^0}{\eta_0\,\dot{\gamma}^0}\cos\tau_{yx}=0 \tag{5.129}$$

$$\mathbb{N}_1+De\frac{\partial}{\partial t}\mathbb{N}_1-2\,\mathbb{S}\,We\cos\tau=0 \tag{5.130}$$

which can be solved for shear stress $\mathbb{S}$ as

$$\mathbb{S}=\frac{1}{2\,We\cos\tau}\left[\mathbb{N}_1+De\frac{\mathrm{d}}{\mathrm{d}\tau}\mathbb{N}_1\right] \tag{5.131}$$

Table 5.2 Dimensionless Variables and Groups

First Normal Stress Difference	$\mathbb{N}_1\overset{\text{def}}{=}\frac{N_1(t)}{\eta_0\,\dot{\gamma}^0}$
Second Normal Stress Difference	$\mathbb{N}_2\overset{\text{def}}{=}\frac{N_2(t)}{\eta_0\,\dot{\gamma}^0}$
Shear rate amplitude	$\dot{\gamma}^0$
Shear strain amplitude	$\gamma^0\overset{\text{def}}{=}\dot{\gamma}^0/\omega$
Shear Stress	$\mathbb{S}\overset{\text{def}}{=}\frac{\tau_{yx}(t)}{\eta_0\,\dot{\gamma}^0}$
Time	$\tau\overset{\text{def}}{=}\omega t$
Weissenberg number	$We\overset{\text{def}}{=}\lambda\dot{\gamma}^0$
Deborah number	$De\overset{\text{def}}{=}\lambda\omega$

We can now substitute Eq. 5.131 into Eq. 5.128 to robtain

$$\left(1+De\tan\tau+We^2\cos^2\tau\right)\mathbb{N}_1+\left(De^2\tan\tau+2\,De\right)\frac{\mathrm{d}}{\mathrm{d}\tau}\mathbb{N}_1 + De^2\frac{\mathrm{d}^2}{\mathrm{d}\tau^2}\mathbb{N}_1+2\,We\cos^2\tau=0 \tag{5.132}$$

The above equation does not have an analytical solution. In fact, the special case for a vanishing Weissenberg number, $We \to 0$, written as

$$\left(1+De\tan\tau\right)\mathbb{N}_1+\left(De^2\tan\tau+2\,De\right)\frac{\mathrm{d}}{\mathrm{d}\tau}\mathbb{N}_1+De^2\frac{\mathrm{d}^2}{\mathrm{d}\tau^2}\mathbb{N}_1=0 \tag{5.133}$$

also does not have an analytical solution. However, we can solve Eq. 5.133 numerically for $\mathbb{N}_1$, then solve for $\mathbb{S}$ using Eq. 5.131. Figure 5.29 presents the Lissajous curves developed using the corotational Maxwell model for various frequencies and deformations. The Pipkin plot presented in Fig. 5.29 clearly shows linear viscoelasticity, corresponding to small amplitude oscillatory shear in the bottom row, while everything above reflects non-linear behavior, corresponding to large amplitude oscillatory shear.

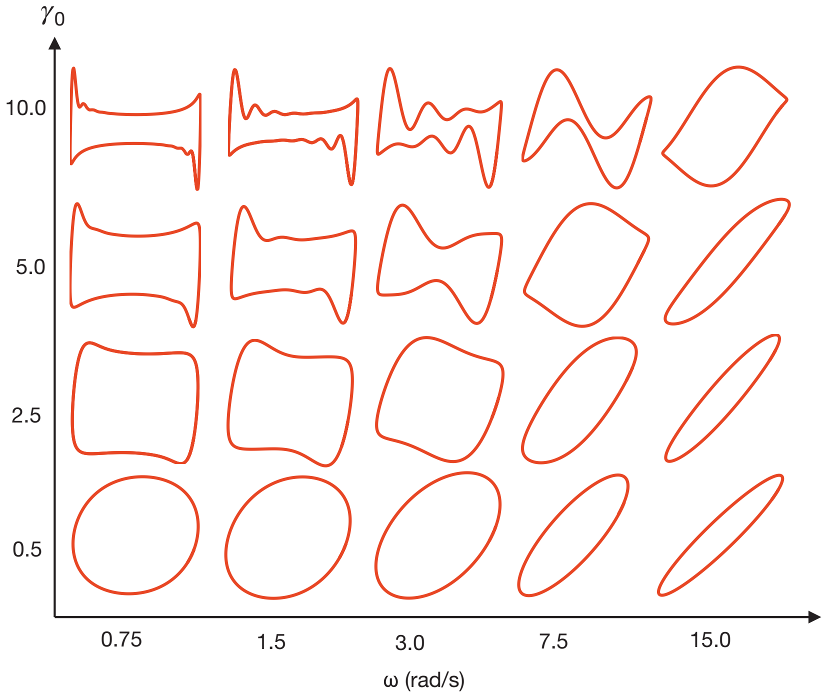

Figure 5.29 Normalized Lissajous curves of a corotational Maxwell model for small and large amplitude oscillatory shear tests.

5.2.3 Integral Viscoelastic Models

Integral models with a memory function have been widely used to describe the viscoelastic behavior of polymers and to interpret their rheological measurements [16–18]. In general, the single integral model can be written as

$$\underline{\underline{\tau}} = \int_{-\infty}^{t} M\left(t - t'\right) \underline{\underline{S}}\left(t'\right) \mathrm{d}t' \tag{5.134}$$

where $M\left(t - t'\right)$ is a memory function, and a deformation-dependent tensor is defined by

$$\underline{\underline{S}}\left(t'\right) = \phi_1\left(I_1, I_2\right) \underline{\underline{\gamma}}_{[0]} + \phi_2\left(I_1, I_2\right) \underline{\underline{\gamma}}^{[0]} \tag{5.135}$$

where I_1 and I_2 are the first invariant of the Cauchy and Finger strain tensors, respectively.

Table 5.3 [19–23] defines the constants ϕ_1 and ϕ_2 for various models. In Eq. 5.135, $\underline{\underline{\gamma}}_{[0]}$ and $\underline{\underline{\gamma}}^{[0]}$ are the finite strain tensors given by

$$\underline{\underline{\gamma}}_{[0]} = \underline{\underline{\Delta}}^{t} \cdot \underline{\underline{\Delta}} - \underline{\underline{\delta}} \quad \text{and} \tag{5.136}$$

$$\underline{\underline{\gamma}}^{[0]} = \underline{\underline{\delta}} - \underline{\underline{E}} \cdot \underline{\underline{E}}^{t} \tag{5.137}$$

Table 5.3 Definition of Constants in Eq. 5.135

Constitutive model	ϕ_1	ϕ_2
Lodge rubber-like liquid	1	0
K-BKZ*	$\dfrac{\partial W}{\partial I_1}$	$\dfrac{\partial W}{\partial I_2}$
Wagner**	$\exp\left(-\beta\right)\sqrt{\alpha I_1 + \left(1-\alpha\right) I_2 - 3}$	0
Papanastasiou-Scriven-Macosko***	$\dfrac{\alpha}{\left(\alpha-3\right) + \beta I_1 + \left(1-\beta\right) I_2}$	0

* $W\left(I_1, I_2\right)$ represents a potential function that can be derived from empiricisms or molecular theory.
** Wagner's model is a special form of the K-BKZ model
*** The Papanastasiou-Scriven-Macosko model is also a special form of the K-BKZ model.

The Lodge rubber-like liquid presented in Table 5.3 is a version of the Maxwell model in integral form. The terms Δ_{ij} and E_{ij} are displacement gradient tensors[5] defined by

---

[5] Another combination of displacement gradient tensors often used are the *Cauchy strain tensor* and the *Finger strain tensor* defined by $\underline{\underline{B}}^{-1} = \underline{\underline{\Delta}}^{t} \cdot \underline{\underline{\Delta}}$ and $\underline{\underline{B}} = \underline{\underline{E}} \cdot \underline{\underline{E}}^{t}$, respectively.

$$\Delta_{ij} = \frac{\partial x_i'(x,t,t')}{\partial x_j} \quad \text{and} \tag{5.138}$$

$$E_{ij} = \frac{\partial x_i(x',t',t)}{\partial x_j'} \tag{5.139}$$

where the components Δ_{ij} measure the displacement of a particle at past time t' relative to its position at present time t, and the terms E_{ij} measure the material displacements at time t relative to the positions at time t'.

A memory function $M(t-t')$ is often applied and leads to commonly used constitutive equations written as

$$M(t-t') = \sum_{k=1}^{n} \frac{\eta_k}{\lambda_k{}^2} \exp\left(-\frac{t-t'}{\lambda_k}\right) \tag{5.140}$$

where λ_k and η_k are relaxation times and viscosity coefficients at the reference temperature T_{ref}, respectively.

Once a memory function has been specified, several material functions can be calculated using [24]

$$\eta(\dot{\gamma}) = \int_0^\infty M(s)\, s\,(\phi_1 + \phi_2)\, \mathrm{d}s \tag{5.141}$$

$$\psi_1(\dot{\gamma}) = \int_0^\infty M(s)\, s^2\,(\phi_1 + \phi_2)\, \mathrm{d}s \quad \text{and} \tag{5.142}$$

$$\psi_2(\dot{\gamma}) = \int_0^\infty M(s)\, s^2\,(\phi_2)\, \mathrm{d}s \tag{5.143}$$

For example, Figs. 5.30 and 5.31 present the measured [25] viscosity and first normal stress difference data, respectively, for three blow molding grade, high density polyethylenes along with a fit obtained from the Papanastasiou-Scriven-Macosko [23] form of the K-BKZ equation. A memory function with a relaxation spectrum of 8 relaxation times was used. The coefficients used to fit the data are summarized in Table 5.4 [17]. The viscosity and first normal stress coefficient data presented in Figs. 5.30 and 5.31 where fitted with the Wagner model [22] form of the K-BKZ equation [20,21]. Luo and Mitsoulis used the K-BKZ model with the data in Table 5.4 to simulate the flow of HDPE through annular dies. Figure 5.32 [17] shows simulation results for a converging, a straight, and a diverging die geometry. The results shown in Fig. 5.32 were in good agreement with experimental results[6].

---

[6] The quality of the agreement between experiment and simulation varied between the resins.

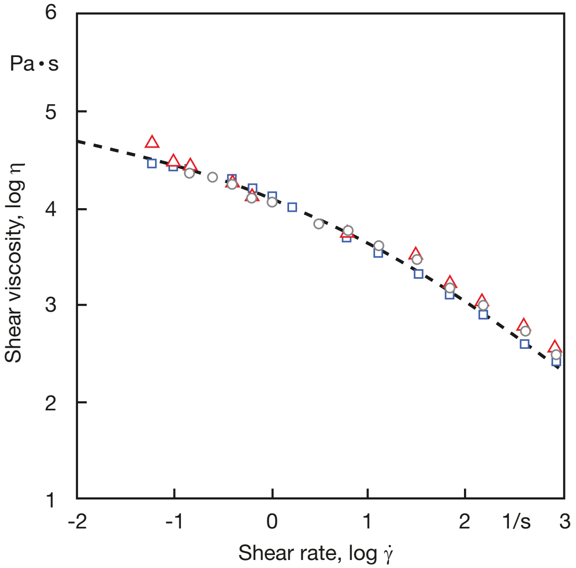

Figure 5.30 Measured and predicted shear viscosity for various high density poly-ethylene resins at 170 °C

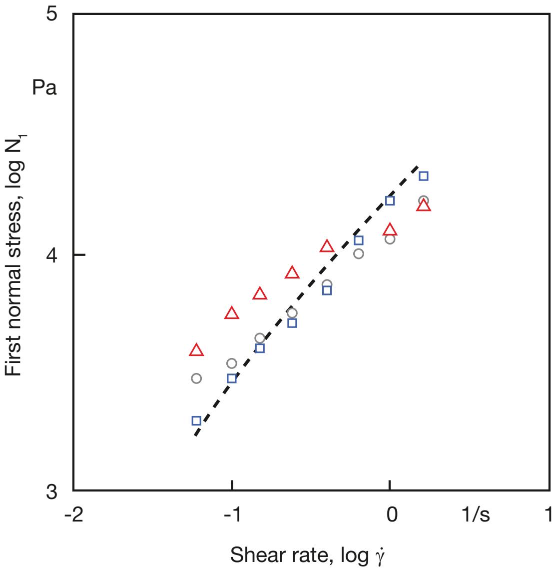

Figure 5.31 Measured and predicted first normal stress difference for various high density polyethylene resins at 170 °C

Table 5.4 Material Parameter Values in Eq. 5.127 for Fitting Data of High Density Polyethylene Melts at 170 °C

k	λ_k (s)	η_k (Pa s)
1	0.0001	52
2	0.001	148
3	0.01	916
4	0.1	4210
5	1.0	8800
6	10.0	21,200
7	100.0	21,000
8	1000.0	600

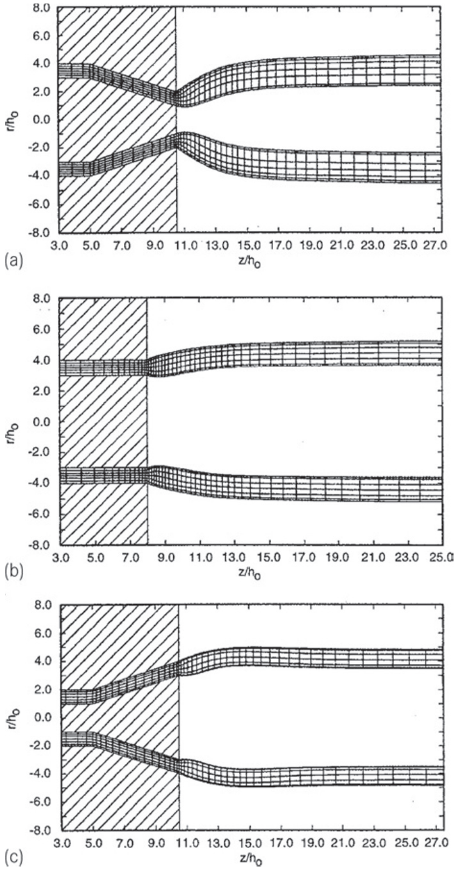

Figure 5.32 Predicted extrudate geometry for:
(a) converging, (b) straight, and (c) diverging annular dies

Example 5.4 Lodge rubber-like liquid

Evaluate the Lodge rubber-liquid in steady, simple, shear flow.

For this problem we consider the flow field

$$u_x = (u/h)\, y$$

$$u_y = 0$$

$$u_z = 0$$

Here, we start with the integral form of the stress tensor

$$\underline{\underline{\tau}} = \int_{-\infty}^{t} M(t-t')\, \underline{\underline{S}}(t')\, \mathrm{d}t' \tag{5.144}$$

which for the Lodge rubber-like liquid reduces to

$$\underline{\underline{\tau}} = \int_{-\infty}^{t} M(t-t')\, \underline{\underline{\gamma}}_{[0]}(t')\, \mathrm{d}t' \tag{5.145}$$

For a simple shear flow, $\underline{\underline{\gamma}}_{[0]}$ is expressed as

$$\underline{\underline{\gamma}}_{[0]} = \begin{pmatrix} \gamma_{yx}^2 & \gamma_{yx} & 0 \\ \gamma_{yx} & 0 & 0 \\ 0 & 0 & 0 \end{pmatrix} \tag{5.146}$$

and the components of the stress tensor are reduced to

$$\tau_{yx}(t) = \int_{-\infty}^{t} M(t-t')\, \gamma_{yx}(t,t')\, \mathrm{d}t' \tag{5.147}$$

$$\tau_{xx}(t) - \tau_{yy}(t) = \int_{-\infty}^{t} M(t-t')\, \gamma_{yx}^2(t,t')\, \mathrm{d}t' \tag{5.148}$$

$$\tau_{yy}(t) - \tau_{zz}(t) = 0 \tag{5.149}$$

where the strain from t to t' is given by

$$\gamma_{yx}(t,t') = \int_{t}^{t'} \dot{\gamma}_{yx}(t'')\, \mathrm{d}t'' \tag{5.150}$$

For steady state, simple shear flow we can re-write the above equations as

$$\tau_{yx}(t) = \int_{-\infty}^{t} M(t-t')\,\mathrm{d}t'\,\gamma_{yx} \tag{5.151}$$

$$\tau_{xx}(t) - \tau_{yy}(t) = \int_{-\infty}^{t} M(t-t')\,\mathrm{d}t'\,\gamma_{yx}^{2} \tag{5.152}$$

$$\tau_{yy}(t) - \tau_{zz}(t) = 0 \tag{5.153}$$

and the material functions reduce to

$$\eta = \sum_{k}^{n} \eta_k \tag{5.154}$$

$$\Psi_1 = 2\sum_{k}^{n} \eta_k\,\lambda_k \tag{5.155}$$

$$\Psi_2 = 0 \tag{5.156}$$

References

[1] Ferry, J. D., Viscoelastic Properties of Polymers, 3rd ed., John Wiley & Sons, New York, (1980).

[2] Wübken, G., Ph.D. Thesis, IKV, RWTH-Aachen, (1974).

[3] Williams, M. L., Landel, R. F., Ferry, J. D., *J. Amer. Chem. Soc., 77*, 3701, (1955).

[4] Münstedt, H., *Rheol. Acta, 14*, 1077, (1975).

[5] Marvin, R. S., Oser, H., *J. Research Natl. Bur. Standards, B66*, 171, (1962).

[6] Bird, R. B., Wiest, J. M., *Annu. Rev. Fluid Mech., 27*, 169, (1995).

[7] Keunings, R., Simulation of Viscoelastic Fluid Flow, in Computer Modeling for Polymer Processing, Ed. C. L. Tucker III, Hanser Publishers, Munich, (1989).

[8] Crocket, M. J., Davies, A. R., Walters, K., Numerical Simulation of Non-Newtonian Flow, Elsevier, Amsterdam, (1984).

[9] Debbaut, B., Marchal, J. M., Crochet, M. J., *J. Non-Newtonian Fluid Mech., 29*, 119, (1988).

[10] Dietsche, L., Dooley, J., *SPE ANTEC, 53*, 188, (1995).

[11] Dooley, J., Hughes, K., *SPE ANTEC, 53*, 69, (1995).

[12] Baaijens, J. P. W., Evaluation of Constitutive Equations for Polymer Melts and Solutions in Complex Flows, Ph.D. Thesis, Eindhoven University of Technology, Eindhoven, The Netherlands, (1994).

[13] Bird, R. B., Armstrong, R. C., Hassager, O., Dynamics of Polymeric Liquids, Vol. 1, John Wiley & Sons, New York, (1977).

[14] A. J. Giacomin, R. B. Bird, L. M. Johnson, A. W. Mix, *J. Non-Newton. Fluid Mech., 166 (19–20)*, 1081–1099, (2011).

[15] F. T. Trouton, *Proc. Roy. Soc., A77*, 426, (1906).

[16] Laun, H. M., *Rheol. Acta, 17*, 1, (1978).

[17] Luo, X.-L., Mitsoulis, E., *J. Rheol., 33*, 1307, (1989).

[18] Kiriakidis, D. G., Mitsoulis, E., *Adv. Polym. Techn., 12*, 107, (1993).

[19] Lodge, A. S., Elastic Liquids, Academic Press, London, (1960).

[20] Kaye, A., Non-Newtonian Flow in Incompressible Fluids, CoA Note No. 134, The College of Aeronautics, Cranfield, (1962).

[21] Bernstein, B., Kearsley, E., Zapas, L., *Trans. Soc. Rheol., 7*, 391, (1963).

[22] Wagner, M. H., *Rheol. Acta, 18*, 33, (1979).

[23] Papanastasiou, A. C., Scriven, L. E., Macosko, C. W., *J. Rheol., 27*, 387, (1983).

[24] Bird, R. B., Armstrong, R. C., Hassager, O., Dynamics of Polymeric Liquids, 2nd ed., Vol. 1, John Wiley & Sons, New York, (1987).

[25] Orbey, N., Dealy, J. M., *Polym. Eng. Sci., 24*, 511, (1984).

6

Rheometry

The measurement of rheological properties and the evaluation of fluid models require specific devices that can be summarized as rheometers. These devices are needed to achieve different objectives. Research needs them for complex measurements such as the investigation of viscosity and normal stress differences as well as deriving and evaluating flow models. In industry they are needed to design machines and fixtures such as mixers, extruders, injection molding machines, and molds. They are needed in product and process design for the selection of materials and for processing simulation, but also for the development of completely new materials. In addition, quality control during production becomes more and more important and requires simple analyses to check material consistency. Rheometers are also used to understand complex behavior of polymers in the large and relatively unexplored field of non-linear viscoelasticity.

Recent improvements in sensor temperature stability and reaction time allow for both inline measurements of the material flow properties and active control of the process.

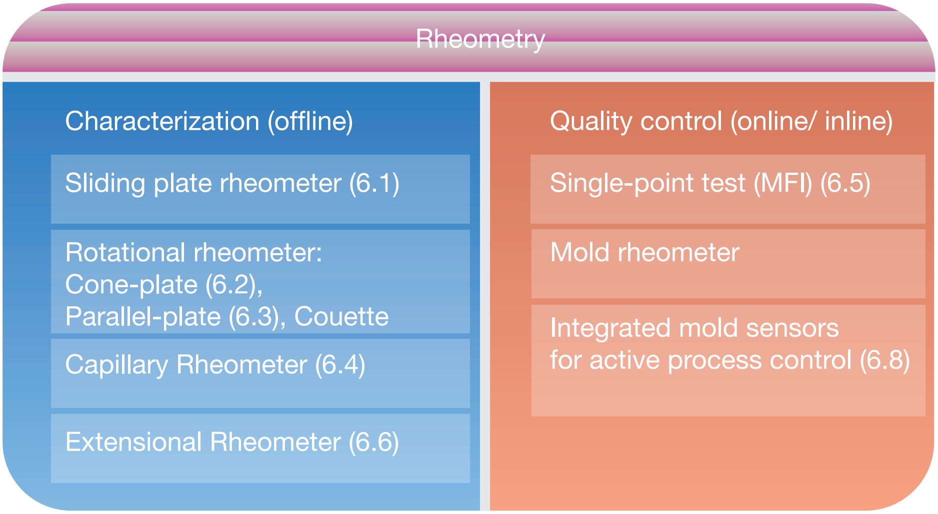

Figure 6.1 Classification of rheometry devices

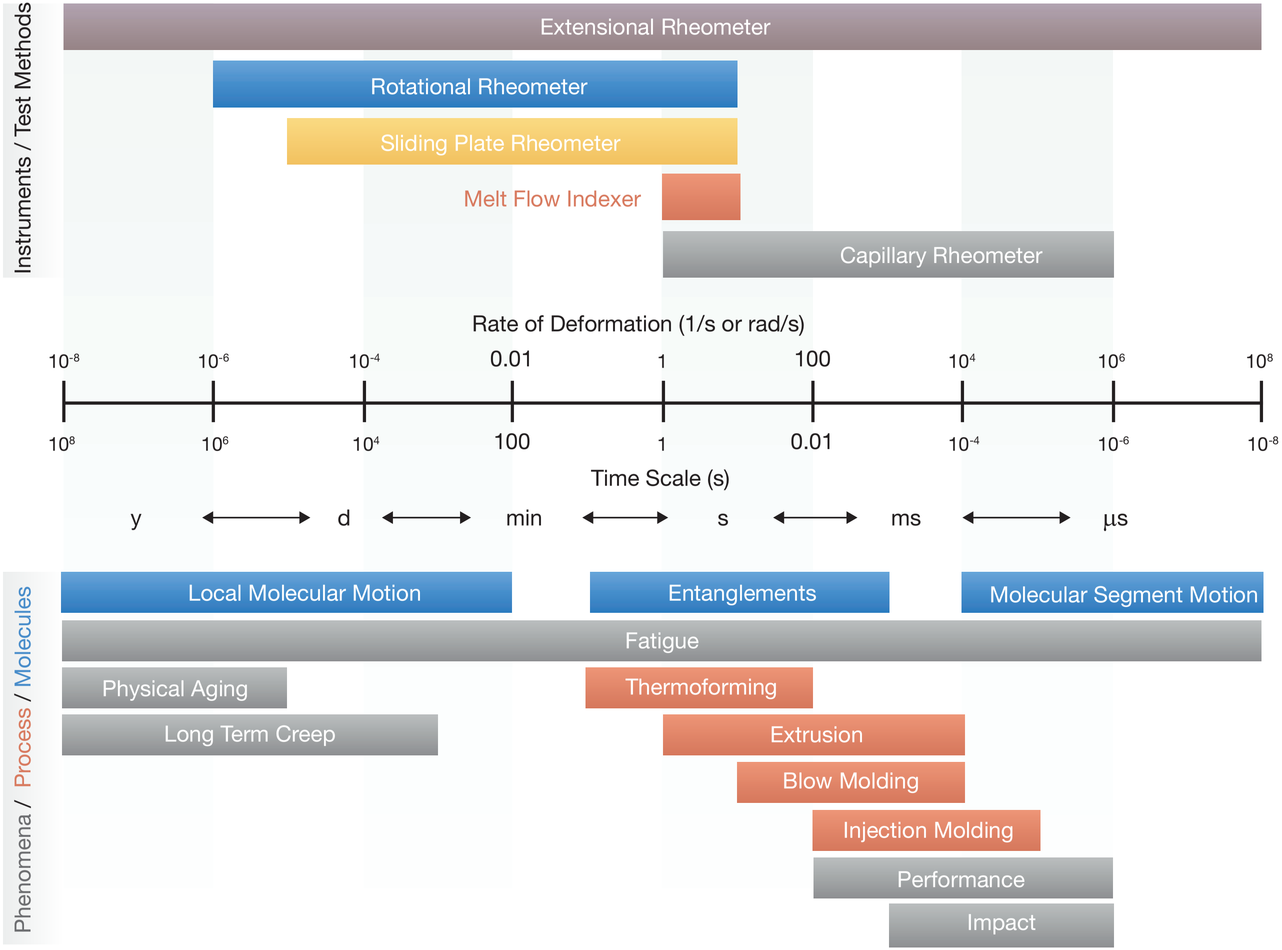

Figure 6.2 Relation between rate of deformation, test methods, and processing

Depending on their application in research and development or in production, rheometers can be classified as offline and online/inline measurement techniques, respectively, see Figure 6.1.

The different test methods will be explained in the subsections identified in Fig. 6.1, except for the Couette device, which is not commonly used in polymer rheology, and mold rheometers, which have been outperformed by integrated mold sensors and are therefore rarely used. However, it is important to know that the choice of rheometer also depends on the phenomenon of interest or the processing technology the data are needed for.

Figure 6.2 shows the rate of deformation achievable with the different measurement techniques. In addition, it explains how the rate of deformation corresponds to the time scale of molecular movement. The diagram also relates the phenomena or properties under investigation and common polymer processes to the different test methods. Slow deformations (on the left) only affect local molecular movement such as rotations, while fast deformations disentangle the molecular chains and allow for changes of location of whole molecular segments. The different time scales are also related to mechanical and failure behavior, such as creep and impact.

Different manufacturing processes expose the material to varying shear rates [1, 2]. While thermoforming and extrusion subject the material to lower rates of deformation, the injection molding process exposes the polymer melt to rates of deformation as high as 10^5 s^{-1}, e.g., in thin wall applications.

This chapter will describe the most common techniques, but will also cover new developments in the area of rheometry to give the reader a comprehensive overview of the state of the art in current measuring techniques.

6.1 The Sliding Plate Rheometer

The simplest form of shear between two parallel plates can be measured with a sliding plate rheometer [3]. This type of rheometer consists of two flat plates, where the lower plate is fixed and the upper plate moves back and forth at a constant velocity. This setup generates a rectilinear flow with a velocity profile between the upper and lower plate. All streamlines are straight and parallel to one another.

The shear rate is given by

$$\dot{\gamma} = \frac{u}{h} \tag{6.1}$$

where h is the gap and u the relative velocity between the plates.

Using the shear stress τ measured by the sensor, the viscosity is computed using

$$\eta = \frac{\tau}{\dot{\gamma}} \tag{6.2}$$

This type of geometry not only avoids the non-uniform flow fields of capillary rheometers and flow irregularities associated with rotational rheometers, but can also be used to investigate orientation effects in filled systems (e.g., fiber reinforced plastics). However, there are downsides to be considered with this setup. First, maintaining the gap between the plates is a difficult task. Because of the positive first normal stress difference in most molten polymers, the shearing deformation translates to a force perpendicular to the moving direction. In order to keep the plates from separating, an opposing force must be employed without introducing mechanical friction, which would interfere with the test measurements when determining the viscosity. More importantly, the second normal stress differences can cause secondary flow in the planar directions, which pushes melt out along the side edges. Thirdly, the movement of the upper plate away from the fixed plate decreases the effective shearing area.

Combining a sliding plate rheometer with a specially designed shear stress transducer allows the measurement of shear stress directly on a small area of one of the plates. This not only eliminates the error sources of conventional sliding plate rheometers, but also allows the measurement of linear and nonlinear viscoelastic properties over a wide range of shear rates. The transducer also facilitates the generation of large, uniform, transient deformations involving high strain rates.

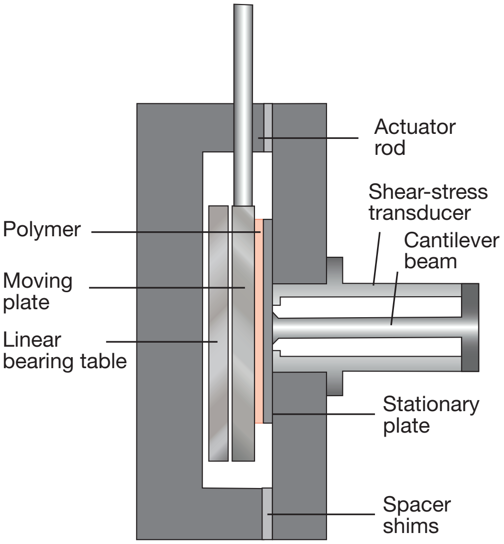

Figure 6.3 Schematic of sliding plate rheometer with shear stress transducer

Therefore, a broad spectrum of nonlinear viscoelastic properties, such as the nonlinear relaxation modulus and the shear stress growth coefficient, can be measured. It also allows for large amplitude oscillatory shear (LAOS) tests, which cannot be generated using rotational and capillary melt rheometers. The sliding plate rheometer is suitable for molten plastics, concentrated polymer solutions, raw elastomers, and other viscoelastic or thixotropic materials, because it can generate steady shear rates from 0.05 to 500 s^{-1}. A schematic of a sliding plate rheometer is shown in Figure 6.3.

6.2 The Cone-Plate Rheometer

The cone-plate rheometer is often used to measure the viscosity and the primary and secondary normal stress coefficient functions as functions of shear rate and temperature. It is the only rheometer that can perform a wide variety of rheological tests, such as stress, creep, relaxation, oscillation, and ramp tests [4, 5]. The geometry of a cone-plate rheometer and the correct filling is shown in Figure 6.4. It is advised to place an excess amount of melt between the cone and the plate to assure that the gap is completely filled, and to compensate the resin inflow due to the Weissenberg effect. The residual gap between cone and plate is the shear gap for the polymer. The geometry is determined by the radius R and the cone angle θ_0.

The experimentally measured quantities are the angular velocity of the cone, Ω, the resulting torque, T, needed to turn the cone, the total force normal to the fixed plate, F, and in some cases the pressure distribution on the fixed plate as a function of R.

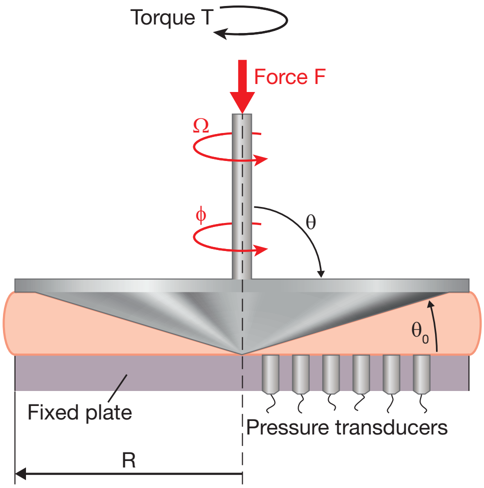

Figure 6.4 Schematic diagram of a cone-plate rheometer

Because the angle θ_0 is chosen to be very small, typically between $1° \leq \theta_0 < 4°$, the shear rate can be considered constant (for $\theta_0 < 3°$ [6]) and is given by

$$\dot{\gamma}_{\theta\phi} = \frac{\Omega}{\theta_0} \tag{6.3}$$

The shear stress can also be considered to be constant and can be related to the measured torque, assuming that the torque acting on the cone is equal to the torque acting on the plate,

$$\tau_{\theta\phi} = \frac{3T}{2\pi R^3} \tag{6.4}$$

The viscosity function can now be obtained from

$$\eta\left(\dot{\gamma}_{\theta\phi}\right) = \frac{\tau_{\theta\phi}}{\dot{\gamma}_{\theta\phi}} = \frac{3T}{2\pi R^3} \cdot \frac{\theta_0}{\Omega} \tag{6.5}$$

The primary normal stress coefficient function, ψ_1, can be calculated from the primary normal stress difference N_1 by measuring the force, F, normal to the fixed plate that is required to maintain the cone in place. Hence, ψ_1 can be computed using

$$\psi_1 = \frac{N_1}{\dot{\gamma}_{\theta\phi}^2} = \frac{2F}{\pi R^2} \cdot \frac{1}{\dot{\gamma}_{\theta\phi}^2} \tag{6.6}$$

The radial stress components within the melt increase towards the center, which results in an increase in pressure. Although it is possible to determine the secondary stress coefficient function ψ_2 from the normal stress or pressure distribution across the plate, see Fig. 6.4, it is very difficult to obtain accurate data. However, the following rule of thumb can be used for an estimate

$$\psi_2 = 0.1 \cdot \psi_1 \tag{6.7}$$

Most cone-plate rheometers have a truncated cone point. Therefore, the distance to the plate must be adjusted so that the imaginary tip of the cone touches the plate in the center. As a result, the truncated or rounded tip of the cone is a distance a away from the plate. For $\theta_0 = 1°$ and $2°$, the distance $a = 50\ \mu\text{m}$. Although the precise setting of this distance complicates the measurement preparation, it has benefits, such as the prevention of wear of the cone point, which would change the measurement geometry over time. The second is the elimination of friction between cone and plate that could incorrectly increase the measured torque. Another advantage is the possibility to measure filled systems. According to a rule of thumb, the particle size d_{part} or size of agglomerates should be

$$d_{\text{part}} \leq \frac{a}{5} \tag{6.8}$$

Larger particle agglomerates would be in contact with the shear surfaces and the increased friction would falsify the measurements [6].

Example 6.1 Cone-plate system

Determine the restrictions of a cone-plate system based on geometrical boundary conditions with the following specifications:

	Minimum	Maximum
Torque T	$2 \cdot 10^{-2}$ N cm	20 N cm
Rotational speed n	10^{-2} min^{-1}	10^{3} min^{-1}
Plate radius R	12.5 mm	25 mm
Cone angle θ	3°	6°

First, the viscosity and shear rate limits should be determined for the maximum plate radius R_2 = 25 mm and cone angle θ_2 = 6°.

The rotational speed n gives the angular velocity of the plate $\Omega = 2\pi n$. The minimum and maximum shear rate for the cone-plate geometry can be determined using Eq. 6.3.

$$\dot{\gamma} = \frac{2\pi n}{\theta}$$

$$\dot{\gamma}_{\min} = \frac{2\pi n_{\min}}{\theta_2} = \frac{2 \cdot 10^{-2}\ \text{min}^{-1} \cdot 180°}{6°} = 10^{-2}\ \text{s}^{-1}$$

$$\dot{\gamma}_{\max} = \frac{2\pi n_{\max}}{\theta_2} = 10^{3}\ \text{s}^{-1}$$

Equation 6.5 gives the viscosity

$$\eta = \frac{3T}{2\pi R^3 \dot{\gamma}}$$

$$\eta\left(\dot{\gamma}_{\min}, T_{\min}\right) = \frac{3T_{\min}}{2\pi R^3 \dot{\gamma}_{\min}} = \frac{3 \cdot 2 \cdot 10^{-2}\ \text{N cm}}{2\pi \cdot 2.5^3\ \text{cm}^3 \cdot 0.01\,\text{s}^{-1}} = 611\ \text{Pa s}$$

$$\eta\left(\dot{\gamma}_{\min}, T_{\max}\right) = 6.11 \cdot 10^{5}\ \text{Pa s}$$

$$\eta(\dot{\gamma}_{\max}, T_{\min}) = 6.11 \cdot 10^{-3}\ \text{Pa s}$$

$$\eta(\dot{\gamma}_{\max}, T_{\max}) = 6.11\ \text{Pa s}$$

Now we can evaluate how the viscosity measurement is affected if the cone angle remains constant but the radius is reduced to R_1 = 12.5 mm.

Reducing the radius by half to R_1 = 12.5 mm means shifting the viscosity to higher values according to

$$\frac{\eta_2(\dot{\gamma}, T)}{\eta_1(\dot{\gamma}, T)} = \left(\frac{R_1}{R_2}\right)^3$$

The shear rate range stays constant because it is unaffected by the radius.

Finally, we can evaluate how the viscosity measurement is affected when the radius remains constant, but the cone angle is reduced to $\theta_1 = 3°$.

Reducing the cone angle to $\theta_1 = 3°$ means shifting the viscosity range to lower values and the shear rate to higher values according to

$$\frac{\eta_2}{\eta_1} = \frac{\theta_2}{\theta_1}$$

and

$$\frac{\dot{\gamma}_2}{\dot{\gamma}_1} = \frac{\theta_1}{\theta_2}$$

6.3 The Parallel-Plate Rheometer

The parallel-plate rheometer, sometimes also referred to as a plate-plate rheometer, consists of two parallel, even plates. Similar to the cone-plate system, the lower plate is typically stationary, while the upper plate rotates (Searle type). The geometry of a parallel-plate rheometer is shown in Figure 6.5.

The gap or distance between the plates, H, should be much smaller than the radius of the plates, R, to assure homogeneous flow in the entire gap. The disadvantage in comparison to the cone-plate system is that the shear rate increases with the distance from the rotational axis ($0 \le r \le R$). In the center ($r = 0$) the shear rate is $\dot{\gamma} = 0$ and at the edge ($r = R$) it reaches its maximum. For the analysis of the measurements, the maximum shear rate at the edge is used. The gap height H also affects the shear rate, as given by

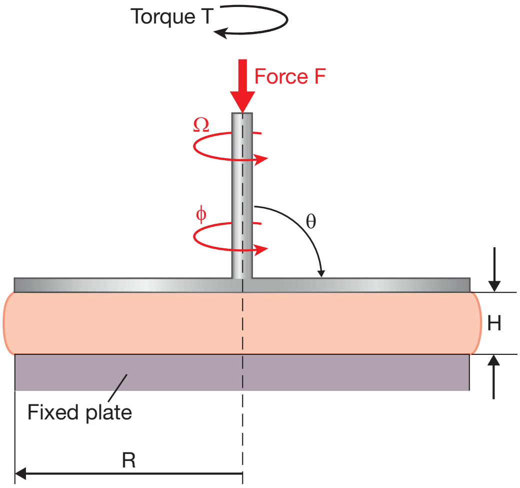

Figure 6.5 Schematic diagram of a parallel-plate rheometer

$$\dot{\gamma}_r = \frac{r \cdot \Omega}{H} \tag{6.9}$$

The maximum shear rate at the edge of the plate is given by

$$\dot{\gamma}_R = \frac{R \cdot \Omega}{H} \tag{6.10}$$

Equations 6.9 and 6.10 illustrate the importance of the gap height. With equal rotational speed, an increase in the gap results in a smaller shear rate. Therefore, a wide range of shear rates can be accomodated with this device.

With increasing gap the inhomogeneity of the shearing also increases. Therefore, the gap H should be ≤ 1 mm [6]. This system is suitable to measure filled systems; however, considering the particle size d_{part}, or the size of agglomerates respectively, the minimum gap height H_{min} should be

$$H_{\mathrm{min}} = 5 \cdot d_{\mathrm{part}} \tag{6.11}$$

When comparing the parallel-plate rheometer and the cone-plate rheometer, the latter is preferred for a wide range of applications, however, the parallel-plate system has some advantages over the cone-plate system, which are presented in Table 6.1.

Despite the many advantages offered by the parallel-plate system, the fact that the cone-plate system provides a constant shear rate in the conical gap makes it the system of choice [6].

Table 6.1 Comparison between Cone-Plate and Parallel-Plate Rheometer

Property/setting	Cone-Plate	Parallel-Plate
Shear rate	**Constant shear rate in the conical gap**	Shear rate gradient from edge of plate to rotational axis; can be varied by adjusting the gap height H
Tests	All basic rheological tests such as tension, creep, relaxation, oscillation and ramp tests; variation of shear rate by adjustment of angular velocity Ω and cone angle θ	Simple variation of shear rate by adjustment of the angular velocity Ω and the gap height H
Normal stresses	Yes	Inaccurate
Materials/ suspensions	Measurement of polymer melts, but particle size is limited ($\leq$ 10 µm), no solids	Measurement of materials with big particles as well as materials with 3D-structures; soft solids (special case: plastic melts at the transition to the solid), curing materials, filled polymer melts, elastomers, powders, and gels
Preload	Smaller preload requires shorter equilibration times	
Temperature range	The effect of thermal expansion or shrinkage is dependent on the gap height	
	e.g., $\Delta H = 5$ µm, for $H = 50$ µm the change in viscosity measurement is 10%	e.g., $\Delta H = 5$ µm, for $H = 1$ mm the change in viscosity measurement is only 0.5%

6.4 The Capillary Rheometer

The most common and simplest device for measuring shear rate viscosity in the processing range is the capillary rheometer. Its main component is a straight tube or capillary, and it was first used to measure the viscosity of water by Hagen [7] and Poiseuille [8]. A capillary rheometer has a pressure driven flow for which the velocity gradient or strain rate, and also the shear rate, will be maximum at the wall and zero at the center of the capillary, making the flow non-homogeneous.

Because pressure driven rheometers employ non-homogeneous flows, they can only measure steady shear functions, such as viscosity, $\eta(\dot{\gamma})$. However, they are widely used because they are relatively inexpensive to build and simple to operate. Despite their simplicity, long capillary rheometers provide the most accurate and process relevant viscosity data available. Another major advantage is that capillary rheometers have no free surfaces in the test region, unlike other types of rheometers such as the cone-plate rheometers. When measuring the strain rate dependent viscosity of polymer melts, capillary rheometers may offer the only satisfactory method of obtaining such data at shear rates $> 100\ \text{s}^{-1}$. This is important for processes with higher rates of deformation, such as mixing, extrusion, and injection molding. Because their design is basic and they only need a pressure head at the entrance, capillary rheometers can easily be attached to the end of a screw- or ram-type extruder for online measurements. This makes the capillary rheometer an efficient tool for industry. The shear rate range is limited to shear rates above 1 s^{-1}, because below this rate the effects of surface tension, gravity, and friction between piston and reservoir are noticeable and must be included in the analysis. Measurements in this region lead to an overprediction of viscosity [9]. The upper shear rate limit is approx. 10^7 s^{-1}, or as soon as melt fracture occurs. Furthermore, viscous dissipation may become significant at those high shear rates.

The basic features of capillary rheometers are shown in Figure 6.6. A capillary tube of radius R and length L is connected to the bottom of a reservoir. The pressure drop and flow rate through this tube are measured at constant temperatures to determine the viscosity.

Standard ISO 11443 [10] defines two possible methods: either measuring the volume flow rate Q or the test pressure p, while keeping the other parameter constant. It is recommended to use capillaries with a length l of either 16 mm or 20 mm and a diameter of 1 mm. For highly filled materials, the diameter may be changed within certain specifications.

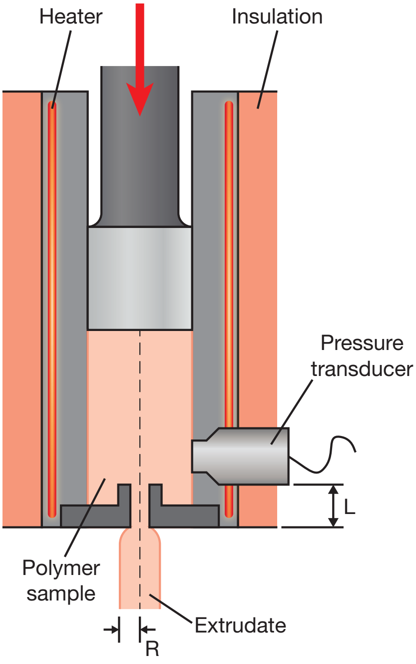

Figure 6.6 Schematic diagram of a capillary viscometer

To derive the viscosity relation, the following assumptions are made:

- no velocity in the radial, r, and the angular, θ, directions of the capillary,
- the polymer is incompressible, and
- flow is fully developed, steady, isothermal, and laminar.

The capillary rheometer can be modeled using the z-component of the equation of motion in terms of stress, τ, as

$$0=\frac{\mathrm{d}p}{\mathrm{d}z}+\frac{1}{r}\frac{\mathrm{d}}{\mathrm{d}r}\left(r\tau_{rz}\right) \tag{6.12}$$

where

$$\frac{\mathrm{d}p}{\mathrm{d}z}=\frac{p_0-p_\mathrm{L}}{L} \tag{6.13}$$

Integrating for the shear stress term gives:

$$\tau_{rz}=\frac{\left(p_0-p_L\right)r}{2L}+\frac{C_1}{r} \tag{6.14}$$

The constant C_1 is assumed to be zero because the stress cannot be infinite at the tube axis.

6.4.1 Computing Viscosity Using the Bagley and Weissenberg-Rabinowitsch Equations

When computing viscosity from data measured using a capillary rheometer, the shear stress at the wall of the capillary must be corrected as proposed by Bagley because of entrance effects [11]. Furthermore, because the shape of the velocity profile is affected by the shear thinning behavior of the polymer, the shear rate at the wall is computed using the Weissenberg-Rabinowitsch correction [12].

At the wall the apparent shear stress is given by

$$\tau_{r=R}=\tau_\mathrm{aw}=\frac{R}{2}\frac{\left(p_0-p_\mathrm{L}\right)}{L}=\frac{R}{2}\frac{\Delta p}{L} \tag{6.15}$$

Equation 6.15 requires that the capillary be sufficiently long to assure fully developed flow that renders entrance effects insignificant. At the same time, capillaries should be short so that viscous dissipation does not have to be considered. Due to end effects, the actual pressure profile along the length of the capillary exhibits a curvature, which is a source of error that must be corrected. This is shown schematically in Figure 6.7 [6].

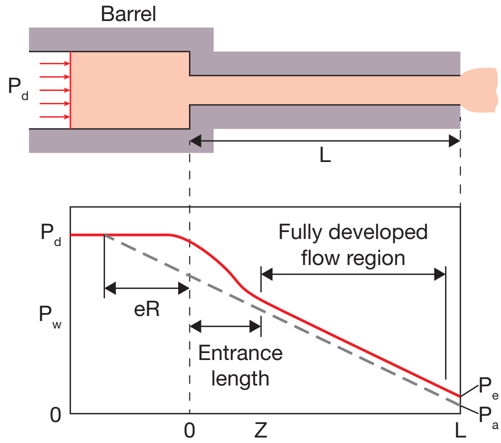

Figure 6.7 Entrance effects in a typical capillary rheometer

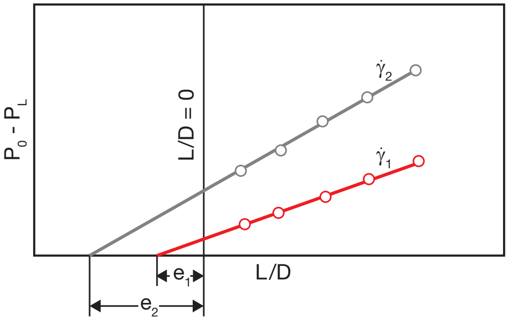

Figure 6.8 Bagley plots for two shear rates

For the correction, measurements with capillary dies of the same diameter and at least two different length-to-diameter ratios L/D must be performed. The correction factor e at a specific shear rate can be found by plotting the pressure drop for various capillary L/D ratios as shown in Figure 6.8 [6].

The true shear stress at the wall can now be calculated using the end correction e as,

$$\tau_{\mathrm{w}} = \frac{1}{2}\frac{(p_0 - p_L)}{(L/D + e)} \qquad (6.16)$$

The equation for shear stress can now be written as

$$\tau_{rz} = \frac{r}{R}\tau_{\mathrm{w}} \qquad (6.17)$$

The apparent or Newtonian shear rate $\dot{\gamma}_{\mathrm{aw}}$ at the wall is

$$\dot{\gamma}_{\mathrm{aw}} = \frac{4Q}{\pi R^3} \tag{6.18}$$

To obtain the true shear rate at the wall, $\mathrm{d}u_z/\mathrm{d}r$, the Weissenberg-Rabinowitsch equation [12] can be used

$$-\frac{\mathrm{d}u_z}{\mathrm{d}r} = \dot{\gamma}_{\mathrm{w}} = \frac{1}{4}\dot{\gamma}_{\mathrm{aw}}\left[3 + \frac{\mathrm{d}(\ln Q)}{\mathrm{d}(\ln \tau)}\right] \tag{6.19}$$

In slit dies the apparent and true shear stress are calculated using

$$\tau_{\mathrm{aw}} = \frac{H \cdot W}{2(H+W)}\frac{\Delta p}{L} \tag{6.20}$$

and

$$\tau_{\mathrm{w}} = \frac{H \cdot W}{2(H+W)}\frac{(p_0 - p_{\mathrm{L}})}{L+e} \tag{6.21}$$

and the apparent and true shear rates are calculated by

$$\dot{\gamma}_{\mathrm{aw}} = \frac{6Q}{W \cdot H^2} \tag{6.22}$$

$$\dot{\gamma}_{\mathrm{w}} = \frac{1}{3}\dot{\gamma}_{\mathrm{aw}}\left[2 + \frac{\mathrm{d}(\ln Q)}{\mathrm{d}(\ln \tau)}\right] \tag{6.23}$$

The viscosity for both capillary and slit dies can now be calculated using

$$\eta = \frac{\tau_{\mathrm{w}}}{\dot{\gamma}_{\mathrm{w}}} \tag{6.24}$$

Slit dies with flush mounted pressure transducers allow the direct measurement of the pressure drop along the flow length. Then the true shear stress is obtained by

$$\tau = \frac{H \cdot W}{2(H+W)}\frac{\Delta p}{\Delta L} \tag{6.25}$$

where H is the thickness and W the width of the slit, and $\Delta p/\Delta L$ is the longitudinal pressure gradient. Although entrance and exit effects can be neglected, for aspect ratios $H/W > 0.1$, corrections for corner effects need to be made.

6.4.2 Viscosity Approximation Using the Representative Viscosity Method

A simplified method to compute viscosity, developed by Schümmer and Worthoff [13], takes advantage of the fact that Newtonian and shear thinning materials have a streamline or radial position at which the strain rate is the same. This is schematically represented in Figure 6.9, where the common streamline is located at r_s.

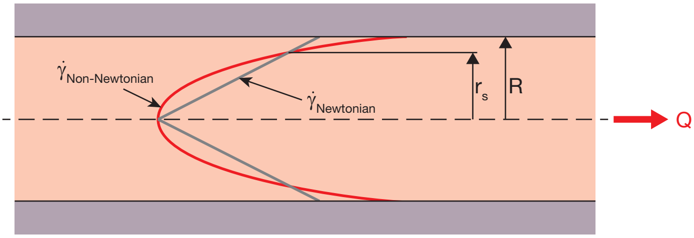

Figure 6.9 Strain rate distribution in Newtonian and non-Newtonian fluids flowing through a capillary

The position of that streamline is related to the power law index

$$r_s = R\left(\frac{2n+1}{3n}\right)^{\frac{n}{n-1}} \tag{6.26}$$

and varies between 0.7715 R and 0.8298 R for power law indices between 1.4 and 0.25. A close approximation is calculated using[1]

$$r_s \approx \frac{\pi}{4} R = 0.07854\, R \tag{6.27}$$

and the strain rate at that point is

$$\bar{\dot{\gamma}} = \frac{4}{\pi}\frac{Q}{R^4} r_s \approx \frac{Q}{R^3} \tag{6.28}$$

The shear stress at the location r_s is given by

$$\bar{\tau} = \left(\frac{p_0 - p_L}{L}\right)\frac{r_s}{2} \approx \frac{\pi}{8} R \left(\frac{p_0 - p_L}{L}\right) \tag{6.29}$$

---

[1] The value $\pi/4$ was not mathematically derived but offers a significant simplification to the equations with a final error in viscosity of less than 5%.

6.5 The Melt Flow Indexer

Because rheological properties of polymers are sensitive to even small molecular weight deviations (see Table 6.2), melt flow indexers are often used in industry as a simple and quick means of quality control. Furthermore, melt flow indexers are typically used to detect degradation during processing or to verify consistent material properties between different batches or in mixtures of virgin and regrind material. A single-point measurement is taken, using standard testing conditions specific to each polymer class on a ram-type extruder or extrusion plastometer, as shown in Figure 6.10.

The standard procedure for testing the flow rate of thermoplastics using an extrusion plastometer is described in ASTM D1238 [14]. During the test, pellets are heated in the barrel to form a melt, which is then extruded from a short cylindrical die using a piston actuated by a weight. The extruded strand is cut after 10 minutes. The weight of the polymer in grams extruded during the 10-minute test is the melt flow index (MFI) of the polymer. Sometimes the melt volume rate (MVR) is given

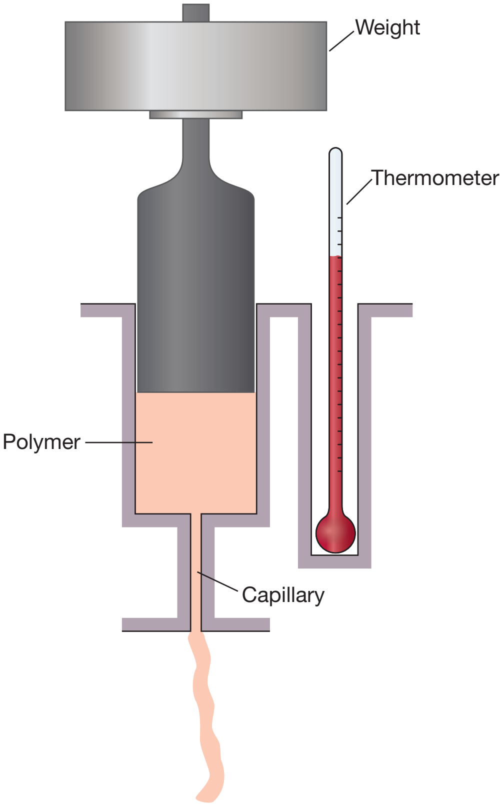

Figure 6.10 Schematic diagram of an extrusion plastometer used to measure the melt flow index

Table 6.2 Relation between MVR and Molecular Weight [15]

			Polycarbonate Makrolon			
Property	Testing conditions	Units	CD2005	2205	2405	2805
MVR	300 °C, 1.2 kg	cm^3/ 10 min	61	36	19	9.5
Number average molecular weight M_n		g/mol	9,000	9,300	11,000	13,600
Weight average molecular weight M_w		g/mol	17,000	20,000	24,200	30,500
Molecular weight distribution M_w/M_n			1.89	2.15	2.20	2.24

instead of the MFI. The MVR is measured in the same way as the MFI, but using the density of the material the weight of the extruded strand is converted to the volume in cm^3. The MVR is given as the volume extruded in 10 minutes. Because testing conditions are specific to each polymer class, MFI data cannot be compared across polymer classes, but only from grade to grade within the same class.

Table 6.2 shows both MVR and molecular weight results for different polycarbonates. It can be seen that the increase in molecular weight (from left to right) corresponds to a decrease in MVR values, indicating that less material can be extruded in the same amount of time.

6.6 Extensional Rheometry

Elongational deformation rather than shear describe polymer processes, such as film blowing, blow molding, thermoforming, fiber spinning, and foam production. Flow in converging or diverging regions of dies and molds and at the flow front during mold filling has large extensional components. Regions of extensional flow strongly influence the properties of the final part because of their high molecular orientation or the orientation of fillers with a large aspect ratios. The equipment described in the previous sections for the measurement of shear behavior of polymers cannot be used to deduce the extensional behavior of polymer melts. Although processors are confronted with extensional flow in almost every manufacturing process, extensional rheometry is the least understood field of rheology. Until the 1970s, the measurement techniques were so cumbersome, especially at processing temperatures that come with low melt viscosities, that this field did not gain much attention [16]. The most common modes of deformation that generate extensional flows are shown in Figure 6.11.

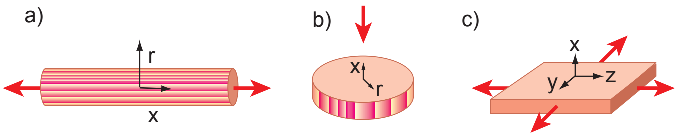

Figure 6.11 Purely extensional flow geometries;
a: simple extension, b: squeezing, c: sheet stretching

The simplest way to measure extensional viscosities is to stretch a polymer rod at elevated temperatures, Figure 6.11 (a). The stretch rate must continuously increase in order to maintain a constant strain rate because of the cross-sectional area reduction of the rod. This uniaxial deformation is dependent on the material's macromolecular structure and important for processes such as fiber spinning and those involving converging flows. The viscosity is easily computed as the ratio of instantaneous axial stress to elongational strain rate. The biggest problem with this measurement is grabbing the rod at its ends as it is pulled apart. The most common way to grab the specimen is with a toothed rotary clamp system that maintains a constant distance between the toothed clamps, and therefore maintains a constant specimen length [17]. However, this test can only be used for solids or highly viscous rubbery liquids. A schematic of Meissner's extensional rheometer using this geometry and rotary clamps is shown in Figure 6.12 [17].

The length L_0 is maintained constant throughout the test, therefore the velocity at the end will be constant and proportional to the angular velocity, Ω, and radius of the rotary clamps, R. Thus the strain rate is

$$\dot{\varepsilon} = \frac{\Omega \cdot R}{L_0} \tag{6.29}$$

Scissors cut the strand in small samples, L_A, to measure the recovery length, L_R, and calculate the strain, ε_R. An oil bath, also called buoyancy bath, is used to measure

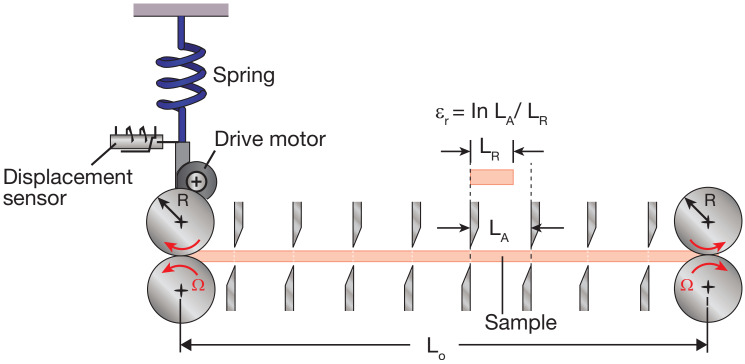

Figure 6.12 Schematic diagram of an extensional rheometer

melts with lower viscosities. The liquid of the bath has to have a higher density than the tested material.

It is not possible to achieve steady state conditions with elongational rheometry tests, because the cross-sectional area of the test specimen constantly diminishes. Therefore, time has to be incorporated into the calculation of the cross-sectional area, A,

$$A(t) = \pi \cdot R_0^2 \cdot e^{-\dot{\varepsilon} t} \tag{6.30}$$

where R_0 is the radius of the polymer strand, $\dot{\varepsilon}$ the strain rate, and t is time. Using this relation, the stress can be calculated with

$$\tau = \frac{F}{A} = \frac{F \cdot e^{\dot{\varepsilon} t}}{\pi \cdot R_0^2} \tag{6.31}$$

where F is the force acting at the end of the rod, measured by the spring and displacement sensor shown in Fig. 6.12. With stress and strain rate, the extensional viscosity, μ, for simple, uniaxial extension can be calculated using

$$\mu = \frac{\tau}{3\dot{\varepsilon}} \tag{6.32}$$

This agrees well with Trouton's rule, that the ratio of elongational to shear viscosity is approximately 3 in the Newtonian plateau. Figure 6.13 [18] examplifies this effect by comparing shear and elongational rheometry data of low density polyethylene. Pure elongational flow shows little thinning at high elongational rates; sometimes even thickening or so called strain hardening is observed [19].

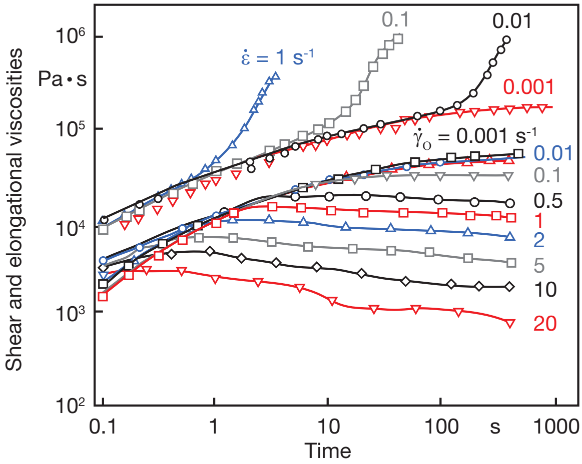

Figure 6.13 Development of elongational and shear viscosities during deformation of polyethylene samples

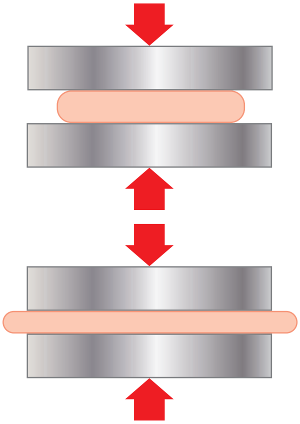

Figure 6.14 Schematic diagram of a squeezing flow

Another method to measure extensional properties that avoids clamping problems and does not generate orientation during measurements is the lubricated squeezing flow [16], which generates an equibiaxial deformation, Fig. 6.11 (b). This kind of deformation causes less orientation and is less sensitive to molecular structure. This mode of deformation applies to processes where equibiaxial deformation are exhibited by the material, such as sheet forming, compression molding, injection compression molding, but also foaming processes. Figure 6.14 shows how squeezing flow is generated. Without lubrication, the no slip conditions at the upper and lower plates significantly contribute to shear deformation of the sample. Therefore, the apparatus can either be immersed in a lubricating bath or the plates can just be coated with a lubricant of lower viscosity. The initial sample has a smaller radius than the plates. Upon compression, the sample becomes thinner as the material expands in the radial direction and is eventually squeezed out from within the plates. The varying sample radius can be calculated using the instantaneous sample thickness.

The biaxial extensional viscosity, μ, is defined as

$$\mu = \frac{\tau}{6\dot{\varepsilon}} \tag{6.33}$$

In contrast to the behavior in uniaxial elongation, a polymer material under biaxial deformation exhibits shear thinning behavior. However, to observe the shear thinning behavior, higher stress or rate of deformation levels are needed when compared to shear dominated tests [16].

Modeled after blow molding and thermoforming processes that are based on sheet stretching, Fig. 6.11 (c), equibiaxial tests are carried out by blowing a bubble and measuring the pressure required and the size of the bubble during the test, see

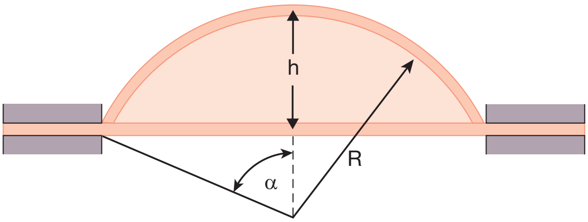

Figure 6.15 Schematic diagram of sheet inflation

Fig. 6.15. This test was successfully used to measure extensional properties of polymer membranes for thermoforming and also blow molding applications. A sheet is clamped between two plates with circular holes and a pressure differential is introduced to deform it. The pressure applied and the deformation of the sheet are monitored over time and related to extensional properties of the material. Assuming an incompressible material, the instantaneous thickness, *t*, of the sheet can be computed using:

$$t = t_0 \left(\frac{D^2}{8Rh} \right) \tag{6.34}$$

The instantaneous radius of curvature of the sheet is related to the bubble height by

$$R = \frac{D^2}{8h} + \frac{h}{2} \tag{6.35}$$

The biaxial strain can be computed using

$$\varepsilon_{\mathrm{B}} = \ln \left(\frac{2\alpha R}{D} \right) \tag{6.36}$$

and the biaxial stress can be calculated using

$$\sigma_{\mathrm{B}} = \frac{R\,\Delta P}{2t} \tag{6.37}$$

By far the easiest technique used to measure extensional properties of polymers is using entrance pressure drop measurements. Data can be readily obtained with a high-pressure capillary rheometer over a wide range of viscosities and rates. As the fluid flows from the large cross section reservoir into a smaller tube, the streamlines converge as seen in Fig. 6.16. With increasing flow rate, circulation zones start to form near the exit, Fig. 6.16 (c), which become increasingly larger, Fig. 6.16 (d).

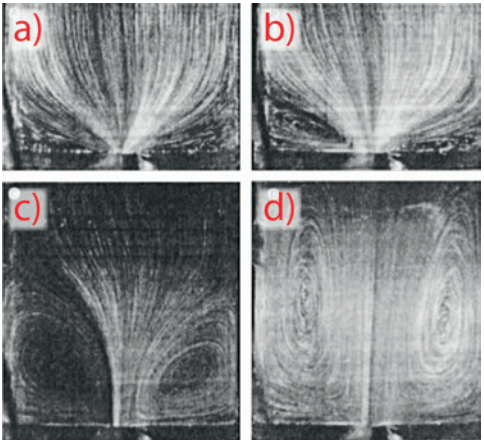

Figure 6.16 Flow fields of a Boger fluid at various flow rates in an axisymmetric contraction with a contraction ratio of 14.375: (a) Throughput Q = 0.08 ml/s, (b) Q = 0.18 ml/s, (c) Q = 0.5 ml/s, and (d) Q = 0.76 ml/s [20]

As the material moves from the large to the small cross-section, the fluid dissipates extra energy, which is reflected in an entrance pressure drop. The converging streamlines indicate the existence of the extensional flow [16]. However, the presence of the walls along the contraction area adds a shear component to the flow. Sedlacek et al. [21] employed a capillary rheometer with two different capillaries (an orifice die with L/D = 0.12 and a long die with L/D = 20) to measure the uniaxial elongational viscosity and steady shear of polymer melts at processing temperatures. Figure 6.17 shows a comparison of different semi-crystalline and amorphous materials.

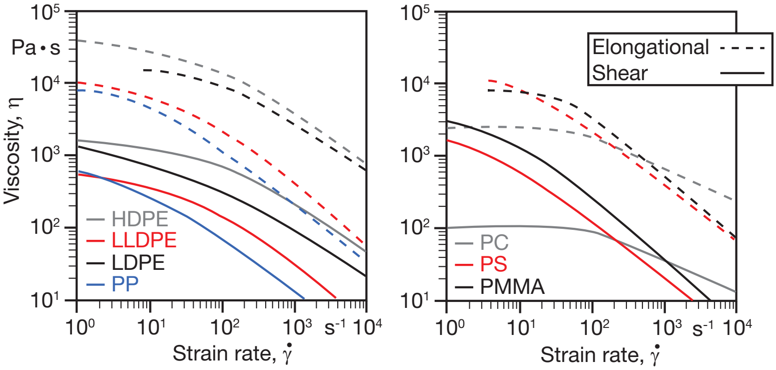

Figure 6.17 Shear (solid) and elongational (dashed) viscosity vs. strain rate curves. Lines represent data fitting [21].
Left: semi-crystalline HDPE at 210 °C, LLDPE at 170 °C, LDPE at 170 °C, and PP at 210 °C. Right: amorphous PC at 280 °C, PS at 190 °C, PMMA at 230 °C

These results agree well with Trouton's rule for the Newtonian plateau. However, with increasing strain rate, the difference between shear and elongational flow does not increase, because the capillary measurements are not solely extensional but also influenced by shear. The analysis of these data is more complex than other methods [22]. However, the advantage of fast measurements at low viscosities and high deformation rates makes it a quick alternative to more complex measuring techniques.

6.7 High Pressure Rheometers

Pressure has the same influence on viscosity as temperature: while increasing pressure or decreasing temperature raises the viscosity, lowering the pressure or increasing the temperature decreases it. This phenomenon was first investigated by Maxwell and Jung in 1957 [23]. They observed that by increasing pressure to 1680 bar, the apparent viscosity of a polyethylene (PE) melt increased 14 times compared to its viscosity at atmospheric pressure. This effect was even more pronounced for polystyrene (PS). Since the 1960s, different research groups have investigated the influence of pressure on viscosity. Hellwege et al. [24] and Herrmann et al. [25] used a Couette-type device designed by Semjonow [26]. They performed frequency sweeps up to $6 \cdot 10^2\ s^{-1}$ at elevated pressure for PS and PMMA and found master curves for the time-temperature and time-pressure superposition. Christmann and Knappe [27, 28] and Christmann and Weber [29] used the same device to measure the zero shear viscosity of PMMA and LDPE with different molecular weights. They found that the shear viscosity is not only pressure and temperature invariant, but also invariant of the molecular weight as long as the structure itself is not changed. Devices that employ a pressurized capillary were developed by Westover [30] and Karl [31]. With a maximum pressure of 5000 bar, they were able to break the high pressure record of all rheometers thus far. Lord [32] was the first to present data for polycarbonate (PC) from a modified injection molding die concept. Since the early measurements, many devices have been built based on different principles. Goubert et al. [33] summarized and evaluated the different achievements and categorized them into four groups, as shown in Fig. 6.18. The simplest measurement requires no special equipment. It is based on the non-linearity of the pressure drop occurring in the Bagley-plots, Fig. 6.8, obtained with capillary flow or on the pressure profile generated during flow in a slit, Fig. 6.18 (a). However, the entrance effects as well as the simultaneous effects of temperature, pressure, and wall slip make it difficult to analyze the results obtained using this technique.

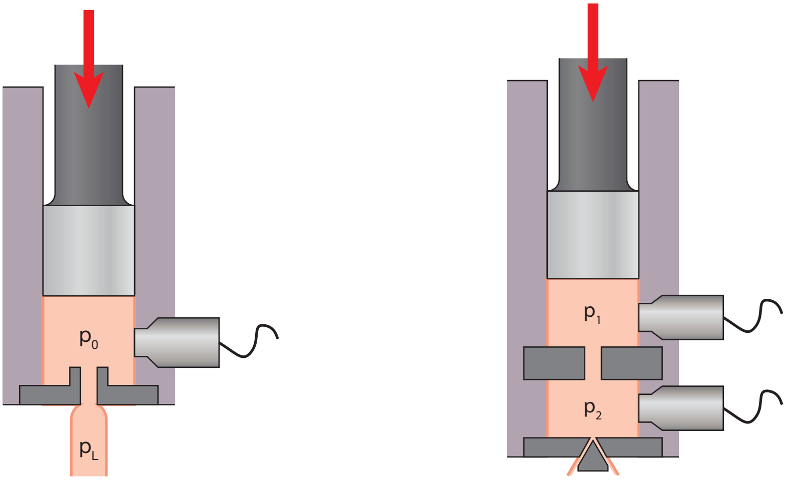

a) Non-linear pressure profile [32, 34–36]

b) Enhanced exit pressure device [33, 37]

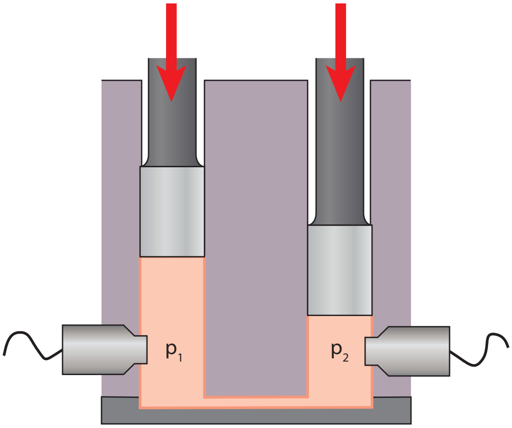

c) Pressurized capillaries or slit dies [23, 30, 31, 38, 39]

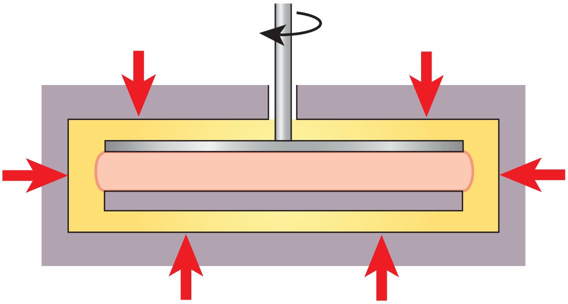

d) Pressurized drag flow devices [24–29, 40]

Figure 6.18 Schematic representation of different methods to determine the effect of pressure on viscosity (after [33])

The direct methods, Fig. 6.18 (b to d), require special devices to measure viscosity under elevated pressure. A simple design is the enhanced exit pressure technique, which uses a pressure chamber at the exit of a capillary rheometer to generate a back pressure, Fig. 6.18 (b). Another option is pressurizing the melt flowing in a slit or capillary by stationary or moving pistons, Fig. 6.18 (c). Figure 6.19 shows viscosity data of PS measured in a pressurized slit built by Kadijk and van den Brule [38]. Increased pressure and temperature shift the viscosity curve to higher or lower values, respectively. It is also clear that the shear thinning effect, represented by the Power Law index *n*, is pressure and temperature invariant [41].

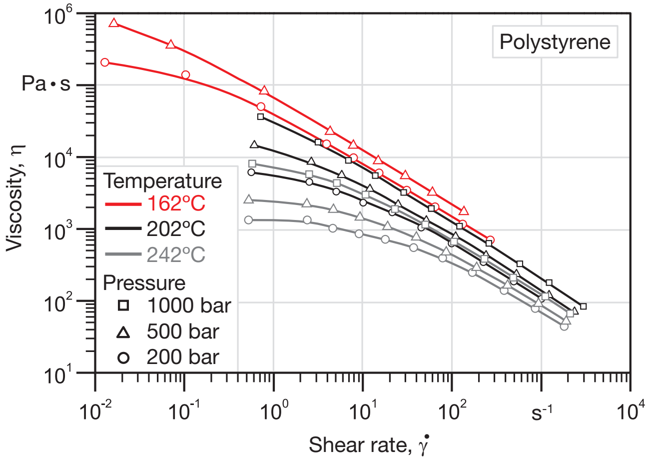

Figure 6.19 Shear rate dependent viscosity at elevated pressures of polystyrene (PS) [38]

All the previously mentioned designs are based on pressure driven flow. They have the disadvantage of creating a non-uniform flow field. In contrast, drag flow devices with uniform pressure, shear rate, and shear stress overcome the difficulties of complicated data analysis. They are useful for the investigation of the behavior at low shear rates or in transient flows. This may be Couette-type devices (as mentioned earlier) or the high pressure sliding plate rheometer (HPSPR), developed by Koran and Dealy [40], Fig. 6.20. Pressures ranging from atmospheric to 700 bar and shear rates between 0.3 and 300 s^{-1} can be explored with this device. This sliding plate rheometer is surrounded by a sealed pressure chamber, containing an inert oil that transmits the pressure onto the specimen.

With these measurements the pressure coefficient β, which is needed for simulations, can be calculated

$$\beta = \left(\frac{\mathrm{d} \ln \eta}{\mathrm{d}p} \right)_T \tag{6.39}$$

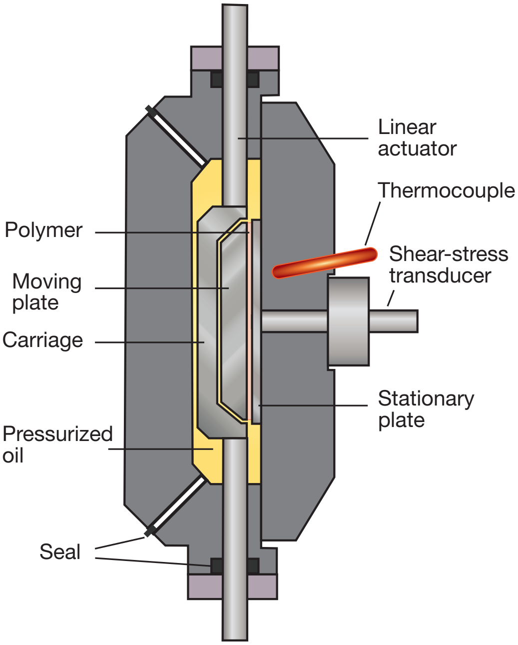

Figure 6.20 Schematic of the high pressure sliding plate rheometer

A comparison of the resulting pressure coefficients measured with devices described in Fig. 6.18 (b to d) showed that the three measuring options produce accurate data, as seen in the results presented in Fig. 6.21. However, the experimental effort varies significantly from lowest for the enhanced exit pressure device, Fig. 6.18 (b), to highest for the pressurized drag flow devices, Fig. 6.18 (d).

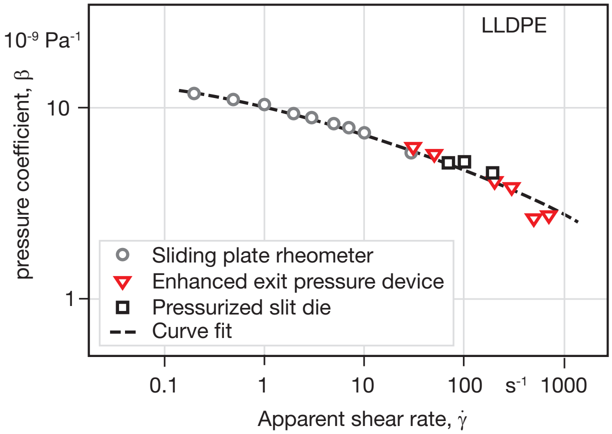

Figure 6.21 Comparison of pressure coefficients β obtained by different methods (Figure 6.18 (b–d)) [33]

Although significant research efforts have been made to measure the pressure dependent viscosity, or the pressure coefficient β, some questions about pressure dependence remain, because different research groups have reported contradicting effects, and the data base is still too small to be able to come to any definitive conclusions.

It is still unclear whether β is shear-rate dependent [35, 40, 42, 43] or shear-rate independent [38, 44]. Furthermore, there is no agreement on the temperature and pressure dependence of β: (1) Some researchers conclude that β decreases with increasing temperature [43, 45, 46]; (2) some say that β is temperature invariant [20, 47, 48]; (3) another group concluded that β increases with temperature [49]. In addition, a pressure dependence of β was observed [31, 38] in contrast to pressure independence [33–35, 42, 43, 50, 51]. Finally, there is not even an agreement as to the effect of molecular weight on β. While Westover [30] found that β increases with molecular weight, Penwell [50] observed a decrease. Clearly, much work needs to be done in this area in order to completely understand pressure effects on viscosity.

Sedlacek et al. [21] measured the shear viscosity of common amorphous and semi-crystalline thermoplastics with an enhanced exit pressure device, Fig. 6.18 (b). Regarding the complexity of their structure, the semi-crystalline materials can be listed in the following order: HDPE → LLDPE → LDPE → PP, where linear HDPE has the simplest possible structure for a polymer, which is very similar to the structure of LLDPE; LDPE is characterized by long chain branching. PP has a methyl group attached to the otherwise same backbone chain. Amorphous polymers, however, have large side groups that not only make them more rigid and hinder their crystallization, but also affect their flow behavior. The investigated materials can be ordered from PC → PS → PMMA, with increasing size of the side groups.

Measurements show that materials with higher temperature sensitivity parameters, α, also exhibit an elevated pressure sensitivity parameter, β, and vice versa. The values of both pressure and temperature coefficients order the materials as follows (from low to high sensitivity): HDPE → LLDPE → LDPE → PP → PC → PS → PMMA, which resembles their structural order. Although the measurements were carried out in the equilibrium state, at which the polymer chains are flexible, take the shape of random coils, and create entanglements, the movements of the coils are affected not only by the structure of the main chain, but by pendant groups attached to the backbone. Strong interactions or bulky side groups increase the stiffness and lower the flexibility of the polymer chain. This makes the structures highly susceptible to increased levels of molecular interaction during flow. Therefore, they are very sensitive to the rise in intermolecular friction caused by an increase in pressure or decrease in temperature that in turn create a reduction in free volume [21, 50]. By comparing shear and elongational viscosities of these polymers it was shown that the pressure coefficients were the same for both types of viscosities. Table 3.8 in Chapter 3 gives a comparison of different values found in the literature.

6.8 Integrated Mold Sensors for Quality Control

There are two basic types of online rheometers: those who are located within the mold and therefore can take measurements directly during processing and those that pull a side stream off the process for analysis. With both approaches, a pressure drop and flow rate over a flow channel of constant cross section must be measured. This is easier to achieve in a by-pass than in the mold or during processing in general. A suitable channel is either part of the product geometry or an appropriate channel must be added, e.g., at the inlet of the cavity. In addition, this section needs to be longer when the pressure gradient in the process is small, as is the case for thicker parts. In the past, different designs were employed [16], among which capillary or slit die rheometer-like devices were the most common.

A recent development following the same principle allows measuring the viscosity inside the cavity for injection molded parts with homogeneous cross section [52]. Here, a pressure and a temperature sensor are consecutively positioned along the flow path, Fig. 6.22.

A common configuration is placing the pressure sensor at the beginning of the cavity and the temperature sensor after 90% of the part length to allow measurements up to the end of filling. Using wall thickness, the distance between the sensors and the flow time, $\Delta t = t_2 - t_1$, between the sensors, the volume flow rate can be calculated, Fig. 6.23.

The pressure difference, Δp, is determined using the pressure at the transducer when the melt reaches the temperature sensor that lies downstream the pressure transducer. The pressure and melt speed allow calculation of the shear stress and shear rate necessary to compute the viscosity. Figure 6.24 shows the result of the measured viscosity at three different temperatures in a capillary rheometer in comparison to this system at known mold temperatures. It can be seen that there is good agreement between the two different measurement techniques.

For fast injection speeds and small distances between the sensors, the reaction time must be in the range of milliseconds. Based on the viscosity measurement, initial adjustments or optimization based on finite element analysis is performed to determine the machine settings. Later on an automated process control system can adjust the machine settings to reach desired molding conditions and molding quality.

Variations in the rheological behavior between cycles can affect the crystalline structure on the surface of semi-crystalline parts, the formation of weld lines, varying surface structures, and also intermittent short shots. The continuous monitoring of the viscosity and adjustment of the machine settings can therefore significantly improve the part quality, while minimizing the production of scrap.

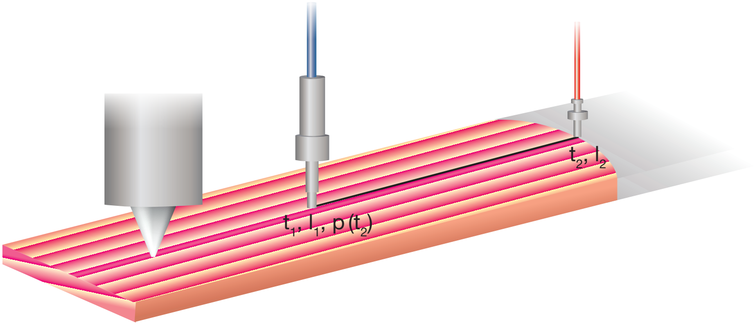

Figure 6.22 Positions of the sensors along the cavity

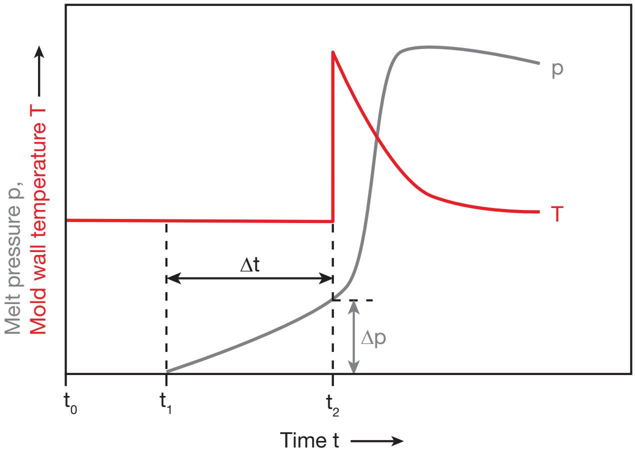

Figure 6.23 Measurement principle of the in-mold-viscosity measurement [53]

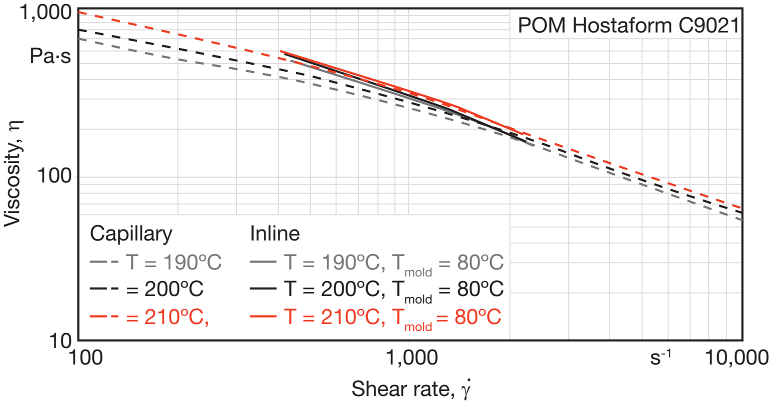

Figure 6.24 Shear rate dependent viscosity of a POM measured with a capillary rheometer and the Priamus BlueLine system [53]

It also enables the manufacturer to switch production between machines because the viscosity control adapts the machine settings for every cycle or machine based on the rheological behavior [53, 54]. In case this system is used in molds with complex geometries and wall thickness variations, adjustments in the viscosity calculations must be made.

Example 6.2 Bagley and Weissenberg-Rabinowitsch Corrections

Apply the corrections to data measured in a capillary rheometer.

The viscosity of a HDPE was measured using a capillary rheometer. Table 6.4 gives the steady state pressure in MPa for various L/D ratios and apparent shear rates calculated using Eq. 6.18.

In order to correct for the entrance effects, the pressure must be plotted as a function of L/D ratios for each shear rate as seen in Fig. 6.8 (Bagley plot). Linear fits to the apparent shear rate curves provide the entrance pressure drops, which are equal to the intercept with the y-axis, as well as the shear stresses, which numerically represent half of the slope values. The results are given in Table 6.5.

Table 6.3 Measured steady state pressures as a function of L/D ratios for a HDPE

HD-PE	$L/D = 1$	$L/D = 2$	$L/D = 5$	$L/D = 10$	$L/D = 15$
Apparent shear rate $\dot{\gamma}_{aw}$ (s^{-1})	Pressure drop p_0 (MPa)				
250	1.68	2.47	3.77	5.61	8.35
120	1.32	1.63	2.53	4.33	5.80
90	1.09	1.43	2.19	3.42	4.94
60	0.97	1.18	1.83	2.99	4.10

Table 6.4 True shear stress τ_w and obtained from linear regression of Bagley plot curves

Apparent shear rate $\dot{\gamma}_{aw}$ (s^{-1})	Pressure drop p_L (MPa)	Slope (MPa)	True shear stress τ_w (MPa)
250	1.40	0.45	0.23
120	1.01	0.32	0.16
90	0.82	0.27	0.14
60	0.76	0.22	0.11

Now the true shear rate at the wall can be calculated with the Weissenberg-Rabinowitsch Eq. 6.19. Alternatively, the apparent shear stress can be plotted in a double logarithmic graph as a function of the true shear stress. Preferably, the unit of the true shear stress is changed from MPa to Pa for this plot. The Weissenberg-Rabinowitsch correction factor is the slope of the linear fit $Y = 1.9516x + 18.59$.

Hence, the correction factor is

$$\frac{d\left(\ln \dot{\gamma}_{aw}\right)}{d\left(\ln \tau_w\right)} = 1.9516$$

The true shear rate is calculated using

$$\dot{\gamma}_w = \frac{4Q}{\pi R^3}\left[3 + \frac{d\left(\ln \dot{\gamma}_{aw}\right)}{d\left(\ln \tau_w\right)}\right] = \frac{1}{4}\dot{\gamma}_{aw}\left\{\frac{1}{4}\left[3 + \frac{d\left(\ln \dot{\gamma}_{aw}\right)}{d\left(\ln \tau_w\right)}\right]\right\}$$

The viscosity can be obtained from Eq. 6.24. The results are summarized in Table 6.6.

Table 6.5 True shear rate $\dot{\gamma}_w$ viscosity obtained by Weissenberg-Rabinowitsch correction

$\ln\dot{\gamma}_{aw}$ (s^{-1})	$\ln\tau_w$ (Pa)	True shear rate $\dot{\gamma}_w$ (s^{-1})	Viscosity η (Pas)
5.52	12.35	309	743
4.79	11.98	149	1077
4.50	11.85	111	1257
4.09	11.61	74	1481

Problems

6.1 Calculate the shear rate within a parallel-plate rheometer (R = 25 mm) at the outer edge and at half the radius. Use the maximal settings in Example 6.1 and a gap height H = 1 mm. Calculate the viscosity at the two positions using the maximal torque.

6.2 Use the data from Example 6.2 to generate the Bagley plot and the correction factor e. Calculate the true shear stress and compare the value with the results from Example 6.2.

6.3 In a capillary rheometer with a capillary radius R = 1 mm and a cone length L = 30 mm the following volume flow Q was measured for various pressure drops Δp:

Table 6.6 Measured volume flow and pressure drop data

Δp (MPa)	5	10	15	20	25	30	35
Q (mm^3/s)	57	121	188	276	522	873	1267

Use the data to calculate the apparent shear rate and shear stress. Assuming Δp to be steady-state pressure, apply the representative viscosity method to obtain the true shear rate and shear stress at the wall.

References

[1] Morton-Jones, D. H., Polymer Processing, 2^{nd} ed., Chapman & Hall, London, (1989), p. 35.

[2] N. N., Understanding Polymer Rheology, TA Instruments, (2004).

[3] Giacomin J. A., A Sliding Plate Melt Rheometer Incorporating a Shear Stress Transducer, PhD thesis, McGill University, Montreal, Canada, (1987).

[4] Pahl, M, Gleißle, W., Laun, H. M., Praktische Rheologie der Kunststoffe und Elastomere, VDI-Gesellschaft Kunststofftechnik, Düsseldorf, (1995).

[5] Dealy, J. M., Rheometers for Molten Plastics, Van Nostrand Reinhold Company, New York, (1982).

[6] Mezger, T., Das Rheologie-Handbuch, Vinzentz, Hannover, (2000).

[7] Hagen, G. H. L., *Annalen der Physik, 46*, 423, (1839).

[8] Poiseuille, L. J., *Comptes Rendus 11*, 961, (1840).

[9] Tadmor, Z., Costas, G. G., Principles of polymer processing, 2^{nd} ed., John Wiley & Sons, Hoboken, (2006).

[10] ISO 11443:2005, Plastics, Determination of the fluidity of plastics using capillary and slit-die rheometers, International Organization for Standardization, Geneva, Switzerland, (2005).

[11] Bagley, E. B., *J. Appl. Phys., 28*, 624, (1957).

[12] Rabinowitsch, B., *Z. Phys. Chem., 145*, 1, (1929).

[13] Schümmer, P., Worthoff, R. H., *Chem. Eng. Sci., 38*, 759, (1978).

[14] ASTM, Vol. 8.01, Plastics (I), ASTM, Philadelphia, (1994).

[15] Rudolph, N., *Druckverfestigung amorpher Thermoplaste*, PhD thesis, Institute of Polymer Technology, Erlangen, (2009).

[16] Macosko, C. W., Rheology: Principles, Measurements and Applications, VCH, (1994).

[17] Meissner, J., *Rheol. Acta, 10*, 230, (1971).

[18] Chatrei, Sh., Macosko, C. W., Winter, H. H., *J. Rheol., 25* , 433, (1981).

[19] Osswald, T., Menges, G., Materials Science of Polymers for Engineers, Hanser Publishers, Cincinnati, (2003).

[20] Binding, D. M., Couch, M. A., Walters, K., *J. Non-Newt. Fluid Mech., 79*, 137, (1998).

[21] Sedlacek, T., Zatloukal, M., Filip, P., Boldizar, A., Saha, P., *Polym. Eng. Sci., 44*, 1328, (2004).

[22] Cogswell, F. N., Converging flow of polymer melts in extrusion dies, *Polym. Sci. Eng., 12*, 64, (1972).

[23] Maxwell, B., Jung, A., Hydrostatic Pressure Effect on Polymer Melt Viscosity, *Modern Plastics, 35*, 174 & 276, (1957).

[24] Hellwege, V. K. H., Knappe, W., Paul, F., Semjonow, W. Druckabhaengigkeit der Viskositaet einiger Polystyrolschmelzen, *Rheol. Acta, 8*, 165, (1967).

[25] Herrmann, H. D., Knappe, W., Die temperatur- und druckinvariante Darstellung der Scherviskositaet von geschmolzenem Polymethylmethacrylat, *Rheol. Acta, 8*, 384, (1969).

[26] Semjonow, V., Ueber ein Rotationsviskosimeter zur Messung der Druckabhaengigkeit der Viskositaet hochpolymerer Schmelzen, *Rheol. Acta, 2*, 138, (1962).

[27] Christmann, L., Knappe, W., Viskositaetsmessungen an Kunststoffschmelzen mit unterschiedlichen Molekulargewichten, *Coll. Polym. Sci., 252*, 705, (1974).

[28] Christmann, L., Knappe, W., Rheologische Messungen an Kunststoff-Schmelzen mit einem neuen Rotationsrheometer, *Rheol. Acta, 15*, 304, (1976).

[29] Christmann, L., Weber, G., Beschreibung des Zusammenhangs von Schubspannung und Schergeschwindigkeit, gemessen an Polyaethylenen hoher Dichte, *Rheol. Acta, 17*, 16, (1978).

[30] Westover, R. F., Effect of Hydrostatic Pressure on Polyethylene Melt Rheology, *SPE Trans, 1*, 14, (1961).

[31] Karl, V. H., Ueber die Druckabhaengigkeit der viskoelastichen und physikalisch-chemischen Eigenschaften von Polymeren. *Angew Makromol Chem, 79*, 11, (1979).

[32] Lord, H. A., Flow of polymers with pressure-dependent viscosity in injection molding die, *Polym. Eng. Sci., 19*, 469, (1979).

[33] Goubert, A., Vermant, J., Moldenaers, P., Goettfert, A., Ernst, B., Comparison of measurement techniques for evaluating the pressure dependence of the viscosity, *Appl. Rheol., 11*, 26, (2001).

[34] Duvdevani, I. J., Klein, I., Analysis of polymer melt flow in capillaries including pressure effects, *Soc. Pet. Eng. J., 23*, 41, (1967).

[35] Laun, H. M., Polymer melt rheology with a slit die, *Rheol. Acta, 22*, 171, (1983).

[36] Klaiber, F., Lopez, I. D. G., Osswald, T., Turng, L. S., Development of a High Pressure Slit Rheometer, *Proceedings of the ANTEC conference 2006*, 2320, (2006).

[37] Driscoll, P. D., Bogue, D. C., Pressure effects in polymer rheology, *J. Appl. Polym. Sci., 39*, 1755, (1990).

[38] Kadijk, S. E., van den Brule, B. H. A. A., On the Pressure Dependency of the Viscosity of Molten Polymers. *Polym. Eng. Sci., 34*, 1535, (1994).

[39] Mackley, M. R., Spitteler, P. H. J., Experimental observations on the pressure-dependent polymer melt rheology of a linear low-density polyethylene using a multipass Rheometer, *Rheol. Acta, 35*, 202, (1996).

[40] Koran, F., Dealy, J. M., A High Pressure Sliding Plate Rheometer for Polymer Melts, *J. Rheol., 43*, 1279, (1999).

[41] van Krevelen, D. W., Properties of Polymers, 3rd ed., Elsevier, Amsterdam, (1990).

[42] Hay, G., Mackay, M. E., Awati, K. M., Park, Y., *J. Rheol., 43*, 1099, (1999).

[43] Liang, J.-Z., *Polymer, 42*, 3709, (2001).

[44] Moldenaers, P., Vermant, J., Mewis, J., Heynderickx, I., *J. Rheol., 40*, 203, (1996).

[45] Penwell, R. C., Porter, R. S., *J. Appl. Polym. Sci., 13*, 2427, (1969).

[46] Christensen, J. H., Kjaer, E. M., *J. Reinf. Plast. Comp., 18*, 651, (1999).

[47] Binding, D. M., Couch, M. A., Walters, K., *J. Non-Newt. Fluid Mech., 87*, 155, (1998).

[48] Cogswell, R. N., McGowan, J. C., *Brit. Polym. J., 4*, 183, (1972).

[49] Ito, K., Tsutsui, M., Kasajima, M., *Appl. Polym. Symp., 20*, 109, (1972).

[50] Penwell, R. C., Porter, R. S., Middleman, S., *J. Polym. Sci., 9*, 731, (1971).

[51] Couch, M. A., Binding, D. M., *Polymer, 41*, 6323, (2000).

[52] Bader, C., Patent WO 2009040077, (2009).

[53] Bader, C., Zeller, S. C., The Discovery of the Melt Front, *Kunststoffe International*, (2010).

[54] Bader, C., Kristiansen, P. M., Hitting the Nail on the Head, *Kunststoffe International*, (2011).

Subject Index

A
annular flow 129
Arrhenius shift 61
aspect ratio 120
axial annular flow 129

B
Bagley equations 198
balance
– energy 114
– equations 106
– momentum 109
Bingham
– fluid 3
– model 71
Biot 103
– number 119
Bird-Carreau model 4, 68
Bird-Carreau-Yasuda model 68
Boltzmann superposition principle 145
branching 31
Brinkman 103
– number 105
Brookfield rotational viscometer 4

C
capillary 103
– rheometer 196
– viscometer 2
Carreau-Arrhenius 69
Carreau-WLF 69
Castro-Macosko
– model 92
– viscosity model 92
Cauchy momentum equations 112
C–C bond 26
chemo-rheology 87
circular annular Couette flow 131
complex
– modulus 49, 50, 150
– shear modulus 161
– viscosity 50
cone-plate rheometer 191
consistency index 66
continuity equation 106
convected
– derivative 167
– Jeffrey’s model 168
corotational
– derivative 167
– Jeffrey’s model 168
– Maxwell model 168, 169, 174
Couette
– device 133
– flow 131
creep 15
– modulus 151
– test 151
creeping flow 132
Cross
– model 4, 70
– WLF model 70
cross-linking 87
curing 87

D
Damköhler 103
Deborah 103
– number 16, 51, 59
deformation 18
degree
– of cure 89
– of polymerization 27
deviatoric stress tensor 18
differential viscoelastic model 166
dimensionality reduction 119

dimensionless groups 102, 103
- Biot 103
- Brinkman 103
- Capillary 103
- Damköhler 103
- Deborah 103
- Fourier 103
- Giacomin 103
- Graetz 103
- Manas-Zloczower 103
- Nahme-Griffith 103
- Nusselt 103
- Péclet 103
- Prandtl 103
- Reynolds 103
- Schmidt 103
- Weissenberg 103

dimensionless variables 121
DMA 144
dynamic
- mechanical test (DMA) 144
- response 47
- tests 150, 160

E

Eisenschitz, Rabinowitsch, Weissenberg triangle 7, 20
elongational
- flow 174
- viscosity 80, 81

energy
- balance 114
- equation 116

equation
- balance 106
- continuity 106
- energy 116
- Hagen-Poiseuille 126
- momentum 112
- motion 112
- of energy 114
- of motion 109

Euler number 102
extensional
- rheometer 204
- rheometry 203

F

first contravariant convected time derivative 167
flow 125
- annular 129
- Couette 131
- parallel circular discs 137
- squeezing 134
- tube 126

Fourier 103
- law 114

four-parameter Maxwell model 156

G

generalized
- Maxwell model 154
- Newtonian fluid 60, 113
  - model 59
- Newtonian model 168

Giacomin 103
Giesekus model 4, 168, 169
glass transition temperature 27, 33, 35, 73, 74, 158, 159, 162
Graetz 103

H

Hagen-Poiseuille
- equation 126
- flow 126

heat conduction 114
Herschel-Bulkley model 72
high pressure rheometers 209
Hookean spring 10

I

integral
- model 179
- viscoelastic model 179

intrinsic viscosity 29

J

Jaumann derivative 167
Jeffrey's model 150

K

K-BKZ 180
- model 4, 179

Kelvin model 148

L

laminar flow 131
LAOS 52
large amplitude oscillatory shear 52, 176, 178

linear
- elasticity 10
- viscoelasticity 144
- viscoelastic model 144

Lissajous curve 53, 163, 176, 178
Lodge rubber-like liquid 179
- model 179

loss
- factor 50
- modulus 49, 50, 88, 150, 161
- tangent 50, 88, 161

lubrication approximation 123

M

macromolecules 25
Manas-Zloczower 103
Mark-Houwink relation 29
mass balance 106
material 107
- derivative 109

Maxwell model 2, 13, 144, 147
- four-parameter 156
- generalized 154

Maxwell-Wiechert model 154
melt
- flow indexer 202
- fracture 45
- strength 45

model
- Bingham 71
- Bird-Carreau 68
- Bird-Carreau-Yasuda 68
- Castro-Macosko viscosity 92
- convected Jeffrey's 168
- corotational Jeffrey's 168
- corotational Maxwell 168
- Cross 70
- differential viscoelastic 166
- generalized Newtonian 168
- generalized Newtonian fluid 59
- Giesekus 168
- Herschel-Bulkley 72
- integral 179
- K-BKZ 179
- linear viscoelastic 144
- Lodge rubber-like liquid 179
- Maxwell 144
- non-linear viscoelastic 164
- Papanastasiou-Scriven-Macosko 179
- Phan-Thien-Tanner 168

model
- power law 66
- simplification 117
- upper convected 168
- viscoelastic 164
- viscous flow 65
- Wagner 179
- White-Metzner 167, 168

modulus
- complex 50
- complex shear 161
- creep 151
- loss 50, 88
- of elasticity 11
- storage 50, 88
- stress relaxation 33

mold sensors 214
molecular
- structure 25
- viscosity average 29

molecular weight 27, 28, 29, 30
- average 29
- distribution 29, 30
- number average 28

momentum
- balance 109
- equations 112

monodispersed polymer 29
motion equation 112

N

Nahme-Griffith 103
Navier-Stokes equation 2, 113
Newtonian
- fluid 7
- plateau 68, 70, 81

non-linear
- viscoelasticity 164
- viscoelastic model 164
- viscoelastic response 164

normal stresses 40
Nusselt 103

O

objectivity 164
order of magnitude analysis 118

P

Papanastasiou-Scriven-Macosko 180
- model 179

parallel circular discs 137
- flow 137

parallel-plate rheometer 194
Péclet 103
Phan-Thien-Tanner model 168, 169
polydispersity index 30
power law
- index 66
- model 66

Prandtl 103
pressure
- dependence 73
- driven flow through a slit 125
- invariant viscosity 75

R

rate
- of deformation 18, 19
- of deformation tensor 60
- of energy input 116

recovery 158
- response 153

reduction dimensionality 119
relaxation 147, 159
- modulus 144
- time 14, 157

representative viscosity method 201
retardation 158
Reynolds 103
- number 102

rheometer
- capillary 196
- cone-plate 191
- extensional 204
- parallel-plate 194
- sliding plate 189

rheometry 187
rubber elasticity 3

S

Schmidt 103
shear thinning behavior 37
sheet inflation 207
shift
- Arrhenius 61
- WLF 63

simple shear flow 9, 115, 120, 165
sliding plate
- rheometer 189
- rheometry 144

slit
- flow 125
- pressure driven flow 125

small amplitude oscillatory shear 176, 178
softening temperature 162
spring constant 11
squeezing flow 134, 206
standard linear solid model 152
start-up flow 44
Staudinger's rule 29
storage modulus 49, 50, 88, 90, 150, 161, 163
stress
- overshoot 44
- relaxation 15, 32, 33, 147
- relaxation modulus 33
- tensor 113

substantial derivative 107, 109, 167
suspension rheology 82
symmetry 120

T

temperature 75
- dependence 61, 67

time scale 16
time-temperature superposition principle 145
transport phenomena 101
Trouton viscosity 3, 81
tube flow 126

U

upper convected model 168

V

van-der-Waals forces 26
velocity gradient 19
viscoelasticity 13, 143
- linear 144
- non-linear 164

viscoelastic model 164
viscometric flows 125
viscosity
- average 29
- complex 50
- elongational 81
- Trouton 81

viscous
- dissipation 114
- flow model 65

vorticity tensor 167

W
Wagner model 179
weight
– average 29
– distribution 30
Weissenberg 103
– number 51
Weissenberg-Rabinowitsch correction 70, 198
White-Metzner model 167, 168, 169
Williams-Landel-Ferry (WLF) 61
WLF 61
– Carreau 69
– equation 63
– relation 69
– shift 61, 63